DESIGN AND IMPLEMENTATION OF VARIABLE SPEED WIND ENERGY INDUCTION GENERATOR SYSTEMS FOR FAULT STUDIES

Prepared by: Paul S. Barendse
Department of Electrical Engineering
University of Cape Town

Prepared for: Department of Electrical Engineering
University of Cape Town

Thesis submitted in fulfillment of the requirements for the degree of Master of Science in Electrical Engineering

December 2004

DECLARATION

I, Paul S. Barendse, submit this thesis in fulfillment of the requirements for Master of Science Degree in Electrical Engineering at the University of Cape Town. I declare that this is my own work and has not been submitted to any other University. All the work from other sources are referenced accordingly.

Signature: Signed by candidate Signature removed Date: 23/12/04

Paul S. Barendse

ACKNOWLEDGEMENTS

I wish to thank the following people for their invaluable support:

- Professor Pragasen Pillay, for his supervision, guidance and positive suggestions throughout the project.

- To my family and friends for their unconditional love and support.

- UCT Machines Group: R. Lutchman, C. Slabbert, A. Khan, T. Mthombeni, H. Douglas, D. Johnson and C. Wozniak.

TERMS OF REFERENCE

The project was proposed by Prof. Pragasen Pillay, Electrical Machines and Drives professor at Clarkson University and part-time professor at the University of Cape Town, on the 15th of January 2003. The purpose of the project is to develop the capabilities to study faults in induction machine wind generator systems.
Prof. Pragasen Pillay's specific instructions were to:

1. Conduct a thorough literature survey on current wind energy generating systems using stator-fed squirrel cage and rotor-fed wound rotor induction generators.

2. Study the dynamic modeling of induction machines and develop a rotor field orientated control strategy for wound rotor induction machines.

3. Test the control strategy using Matlab Simulink and implement the system experimentally.

4. Using a commercially available drive, implement experimentally a stator-fed squirrel cage induction generator Wind Energy Conversion System.

5. Develop methods to simulate faults on the doubly-fed wound rotor induction machine and the stator-fed cage rotor induction machine.

6. Attempt to identify the faults using Time Domain Analysis and Motor Current Signature Analysis.

SYNOPSIS

Due to the economical and environmental benefits, Wind Energy Conversion Systems (WECS) have received tremendous growth in the past decade. The increased interest in wind energy has made it necessary to model and experimentally evaluate entire WECS, so as to attain a better understanding and to assess the performance of various systems. As a direct consequence of the increase in wind generation systems, comes the need for the reduction of operational and maintenance costs of these wind generators. The most efficient way of reducing these costs is by the early detection of the degeneration of these generators health, thus facilitating a proactive response, minimizing downtime, and maximizing productivity. The more common induction machine failures are caused by the deterioration of the stator insulation and by the breaking of rotor bars.

The thesis describes the design, modeling and implementation of two different variable speed induction generator systems for studying faults in wind energy applications. This project served as a platform for further research into the development and evaluation of a non stationary fault detection technique suitable for wind energy induction generator purposes. Some common faults are implemented on the wind generators in an attempt to identify them from measurements and by using a steady state fault analysis technique (Motor Current Signature Analysis).

For variable speed wind generation, there are two systems using induction generators. The first consist of a squirrel cage induction generator, which uses back-to-back converters in the stator circuit, as shown in Fig. 0.1. The second consists of a wound rotor induction generator, whereby the stator is directly connected to the grid and the rotor circuit consists of back-to-back converters, as shown in Fig. 0.2. When both the rotor and stator are capable of delivering power as with the wound rotor induction generator, they are known as doubly-fed induction generators (DFIG).

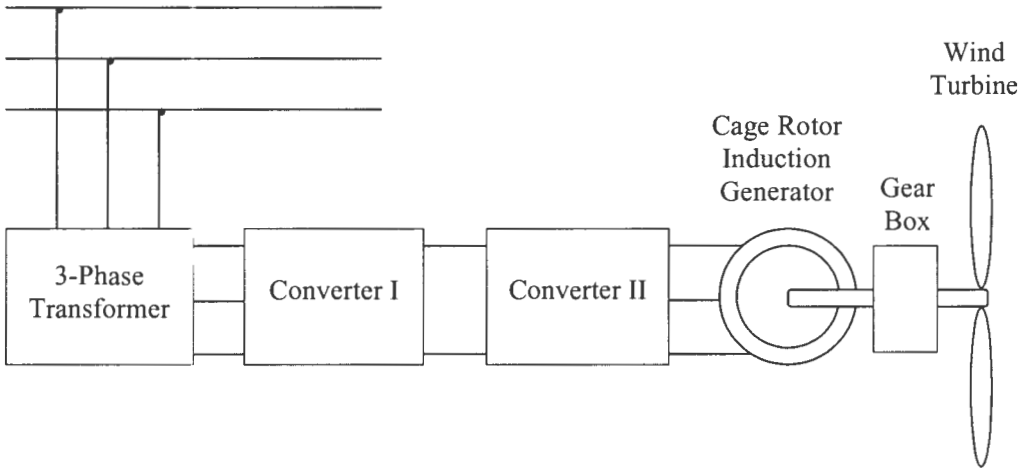

Figure 0.1: Principle layout of the Variable Speed WECS using a Cage Rotor Induction Generator

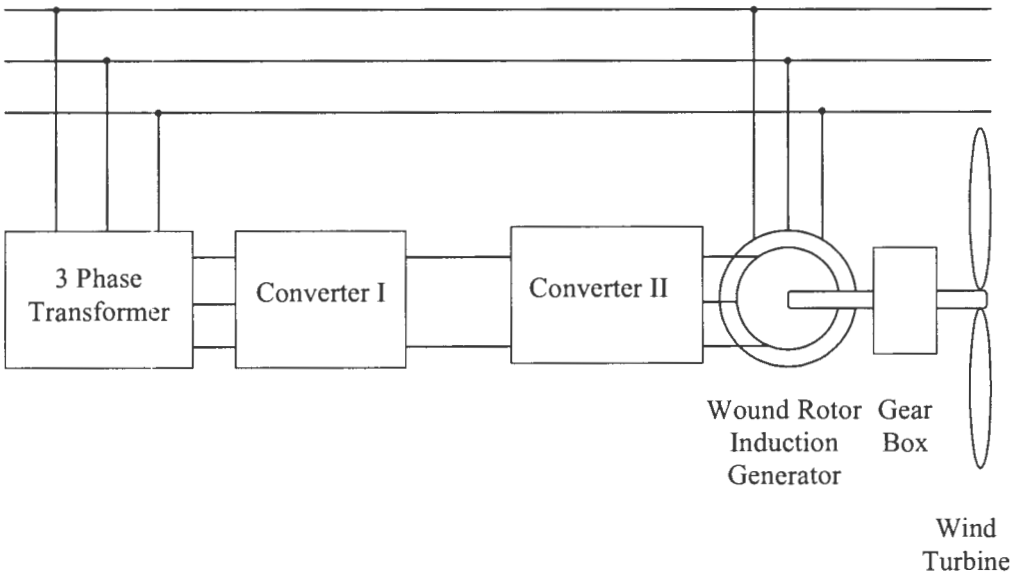

Figure 0.2: Principle layout of the Variable Speed WECS using a Wound Rotor Induction Generator

The two systems have been modeled and implemented experimentally as shown in Fig's 0.3&0.4. A commercial drive is used for the squirrel cage induction generator, whereas the doubly-fed drive is designed and constructed from fundamental principles. The wind turbine is simulated with the use of a DC machine and a current controlled thyristor converter. Tests are then carried out on the systems to illustrate their operation during steady state and transient conditions.

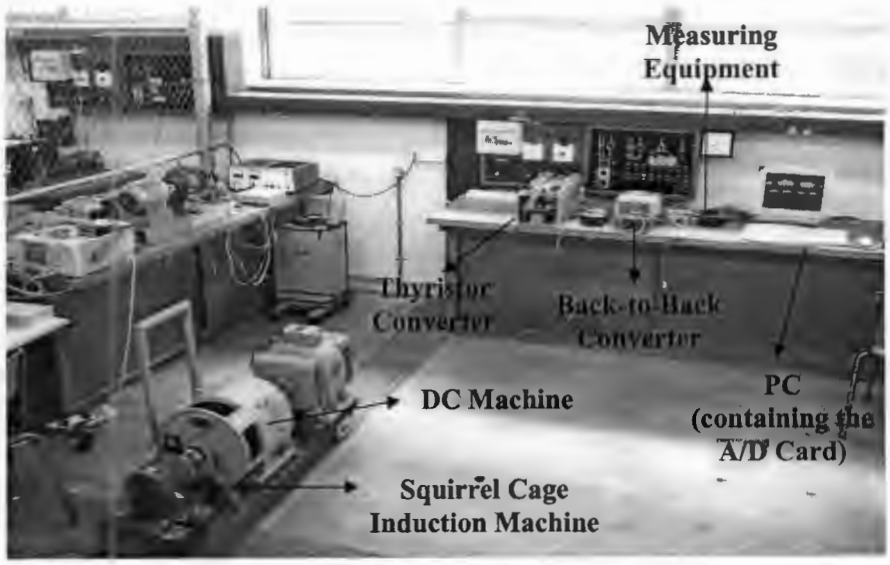

Figure 0.3: Experimental setup of the squirrel cage induction generator WECS

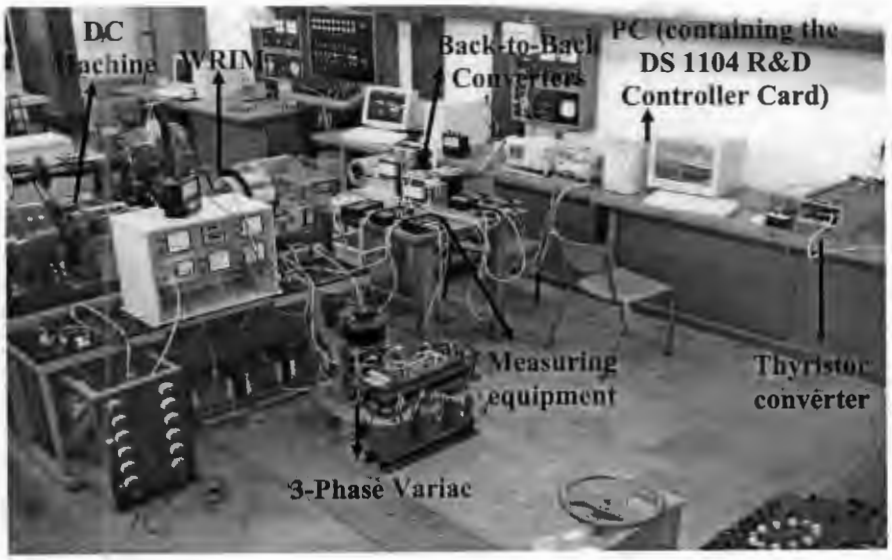

Figure 0.4: Experimental setup of the DFIG WECS

An inter-turn stator fault is simulated on the wound rotor induction machine, with the use of a resistor in parallel with a stator phase coil. A broken rotor bar fault is placed in the squirrel cage induction machine by drilling through a rotor bar. An attempt is then made to identify these faults by analysing the stator currents in the time and the frequency domains using Motor Current Signature Analysis (MCSA).

TABLE OF CONTENTS

SECTION PAGE

SECTION PAGE

SECTION PAGE

LIST OF ILLUSTRATIONS

FIGURES PAGE

FIGURES PAGE

FIGURES PAGE

FIGURES PAGE

TABLES **PAGE**

Chapter 1

1. INTRODUCTION

1.1 Overview

The thesis describes the design, modeling and implementation of two variable speed induction generator systems for studying faults in wind energy applications. The more common faults are then implemented on the wind generators and attempts are made to identify them from measurements by using Motor Current Signature Analysis. This project served as a platform for further research into the development and evaluation of a non stationary fault detection technique suitable for wind energy induction generator purposes.

1.2 Research Background

In recent years, there's been a renewed interest in renewable energy sources due to environmental problems and the eventual shortage of fossil fuels. Wind energy made considerable strides especially in Europe, particularly Denmark and Germany [1, 2]. Variable Speed Induction Generators prove to be extremely attractive for wind generation purposes, since they are able to extract greater amounts of energy from wind compared to fixed speed systems [3].

Wind generators are difficult to maintain because they are inaccessible. A large portion of these costs may be eliminated by continuously monitoring the condition of these generators, allowing for early detection of faults which in turn facilitates a proactive response, minimising downtime and increasing productivity. Almost all condition monitoring techniques are based on steady state analysis, however since wind generators operate predominantly in the transient, new research needed to be devised to detect faults during transients.

1.3 Objectives

The objectives of the thesis are to:

- conduct a thorough literature review of Wind Energy Conversion Systems using induction generators
- design from fundamental principles a vector controlled doubly-fed wound rotor induction generator drive with back-to-back converters in the rotor circuit
- using a commercially available drive, implement experimentally a stator-fed squirrel cage induction generator Wind Energy Conversion System
- develop methods to implement faults on wind generator systems and generate associated results
- perform an in depth analysis on the fault results of the two wind generator systems using Motor Current Signature Analysis
- draw conclusions on the design and implementation of the wind generator systems and the ability to implement and identify faults on the two systems

1.4 Background on Wind Energy

1.4.1 Wind Turbine Torque and Power Characteristics

The shaft torque T and power output P of a wind turbine are given by the following equations [4]

$$P = \frac{1}{2}\rho \quad A \quad Cp \quad V^3 \qquad (1.1)$$

$$T = \frac{1}{2}\rho \quad A \quad Ct \quad R \quad V^2 \qquad (1.2)$$

where ρ mass density of air

A area swept by rotor blades

V wind speed

Cp non-dimensional power coefficient

Ct non-dimensional torque coefficient

R wind turbine rotor radius

The non-dimensional power coefficient Cp is limited theoretically, to a maximum of 0.59. This is known as the Betz Limit. Cp is expressed as a function of the tip-speed ratio λ [4]

$$\lambda = \frac{\Omega R}{V} \qquad (1.3)$$

where Ω mechanical angular velocity of the wind turbine

V wind speed

R wind turbine rotor radius

From equation 1.1, it is evident that for the turbine to extract maximum energy from the wind, Cp has to be maintained at its maximum value. Since Cp is dependent on λ, it stands to reason that λ should be at its optimum value, ensuring that Cp is at its maximum value. To maintain λ at its optimum value, the rotor angular velocity must vary proportional to the wind speed. Thus maintaining the tip speed ratio λ at its optimum value and in turn, the power coefficient Cp at its maximum value ensures maximum energy capture from the turbine. This is known as Maximum Power Point Tracking (MPPT) [5].

1.4.2 Cp-λ Curves

The rotor power for any combination of wind and rotor speeds, may be obtained by the Cp-λ curves and facilitates in the design of the wind turbine. They provide immediate information about the maximum power coefficient Cp and optimum tip-speed ratio λ. Cp-λ curves for a particular wind turbine may be found from turbine tests or from modeling, however numerous variables influence the outcome of these curves. Some of these variables include lift and drag coefficients of the airfoils, which may vary as a function of flow conditions [4].

For a typical wind turbine, Cp can be expressed as a function of λ with a 6^{th} order polynomial [8].

$$Cp = a_0 + a_1\lambda + a_2\lambda^2 + a_3\lambda^3 + a_4\lambda^4 + a_5\lambda^5 + a_6\lambda^6 \qquad (1.4)$$

Where a_0, a_1, a_2, a_3, a_4, a_5, and a_6 are constants.

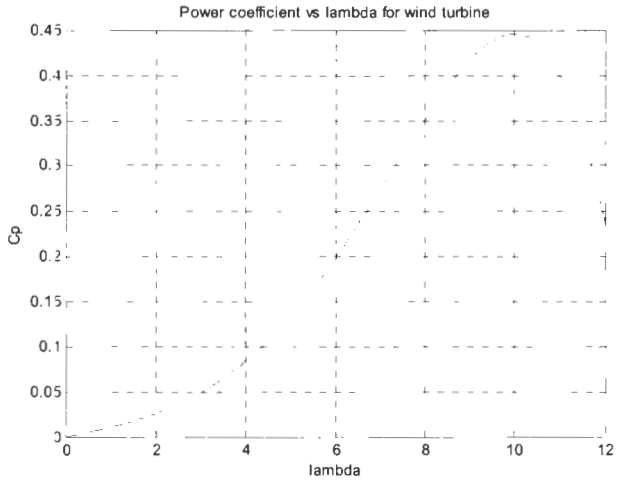

Figure 1.1: Power coefficient *Cp* versus tip speed ratio λ

The above *Cp*-λ curve, which is attained from equation 1.4, will be used to illustrate certain concepts in the forthcoming sections.

1.5 Literature Survey on Wind Energy Conversion Systems (WECS) using Induction Generators

1.5.1 Introduction

There are essentially 2 types of Wind Energy Conversion Systems (WECS), namely Constant Speed WECS and Variable Speed WECS. Variable speed generation systems capture far more energy than fixed speed systems. The energy capture efficiency of WECS is dependent upon the ratio of rotor shaft speed to wind speed. Maximum efficiency is achieved when wind speed varies proportionally to rotor shaft speed.

There are three Induction Generator WECS topologies covering the two categories mentioned above (i.e. Constant and Variable WECS). They are:
(1) Conventional Fixed Speed WECS using a Cage Rotor Induction Generator connected directly to the grid.
(2) Variable Speed WECS using a Cage Rotor Induction Generator with the converter connected to the stator circuit.

(3) Variable Speed WECS using a Wound Rotor Induction Generator (Doubly-Fed Induction Generator) with the converter connected to the rotor circuit.

The three topologies will be discussed in greater depth in the following sections.

1.5.2 Literature Survey on Constant Speed WECS

A constant speed WECS is a reliable and simple configuration where the induction generator is directly connected to the electrical grid and is connected to the turbine through the drive train (gearbox, bearings, couplings, a brake, etc.). As a result, the speed of the wind turbine is determined by the grid frequency and varies based only on slip. Thus the speed is strictly speaking not constant, but the speed is not controlled and is commonly referred to as Constant Speed WECS. The diagram below indicates such a system, whereby the generator is a Cage Rotor Induction Machine.

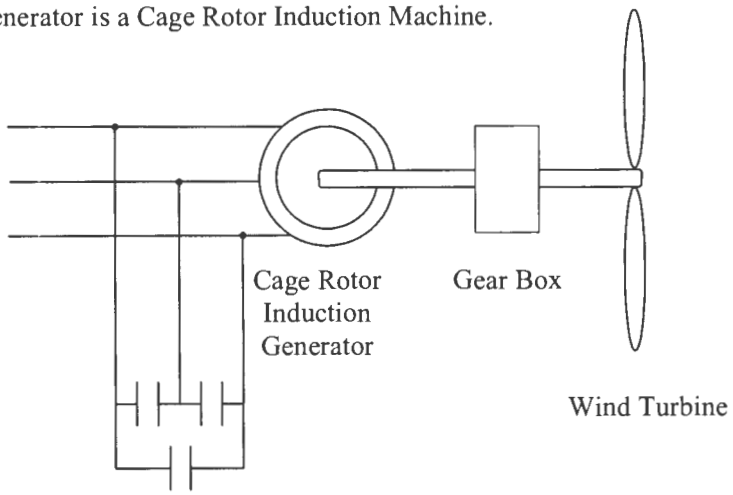

Figure 1.2: Layout of the Constant Speed WECS using an Induction Generator

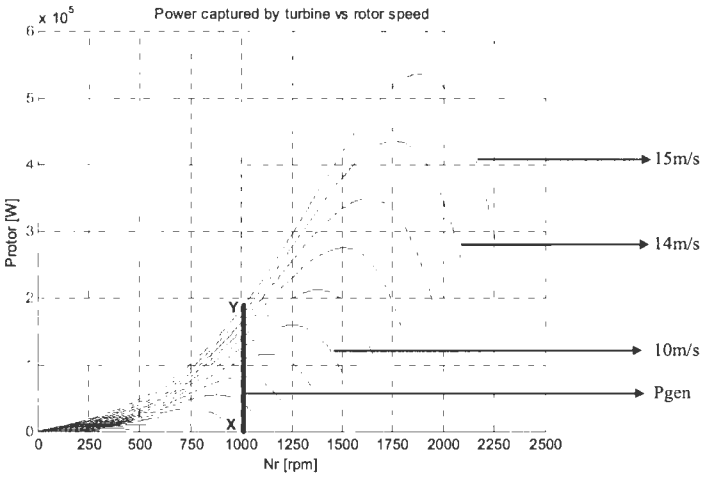

Figure 1.3: Wind turbine power *P* versus generator shaft speed *V* for a fixed speed system [6]

Fig. 1.3 indicates the various power curves attained from a wind turbine for different wind velocities (the various power curves are attained from equation 1.1 and from the *Cp* vs λ curve in Fig. 1.1). The generator used in the diagram is assumed to be a 225kW, 50Hz induction, 6 pole generator with a rated speed of 1008 r/min, which has been attained from [6]. It may be necessary to use pitch control of the blades to optimize the system performance (pitch control is where the pitch angle of the blade is varied, so as to limit the amount of turbine power). Line X-Y indicates the operating locus for the given system. It is clearly evident that the system does not capture maximum energy for various wind speeds.

Some of the more important features of a constant speed system are as follows:

- Some fixed speed systems require the large induction machine to be started using a soft starter and stopped using a mechanical breaking unit, which is quite costly.
- In an attempt to attain greater energy capture at lower wind conditions, a second winding of lower power capacity and fewer pole pairs may be added to the induction machine, thus reducing the synchronous speed. Control is needed to switch to the secondary winding at lower wind

speeds. This modification to the induction machine is however non-standard and expensive [6].

- The induction machine introduces a lagging power factor. This can be compensated by introducing large capacitor banks across the machine's terminals [6].
- The constant-speed WECS are designed for lower shaft speeds where the power curves of the system are closer together [6].
- When introducing pitch control to optimise the performance of the fixed speed system, additional control system costs are introduced.

1.5.3 Literature Survey on Variable Speed WECS

In the case of Variable Speed WECS, their speed is variable over a wide range depending on the wind speed. Fig. 1.4 indicates the layout of the stator-fed Variable Speed WECS.

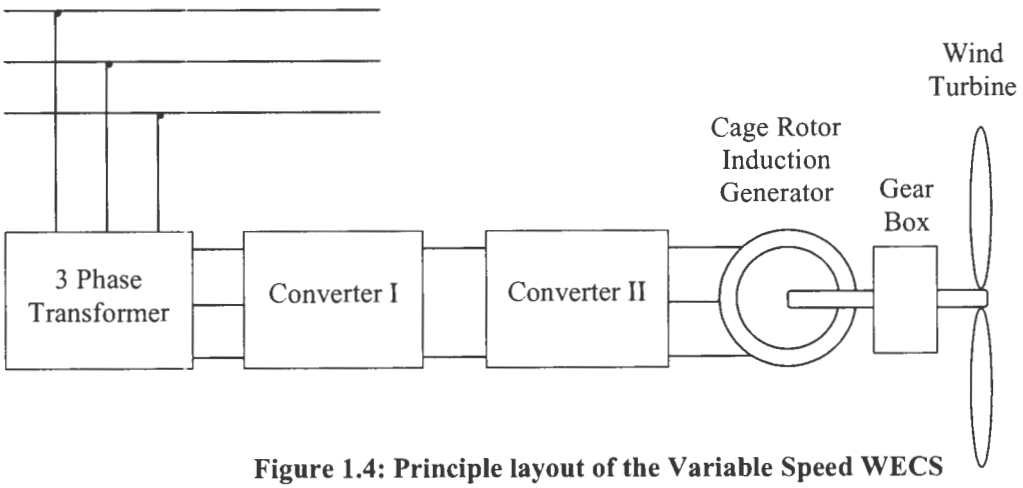

Figure 1.4: Principle layout of the Variable Speed WECS using a Cage Rotor Induction Generator

Fig. 1.5 indicates the layout of the wound rotor induction generator Variable Speed WECS.

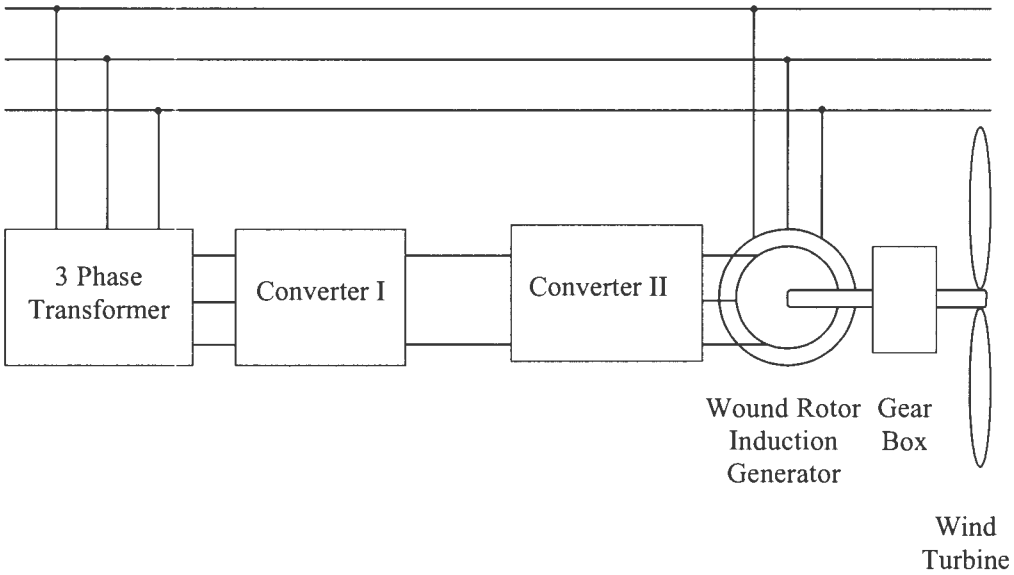

Figure 1.5: Principle Layout of the Variable Speed WECS using a Wound Rotor Induction Generator

In Variable Speed WECS the generator is not directly connected to the grid, as in the case of the Constant-Speed WECS. Instead the rotor is permitted to rotate at variable speed, which is achieved using power electronic converters. The selection criteria for the most appropriate system, with regard to type of generator and converters, is non trivial. Some of the factors influencing the selection criteria are as follows: cost of components, reliability, maintenance, output power factor, harmonics, etc. [10]. The power limit of the system is dependant upon the generator rating and electronic converter ratings, while the speed limit is governed by the mechanical design of the turbine and tower [6]. The important advantages of Variable Speed WECS is its improved output power quality, reduction of the drive train mechanical stresses in high wind speeds, reduced noise emission, enhanced energy capture and improved power factor displacement associated with induction generators [10].

In [10], a comparison is made between Constant Speed WECS, a Cage Rotor Induction Generator WECS using voltage and current source converters and a

Wound Rotor Induction Generator WECS with regard to their dynamic behavioural performance. This paper will constantly be referred to when taking a more in-depth look at the two topologies being discussed. The two topologies will now be looked at in greater detail.

1.5.3.1 Cage Rotor Induction Generator WECS

Cage Rotor Induction Generators are less expensive and more reliable than wound rotor induction generators. However, the converter cost is higher. The layout of a Cage Rotor Induction Generator WECS is shown in Fig. 1.4, where back-to-back converters are applied to the stator winding. Unlike Constant Speed WECS, the power electronic converter allows a wider rotor speed variation relative to the grid frequency. Converter II, is responsible for supplying the required reactive power, together with managing the active power generated by the induction machine. The DC bus voltage is regulated by Converter I, while also transferring the generated active power at unity power factor to the grid [6]. Various control strategies will now be examined.

In [11], a simple Maximum Power Point Tracking control strategy for induction machines is proposed. The frequency of a standard V/Hz converter is used to attain a desired power at a given turbine speed. Fig. 1.6 is a block diagram of the control strategy.

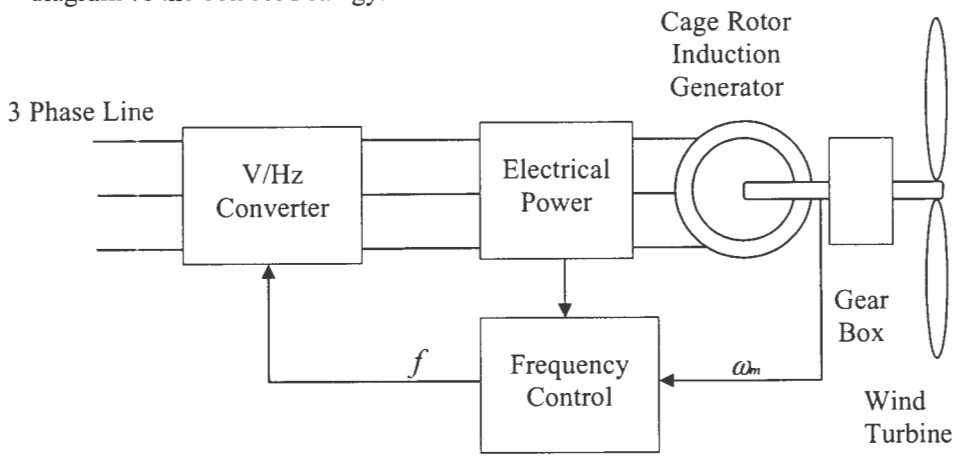

Figure 1.6: Block diagram for a frequency control strategy

Results show that this scheme is capable of tracking the maximum power points, while also placing limits on the speed and power.

In [10], Dual PWM Voltage Source Converters are used, allowing for bidirectional power flow. This is used in the starting of stall regulated wind turbines. They also allow for power factor regulation and reduce the harmonic injection into the grid. Vector and scalar control strategies were examined on the system mentioned. The control systems correspond to commercially available units.

Fig. 1.7 indicates the operating region of a typical Cage Rotor Induction Generator WECS in terms of the Turbine Power and Generator Shaft Speed plane for various wind speeds [6]. The generator used in the diagram is assumed to be rated at 300kW, 50Hz induction, 6-poles with a synchronous speed of 1000 r/min [6]. This will be used to emphasise the difference between the Cage Rotor Induction Generator WECS and the Wound Rotor Induction Generator WECS in capturing energy.

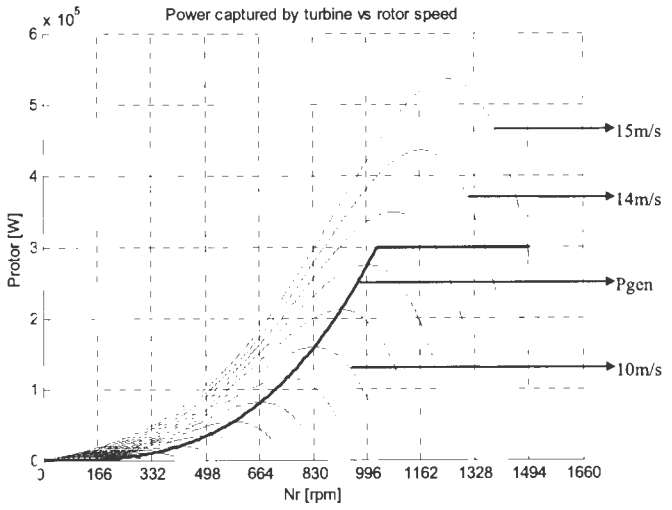

Figure 1.7: Wind turbine power versus generator shaft speed for a variable speed system using a Cage Rotor Induction Generator [6]

When the cut-in wind velocity is reached, the system is connected to the grid and generation takes place. When the system operates within the rated wind speed, the system will continue to generate in the peak-power tracking mode. Once the rated power of the generator is reached (which occurs at synchronous speed-1000rpm), the power is maintained with increasing speed. This is attained through field weakening in an attempt to reduce the torque. If the speed continues to increase past some threshold, the turbine goes into pitch control [6].

It is evident from Fig. 1.7, that Cage Rotor Induction Generator WECS can attain maximum power at various wind speeds within the rated wind speed region through maximum power point tracking (MPPT). Thus, it is able to extract more energy compared to the Constant Speed WECS. However, the power is kept constant at the generator's power rating and further maximum power point tracking is no longer possible. There are definite benefits to using a Variable Speed Cage Rotor Induction Generator system, however the converters used in the stator circuit need to handle the full stator power and therefore the cost of the converters are expensive.

1.5.3.2 Wound Rotor Induction Generator WECS

Fig. 1.5 illustrates the layout of the Wound Rotor Induction Generator (also known as a Doubly-Fed Induction Generator) WECS. The stator is directly connected to the grid, whereas the rotor is connected to back-to-back converters. This is an extremely attractive approach, especially when the speed range is limited. The rotor circuit is capable of bi-directional power flow, and during a particular mode of operation, output power can be attained from both the stator and the rotor circuits. There are two modes of operation, namely sub-synchronous and super-synchronous generation [6]. During sub-synchronous generation, the rotor speed is lower than the synchronous speed and the rotor circuit absorbs power from the supply. However, in super-synchronous generation, the rotor speed is greater than the synchronous speed and both the rotor and stator generates power. The rating of the converter is dependent upon rated rotor power, which is less than the rated stator power,

when operating over a limited speed range. Various control schemes will now be examined.

In [10], the power electronic converters used to control the wound rotor induction generator consist of a diode rectifier for Converter II and a line commutated thyristor inverter for Converter I. This scheme only allows for generation at supersynchronous speeds and is also known as the Kramer drive.

In [12], a Scherbius drive is used as the AC-AC converter. Due to the restriction of the speed range of WECS, the Scherbius system is regarded as a natural application to WECS. Scherbius Doubly-Fed Induction Generators WECS commonly implement either a current-fed DC-link converter or a cycloconverter in the rotor circuit. Both schemes are accompanied by numerous disadvantages. The current-fed DC-link converter requires an extra commutation circuit for operation at synchronous speed, which results in poor performance at low slip speeds [12]. The DC-link choke is also costly. The problem with operation at synchronous speed may be solved with the use of a cycloconverter, however it requires a transformer to provide a neutral point, which also increases the cost. These disadvantages may be overcome with the use of back-to-back PWM voltage-fed current regulated inverters [12].

A block diagram of the experimental system used in [12] is given in Fig. 1.8 below. The wound rotor induction machine used was a 7.5kW, 415V, 50Hz, 6 pole machine. The generator speeds were limited to 500rpm to 1500rpm. The generator was driven by a torque controlled 15kW DC motor drive, simulating a wind turbine. Bipolar transistor PWM inverters were used as the converters with a maximum switching frequency of 1kHz. Vector control is used for both converters. Two optimal tracking schemes have been described and they include the speed-mode control and current-mode control. Further details as to the experimental setup and control strategies is given in [12].

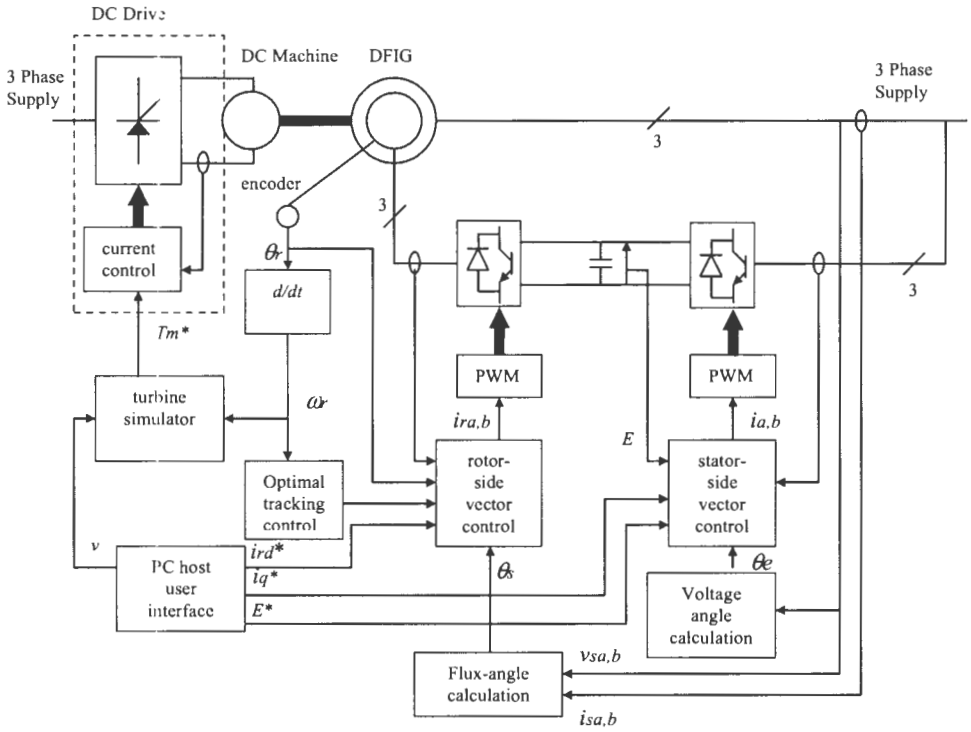

Figure 1.8: Block diagram of the experimental setup using back-to-back PWM converters [12]

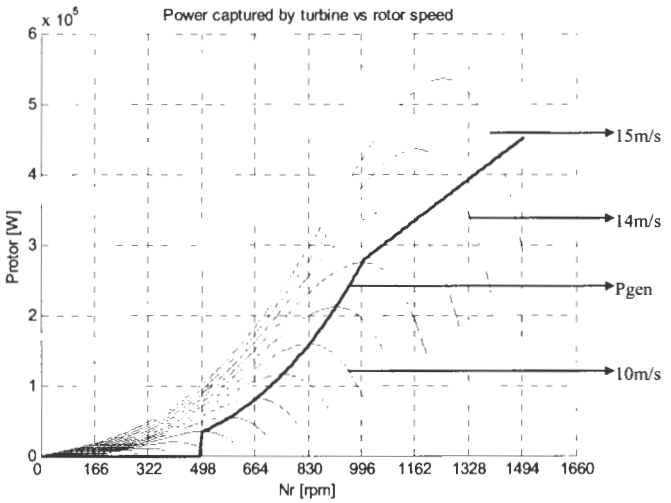

Figure 1.9: Wind turbine power versus generator shaft speed for a variable speed system using a Wound Rotor Induction Generator [6]

Fig. 1.9 indicates a typical Turbine Power versus Generator Shaft Speed for a Wound Rotor Induction Generator WECS, for different wind speeds [6]. The generator used in the diagram is identical to that of the Cage Rotor Induction Generator WECS (i.e. 300kW, 50Hz , 6 pole induction generator with a synchronous speed-n_s of 1000 r/min)[6]. The rotor shaft speed will be limited to $n_s(1\pm0.5)$ (i.e. 500rpm to 1500rpm). Once the cut-in wind velocity is reached, the system is connected to the grid. The converter control system is switched on, and some power is absorbed by the rotor. Since the operating region is chosen to be between $n_s(1\pm0.5)$ (i.e. 500rpm to 1500rpm), once the cut-in value is reached, the speed of the generator will remain at $0.5n_s$ until a certain power level is reached. Once this power level is reached, maximum power point tracking begins and the stator alone delivers power to the grid. When the rated stator power is reached (i.e. at n_s), the power being absorbed from the rotor is zero. Super-synchronous generation begins (i.e. for n_s to $1.5n_s$) and it now operates at constant rated torque. Power is also delivered to the grid, from the rotor via the converters until the rated power is reached and pitch control mode is entered.

The ability of the system to perform MPPT, allows the system to extract a greater amount of energy compared to the fixed speed system. The advantage of using the Wound Rotor Induction Generator over the Cage Rotor Induction Generator, is the reduction in costs of the converters, since the power converters need only handle rotor power. However, the wound rotor induction machine is more expensive than the cage rotor induction machine.

1.6 Summary and Discussion of the Project

The relevant literature survey of wind energy induction generator systems have been discussed. These surveys form the basic foundation of the undertaken research project.

Since variable speed wind energy induction generator systems are far more advantageous and more commonly used than the constant speed system, the two variable systems (using the cage rotor induction machine and the wound rotor induction machine) are modeled and implemented experimentally, with the ability to implement faults. The control strategy implemented for the doubly-fed drive is derived from fundamental principles and is fully described, whereas a commercial drive is used for the cage rotor system.

Common faults are then implemented on the two laboratory generator systems to allow for the development of fault detection techniques. The primary contribution of this thesis is the development of flexible test beds for fault analysis of variable speed WECS.

Chapter 2

2. DYNAMIC MODEL & FIELD ORIENTATED CONTROL OF AN INDUCTION MACHINE

2.1 Introduction to Dynamic Modeling of an Induction Machine

Modeling of a 3-phase induction machine is a means of representing the operation of the machine by a set of equations or by an equivalent circuit. It is used as a critical tool in developing a better understanding of the machine.

The steady state model of the 3-phase induction machine has been used for many years as an instrument for calculating basic steady state quantities, such as the stator currents, developed torque, etc. The steady state conditions placed on the machine include a balanced sinusoidal supply voltage while the machine operates at a constant speed. The reliable, yet insufficient steady state model does not allow for analysis of the machine under transient operating conditions.

To explain the dynamic modeling of the 3-phase induction machine, the concept of space vectors will now be introduced. The model introduced is applicable to both squirrel-cage and wound rotor induction machines [13].

However, [13] only develops the theory of Field Orientated Control (FOC) using stator currents, and thus the equations for FOC using the rotor currents had to be formulated here.

2.2 Space Vectors in the Stationary (Stator) Reference Frame

To introduce the concept of space vectors, the cross section of both the rotor and the stator of a 3-phase, 2-pole induction machine is shown in Fig. 2.1.

For simplicity, only the stator will be analysed, however the concepts will be transferred to the rotor. It is assumed that each phase winding consists of only one turn. It should be noted that all vectors are denoted in bold letters, while a superscript denotes a particular reference frame.

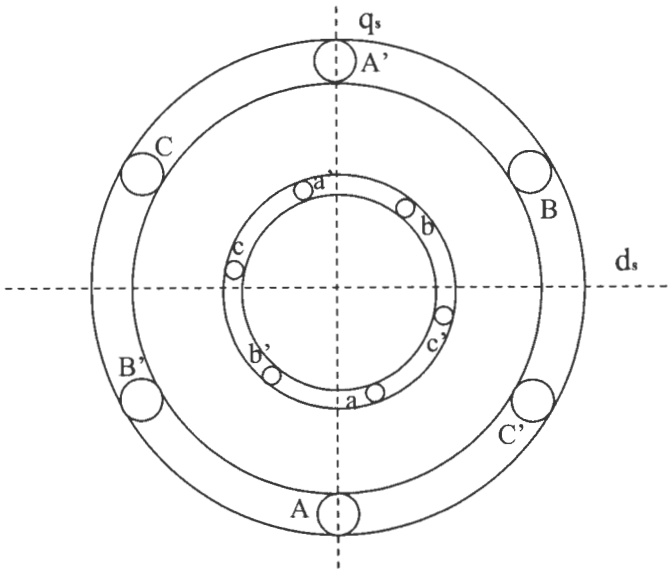

Figure 2.1: Elementary 3 phase, 2-pole stator and rotor

The axis of a winding is defined as being perpendicular to the plane in which the coil lies. The stationary (stator) reference frame is defined by the direct axis, $\mathbf{d_s}$, and the quadrature axis, $\mathbf{q_s}$, which are aligned along the horizontal and vertical geometrical axes of the stator. The direct axis is physically referenced along the axis of the phase-A winding of the stator. Currents entering the coil ends marked A, B, C (in Fig. 2.1) have been defined as being positive. The currents are negative when entering ends A', B' and C' [13]. The phases are spatially displaced by 120°, which is indicated in Fig. 2.2.

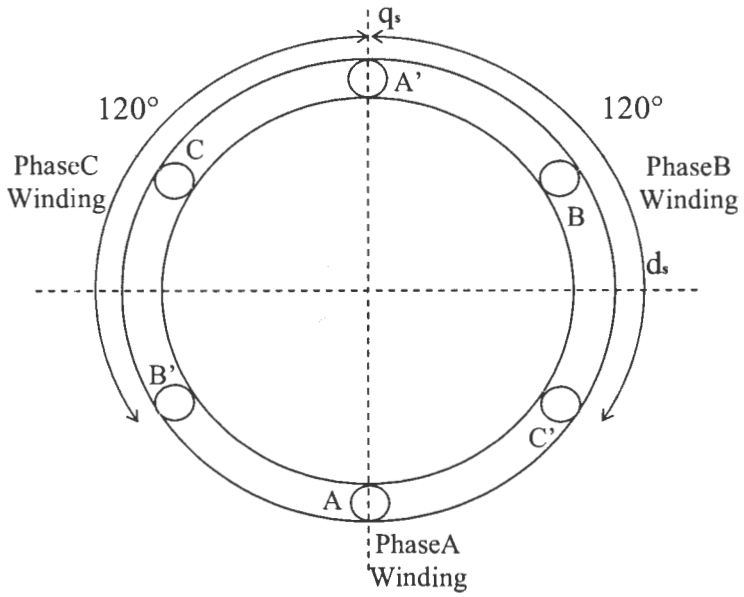

Figure 2.2: Spatial displacement of the 3 phases

If the currents entering the coils are supplied from a balanced 3-phase source, with radian frequency ω, the currents may be represented as follows

$$i_{as}(t) = I_s cos(\omega t) = I_s\, Re\{e^{j\omega t}\} \tag{2.1}$$

$$i_{bs}(t) = I_s cos(\omega t - 2\pi/3) = I_s\, Re\{e^{(j\omega t - 2\pi/3)}\} \tag{2.2}$$

$$i_{cs}(t) = I_s cos(\omega t + 2\pi/3) = I_s\, Re\{e^{(j\omega t + 2\pi/3)}\} \tag{2.3}$$

where I_s represents the peak stator current. Fig. 2.3 indicates the currents over several cycles.

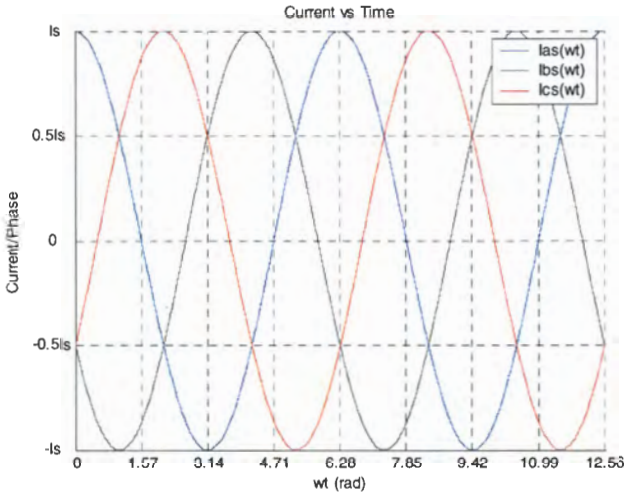

Figure 2.3: Instantaneous values of the 3 phase currents

The current flowing in a phase produces a magneto-motive force (mmf), along the axis of the winding. These currents may also be represented as vectors, along the axis of the winding. The length of the current vector would be proportional to the instantaneous magnitude of the current, while the direction would be along the axis of the winding. This arrangement is known as Space Vectors [15].

The phase current space vectors (at ωt=0) are illustrated in Fig. 2.4, together with the resultant current space vector, which is attained by vector addition of the instantaneous phase current space vectors. Each phase current space vector, may also be written in complex form and the resultant attained (where the *d*-axis represents the real axis and the *q*-axis represents the imaginary axis).

$$\boldsymbol{i_{as}} = i_{as}e^{j0} \quad , \boldsymbol{i_{bs}} = i_{bs}e^{j2\pi/3} \quad , \boldsymbol{i_{cs}} = i_{cs}e^{j4\pi/3} \tag{2.4}$$

$$\boldsymbol{i_s}^s = \boldsymbol{i_{as}} + \boldsymbol{i_{bs}} + \boldsymbol{i_{cs}} \tag{2.5}$$

$$\boldsymbol{i_s}^s = \frac{3}{2} I_s e^{j(wt)} \tag{2.6}$$

At ωt=0

$$i_{as}(0) = I_s \;;\; i_{bs}(0) = -\frac{1}{2}I_s \;;\; i_{cs}(0) = -\frac{1}{2}I_s \tag{2.7}$$

$$i_s^s = I_s e^{j0} - \frac{1}{2}I_s e^{j2\pi/3} - \frac{1}{2}I_s e^{j4\pi/3} \tag{2.8}$$

$$i_s^s = 1.5 I_s e^{j0} \tag{2.9}$$

which is illustrated in Fig. 2.4.

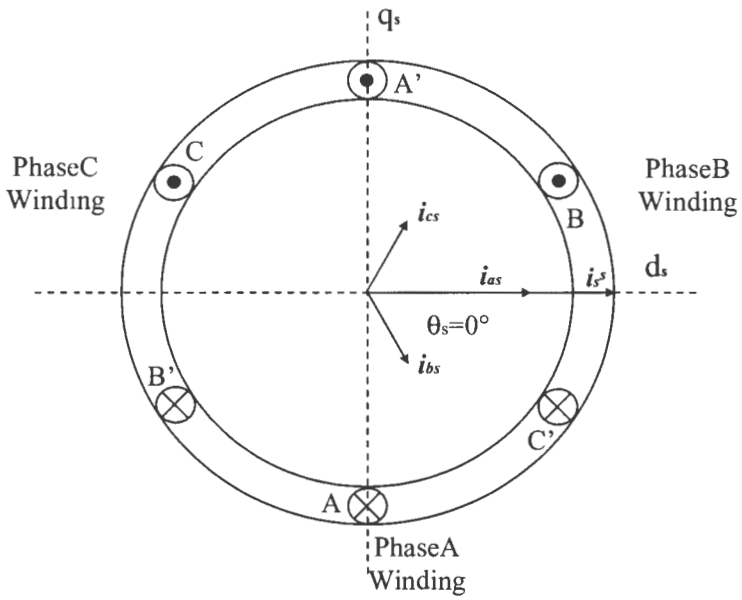

Figure 2.4: Stator current space vectors at ωt=0

At ωt=π/3

$$i_{as}(\pi/3) = \frac{1}{2}I_s \;;\; i_{bs}(\pi/3) = \frac{1}{2}I_s \;;\; i_{cs}(\pi/3) = -I_s \tag{2.10}$$

$$i_s^s = \frac{1}{2}I_s e^{j0} + \frac{1}{2}I_s e^{j2\pi/3} - I_s e^{j4\pi/3} \tag{2.11}$$

$$i_s^s = 1.5 I_s e^{j\pi/3} \tag{2.12}$$

which is illustrated in Fig. 2.5.

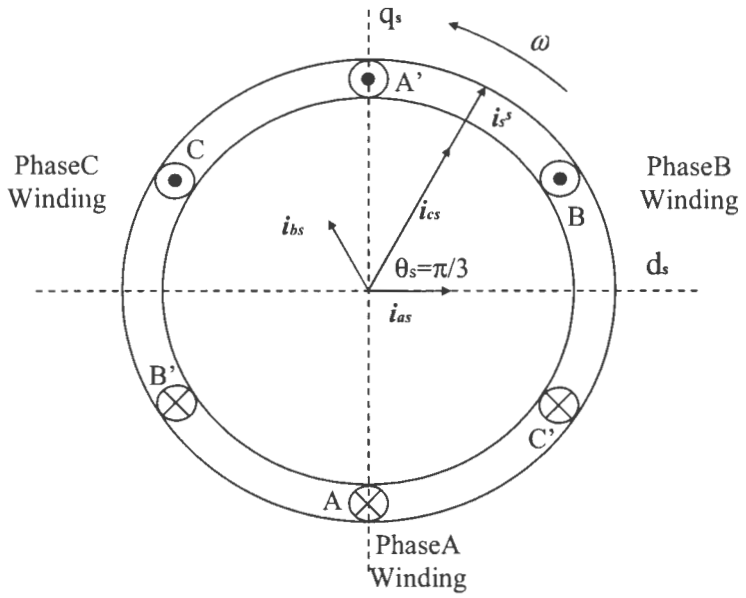

Figure 2.5: Stator current vectors at $\omega t=\pi/3$

θ_s represents the angular position of the resultant current space vector. It is evident from Fig. 2.4 and Fig. 2.5, that the resultant current space vector has a constant magnitude of $1.5I_s$ and rotates with angular frequency ω. The concept of space vectors may also be extended to all other quantities (i.e. voltage (v), flux linkage (λ), mmf, etc.)[13].

$$v_s^s = v_{as}e^{j0} + v_{bs}e^{j2\pi/3} + v_{cs}e^{j4\pi/3} \qquad (2.13)$$

$$\lambda_s^s = \lambda_{as}e^{j0} + \lambda_{bs}e^{j2\pi/3} + \lambda_{cs}e^{j4\pi/3} \qquad (2.14)$$

Space vectors allows for the transformation of a 3 phase induction machine into that of an equivalent 2-phase induction machine.

2.3 Transformations between the 3-phase and 2-phase Quantities

In the previous section, the 3-phase time variant stator currents of the machine were mapped to a time variant current space vector, which rotates on a complex plane perpendicular to the machine shaft. The complex plane was formed by the quadrature and direct axis.

Using Euler's Identity $e^{j\omega t} = \cos(\omega t) + j\sin(\omega t)$, the resultant stator current space vector may be decomposed into its quadrature and direct components. This is indicated below by substituting equation 2.4 into 2.5.

$$i_s^s = i_{as}e^{j0} + i_{bs}e^{j2\pi/3} + i_{cs}e^{j4\pi/3} \tag{2.15}$$

$$\begin{aligned} i_s^s = {} & i_{as}[\cos(0) + j\sin(0)] + i_{bs}[\cos(2\pi/3) + j\sin(2\pi/3)] \\ & + i_{cs}[\cos(4\pi/3) + j\sin(4\pi/3)] \end{aligned} \tag{2.16}$$

$$i_s^s = \left(i_{as} - \frac{1}{2}i_{bs} - \frac{1}{2}i_{cs}\right) + j\left(\frac{\sqrt{3}}{2}i_{bs} - \frac{\sqrt{3}}{2}i_{cs}\right) \tag{2.17}$$

$$i_s^s = i_{ds} + ji_{qs} \tag{2.18}$$

This may be represented in matrix form as shown below

$$\begin{bmatrix} i_{ds}^s \\ i_{qs}^s \end{bmatrix} = \begin{bmatrix} 1 & -\frac{1}{2} & -\frac{1}{2} \\ 0 & \frac{\sqrt{3}}{2} & -\frac{\sqrt{3}}{2} \end{bmatrix} \begin{bmatrix} i_{as} \\ i_{bs} \\ i_{cs} \end{bmatrix} \tag{2.19}$$

The derived expression is referred to as the Clarke Transform [16]. The resulting matrix allows for a direct method of mapping 3-phase quantities to the stator reference frame. The inverse of the matrix above can easily be solved for and the expression in (2.20) is referred to as the Inverse Clarke Transform [16].

$$\begin{bmatrix} i_{as} \\ i_{bs} \\ i_{cs} \end{bmatrix} = \begin{bmatrix} \frac{2}{3} & 0 \\ -\frac{1}{3} & \frac{1}{\sqrt{3}} \\ -\frac{1}{3} & -\frac{1}{\sqrt{3}} \end{bmatrix} \begin{bmatrix} i_{ds}{}^{s} \\ i_{qs}{}^{s} \end{bmatrix} \tag{2.20}$$

2.4 Transformations of Space Vectors Between Different Reference Frames

2.4.1 Rotor Reference Frame

As shown in the previous section, although i_s^s was referenced to a plane perpendicular to the rotor shaft and stationary to the stator, it may also be referenced to other planes, with their orthogonal axis rotating at various speeds. The rotor reference frame will be looked at as an example.

The currents flowing in the rotor operate at a frequency, which is proportional to the slip, as shown below.

$$\omega_{slip} = s\omega = \frac{d\theta_{slip}}{dt} \tag{2.21}$$

where

$$s = \frac{\frac{2\omega}{p} - \omega_r}{\frac{2\omega}{p}} \tag{2.22}$$

θ_{slip} = slip angular position

ω_{slip} = slip angular frequency

ω_r = rotor angular frequency

s = slip

p = number of poles

The rotor reference frame is defined by having its real and imaginary axis aligned with the vertical and horizontal geometrical axis of the rotor. The real

axis (direct axis, $\mathbf{d_r}$), is physically referenced along the axis of the phase-a coil of the rotor.

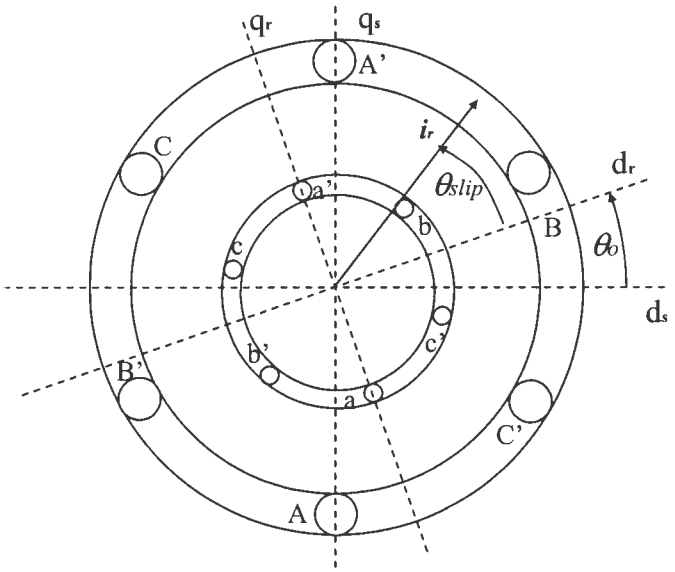

Figure 2.6: Resultant rotor current space vector relative to the stationary and rotor reference frames

The angular speed at which the rotor reference frame rotates relative to the stator reference frame is $\omega_b = \frac{p}{2}\omega_r$. The angular position is $\theta_b = \int \omega_b dt$. The currents in the rotor cause a resultant current space vector, which is denoted i_r, in the above diagram. The angular position of i_r relative to the rotor reference frame is denoted as θ_{slip} and may calculated from the slip frequency (i.e. $\theta_{slip} = \int \omega_{slip} dt$).

The resultant rotor current space vector relative to the rotor reference frame may be expressed as follows

$$i_r^r = 1.5 I_r e^{j\theta_{slip}} \qquad (2.23)$$

where

I_r = peak rotor current

To now project the resultant rotor current space vector onto the stationary reference frame, we observe from Fig. 2.6, that the angle change between the stator and rotor reference frames has to be included. Thus using Euler's Identity, $e^{j\theta_o} = \cos(\theta_o) + j\sin(\theta_o)$, the equivalent rectangular representation is as follows

$$\begin{aligned} \boldsymbol{i}_r{}^s &= \boldsymbol{i}_r{}^r e^{j\theta_o} \qquad (2.24)\\ &= \left(i_{dr}{}^r + j i_{qr}{}^r\right)\left(\cos(\theta_o) + j\sin(\theta_o)\right) \\ &= \left(i_{dr}{}^r \cos(\theta_o) - i_{qr}{}^r \sin(\theta_o)\right) \\ &\quad + j\left(i_{qr}{}^r \cos(\theta_o) + j i_{dr}{}^r \sin(\theta_o)\right) \qquad (2.25) \end{aligned}$$

Representing the above in matrix form

$$\begin{bmatrix} i_{dr}{}^s \\ i_{qr}{}^s \end{bmatrix} = \begin{bmatrix} \cos(\theta_o) & -\sin(\theta_o) \\ \sin(\theta_o) & \cos(\theta_o) \end{bmatrix} \begin{bmatrix} i_{dr}{}^r \\ i_{qr}{}^r \end{bmatrix} \qquad (2.26)$$

The inverse of the above expression is as follows

$$\begin{bmatrix} i_{dr}{}^r \\ i_{qr}{}^r \end{bmatrix} = \begin{bmatrix} \cos(\theta_o) & \sin(\theta_o) \\ -\sin(\theta_o) & \cos(\theta_o) \end{bmatrix} \begin{bmatrix} i_{dr}{}^s \\ i_{qr}{}^s \end{bmatrix} \qquad (2.27)$$

2.4.2 Synchronous Reference Frame

The purpose of transformations is for convenience of control. AC quantities are not easy to deal with, and thus transformations to various reference frames, enables the conversion of these alternating quantities to direct quantities.

The synchronous reference frame rotates at synchronous speed, ω, and the direct axis is referenced along the peak of the flux density in the air gap [14].

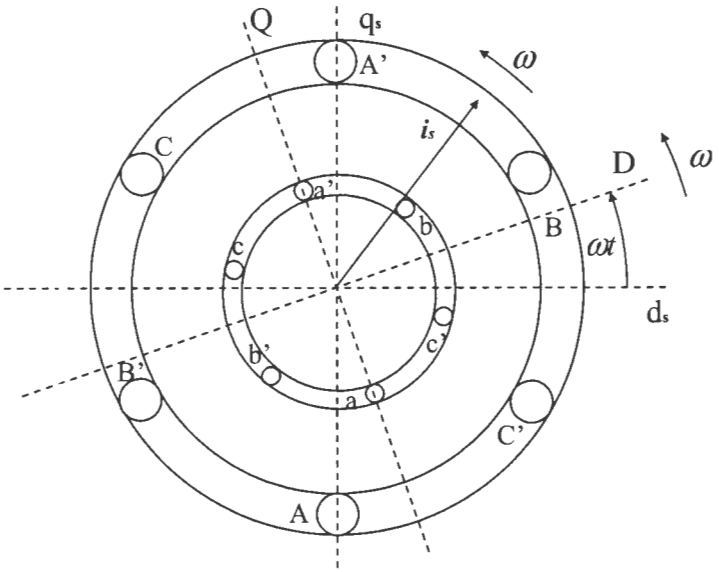

Figure 2.7: Resultant stator current space vector relative to the stationary and synchronous reference frames

The instantaneous angle formed between the stationary reference frame and the synchronous reference is ωt. The resultant stator current space vector appears to rotate at ω when observed from the stationary reference frame. When observed from the synchronous reference frame, it appears to be stationary. It may then be resolved into its two time invariant components, along its real and imaginary axes.

The relationship between the stator and synchronous reference frames can be expressed as follows (the resultant stator current space vector in the synchronous reference frame is i_s^e)

$$i_s^s = i_s^e e^{j\omega t} \tag{2.28}$$

$$i_s^e = i_s^s e^{-j\omega t} \tag{2.29}$$

Similarly

$$v_s^s = v_s^e e^{j\omega t} \tag{2.30}$$

$$\lambda_s^s = \lambda_s^e e^{j\omega t} \tag{2.31}$$

The equivalent rectangular co-ordinates are as follows

$$\begin{aligned} i_{ds}{}^{s} + j i_{qs}{}^{s} &= \left(i_{Ds}{}^{e} + j i_{Qs}{}^{e}\right)\left(\cos(\omega t) + j\sin(\omega t)\right) \\ &= \left(i_{DS}{}^{e}\cos(\omega t) - i_{QS}{}^{e}\sin(\omega t)\right) \\ &\quad + j\left(i_{DS}{}^{e}\sin(\omega t) + j i_{QS}{}^{e}\cos(\omega t)\right) \end{aligned} \tag{2.32}$$

$$\begin{aligned} i_{DS}{}^{e} + j i_{QS}{}^{e} &= \left(i_{ds}{}^{s} + j i_{qs}{}^{s}\right)\left(\cos(-\omega t) + j\sin(-\omega t)\right) \\ &= \left(i_{ds}{}^{s}\cos(\omega t) + i_{qs}{}^{s}\sin(\omega t)\right) \\ &\quad + j\left(-i_{ds}{}^{s}\sin(\omega t) + j i_{qs}{}^{s}\cos(\omega t)\right) \end{aligned} \tag{2.33}$$

Representing the above in matrix form

$$\begin{bmatrix} i_{DS}{}^{e} \\ i_{QS}{}^{e} \end{bmatrix} = \begin{bmatrix} \cos(\omega t) & \sin(\omega t) \\ -\sin(\omega t) & \cos(\omega t) \end{bmatrix} \begin{bmatrix} i_{ds}{}^{s} \\ i_{qs}{}^{s} \end{bmatrix} \tag{2.34}$$

whereby the above expression is known as the Park Transform [16].

The inverse is

$$\begin{bmatrix} i_{ds}{}^{s} \\ i_{qs}{}^{s} \end{bmatrix} = \begin{bmatrix} \cos(\omega t) & -\sin(\omega t) \\ \sin(\omega t) & \cos(\omega t) \end{bmatrix} \begin{bmatrix} i_{DS}{}^{e} \\ i_{QS}{}^{e} \end{bmatrix} \tag{2.35}$$

which is known as the Inverse Park Transform [16].

Thus the transformation between various reference frames incorporates the theory of relativity. The choice of the reference frame depends on the problem to be solved.

2.5 Dynamic Model of the Induction Machine in the Stationary Reference Frame

The windings on either the stator or rotor may be represented in the form of interconnected resistor-inductor circuit elements. Fig. 2.8 indicates such a circuit, whereby voltage, current and flux vectors are used instead of time variant ac signals.

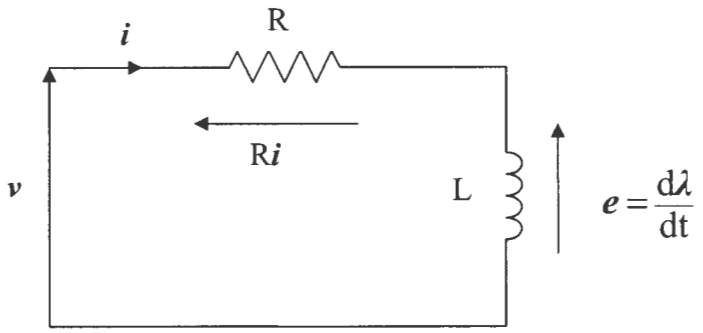

Figure 2.8: Equivalent circuit representing the stator or rotor winding

The stator winding is represented as follows

$$v_s^{\ s} = R_s i_s^{\ s} + \frac{d\lambda_s^{\ s}}{dt} \tag{2.36}$$

The rotor winding is represented as follows

$$v_r^{\ r} = R_r i_r^{\ r} + \frac{d\lambda_r^{\ r}}{dt} \tag{2.37}$$

Mapping the rotor equivalent equation to the stator, the following substitutions have to occur

$$v_r^{\ r} = v_r^{\ s} e^{-j\theta_r} \tag{2.38}$$

$$i_r^{\,r} = i_r^{\,s} e^{-j\theta_b} \tag{2.39}$$

$$\lambda_r^{\,r} = \lambda_r^{\,s} e^{-j\theta_b} \tag{2.40}$$

$$\frac{d\lambda_r^{\,r}}{dt} = \frac{d\left(\lambda_r^{\,s} e^{-j\theta_b}\right)}{dt} \tag{2.41}$$

Differentiation by parts, we get

$$\begin{aligned}\frac{d\lambda_r^{\,r}}{dt} &= \frac{d\lambda_r^{\,s}}{dt} e^{-j\theta_b} + \frac{d\left(e^{-j\theta_b}\right)}{dt} \lambda_r^{\,s} \\ &= \frac{d\lambda_r^{\,s}}{dt} e^{-j\theta_b} - j\frac{d\theta_b}{dt} \lambda_r^{\,s} e^{-j\theta_b}\end{aligned} \tag{2.42}$$

Whereby

$$\omega_b = \frac{d\theta_b}{dt} \tag{2.43}$$

Thus

$$\begin{aligned}\frac{d\lambda_r^{\,r}}{dt} &= \frac{d\lambda_r^{\,s}}{dt} e^{-j\theta_b} - j\omega_b \lambda_r^{\,s} e^{-j\theta_b} \\ &= e^{-j\theta_b}\left(\frac{d\lambda_r^{\,s}}{dt} - j\omega_b \lambda_r^{\,s}\right)\end{aligned} \tag{2.44}$$

Substituting equations 2.38, 2.39, 2.44 into equation 2.37, we get

$$v_r^{\,s} e^{-j\theta_b} = R_r i_r^{\,s} e^{-j\theta_b} + e^{-j\theta_b}\left(\frac{d\lambda_r^{\,s}}{dt} - j\omega_b \lambda_r^{\,s}\right) \tag{2.45}$$

dividing by $e^{-j\theta_b}$

$$v_r^{\,s} = R_r i_r^{\,s} + \frac{d\lambda_r^{\,s}}{dt} - j\omega_b \lambda_r^{\,s} \tag{2.46}$$

Interchanging $\frac{d}{dt}$ with p

$$v_s^{\,s} = R_s i_s^{\,s} + p\lambda_s^{\,s} \tag{2.47}$$

$$v_r^s = R_r i_r^s + \lambda_r^s (p - j\omega_b) \tag{2.48}$$

Expressing the above voltage equations in terms of the stator and rotor current vectors, the flux vectors have to be expressed in terms of currents and inductances, which is expressed below

L_{ls} = leakage stator inductance
L_{lr} = leakage rotor inductance
L_m = mutual inductance

Let

$$L_s = L_{ls} + L_m \tag{2.49}$$
$$L_r = L_{lr} + L_m \tag{2.50}$$

$$\lambda_s^s = L_s i_s^s + L_m i_r^s \tag{2.51}$$
$$\lambda_r^s = L_m i_s^s + L_r i_r^s \tag{2.52}$$

Substituting equations 2.51 and 2.52 into equations 2.47 and 2.48, the voltages are expressed as follows

$$v_s^s = (R_s + pL_s) i_s^s + pL_m i_r^s \tag{2.53}$$
$$v_r^s = (p - j\omega_b) L_m i_s^s + (R_r + (p - j\omega_b) L_r) i_r^s \tag{2.54}$$

This may be re-written in rectangular complex form

$$v_{ds}^s = (R_s + pL_s) i_{ds}^s + pL_m i_{dr}^s \tag{2.55}$$
$$v_{qs}^s = (R_s + pL_s) i_{qs}^s + pL_m i_{qr}^s \tag{2.56}$$
$$v_{dr}^s = pL_m i_{ds}^s + \omega_b L_m i_{qs}^s + (R_r + pL_r) i_{dr}^s + \omega_b L_r i_{qr}^s \tag{2.57}$$
$$v_{qr}^s = -\omega_b L_m i_{ds}^s + pL_m i_{qs}^s - \omega_b L_r i_{dr}^s + (R_r + pL_r) i_{qr}^s \tag{2.58}$$

This may be expressed in matrix form as follows

$$\begin{bmatrix} v_{ds}^{s} \\ v_{qs}^{s} \\ v_{dr}^{s} \\ v_{qr}^{s} \end{bmatrix} = \begin{bmatrix} R_s + pL_s & 0 & pL_m & 0 \\ 0 & R_s + pL_s & 0 & pL_m \\ pL_m & \omega_b L_m & R_r + pL_r & \omega_b L_r \\ -\omega_b L_m & pL_m & -\omega_b L_r & R_r + pL_r \end{bmatrix} \begin{bmatrix} i_{ds}^{s} \\ i_{qs}^{s} \\ i_{dr}^{s} \\ i_{qr}^{s} \end{bmatrix} \quad (2.59)$$

The two equivalent circuits below represent the *d*-axis and the *q*-axis of the equations above.

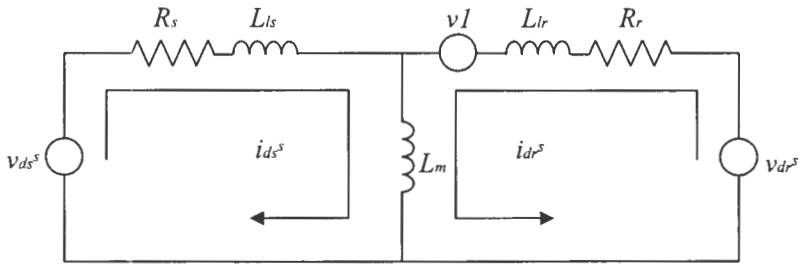

Figure 2.9: Dynamic equivalent circuit of the *d*-axis in the stationary reference frame

Where

$$v1 = -\omega_b(L_r i_{qr}^{s} + L_m i_{qs}^{s}) \quad (2.60)$$

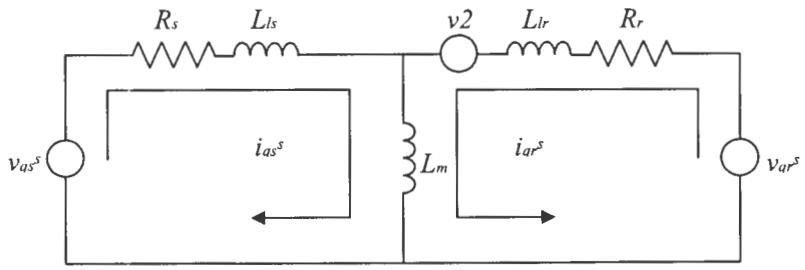

Figure 2.10: Dynamic equivalent circuit of the *q*-axis in the stationary reference frame

Where

$$v2 = \omega_b(L_r i_{dr}^{s} + L_m i_{ds}^{s}) \quad (2.61)$$

2.6 Dynamic Model of the Induction Machine in the Synchronous Reference Frame

As indicated in the previous section, the dynamic model of the induction machine in the stationary reference frame is given, this included both the equivalent circuits and equations. Using equations 2.28, 2.30 and 2.31 (i.e. mapping v_s^s, i_s^s, λ_s^s from the stationary reference frame to the synchronous reference frame), substituting into equations 2.47 and 2.48.

$$v_s^e e^{j\omega t} = R_s i_s^e e^{j\omega t} + p\lambda_s^e e^{j\omega t} \tag{2.62}$$

$$v_r^e e^{j\omega t} = R_r i_r^e e^{j\omega t} + \lambda_r^e e^{j\omega t}(p - j\omega_b) \tag{2.63}$$

Substituting p with $\frac{d}{dt}$ and simplifying the stator equation

$$v_s^e e^{j\omega t} = R_s i_s^e e^{j\omega t} + \frac{d\left(\lambda_s^e e^{j\omega t}\right)}{dt}$$

$$v_s^e e^{j\omega t} = R_s i_s^e e^{j\omega t} + \frac{d\left(\lambda_s^e\right)}{dt} e^{j\omega t} + \frac{d\left(e^{j\omega t}\right)}{dt} \lambda_s^e$$

$$v_s^e e^{j\omega t} = R_s i_s^e e^{j\omega t} + \frac{d\left(\lambda_s^e\right)}{dt} e^{j\omega t} + j\omega\lambda_s^e e^{j\omega t}$$

$$v_s^e = R_s i_s^e + (p + j\omega)\lambda_s^e \tag{2.64}$$

Simplifying the rotor equation

$$v_r^e e^{j\omega t} = R_r i_r^e e^{j\omega t} + \frac{d\left(\lambda_r^e e^{j\omega t}\right)}{dt} - j\omega_b\lambda_r^e e^{j\omega t}$$

$$v_r^e e^{j\omega t} = R_r i_r^e e^{j\omega t} + \frac{d\left(\lambda_r^e\right)}{dt} e^{j\omega t} + \frac{d\left(e^{j\omega t}\right)}{dt} \lambda_r^e - j\omega_b\lambda_r^e e^{j\omega t}$$

$$v_r^e e^{j\omega t} = R_r i_r^e e^{j\omega t} + \frac{d\left(\lambda_r^e\right)}{dt} e^{j\omega t} + j(\omega - \omega_b)\lambda_r^e e^{j\omega t}$$

$$v_r^e = R_r i_r^e + (p + j\omega - j\omega_b)\lambda_r^e \tag{2.65}$$

Since

$$\omega_{slip} = s\omega = \omega - \omega_b$$

$$v_r^e = R_r i_r^e + (p + j\omega_{slip})\lambda_r^e \tag{2.66}$$

Transforming equations 2.51 and 2.52 to the synchronous reference frame, the flux may be expressed as follows

$$\lambda_s^e = L_s i_s^e + L_m i_r^e \tag{2.67}$$

$$\lambda_r^e = L_m i_s^e + L_r i_r^e \tag{2.68}$$

Substituting into equations 2.64 and 2.66 the following is attained

$$v_s^e = [R_s + (p + j\omega)L_s]i_s^e + (p + j\omega)L_m i_r^e \tag{2.69}$$

$$v_r^e = (p + j\omega_{slip})L_m i_s^e + [R_r + (p + j\omega_{slip})L_r]i_r^e \tag{2.70}$$

and representing these in matrix form

$$\begin{bmatrix} v_{Ds}^e \\ v_{Qs}^e \\ v_{Dr}^e \\ v_{Qr}^e \end{bmatrix} = \begin{bmatrix} R_s + pL_s & -\omega L_s & pL_m & -\omega L_m \\ \omega L_s & R_s + pL_s & \omega L_m & pL_m \\ pL_m & -\omega_{slip}L_m & R_r + pL_r & -\omega_{slip}L_r \\ \omega_{slip}L_m & pL_m & \omega_{slip}L_r & R_r + pL_r \end{bmatrix} \begin{bmatrix} i_{Ds}^e \\ i_{Qs}^e \\ i_{Dr}^e \\ i_{Qr}^e \end{bmatrix} \tag{2.71}$$

The two equivalent circuits, shown below represent the above matrix.

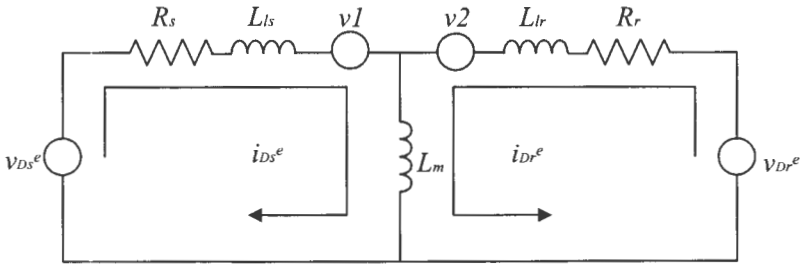

Figure 2.11: Dynamic equivalent circuit of the *D*-axis in the synchronous reference frame

Where

$$v1 = \omega(L_s i_{Qs}^e + L_m i_{Qr}^e) \tag{2.72}$$

$$v2 = \omega_{slip}(L_r i_{Qr}^e + L_m i_{Qs}^e) \tag{2.73}$$

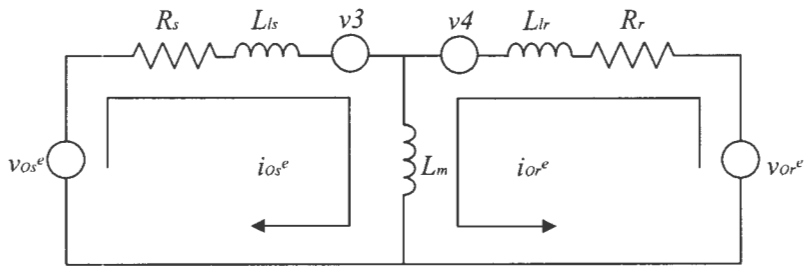

Figure 2.12: Dynamic equivalent circuit of the *Q*-axis in the synchronous reference frame

Where

$$v3 = -\omega(L_s i_{Ds}^e + L_m i_{Dr}^e) \tag{2.74}$$

$$v4 = -\omega_{slip}(L_r i_{Dr}^e + L_m i_{Ds}^e) \tag{2.75}$$

2.7 Electromagnetic Torque Developed by the Induction Machine

In the transformation of the 3-phase winding to a fictitious 2-phase winding, relative to the stationary reference frame (Fig. 2.5), the resultant stator and rotor current vectors may each be represented by a single fictitious coil. This is depicted in Fig. 2.13.

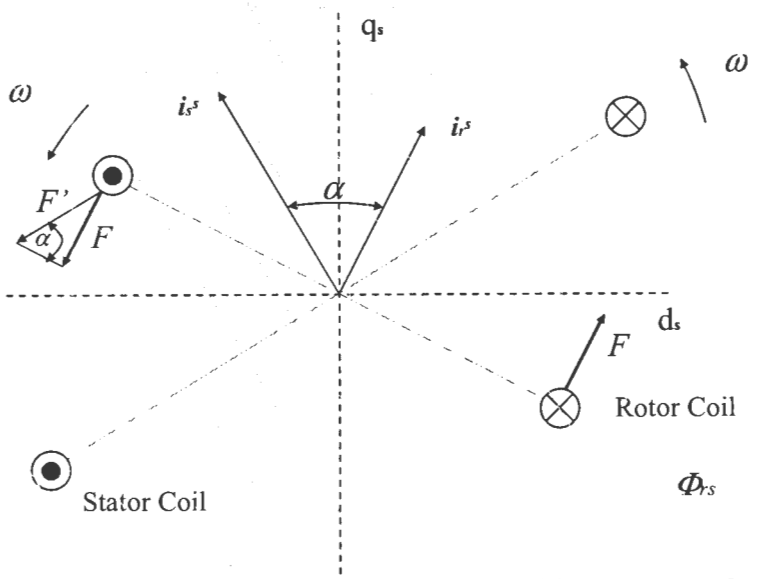

Figure 2.13: Forces acting on fictitious stator and rotor coils

The magnetic flux, Φ_{rs}, produced by the stator, represented by the dashed lines and the radius of the rotor is represented by r. The angle between the stator and rotor current vectors is α. The flux produced by the stator coil results in an electromagnetic force, F, experienced by the rotor coil, perpendicular to the direction of the flux. The torque exerted on the rotor coil is caused by the force component, which lies perpendicular to the plane of the coil [13]. The force is expressed as follows

$$F = F'\sin(\alpha) \tag{2.76}$$

Where

$$F' = Bli_r \tag{2.77}$$

B = flux density of the magnetic field caused by the stator winding

l = length of the coil side

The torque produced in both the coil sides is

$$\begin{aligned} T' &= 2Fr \\ &= 2F'\sin(\alpha)r \\ &= 2lrB_{rs}i_r\sin(\alpha) \end{aligned} \tag{2.78}$$

Since the stator coil is a single turn, the flux density may be expressed in terms of the flux linkage by the following equation

$$\begin{aligned} B_{rs} &= \frac{\Phi_{rs}}{A_r} \\ &= \frac{\lambda_{rs}}{2lr} \end{aligned} \tag{2.79}$$

A_r = area occupied by the rotor coil

Substituting this back into the torque equation,

$$T' = \lambda_{rs}i_r\sin(\alpha) \tag{2.80}$$

Whereby the flux linkage may be represented in terms of the stator current as follows

$$\lambda_{rs} = L_m i_s \tag{2.81}$$

Substituting into the torque equation,

$$T' = L_m i_s i_r \sin(\alpha) \tag{2.82}$$

Expressing $\sin(\alpha)$ in terms of the currents rectangular complex components

$$\begin{aligned}\sin(\alpha) &= \sin(\theta_s - \theta_r) \\ &= \sin(\theta_s)\cos(\theta_r) - \cos(\theta_s)\sin(\theta_r) \\ &= \frac{i_{qs}^{\ s}}{i_s}\frac{i_{dr}^{\ s}}{i_r} - \frac{i_{ds}^{\ s}}{i_s}\frac{i_{qr}^{\ s}}{i_r} \\ &= \frac{1}{i_s i_r}\left(i_{qs}^{\ s} i_{dr}^{\ s} - i_{ds}^{\ s} i_{qr}^{\ s}\right) \qquad (2.83)\end{aligned}$$

After substituting into equation 2.82, the torque equation is now expressed in terms of the stator and rotor current complex components.

$$T' = L_m\left(i_{qs}^{\ s} i_{dr}^{\ s} - i_{ds}^{\ s} i_{qr}^{\ s}\right) \qquad (2.84)$$

The analysis done this far has been for a 2-pole induction machine. A machine with P-poles rotates P/2 times slower than the 2-pole machine. Thus, for the same size machine, the torque developed must be P/2 times to compensate for the drop in speed (since Power(W)=Torque(N.m) x Speed(rad/s)). The total apparent power attained by the fictitious 2-phase system, is $\frac{3}{2}$ times greater than the actual apparent power of the machine [13]. This is proven below.

$$i_s = \frac{3}{2} I_{s,max} \qquad (2.85)$$

$$v_s = \frac{3}{2} V_{s,max} \qquad (2.86)$$

$$S_s' = v_s i_s = \frac{9}{4} I_{s,max} V_{s,max} \qquad (2.87)$$

The actual apparent power of the machine is

$$S_s' = 3\frac{I_{s,max}}{\sqrt{2}}\frac{V_{s,max}}{\sqrt{2}} \qquad (2.88)$$

Thus the actual power of the machine and the fictitious machine differs by a factor of $\frac{3}{2}$, which is compensated for by multiplying the torque by $\frac{2}{3}$. The resulting torque equation is as follows

$$T = \frac{P}{2}\frac{2}{3}L_m\left(i_{qs}{}^s i_{dr}{}^s - i_{ds}{}^s i_{qr}{}^s\right)$$

$$T = \frac{P}{3}L_m\left(i_{qs}{}^s i_{dr}{}^s - i_{ds}{}^s i_{qr}{}^s\right) \qquad (2.89)$$

Similarly the above may be proven for the transformation to the synchronous reference frame in which the following Torque equation will emerge

$$T = \frac{P}{2}\frac{2}{3}L_m\left(i_{Qs}{}^e i_{Dr}{}^e - i_{Ds}{}^e i_{Qr}{}^e\right) \qquad (2.90)$$

$$T = \frac{P}{3}L_m\left(i_{Qs}{}^e i_{Dr}{}^e - i_{Ds}{}^e i_{Qr}{}^e\right) \qquad (2.91)$$

2.8 Simulated Results of the Induction Machine in the Stationary and Synchronous Reference Frame

Incorporating the dynamic model of the machine in the synchronous and stationary reference frames, together with the developed torque equations, simulations were performed in PSPICE for start-up under no load conditions. The equivalent induction machine parameters used to perform the simulations were attained from 2.2kW, 3-phase, 380V, 4 pole wound rotor induction machine. The machine parameters were acquired by performing the no load and blocked rotor test on the machine, as explained in Chapter 4.

2.8.1 Stationary Reference Frame

The simulated results in this section shows the dynamic response of the induction machine during direct online start-up using the dynamic *d*- and *q*-axis equations in the stationary reference frame which is shown in Fig. 2.9 and Fig. 2.10 respectively. The model used to attain the results is shown in Appendix A. To attain the *d*-and *q*-axis supply voltage in the stationary

reference frame, the Clarke Transform was performed on the 3-phase supply voltage (380V). This is shown in Fig. 2.14, whereby the *d*-and *q*-axis signals are sinusoids displaced by 90°, representing the rotating voltage vector.

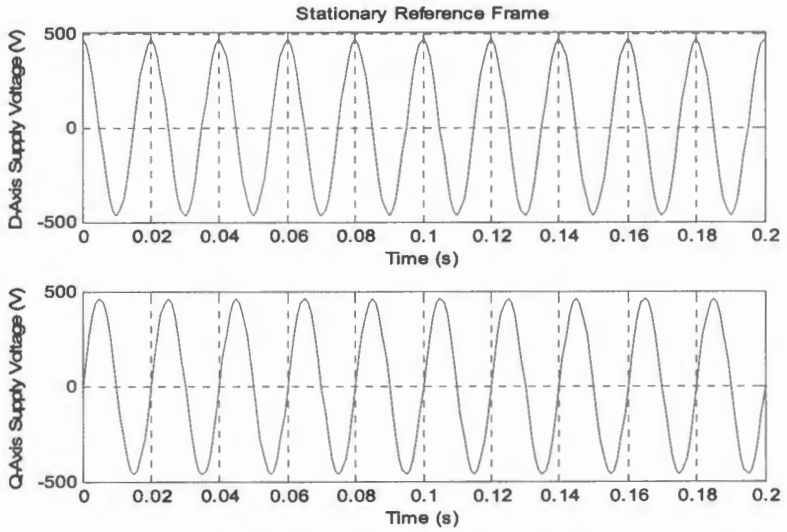

Figure 2.14: *d*-axis and *q*-axis supply voltages in the stationary reference frame

Fig. 2.15 shows the *d*-and *q*-axis stator currents once the *d*-and *q*-axis supply voltage is applied to the dynamic equivalent circuits in the stationary reference frame, representing a direct online startup. The large inrush current is evident which is due to the high slip and low motor input impedance. Fig.2.16 shows the currents over 0.2 seconds whereby the sinusoidal, lagging currents are evident.

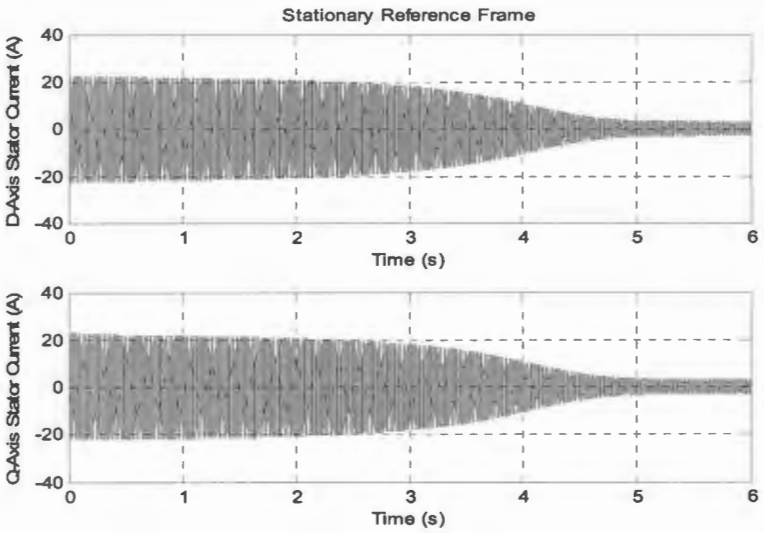

Figure 2.15: *d*-axis and *q*-axis stator currents in the stationary reference frame (6sec)

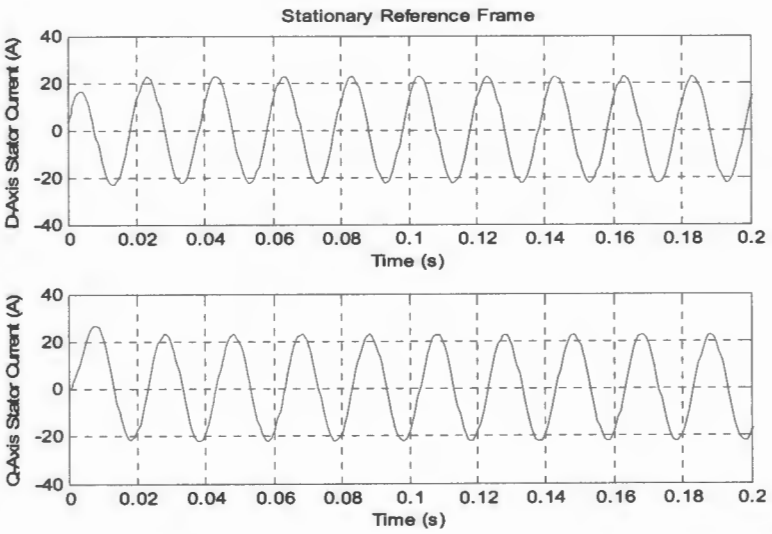

Figure 2.16: *d*-axis and *q*-axis stator currents in the stationary reference frame (0.2sec)

Fig. 2.17 and Fig. 2.18 show the *d*-and *q*-axis rotor currents over a 6sec and 0.2 sec period, respectively. The inrush currents are also reflected in the rotor as shown in Fig. 2.17.

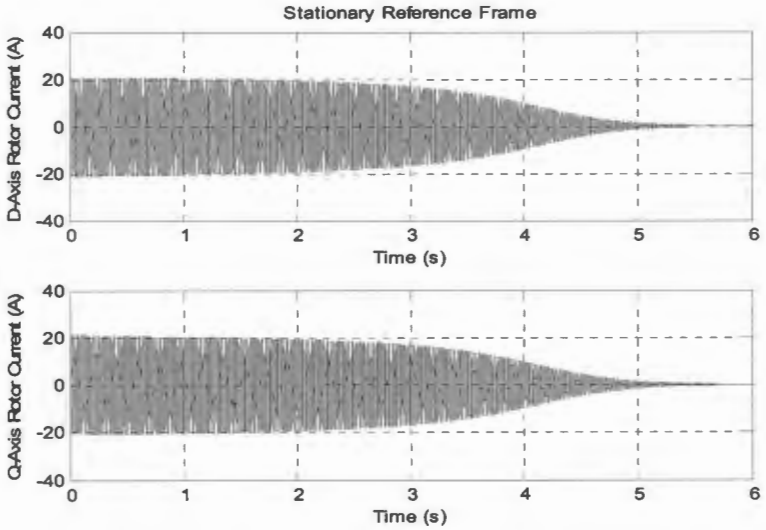

Figure 2.17: *d*-axis and *q*-axis rotor currents in the stationary reference frame (6sec)

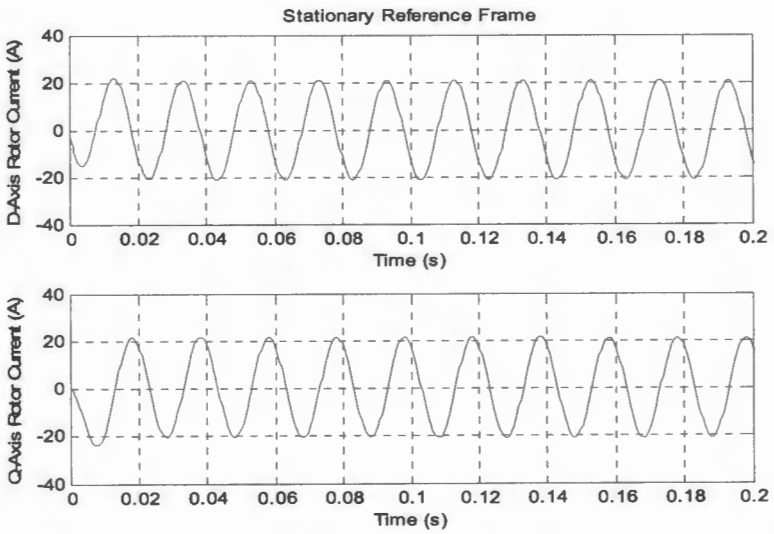

Figure 2.18: *d*-axis and *q*-axis rotor currents in the stationary reference frame (0.2sec)

Fig. 2.19 shows the dynamic electromagnetic torque response of the machine during a direct online start as the machine runs from maximum slip to operating slip speed. Once the operating slip speed is achieved, the machine then matches the load torque condition (no load in this case). Fig. 2.20 shows the respective speed response.

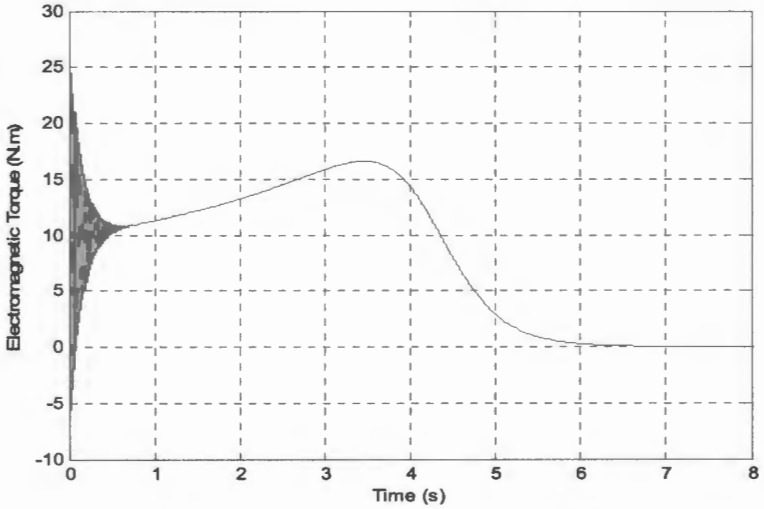

Figure 2.19: Electromagnetic Torque response during direct online start-up

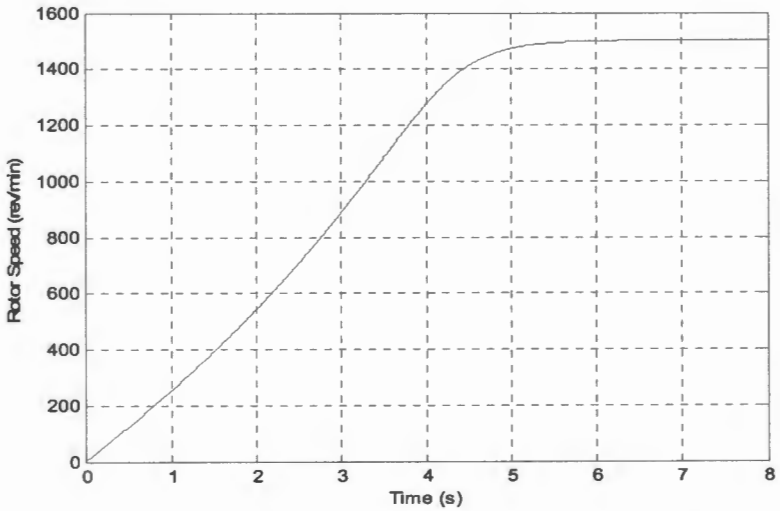

Figure 2.20: Rotor speed response during direct online start-up

2.8.2 Synchronous Reference Frame

The following results show the dynamic response of the induction machine during direct online start-up using the dynamic equivalent circuits of the *d*- and *q*-axes in the synchronous reference frame which is shown in Fig's 2.11

and 2.12 respectively. The simulated model used to attain the results is in Appendix A. The Park Transform was performed on the stationary reference frames, *d*-and *q*-axes supply voltage to attain the *D*-and *Q*-axes supply voltage in the synchronous reference frame. The *D*-axes of the synchronously rotating reference frame was aligned along the supply voltage vector position. The *D*- and *Q*-axes is shown in Fig. 2.21, whereby the *D*-and *Q*-axes signals are direct quantities.

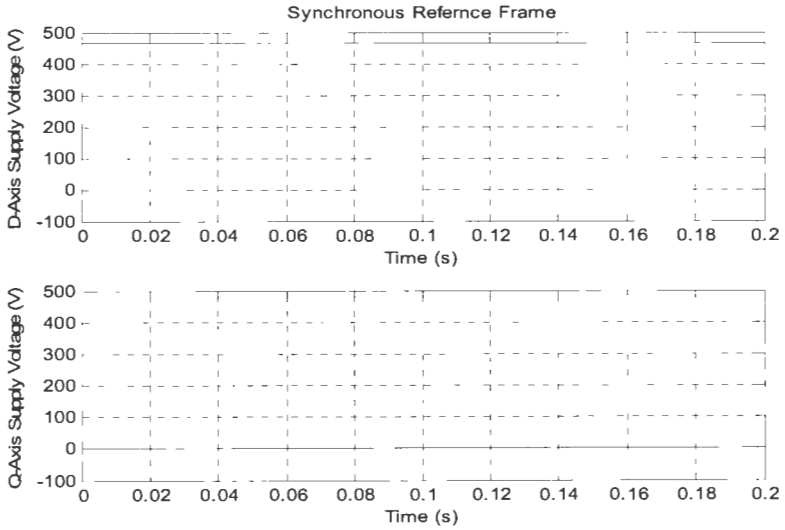

Figure 2.21: *D*-axes and *Q*-axes supply voltages in the synchronous reference frame

Fig. 2.22 shows the *D*-and *Q*-axes stator currents once the *D*-and *Q*-axes supply voltage is applied to the dynamic equivalent circuits in the synchronous reference frame, representing a direct online start. The currents are direct signals, while their magnitudes are large at startup but decrease once slip speed is attained, as with the stationary reference frame. Fig.2.23 shows the *D*- and *Q*-axes rotor currents.

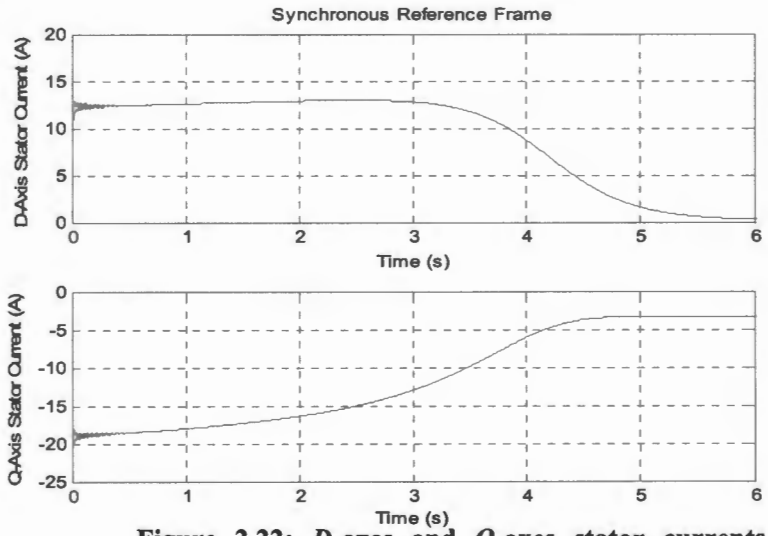

Figure 2.22: *D*-axes and *Q*-axes stator currents in the synchronous reference frame

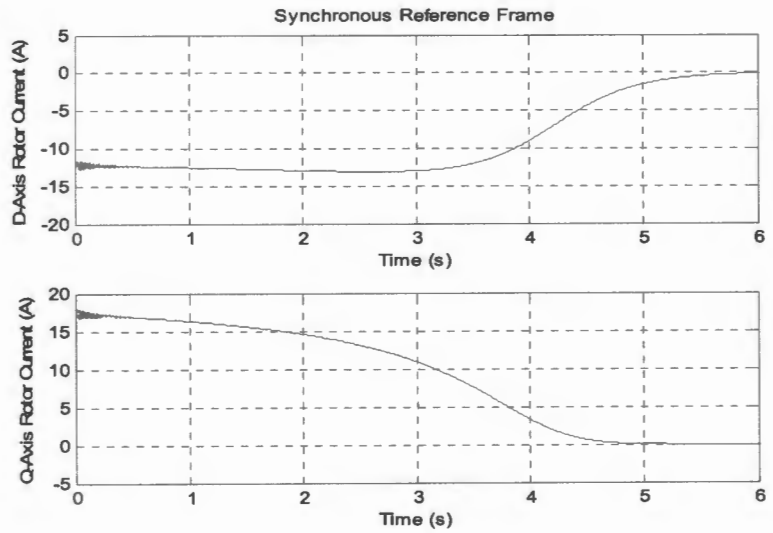

Figure 2.23: *D*-axes and *Q*-axes rotor currents in the synchronous reference frame

Fig. 2.24 and Fig. 2.25 shows the dynamic electromagnetic torque and speed response of the machine during direct online startup as the machine runs from maximum slip to operating slip speed. This is for the synchronously rotating reference frame model and it is evident that the dynamic torque and speed responses are identical to the stationary reference frame model.

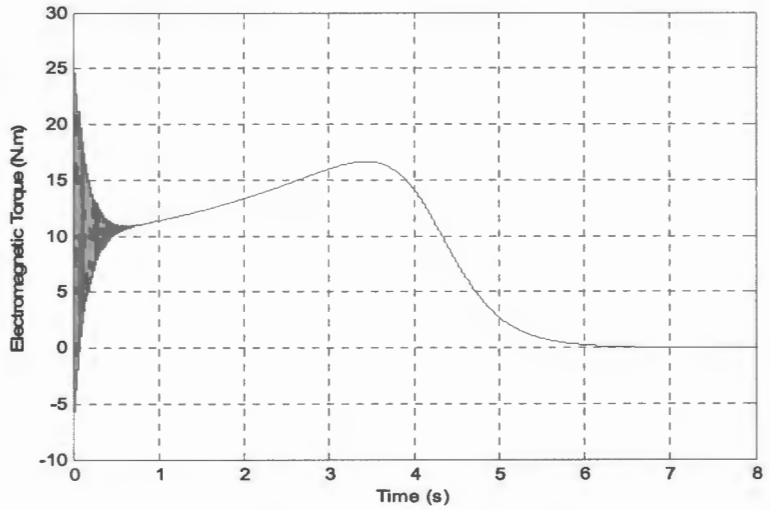

Figure 2.24: Electromagnetic Torque response during direct online start-up

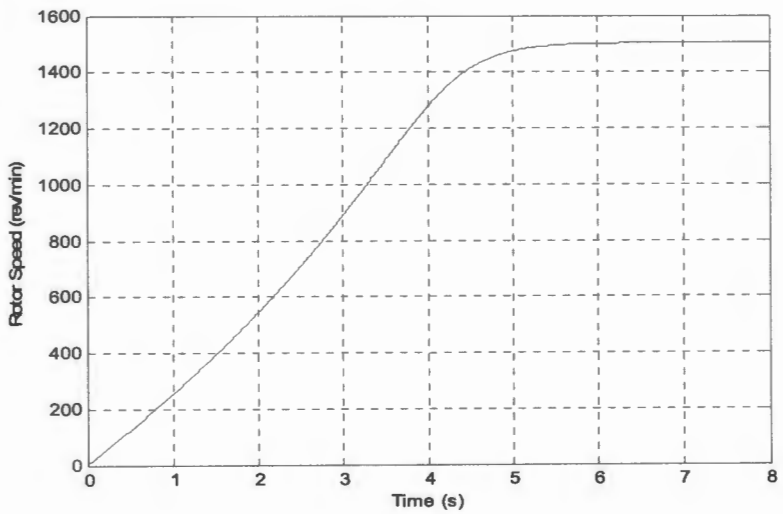

Figure 2.25: Rotor speed response during direct online start-up

2.9 Introduction to Field Orientated Control

The torque developed by an electrical machine is essentially a result of the interaction between the current passing through a conductor (i.e. the armature) while exposed to a magnetic field. In a separately excited DC machine, one has access to independent control of both the magnetic field (via the field winding) and the armature current (via the armature winding) [13].

When the magnetic field of the separately excited DC machine is constant, the torque developed by the machine is directly proportional to the armature current. However, in squirrel cage induction machines, one only has access to the stator winding. The stator current establishes both the magnetic field and the armature current. Since there is no independent control of the torque and magnetic field, the control is more complex than with DC machines.

The concept of Field Orientated Principles defines conditions for decoupling the field and torque control of the induction machine. It also allows for optimal torque production.

2.10 Optimal Torque Conditions

Optimal torque conditions are achieved when the plane of a current carrying coil lies parallel to an externally generated magnetic field. The diagrams below illustrate two situations whereby the current vector and the field are not perpendicular to each other (non-optimal conditions) and the other where they are (optimal conditions) [13].

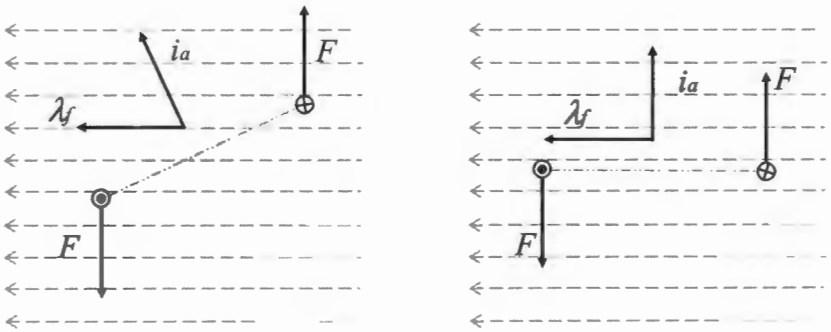

(a) (b)

Figure 2.26: (a) Non-optimal torque conditions (b) Optimal torque conditions

Although the forces acting on the conductor are equal in both cases, the torque acting on the coil is reduced (in the non-optimal case) due to the spatial position of the coil relative to the field. Thus, for optimal torque conditions to occur, the current vector and flux vector must be perpendicular to each other.

In DC machines, these conditions are satisfied due to the physical location of the armature winding relative to the field. The equation representing the torque of a DC machine is

$$T = k_T i_a \lambda_f \qquad (2.92)$$

k_T = constant

i_a = armature current

λ_f = flux vector

The diagram below represents the torque equation for a separately excited DC machine.

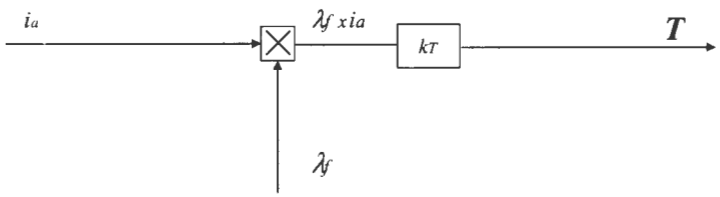

Figure 2.27: Block diagram representing the torque production of a separately excited DC machine

The purpose of the Field Orientation Principle is to represent the induction machine as an equivalent separately excited DC machine, which proves to be an extremely useful tool for control of the machine. The following section represents the dynamic model of the induction machine in the synchronous reference frame as an equivalent block diagram [13].

2.11 Dynamic Block Diagram of a Wound Rotor Induction Machine in the Synchronous Reference Frame – Rotor Side Control

Equation 2.91 represents the electromagnetic torque developed by the induction machine in terms of rotor and stator currents. The application requires speed control from the rotor side, thus the torque equation will have to be expressed in terms of the rotor currents.

The first step is to represent the torque in terms of rotor currents and the stator flux. From equation 2.67

$$i_s^e = \frac{1}{L_s}\left(\lambda_s^e - i_r^e L_m\right) \qquad (2.93)$$

Substituting into equation 2.91

$$T = \frac{P}{3R_s}\frac{L_m}{\tau_s}\left(\lambda_{Qs}^e i_{Dr}^e - \lambda_{Ds}^e i_{Qr}^e\right) \qquad (2.94)$$

where

$$\tau_s = \frac{L_s}{R_s} \tag{2.95}$$

To represent the torque equation in terms of rotor currents, the stator fluxes have to be expressed in terms of the rotor currents, which is achieved as follows. Substituting equation 2.93 into equation 2.64

$$\boldsymbol{v}_s{}^e = \frac{R_s}{L_s}\left(\boldsymbol{\lambda}_s{}^e - \boldsymbol{i}_r{}^e L_m\right) + (p + j\omega)\boldsymbol{\lambda}_s{}^e \tag{2.96}$$

Let

$$p = \frac{d}{dt}$$

Therefore

$$\boldsymbol{\lambda}_s{}^e = \frac{1}{p}\left(\boldsymbol{v}_s{}^e + \frac{L_m}{\tau_s}\boldsymbol{i}_r{}^e - \left(\frac{1}{\tau_s} + j\omega\right)\boldsymbol{\lambda}_s{}^e\right) \tag{2.97}$$

$$\lambda_{DS}{}^e = \frac{1}{p}\left(v_{DS}{}^e + \frac{L_m}{\tau_s} i_{Dr}{}^e - \frac{\lambda_{DS}{}^e}{\tau_s} + \omega\lambda_{QS}{}^e\right) \tag{2.98}$$

$$\lambda_{QS}{}^e = \frac{1}{p}\left(v_{QS}{}^e + \frac{L_m}{\tau_s} i_{Qr}{}^e - \frac{\lambda_{QS}{}^e}{\tau_s} - \omega\lambda_{DS}{}^e\right) \tag{2.99}$$

The dynamic block diagram for an induction machine in the synchronous reference frame (rotor side control) is shown in Fig. 2.28.

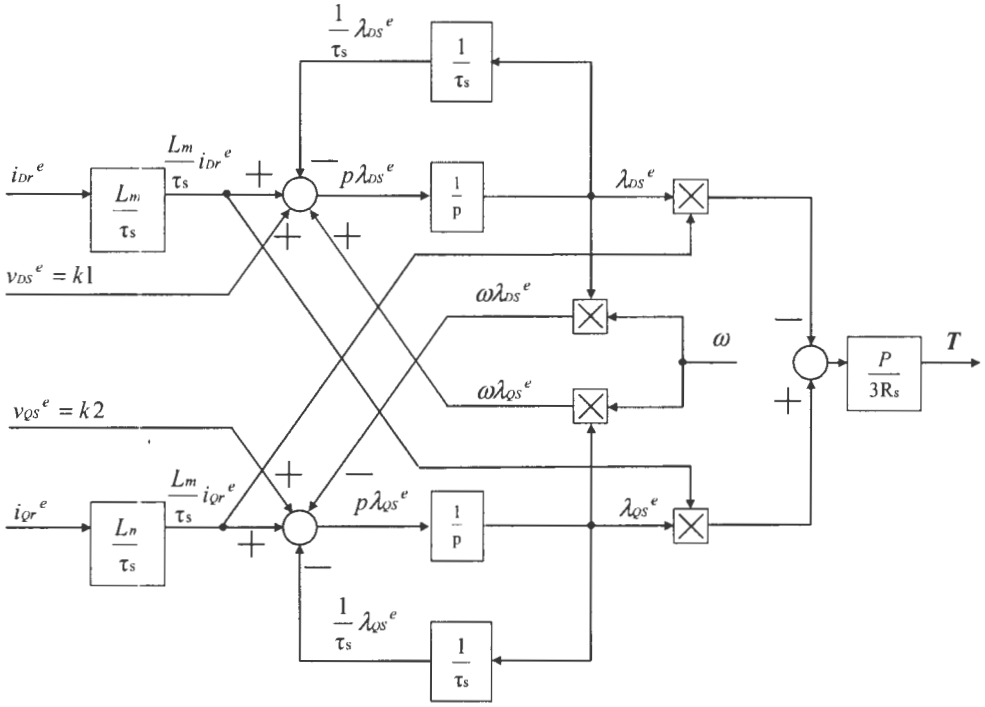

Figure 2.28: Dynamic Block Diagram for an Induction Machine in the Synchronous Reference Frame (Rotor-Side Control)

Fig. 2.28 does not take the form of the separately excited DC machine's block diagram, however by placing certain conditions, we are able to simplify the induction machine model. Thus the Field Orientation Principle represents a special case of the model illustrated above.

2.12 Field Orientated Conditions with Respect to the Stator Flux Vector

Since the induction machine is controlled in the synchronously rotating reference frame, by aligning the *d*-axes along the stator flux vector position, the *q*-axes stator flux component is set to zero.

i.e.

$$\lambda_{Qs}{}^{e} = 0 \tag{2.100}$$

then

$$T = -\frac{P}{3R_s}\frac{L_m}{\tau_s}\lambda_{DS}{}^{e} i_{Qr}{}^{e} \tag{2.101}$$

Let

$$k_T = -\frac{P}{3R_s}\frac{L_m}{\tau_s} \tag{2.102}$$

$$T = k_T \lambda_{DS}{}^{e} i_{Qr}{}^{e} \tag{2.103}$$

Where $\lambda_{DS}{}^{e}$=constant

In this way, a decoupled control between the electrical torque and the magnetic field is obtained. This clearly indicates the correlation between the separately excited DC machine and the field orientated control of the induction machine. Below is the block diagram of the simplified induction machine model ($\lambda_{Qs}{}^{e} = 0$).

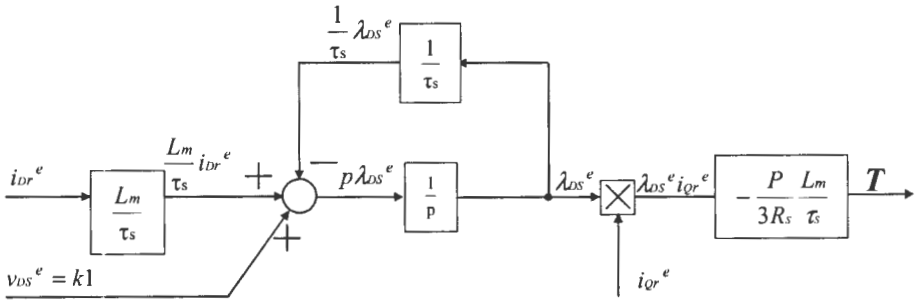

Figure 2.29: Block Diagram of Rotor-Side Control of an Induction Machine where Field Orientation is with respect to the Stator flux vector ($\lambda_{Qs}{}^{e}$=0)

The above diagram may now be simplified to represent the field orientated induction machine.

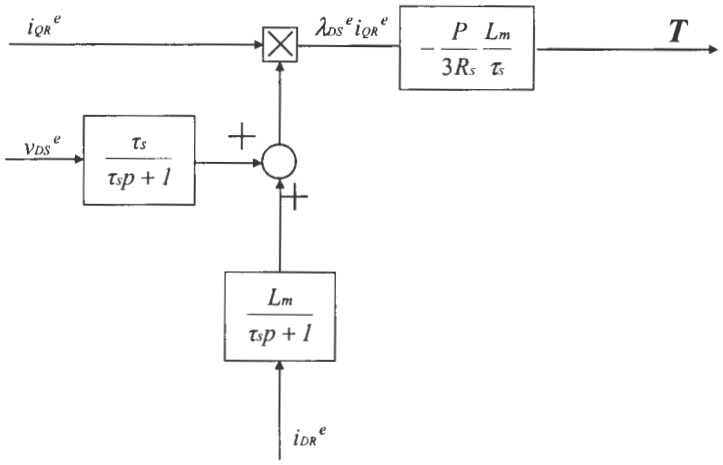

Figure 2.30: Simplified block diagram

The simplified block diagram illustrates the independent control of the flux and torque, using the direct and quadrature current components.

2.13 Conclusions

This chapter has renewed dynamic modelling and rotor field orientated control of an induction machine. The dynamic modelling of the induction machine is critical in developing the fundamental equations for field orientated control from the rotor-side of the wound rotor induction machine. Simulations were also performed using the dynamic models of the machine in the stationary and synchronous reference frames, to indicate the dynamic response of the machine variables during startup. The equations and initial conditions derived for the rotor field orientated control is used to attain control of the wound rotor induction machine with the use of back-to-back converters, as will be shown in the next chapter.

Chapter 3

3. CONTROL OF A DOUBLY-FED INDUCTION GENERATOR (DFIG) USING BACK-TO-BACK CONVERTERS

3.1 Introduction

In this chapter, the control of the wound rotor induction generator using back-to-back converters is examined. The rotor windings are attached to an external electric circuit, which serves as an active source (i.e. converter). The use of the converters in the rotor circuit allows for control of the torque-speed characteristics of the machine. In its application to wind energy, it would control the speed of the wind turbine allowing for maximum power capture. When both the rotor and stator are responsible for the transfer of power in an induction generator, it is known as Doubly-Fed Induction Generator (DFIG) [17].

3.2 A Description of the Overall System

The DFIG system uses an AC-AC converter in the rotor circuit. The vector control of the machine is achieved via the rotor-side converter, which allows for independent control of the torque and rotor excitation of the induction generator. The supply-side converter is responsible for maintaining a constant DC-link voltage, as well as control over the power factor [9].

When the DFIG system operates in steady state, the relationship between the stator, rotor, mechanical and overall power is given by the following equations (neglecting losses) [20]:

$$P_s = \omega_s T_m \tag{3.1}$$

$$P_r = -sP_s \tag{3.2}$$

$$P_m = (1-s)P_s = \omega_r T_m \tag{3.3}$$

$$P_g = P_s + P_r \tag{3.4}$$

where

P_m = mechanical power delivered to the generator

P_s = power delivered by the stator

P_r = power delivered by the rotor

P_s = total power generated and delivered to the grid

ω = synchronous speed (rad/s)

T_m = mechanical torque

ω_r = rotor speed (rad/s)

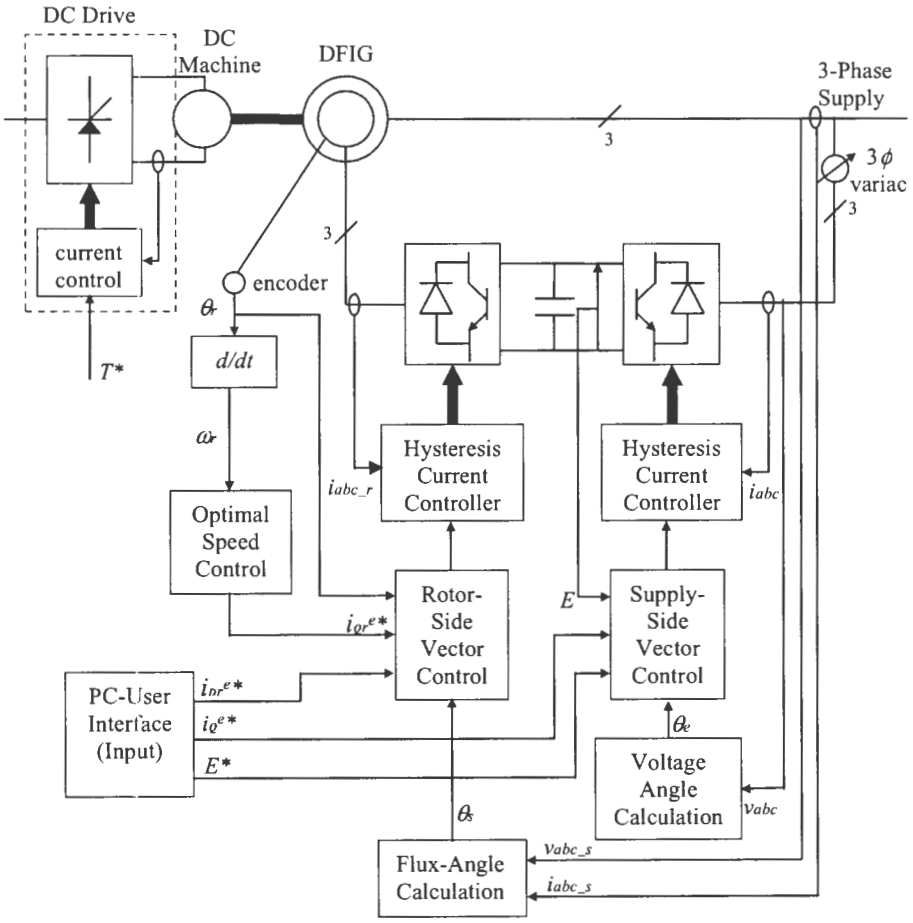

Figure 3.1: Schematic of a vector control system for a doubly-fed induction generator using back-to-back converters

Fig. 3.1 represents the overall lay out of the system. Both converters are current controlled, allowing bi-directional power flow. When the system operates below synchronous speed (sub-synchronous region), the rotor absorbs power. However, once the system surpasses synchronous speed, the rotor

delivers power (super-synchronous region). The rotor power is dependent upon the slip, as shown in equation 3.2.

The design of the system is based on the machine parameters attained from an actual 2.2kW, 3-Ph, 380V, 50Hz, 4 pole induction machine. The machine parameters are acquired by performing the no load and blocked rotor test on the machine. The extra resistors and inductors added onto the supply-side converter is, R =0.1Ω and L=20mH. The DC-link voltage is maintained at 300V and the supply-side 3-phase voltage is set to 100V.

3.3 Control of the Supply-Side Converter

The supply-side converter is used to keep the DC-link voltage constant, regardless of the rotor power direction. A vector control approach is used, whereby independent control of active and reactive power is achieved. The synchronous reference frame is orientated along the supply voltage vector. i_D^e is used to establish the DC-link voltage and i_θ^e is used to regulate the reactive power. Fig. 3.2 illustrates the schematic of vector control for the supply-side converter.

The supply voltage angle calculation is achieved as follows

$$\theta_e = \arctan\left(\frac{v_q{}^s}{v_d{}^s}\right) \tag{3.5}$$

where θ_e represents the supply voltage vector position[9].

i_D^{e*} is attained by processing the error DC-link voltage with a PI controller. The proportional and integral gains for the DC-link voltage controller are attained experimentally and from the literature. The DC-link voltage controller for T=0.01s is as follows

$$k(z) = 1.6859\left(\frac{z-0.9989}{z-1}\right) \tag{3.6}$$

Once the setpoint 3-phase currents have been determined, they are then processed by a hysteresis current controller, which then triggers the switching of the IGBT converter. A description of the hysteresis current controlleris described later.

When power is transferred from the 3 phase supply to the capacitor, the current flowing from the supply will be in phase with the supply voltage. When power is being transferred in the opposite direction, the current is 180° out of phase with the supply voltage (is true for i_{Q^e}*=0). When i_{Q^e}* is varied, it causes phase shifts in the currents which is thus responsible for the transfer of reactive power to and from the supply.

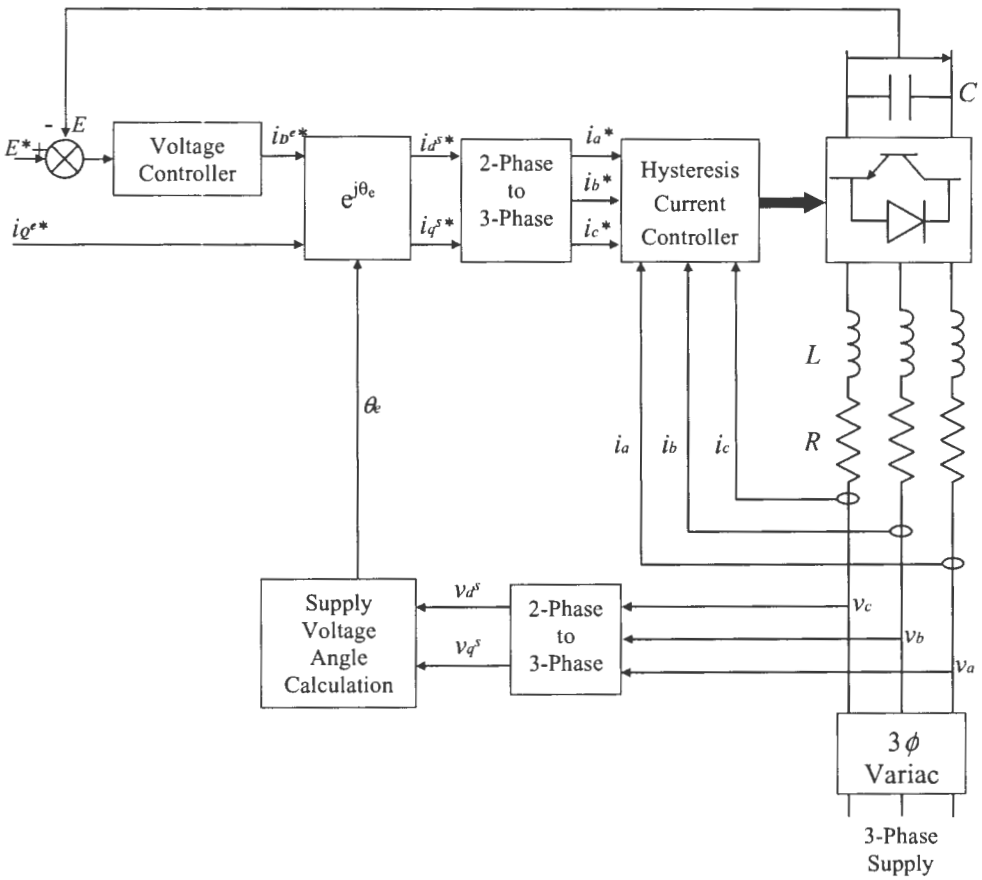

Figure 3.2: Schematic of vector control for the supply-side converter

3.4 Control of the Rotor-Side Converter

Control of the induction machine is achieved in the synchronously rotating *DQ* reference frame. The *D*-axis is aligned with the stator-flux vector position, which sets the *Q*-axis stator-flux component to zero. In this way, a decoupled control between the electrical torque and the magnetic field is obtained [9].

Since

$$\lambda_{Qs}{}^{e} = 0 \tag{3.7}$$

the torque is described as follows

$$T = -\frac{P}{3R_s}\frac{L_m}{\tau_s}\lambda_{Ds}{}^{e} i_{Qr}{}^{e} \tag{3.8}$$

as shown in Chapter 2.

Fig's 3.3 and 3.4 indicate schematic block diagrams for the machine control, with each representing a different method for calculating the stator flux and the stator flux angular position. $i_{Dr}{}^{e}$* is used to control the rotor excitation, however assuming that the reactive power to the machine is supplied by the stator, $i_{Dr}{}^{e}$* may be set to zero [9]. The torque is proportional to $i_{Qr}{}^{e}$, thus once T* is determined, $i_{Qr}{}^{e}$* is calculated (using equation 3.8). The 3-phase current setpoints are then achieved via the current transformations, and the actual currents into the machine are attained with the use of hysteresis current controllers.

The stator flux and the stator flux angular position may be calculated in two ways, which will be referred to as *method 1* (Fig. 3.3) and *method 2* (Fig. 3.4).

In *method 1,* the stator flux is calculated as follows

$$\lambda_{ds}{}^{s} = \int (v_{ds}{}^{s} - R_s i_{ds}{}^{s})dt \tag{3.9}$$

$$\lambda_{qs}{}^{s} = \int (v_{qs}{}^{s} - R_s i_{qs}{}^{s})dt \tag{3.10}$$

The stator flux angle is calculated from

$$\theta_s = \arctan\left(\frac{\lambda_{qs}{}^s}{\lambda_{ds}{}^s}\right) \tag{3.11}$$

where θ_s represents the stator flux position [9].

The ω_r error is processed by a PI controller to give the setpoint torque (T^*). The proportional and integral gains for the speed PI controller are attained experimentally and from the literature. The speed controller for T=0.1s is as follows

$$k(z) = 0.3388\left(\frac{z-0.9779}{z-1}\right) \tag{3.12}$$

The PI controller above is used for both methods.

Fig. 3.3 indicates the complete vector control for the rotor-side converter using (3.11) & (3.12) to calculate the stator flux and stator flux angle.

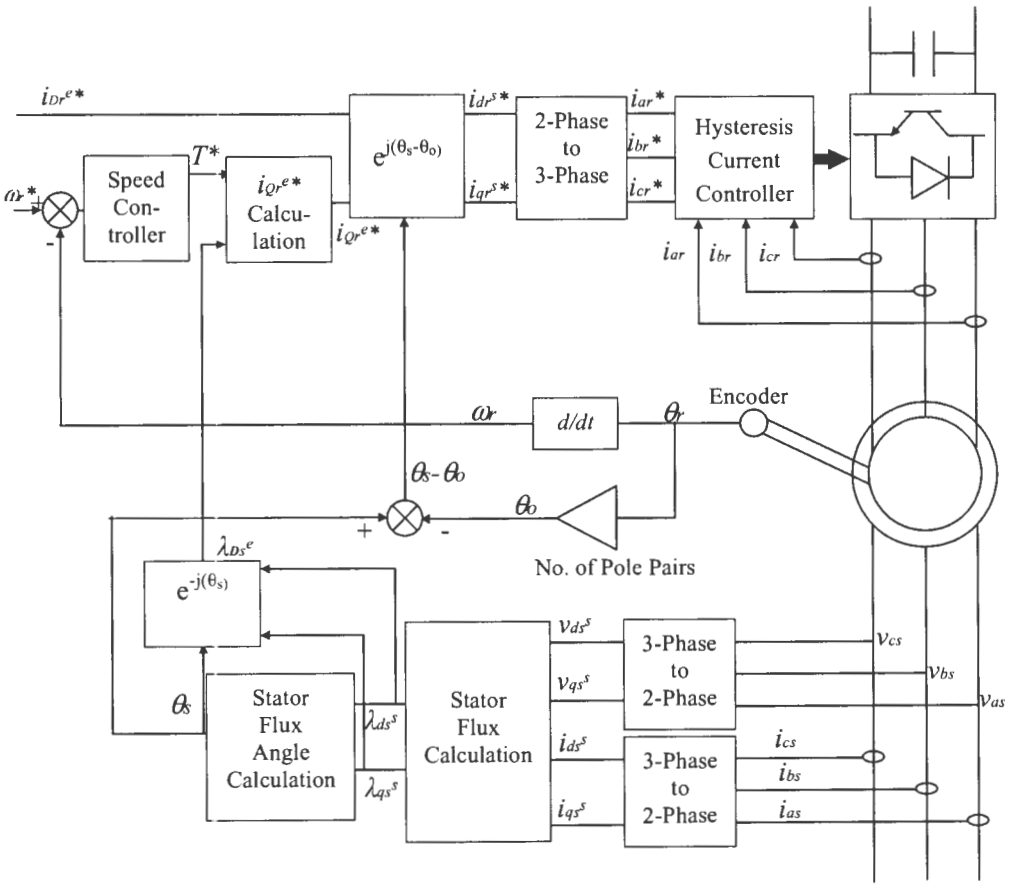

Figure 3.3: Schematic of vector control for the rotor-side converter using *method 1*

In *method 2,* the stator flux $\lambda_{Ds}{}^{e}$ and the stator flux position θ_s may also be calculated as follows. Since $\lambda_{Qs}{}^{e} = 0$, equation 2.93 may be re-written as shown below

$$\boldsymbol{i_s}^{e} = \frac{1}{L_s}\left(\lambda_{Ds}{}^{e} - \boldsymbol{i_r}^{e} L_m\right) \tag{3.13}$$

When substituting into equation 2.64

$$\boldsymbol{v_s}^{e} = \frac{R_s}{L_s}\left(\lambda_{Ds}{}^{e} - \boldsymbol{i_r}^{e} L_m\right) + (p + j\omega)\lambda_{Ds}{}^{e} \tag{3.14}$$

$v_{Ds}{}^{e}$ and $v_{Qs}{}^{e}$ may then be expressed as follows

$$v_{Ds}{}^{e} = \left(\frac{R_s}{L_s} + p\right)\lambda_{Ds}{}^{e} - \frac{R_s L_m}{L_s} i_{Dr}{}^{e} \tag{3.15}$$

$$v_{Qs}{}^{e} = \omega\lambda_{Ds}{}^{e} - \frac{R_s L_m}{L_s} i_{Qr}{}^{e} \tag{3.16}$$

$\lambda_{Ds}{}^{e}$ may be obtained from equation 3.15 and ω may be obtained from equation 3.16.

$$\lambda_{Ds}{}^{e} = \frac{\frac{L_s}{R_s} v_{Ds}{}^{e} + L_m i_{Dr}{}^{e}}{1 + \frac{L_s}{R_s}} \tag{3.17}$$

$$\omega = \frac{1}{\lambda_{Ds}{}^{e}}\left(v_{Qs}{}^{e} + \frac{R_s L_m}{L_s} i_{Qr}{}^{e}\right) \tag{3.18}$$

Fig. 3.4 illustrates the vector control for the rotor-side converter using *method 2.*

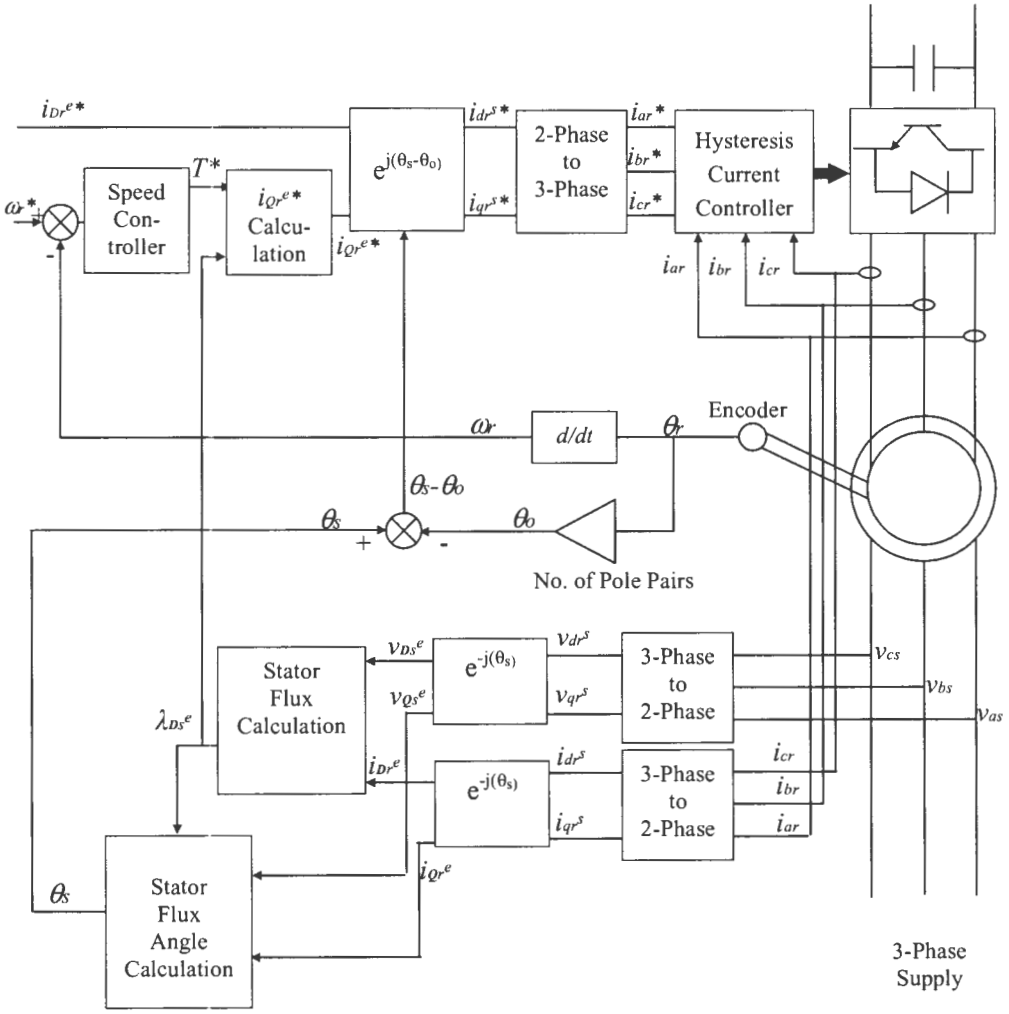

Figure 3.4: Schematic of vector control for the rotor-side converter using *method 2*

3.5 Hysteresis Current Controller

Fig. 3.5 illustrates the scheme used by the hysteresis current controller and Fig. 3.6 indicates the converter power circuit used by the DFIG, however the IGBT's have been replaced by ideal switches. This will be used to illustrate the switching pattern implemented by the hysteresis current controller.

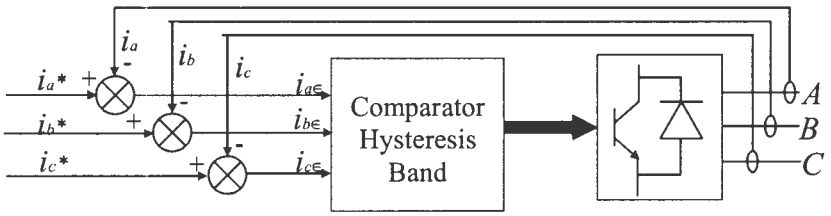

Figure 3.5: Block Diagram of the Hysteresis Current Controller

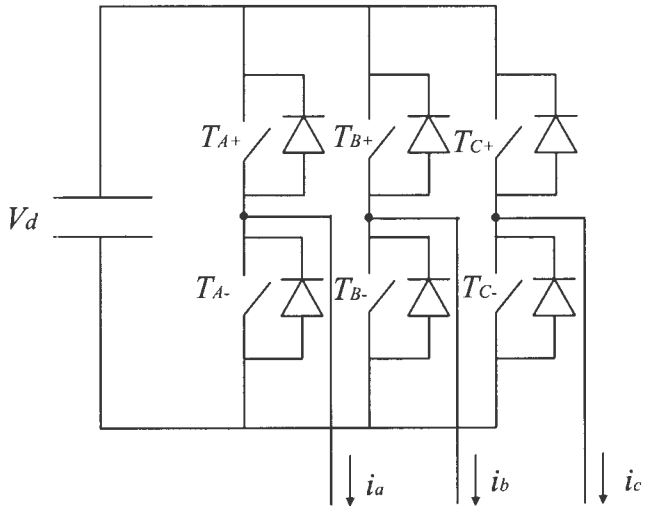

Figure 3.6: The Converter Power Circuit

Phase-A will be analysed to describe the concepts used by the controller, however this strategy is applied by all 3 phases. The strategy used by the controller occurs as follows: The actual currents are measured and read in by the controller together with the reference currents. Switches T_{A+} and T_{A-} are used to control the actual phase-A current. The reference current (i_a*) and actual current (i_a) are continuously compared. The comparison between the currents constitutes an error ($i_{a\epsilon}$). If this error lies outside a predetermined set value (Δi), a particular switching pattern is chosen from a table so as to reduce the error (the switching pattern will be explained later). The set value (Δi) determines the hysteresis band which limits the extent from which the actual

current may deviate from the reference current. The same logic applies to the other two phases.

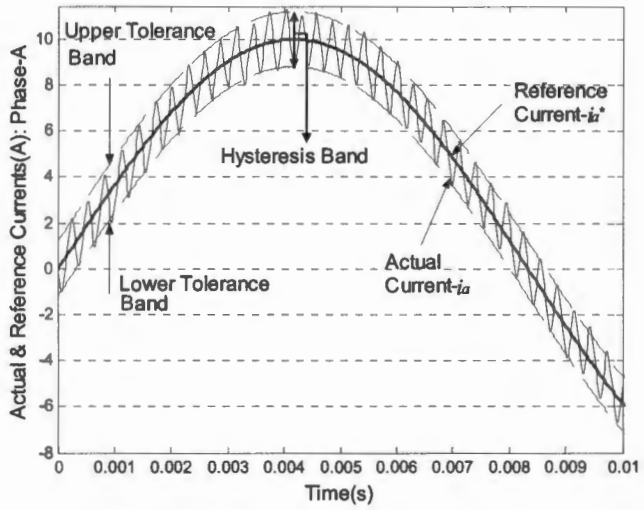

Figure 3.7: Actual and Reference Currents for a Sinusoidal Reference Signal

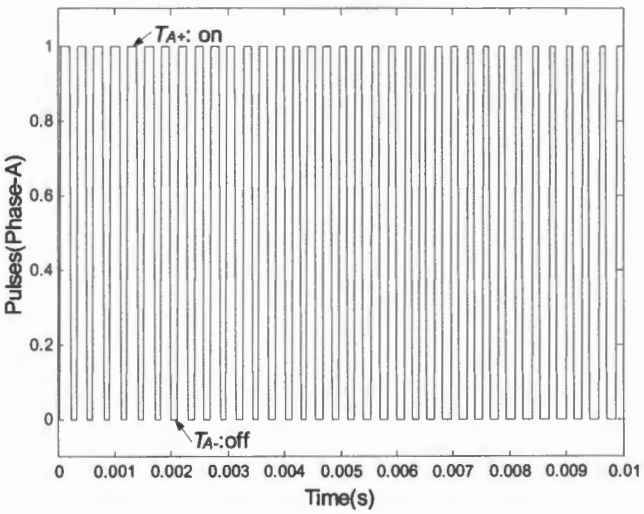

Figure 3.8: Pulses used for the control of Phase-A switches

The switching pattern occurs as follows: when the actual current i_a lies below the reference current i_a^* and below the lower tolerance band, $i_a^*-\Delta i$, T_{A+} switches on (T_{A-} switches off), thus increasing the actual current. T_{A+} is kept on until the actual current surpasses the upper tolerance band, whereby the

opposite switching pattern occurs (i.e. T_{A+} switches off and T_{A-} switches on), thus reducing the actual current. Fig. 3.7 illustrates the actual and reference currents for a sinusoidal reference, while Fig. 3.8 indicates the pulses used to control the switching of T_{A+} and T_{A-} [19].

By reducing the hysteresis band, the error between the actual and reference currents are reduced, thus providing a better approximation of the reference current. However, this introduces higher switching frequencies which has practical limitations since the frequency range is dependent on the power devices switching capabilities. Another disadvantage of increasing the switching frequency is the increase in losses of the converter [18].

The diagram below shows the simulation results of the 3-phase setpoint rotor currents and the corresponding actual rotor currents attained when controlling the induction machine. Both the setpoint and the actual currents are then fed into a hysteresis current controller which provides a particular switching pattern for the converter to produce the actual currents. The hysteresis band is set to 0.1A.

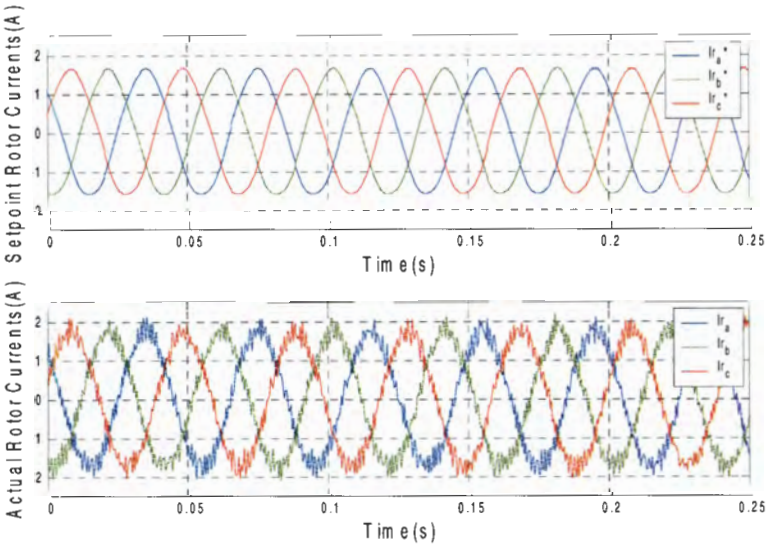

Figure 3.9: Simulation results illustrating the use of the hysteresis current controller

3.6 Conclusions

This chapter has described the implementation of the control strategies for the wound rotor induction machine with the use of the fundamental equations derived for the rotor field orientated control in Chapter 2. The vector control strategies for both converters are fully described and the operating principles of the hysteresis current controller are also outlined. A current controller was the preferred choice since this simplified the control strategies of the machine. The supply-side converter is shown to control the DC-link voltage and regulate the power factor. The rotor-side converter controls the speed of the machine, allowing maximum power absorption from the wind turbine.

Chapter 4

4. EXPERIMENTAL SETUP – HARDWARE & SOFTWARE DESIGN

4.1 Introduction

This chapter describes the experimental setups for the doubly-fed induction wind generator system and the cage rotor induction wind generator system.

4.2 Description of the Doubly-Fed Induction Generator Experimental Setup

Fig 4.1 shows the overall schematic of the experimental setup. The control strategies employed are mentioned in Chapter 3, with slight adjustments due to limitations in the capabilities of equipment.

All computational tasks are processed by the DS 1104 R&D Controller Card, as shown in Fig. 4.1. Measured signals are firstly buffered before being read in by the DS 1104 R&D Controller Card. A PC serves as an interface for the monitoring and control of the system. R and L have the same value as mentioned in Chapter 3, i.e. 0.1Ω and 20mH respectively. A DC drive is used to emulate the wind turbine in the presence of wind and consists of the DC machine connected to a thyristor converter. The Quad Differential Line Driver is used to preserve the data transmitted by the position encoder.

Fig. 4.2 shows a picture of the experimental setup in the laboratory.

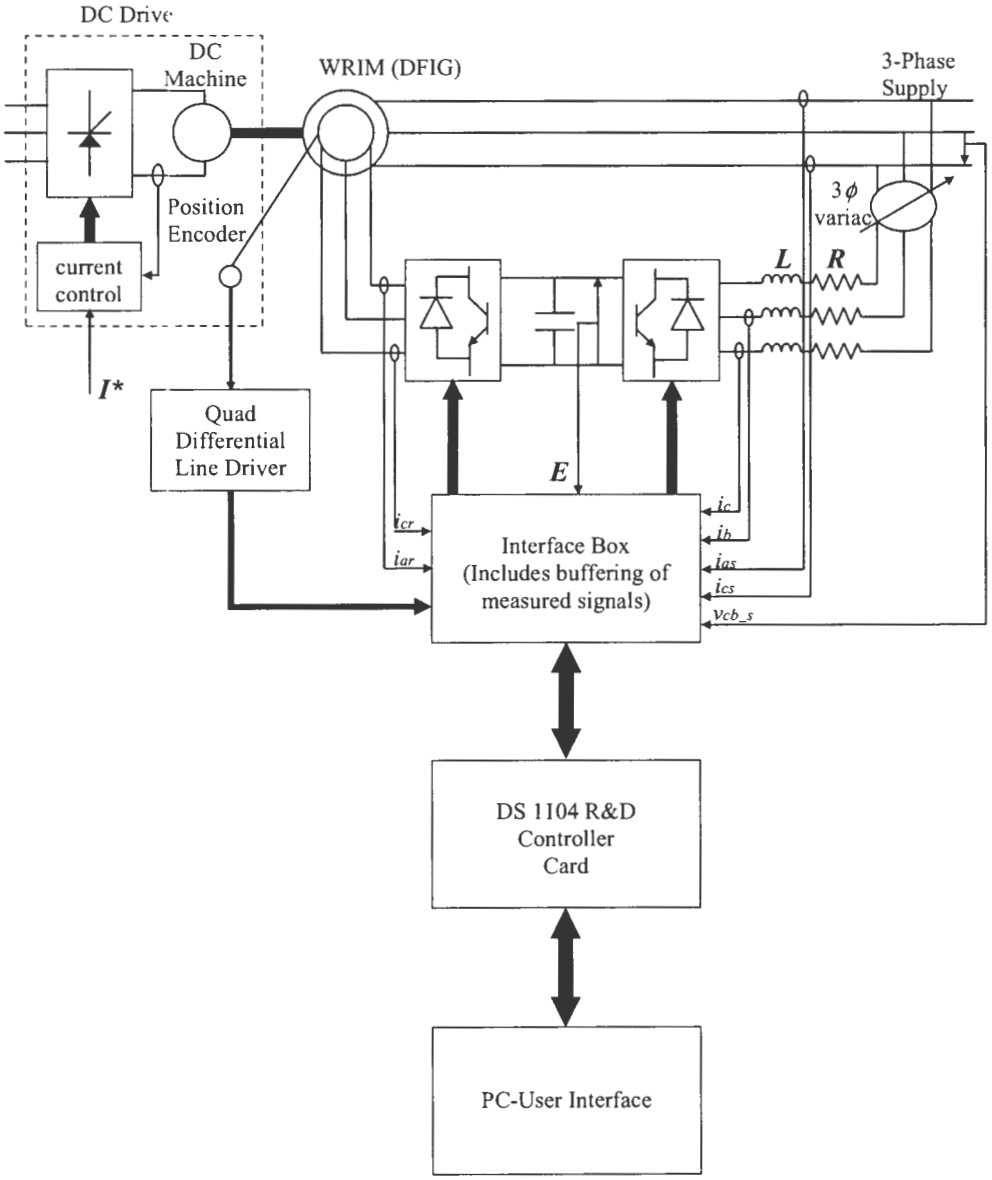

Figure 4.1: Schematic of the overall experimental DFIG setup

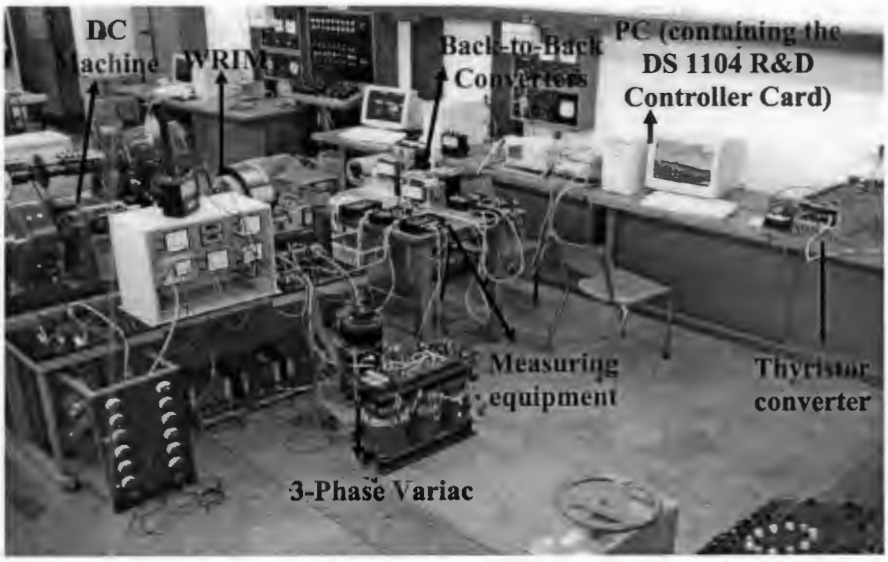

Figure 4.2: Experimental setup in the Machines Laboratory

4.3 Hardware Design for the Doubly-Fed Induction Wind Generator System

4 3.1 Converters

Fig. 4.3 shows the back-to-back converters located in the rotor circuit of the wound rotor induction machine. One converter forms part of the supply-side control and the other forms part of the rotor-side control (both control strategies are mentioned in the previous chapter). Before the supply-side converter and the rotor-side converter are connected together, they are first tested independently of each other. Once validating that they operated in close proximity to the theoretical predictions, the two converters are connected together, and further tests are carried out on the entire DFIG system.

Each converter consists of the following key components; an IGBT 6-pack, a DC-link capacitor and a driver board. The entire converter units may be attained from Semikron and is referred to as a Semistack.

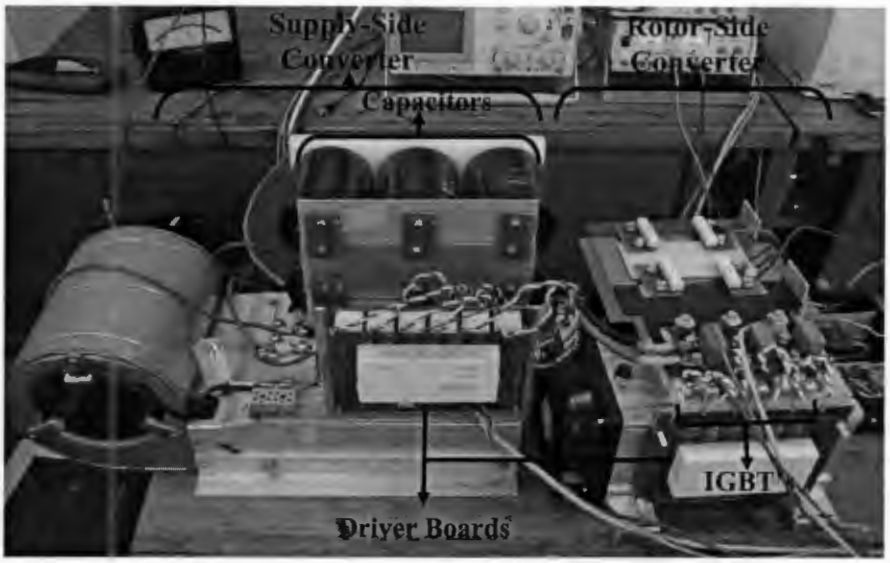

Figure 4.3: Back-to-back converters used in the rotor circuit of the wound rotor induction machine

4.3.1.1 Insulated Gate Bipolar Transistors (IGBTs)

The power electronic devices used for switching consist of IGBTs (Insulated Gate Bipolar Transistors). These semiconductor switches are voltage controlled and their terminals are identified as the same as that of a transistor. They are able to handle larger collector currents compared to other semiconductor devices (i.e. MOSFETS), and therefore have higher power ratings. They are also capable of switching at extremely high-speeds, making the size and cost of the associated transformers, capacitors and inductors, smaller and less expensive [21].

The IGBTs used forms part of Semikron's range of power electronic devices. The IGBT modules consist of dual IGBTs forming one leg of the three-phase-bridge circuits. The modules used for the rotor-side converter are the SKM 100 GB 123D (Appendix B) and the modules used for the supply-side converter are the SKM 200 GB 123D (Appendix B). The ratings of the modules far surpass the rating of the machine and the reason for this difference is due to the availability of equipment in the machine's laboratory.

4.3.1.2 Driver Board

The driver board is responsible for providing the correct output voltage for the switching of the IGBTs. The Semikron SKHI 61 driver boards are selected for both 6-packs. The data sheet of this device is shown in Appendix C. The SKHI 61 is a 6-pack driver for IGBT modules in three-phase-bridge circuits. These devices have a large amount of protection schemes to protect both the IGBTs and the controller card. Some of the more important features include: short circuit protection by monitoring the voltage across the collector and the emitter, the transmission of the signals via opto-couplers, supply under-voltage protection, etc.

The driver inputs directly accept the controller card-output voltages of 0V=Off and +5V=On and outputs the turn-off= -6.5V and turn-on= 14.9V threshold voltages of the IGBTs. Table 1 of Appendix C indicates the input voltage levels and input impedances of the driver while Table 4 of Appendix C indicates the output gate-emitter voltage of the driver. The only external components which are added to the driver are the gate resistors for each IGBT. The gate resistor should be a minimum of 10Ω as stipulated in Appendix C. Therefore the gate resistor is selected to have a value of 22Ω.

The driver also ensures that no 2 IGBTs of the same bridge may be switched on simultaneously. The time set by the board to ensure that both IGBTs are off before the alternate IGBT is switched on is known as the interlocking time. This time is set to 4μs, however it may be altered by varying the connections to the configuration pins. The factory setting of 4μs provided a good safety margin and therefore is used for the setting of both drivers.
The collector-emitter voltage (V_{CE}) is monitored by connecting the driver collector pin to the collector of the IGBT. The turn-off voltage threshold for short circuit protection may be reduced by connecting a resistor between the $V_{CE\ -threshold}$ (pin1) and $V_{CE\ -threshold}$ (pin2) of the driver, as shown in Fig. 4 Appendix C. A capacitor needs to be included with the resistor, so as to set the

blanking time. The blanking time is the time between the turn-on of the IGBT and V_{CE} registration. Without any resistor and capacitor connected for setting the V_{CE} threshold and blanking time, the driver reverts back to the factory setting. This sets the V_{CE} threshold at 5.8V and the blanking time to 3.54μs, which is sufficient for this application.

4.3.2 3-Phase Wound Rotor Induction Machine

This section deals with the calculation of the equivalent circuit parameters of the wound rotor induction machine. The machine used is a 3-phase, 2.2kW, 380V, 50Hz, 4-pole wound rotor induction machine, as shown in Fig. 4.4. The recommended IEEE Standard 112B for determining the parameters of the steady-state per-phase equivalent circuit of an induction machine is used, as shown in Fig. 4.5. Both the no-load and blocked rotor tests are performed to calculate the necessary parameters. The two watt meter method is used to measure the input power into the machine.

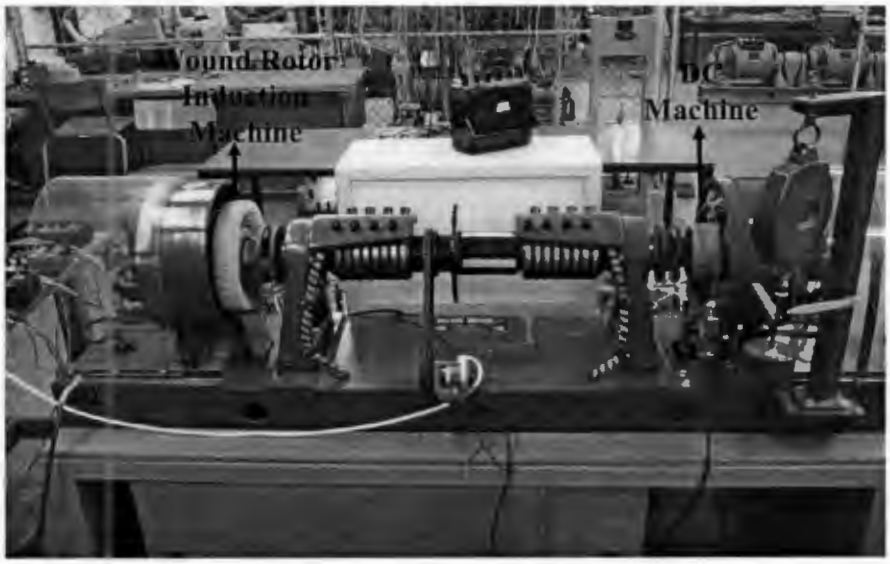

Figure 4.4: DC machine and Wound Rotor Induction Machine

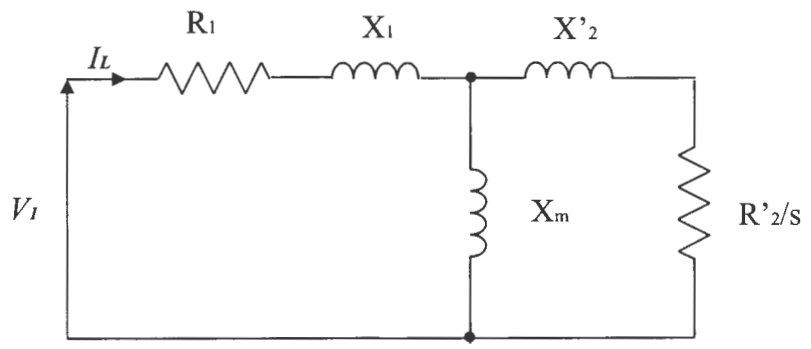

Figure 4.5: IEEE recommended steady-state per-phase equivalent circuit for an induction machine

In the circuit above, the parameters are as follows

R_1 – stator resistance

X_1 – leakage reactance

X_m – mutual flux linkage common to both the stator and rotor

R'_2 – rotor resistance transferred to the stator side

X'_2 – rotor leakage reactance transferred to the stator

V_l – line-to-neutral voltage

I_L – line current

4.3.2.1 No Load Test

During the no load test, the rotor is not connected (coupled) to any load. The rated voltage at rated frequency is applied to the stator windings while the rotor windings are shorted. This gives information about the excited current and rotational losses [22]. The IEEE equivalent circuit for the no load test is shown in Fig. 4.6.

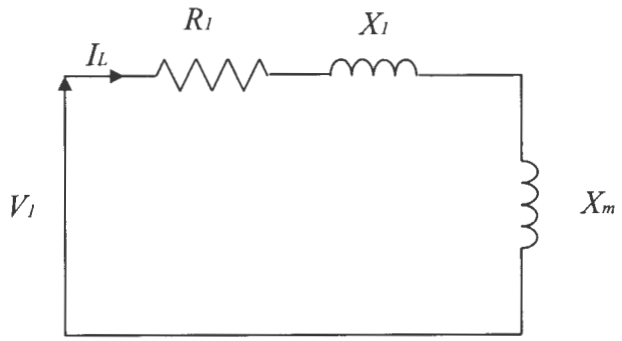

Figure 4.6: IEEE recommended steady-state per-phase equivalent circuit for the no load test

From the no load test, the rotational power loss, P_{ROT}, and the no load impedance, $X_{NL} = X_1 + X_m$, may be obtained. The calculations are explained below.

The measured line-to-line voltages, line currents, total input power and stator line resistance is $V_{LL} = 376V$, $I_L = 1.5A$, is $P_{TOT} = 229W$ and $R_1 = 6.6\Omega$.

Therefore the line-to-neutral voltage is: $V_1 = \frac{V_{LL}}{\sqrt{3}} = 217.08V$

The per-phase power is: $P_{PH} = P_{TOT}/3 = 76.3W$

The per-phase apparent power is: $S_{PH} = \frac{V_{LL}I_L}{\sqrt{3}} = 325.6VA$

The per-phase reactive power is: $Q_{PH} = \sqrt{S_{PH}^2 - P_{PH}^2} = 316.5VAR$

The per phase rotational power loss is: $P_{ROT/PH} = P_{PH} - I_L^2 R_1 = 61.45W$

The no load impedance is calculated using the equation below.

$$Z_{NL} = \frac{V_1}{I_L} = 143.9\Omega$$

The no load resistance is then calculated as follows:

$$R_{NL} = \frac{P_{PH}}{I_L^2} = 33.9\Omega$$

From the no load impedance and the no load resistance, the no load reactance may be calculated

$$X_{NL} = \sqrt{Z_{NL}^2 - R_{NL}^2} = 139.85\Omega$$

$$X_{NL} = X_1 + X_m = 139.85\Omega$$

4.3.2.2 Blocked Rotor Test

During the blocked rotor test the rotor is locked, and rated currents are supplied to the stator terminals. Information about the leakage impedance of the machine may be extracted from the blocked rotor test [22]. The IEEE equivalent circuit for the blocked rotor test is given in Fig. 4.7.

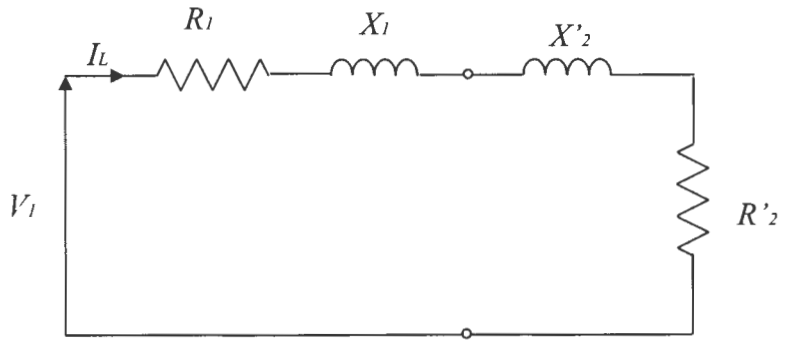

Figure 4.7: IEEE recommended steady-state per-phase equivalent circuit for the blocked rotor test

The following parameters are calculated from the blocked rotor test: X_1, X_m, X'_2, R'_2. These parameters are calculated as follows.

The measured line-to-line voltages, line currents, total input power and stator line resistance is V_{LL} = 137V, I_L=3.78A, P_{TOT} = 480.9W and R_1 = 6.6Ω.

Therefore the line-to-neutral voltage is: $V_1 = \frac{V_{LL}}{\sqrt{3}} = 79.097V$

The per-phase power is: $P_{PH} = P_{TOT}/3 = 160.3\text{W}$

The per-phase apparent power is: $S_{PH} = \frac{V_{LL}I_L}{\sqrt{3}} = 298.99\text{VA}$

The per-phase reactive power is: $Q_{PH} = \sqrt{S_{PH}^2 - P_{PH}^2} = 252.38\text{VAR}$

Therefore the blocked rotor resistance may be calculated as follows

$$R_{BL} = \frac{P_{PH}}{I_L^2} = 11.21\Omega$$

$$R = R_{BL} - R_1 = 4.61\Omega$$

The blocked rotor impedance is then calculated using the line current and line-to-line impedance

$$Z_{BL} = \frac{V_1}{I_L} = 20.925\Omega$$

The blocked rotor reactance is then calculated

$$X_{BL} = \sqrt{Z_{BL}^2 - R_{BL}^2} = 17.66\Omega$$

From which X'_1 and X'_2 may be attained

$$X_1 + X'_2 = X_{BL} = 17.66\Omega$$

$$X_1 = X'_2 = 8.83\Omega$$

The magnetising reactance may be calculated from equation $X_{NL}=X_m+X_1$

$$X_m = 131\Omega$$

The rotor resistance may then be calculated

$$R'_2 = \left[\frac{X'_2 + X_m}{X_m}\right]^2 R = 5.25\Omega$$

4.3.2.3 Complete equivalent circuit with parameters

The diagram below represents the equivalent circuit of the induction machine with the circuit parameters attained from the no load and blocked rotor tests.

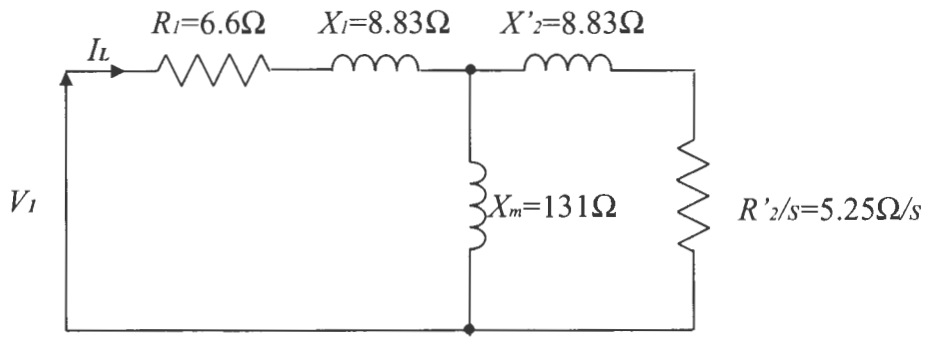

Figure 4.8: IEEE recommended steady-state per-phase equivalent circuit for an induction machine with circuit parameters

4.3.3 DC Drive

The DC drive, which consists of a DC machine and thyristor converter, is responsible for emulating the wind turbine. This is done by providing the desired torque to the shaft of the wound rotor induction machine, while in current control mode. The DC machine and wound rotor induction machine forms part of a test set, as shown in Fig. 4.4. The DC machine is rated at 2.2kW. The field of the DC machine is excited from a 220V DC supply and the thyristor converter, shown in Fig. 4.9, provides the controlled supply to the armature.

Figure 4.9: The 4-Quadrant Thyristor Converter

4.3.4 Current and Voltage Transducers

Voltage and current measurements are performed using specialised current and voltage transducers. The LEM modules (current and voltage transducers for industrial applications) are best suited for this application. The transducers selected from the LEM module range, are the voltage transducers LV 25-P (Appendix D) and the current transducers LA 25-NP (Appendix D). Fig. 4.10 shows the boxes containing the Lem modules, which are used for voltage and current measurements.

Some of the advantages of using the LEM modules over other measuring devices include:

- High precision over a very wide frequency bandwidth
- Excellent linearity
- Galvanic isolation between the primary circuit and the secondary circuit
- Low thermal drift
- Very robust

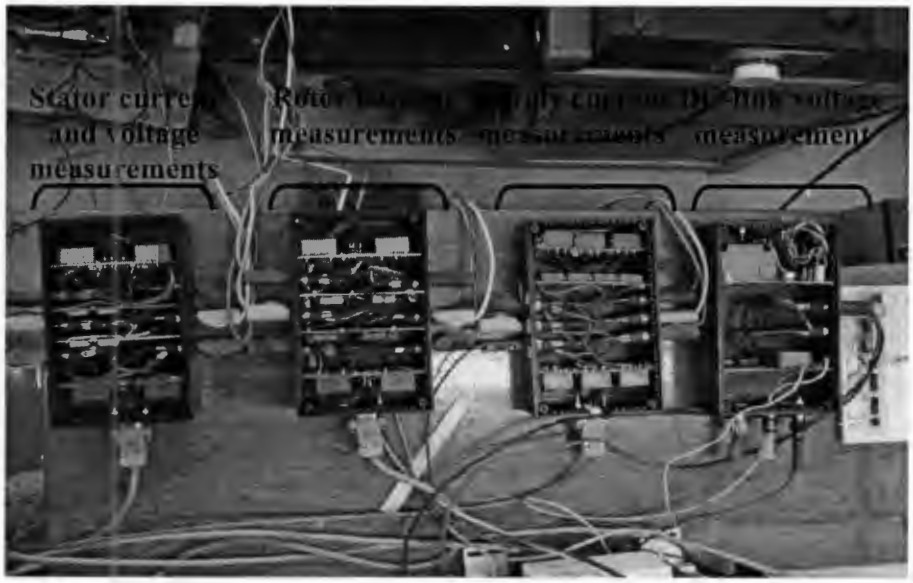

Figure 4.10: Lem modules used for voltage and current measurements

These current and voltage transducers require that certain resistances be connected externally as well as an external supply voltage of ±15V. These resistance values need to be selected so as to ensure that the voltages and currents stay within the maximum range and that saturation does not occur. Their values are determined by the maximum input voltages and currents connected to the primary circuit and the desired output voltages on the secondary side. The output voltage of the secondary side would in turn be determined by the input range of the ADC, which lies between ±10V.

4.3.4.1 Selection of external devices to be connected to the LV 25-P

Two LV 25-P devices are used to measure the DC-link voltage and the grid line-to-line voltage. Fig. 4.11 illustrates a schematic of the LV 25-P device as well as the external connections to the power supply and necessary resistances.

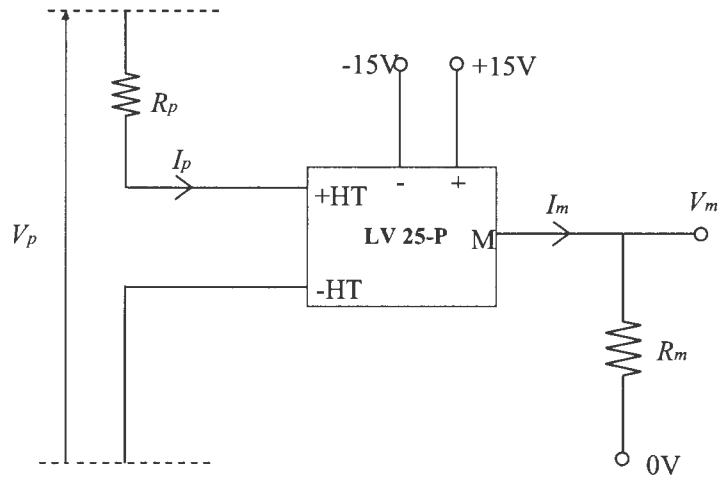

Figure 4.11: The schematic of the LV 25-P device and the external connections

The selection process of the resistances R_p and R_m for a specific input voltage is as follows. If the desired voltage to be measured has a range of $\pm V_1$ V, then the primary current (I_p) range of the LV 25-P must be within ±14mA ($\pm I_{pmax}$). Therefore the resistance R_p must be selected to ensure that the maximum primary current range is adhered to. This is shown in the equation below.

$$R_p \geq \frac{V_1}{I_{p\,\max}}$$

A secondary current (I_m) is then produced in the secondary coil, which is an exact scaled up representation (2500:1000) of the primary current.

$$I_m = I_p \times 2.5$$

The secondary current is then converted to the measurement voltage (V_m) using R_m, however R_m must be in the range 100-190Ω.

$$V_m = I_m \times R_m$$

These selection criteria of resistances will be illustrated in the selection of resistances for the two voltage measurements mentioned above.

The maximum DC-link voltage is 600V and the primary current measuring range for the LV 25-P is ±14mA. Therefore R_p must be greater than 600V/14mA= 42.857kΩ. R_p is selected as 108kΩ thus making I_p = 5.55mA. This makes the secondary current, I_s =5.5mAx2.5=13.88mA. To ensure that the output secondary voltage (V_m) stays within the input range of the ADC (±10V), R_m is selected to be 180Ω, giving a maximum output secondary voltage of 2.5V.

Table 4.1: External components and gains for the DC-link voltage measurement

Components	Values
Primary Resistor (R_p)	108kΩ
Measuring Resistor (R_m)	180Ω
Scaling Current Factor(K)	2500/1000

The line-to-line voltage is $380V_{(rms)}$. Allowing a 20% error region, the maximum line-to-line voltage is $1.2x380V_{(rms)}$=456 $V_{(rms)}$. R_p must be greater than $\left(456V \times \sqrt{2}\right)/14mA = 46.063k\Omega$. R_p is selected as 94kΩ thus making $I_p = \left(456 \times \sqrt{2}\right)/94k\Omega = 6.86mA$. Taking the scaling factor into account, the secondary current, I_s would then be I_s=6.86mAx2.5=17.15mA. Ensuring that the output secondary voltage (V_m) stays below the input range for the ADC, R_m is selected to be 100Ω, giving an output secondary voltage of 1.715V.

Although different resistor values may be used to attain larger measuring voltages, these resistance values allowed for a greater amount of tolerance in the error region of the assumptions made to the maximum DC-link voltage and the line-to-line voltage.

Table 4.2: External components and gains for line-to-line voltage measurement

Components	Values
Primary Resistor (R_p)	94kΩ
Measuring Resistor (R_m)	100Ω
Scaling Current Factor(K)	2500/1000

4.3.4.2 Selection of external devices to be connected to the LA 25-NP

Six LA 25-NP devices are used to make six current measurements. The current measurements include 2 rotor currents, 2 stator currents and 2 supply currents. Fig. 4.12 illustrates the schematic of the LA 25-NP device as well as the external connections to the power supply and the measurement resistor.

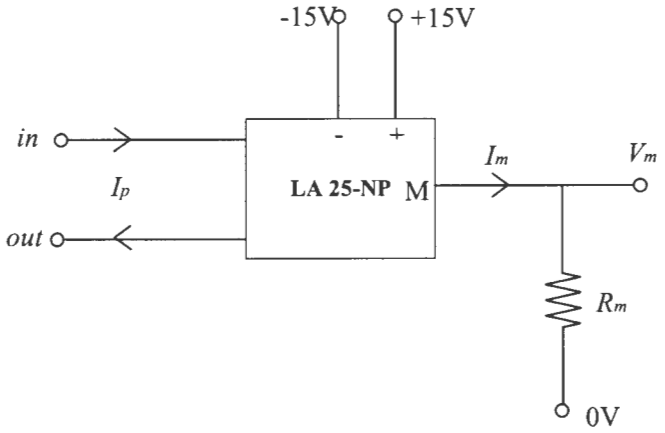

Figure 4.12: The schematic of the LA 25-NP device and the external connections

The selection of the measurement resistor occurs as follows. The LA 25-NP produces a secondary current in the secondary coil, which is a scaled down replica of the primary current flowing in the primary coil. The scaling factor (K) may be set externally. The equation below shows the relationship between the primary current and the secondary current (also known as the measurement current, I_m).

$$I_m = \frac{I_p}{K}$$

The measurement resistor is then chosen to ensure that the output (measurement) voltage does not surpass the input range to the ADC (±10V).

$$R_m = \frac{V_m}{I_m}$$

The LEM modules setting for the measuring of the rotor, stator and supply

currents are the same. The approximate maximum peak current entering the machine (under rated conditions) is

$$I_{rated(rms)} \times \sqrt{2} = 4\text{A} \times \sqrt{2} = 5.66\text{A}$$

Therefore assuming rated conditions, the primary current, I_p = ±5.66A. The scaling factor has been set to, K = 0.002. This is selected to make the most of the ADC input range allowing for higher precision.

Using the above equation, the secondary current may then be calculated as follows:

$$I_m = \frac{\pm 5.66\text{A}}{500} = \pm 11.32\text{mA}$$

R_m is then calculated to ensure that the measurement voltage does not surpass ±10V. A 680Ω resistor is selected for R_m. This ensured a maximum measurement voltage of

$$V_m = \pm 11.32\text{mA} \times 680\Omega = \pm 7.7\text{V}$$

The measurement voltage is for rated current into the machine and ensures that the voltage is within ±10V, while allowing for 30% tolerance region on the peak current entering the machine.

Table 4.3: External component values and gain for stator, rotor and supply current measurement

Components	Values
Measuring Resistor (R_m)	680Ω
Current Scaling Factor (K)	1/500

4.3.5 Position Encoder

The position (incremental shaft) encoder is used to locate the exact position of the rotor. The RS58-0/1000 incremental shaft encoder, from RS-Components, is selected to detect the rotor's position. This is a universal standard encoder and is compatible with the DS 1104 R&D Controller Card. It also ensures high signal accuracy and it is capable of measuring up to speeds of 10 000rpm. Appendix E shows the data sheet of the encoder with further specifications. The position encoder, shown in Fig. 4.13, is mounted next to the shaft of the

two machines whereby a 1:1 gearing system is used to track the exact position of the rotor.

The controller card supplied the encoder with 0V and +5V. The incremental encoder provides the 2 encoder signals A (PHI0) and B (PHI90), the index signal, and it also makes provision for an error signal. The encoder signals produce 1000 pulses per revolution, which is generated on signals A and B. Signal B is 90° out of phase with signal A, and provides information about the direction of rotation. The index signal is used to provide a trigger for resetting the encoder position, once completing a revolution.

To preserve the data transmitted by the encoder, the signals are passed through a Quad Differential Line Driver (National Semiconductor DS 26LS31C), as shown in Appendix F, which converts the single-ended TTL signals to Differential RS422 signals. These signals are compatible with the controller card.

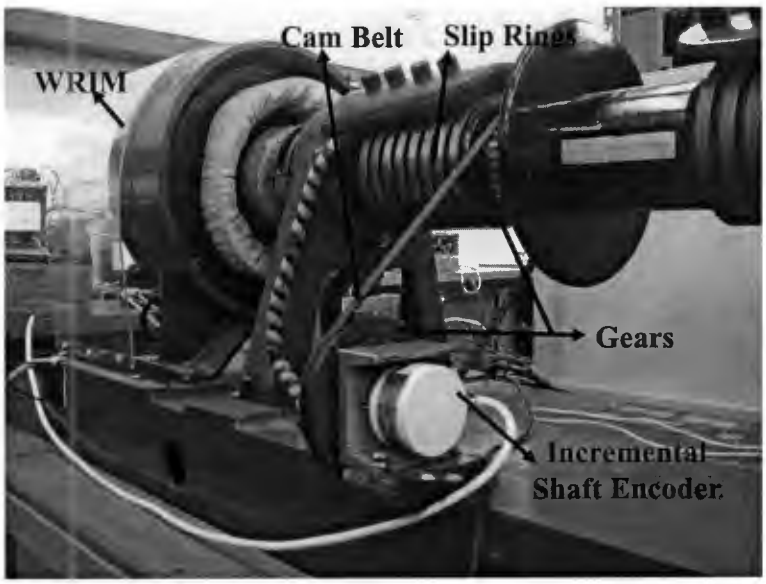

Figure 4.13: Position encoder and mounting

4.3.6 *Interface Box*

Fig. 4.14 shows the interface box, which buffers the measured signals from the Lem modules using opamps (Appendix G), before connecting them to the controller card. It also serves as an interface between the controller card and the driver boards of the back-to-back converters as well as an interface between the controller card and the quad differetial line driver, as shown in Fig. 4.1.

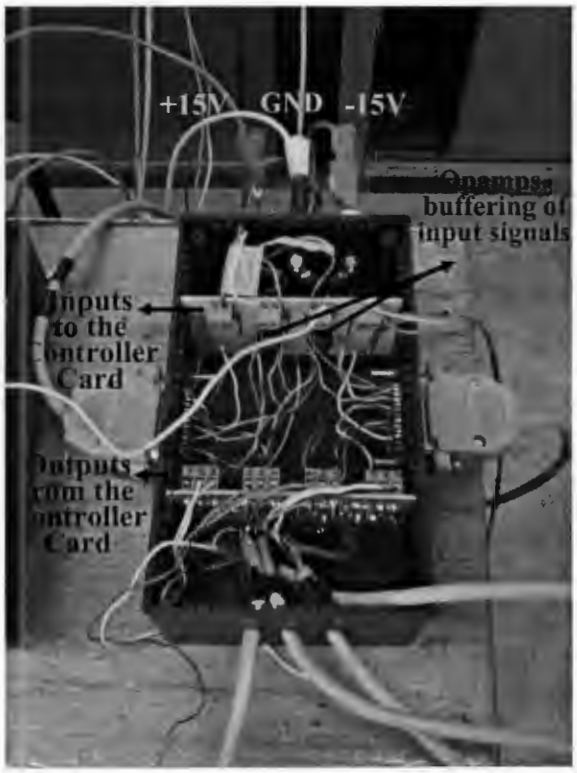

Figure 4.14: Interface Box

4.3.7 *DS 1104 R&D Controller Card*

The DS 1104 R&D Controller Card, shown in Fig. 4.15, is slotted into the PC's mother board. It is used to perform all computational and control tasks for both converters.

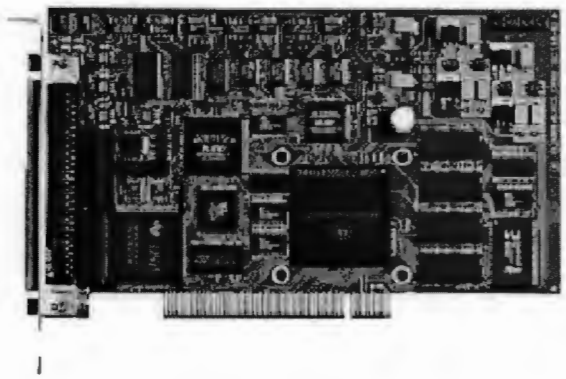

Figure 4.15: DS 1104 R&D Controller Card

The controller card forms part of the Advanced Control Educational Kit (ACE Kit), manufactured by dSPACE, and is fully programmable from the Matlab-Simulink block diagram environment. This is the case, provided that the implementation (real-time interface) software, supplied by dSPACE, is installed.

This software translates the simulink model into equivalent C-code for processing by the main processor. Although this doesn't prove to be the most efficient means of control, it does allow for rapid testing of control prototypes. The card may also be programmed from C-code making the card as efficient as any other processor.

The ACE Kit also consists of an experimental software package, called ControlDesk, which allows for real-time control of the system. Fig. 4.16 shows the relationship between the controller card and the software packages. The kit essentially upgrades a PC into a development system for rapid control prototyping.

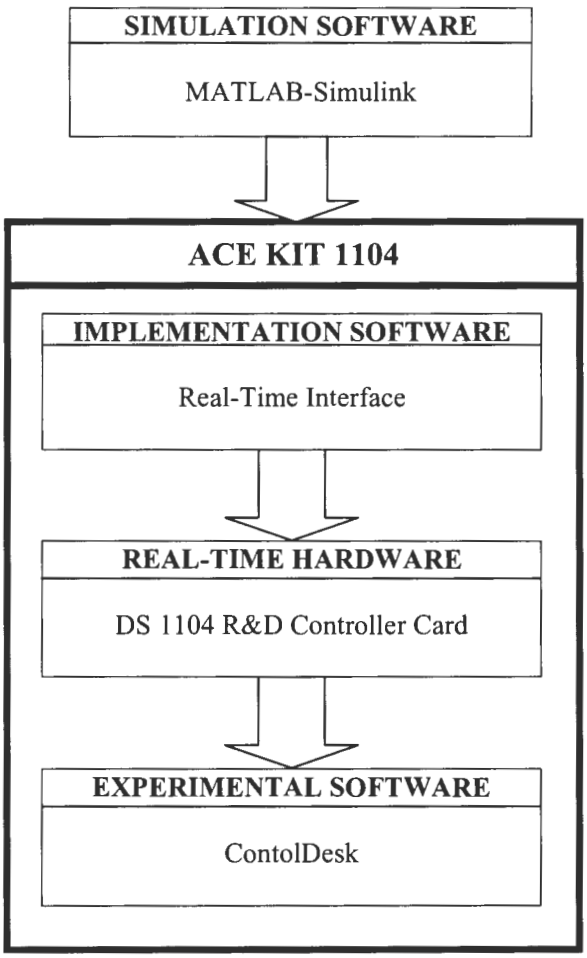

Figure 4.16: Flow chart of the Simulation Software and the ACE Kit

Appendix H gives the specifications of the card. Some of the more important features of the card include the main processor, which is a MPC 8420, PowerPC 603e core with a 250MHz clock frequency. It also consists of 8 ADC channels, 20-bit digital I/O ports and a slave DSP subsystem from Texas instruments (i.e. DSP TMS 320F240). The card also makes provision for the integration of 2 position encoders. As shown in Fig. 4.1, 8 analogue signals are read in via the 8 ADC channels and the position encoder is read via the cards encoder inputs. Twelve I/O ports of the card are used as bit-outputs for the switching of the converters IGBT's.

The most noticeable difference between Fig. 3.1 and Fig. 4.1, is the difference in the number of voltage and current measurements. This is due to the limited number of analogue inputs to the controller card, as shown in Appendix H. The controller card only has 8 analogue inputs and since 19 signals need to be measured, certain adjustments are made. These include the measurement of line-to-line voltages instead of line-to-neutral voltages and the reconstruction of certain signals. As shown in Fig. 4.1, V_{cb_s} is measured, and from this, V_{ab_s} is constructed since

$$V_{ab\_s} = V_{cb\_s} \angle 60^0$$

Since the supply line-to-line voltage is maintained at 100V, this too can be reconstructed from V_{ab_s} and V_{cb_s}, as follows

$$V_{ab} = \frac{100}{380} V_{ab\_s}$$

$$V_{cb} = \frac{100}{380} V_{cb\_s}$$

Using these methods it is possible to create V_{ab}, V_{cb} and V_{ab_s} from V_{cb_s}. The DC-link voltage is measured and occupies one channel.

Instead of 3 stator, 3 rotor and 3 supply currents being measured, only 2 stator, 2 rotor and 2 supply currents are measured and the third is created using the following relationship for a balanced 3-phase system.

$$i_{as} + i_{bs} + i_{cs} = 0$$

therefore, $i_{bs} = -i_{cs} - i_{as}$

$$i_a + i_b + i_c = 0$$

therefore, $i_a = -i_c - i_a$

$$i_{ar} + i_{br} + i_{cr} = 0$$

therefore, $i_{br} = -i_{cr} - i_{ar}$

In Chapter 6, a fault is applied to a single stator phase thus resulting in an unbalanced system. For this case, a different approach is used when reconstructing the stator current. It is essential that the phase to which the fault is applied be measured (i.e. i_{cs}). It is then assumed that the two remaining currents are identical in shape and magnitude, however differ in phase. Therefore only one of the two currents need to be measured, and the other reconstructed. The reconstruction of the signal is achieved by measuring one of the unfaulted phases (i.e. i_{as}) and then phase shifting it by the correct amount, to attain the second unfaulted phase (i.e. i_{bs}). The differences in the assumptions made can be observed in the Simulink block diagrams (shown in Appendix J), which are used to program the card.
In each of the assumptions made above, various tests were performed to ensure that the reconstructed signals were in very close proximity to the actual signals, thus validating the use of each assumption.

In section 3.4, 2 methods are discussed for the rotor-side control. Although both methods yield identical simulation results, *method 1* is employed in the experimental configuration as it reduced the run-time (cycle time) of the card, which allows for higher switching frequencies of the converters. The converters are switched at 5kHz as this is the highest switching frequency attained using *method 1*.

4.4 Software Design for the Doubly-Fed Induction Wind Generator System

Essentially 3 software packages are critical in the development and control of the system. These packages are listed below in sequence of usage:

(1) Matlab-Simulink
(2) Real-Time Interface
(3) ControlDesk

As mentioned above, the Real-Time Interface software package, ControlDesk software package and the controller card form part of the ACE Kit. The flow chart shown in Fig. 4.16 shows the link between the kit and the Simulink environment.

The first software package, Matlab-Simulink, is a simulation based software package. All simulated results shown in Chapter 6, are attained using Simulink The simulations form a critical part in the initial design. Appendix I show the schematics of the models used during the simulation of the system. A critical step in the simulation is the selection of a particular solver, step size (sample time), tolerance level and the time taken to complete the response. Careful consideration should be given to this selection as this could affect the output response of the system. The solver used for both methods is the Fixed-Step solver with a step size of 0.0002 seconds. Although the step size can be decreased, the simulation is used to validate the experimental results, and in doing so, the sampling and switching frequency is set to the same as that of the experimental sampling and switching frequency of 5kHz.

The second software package is the Real-Time Interface package which is an implementation based software package. This allows the Simulink model to be converted into a real-time simulation running on the controller card. To convert the simulation to a real-time simulation, I/O interfaces need to be introduced to the model, which is provided by this package. An example of this would be the replacement of the induction machine in the simulation with the measured currents and voltages of the actual machine, which would be read in by the controller card. Once all necessary Simulink blocks have been converted to their corresponding I/O interface blocks, the application is firstly checked for coding errors. Once the application is error free, it is converted to equivalent C-code and downloaded onto the controller card. Appendix J shows the entire system, complete with the I/O interface blocks. The step size of the system is set to 0.0002sec. From the diagram, the measured signals and the bit-I/O ports are evident, however the blocks which perform the calculations remain the same as those used in the simulations.

ControlDesk is the experimental software and it is the final software package required for real-time control. It provides all the tools required to control, monitor and automate experiments. Within the ContolDesk environment, one can manage various experiments as well as design and implement interfaces to monitor and control various aspects of the experiment. Once the C-code has been written to the controller card, various interfaces can be designed to facilitate the monitoring and control of the system. The diagrams below indicate the interfaces designed and used to facilitate this process. Fig. 4.17 shows the interface used to switch the converters. It is evident from the diagram that each inverter has an "on" and "off" state. During the "off" state, no IGBTs are activated and no switching takes place. During the "on" state, the IGBTs are switched. The following diagram then shows the interface used to set the desired speed of the machine. This occurs in the column stating "Setpoint Speed". The column on the right, is used to monitor the actual speed of the machine. From this column, both a digital read-out and a graph is used to indicate the actual speed. Fig. 4.19 shows the interface used to set and monitor the DC-link voltage. The desired DC-link voltage is set in the left column, and the actual DC-link voltage is again monitored in the right column, using the digital read-out and a graph. Fig. 4.20 displays the layout used to monitor the stator currents. The same layout is used to capture all other signals being measured.

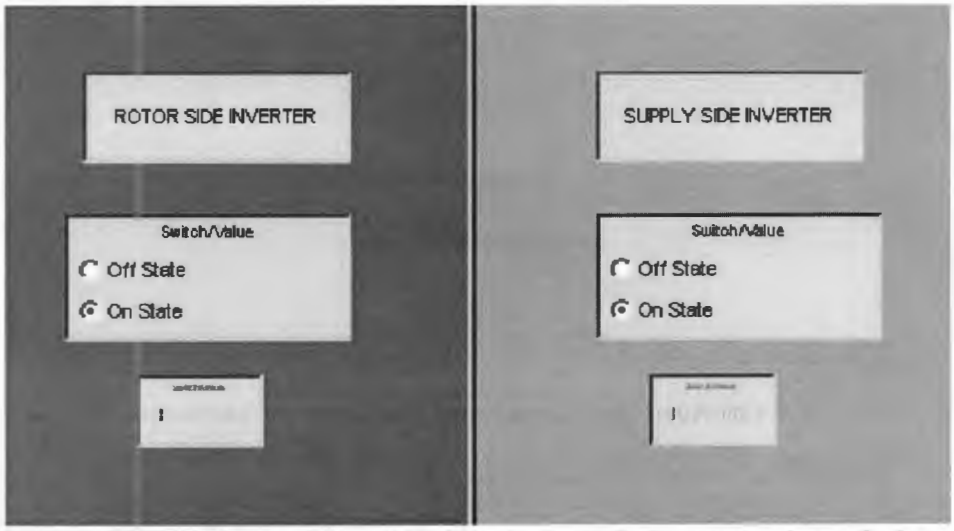

Figure 4.17: User-interface used for activation of the supply-and rotor-side converters

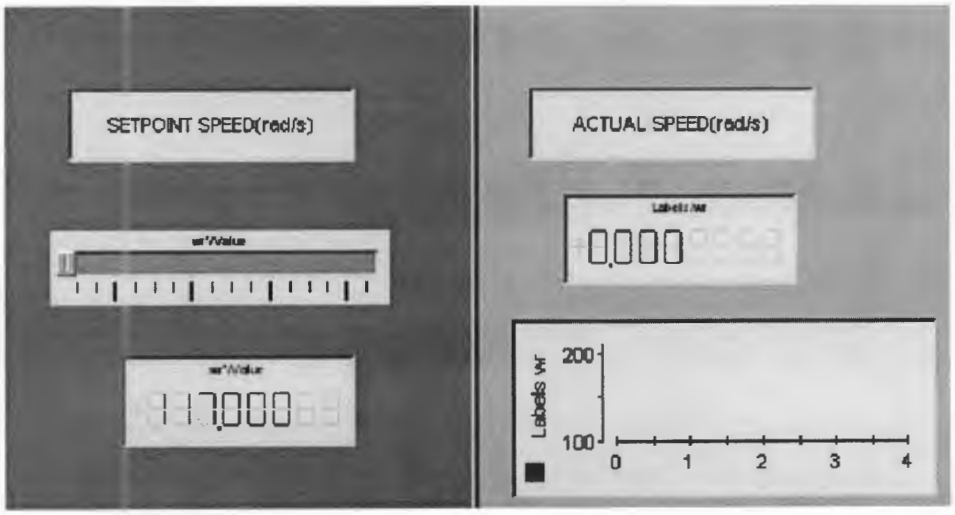

Figure 4.18: User-interface used for setting the desired speed and for monitoring the actual speed

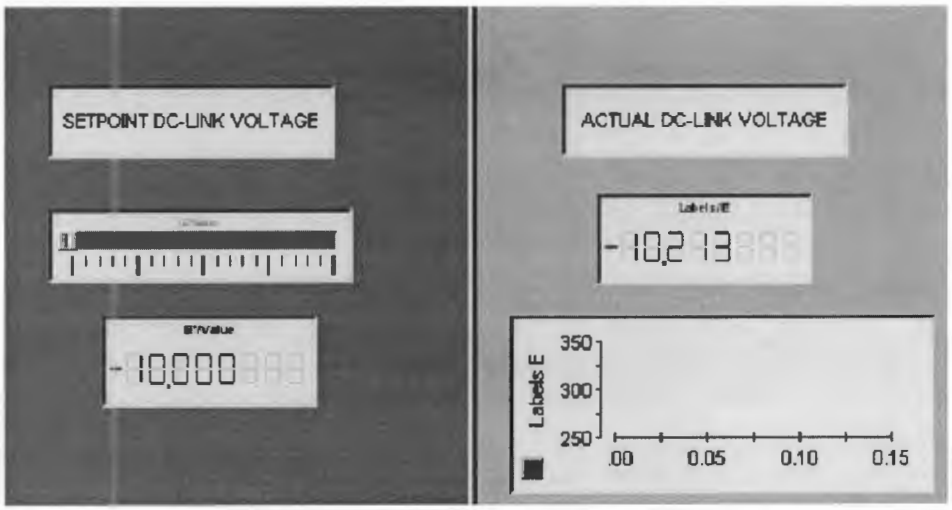

Figure 4.19: User-interface used for setting the desired DC-link voltage and for monitoring the actual DC-link voltage

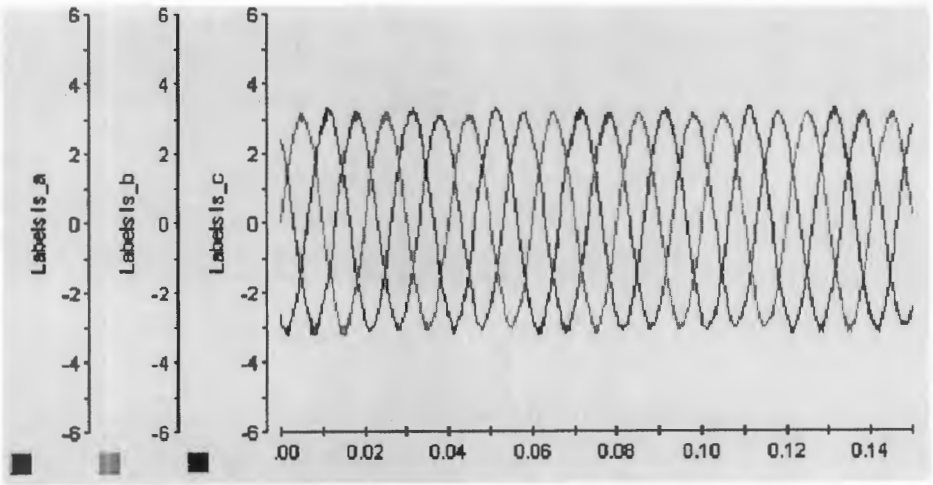

Figure 4.20: User-interface used for monitoring the stator currents

4.5 Description of the Cage Rotor Induction Generator Experimental Setup

Fig. 4.21 shows the schematic of the squirrel cage induction generator WECS used in the laboratory. A DC drive consisting of a 2.2 kW DC machine and a thyristor converter is used to emulate the wind turbine. The DC drive is current controlled so as to provide a desired setpoint torque the shaft of generator. The squirrel cage induction generator is a 0.5 kW, 3-Ph, 380V, 50Hz, 4-pole machine. The drive situated in the stator circuit are standard commercially available PWM-VSI converters (part of the Hitachi range), responsible for control of the machine speed by changing the voltage and frequency accordingly. These standard induction machine drives eliminated the need for the design of these units, thus simplifying the implementation of the system. The stator currents are measured using the current Lem modules mentioned in section 4.3.4, captured using an A/D card and processed using Matlab. The A/D card used is a PC 30 D board which is compatible with IBM PCs, and the signals are sampled at 5kHz. Fig. 4.22 shows a picture of the experimental setup.

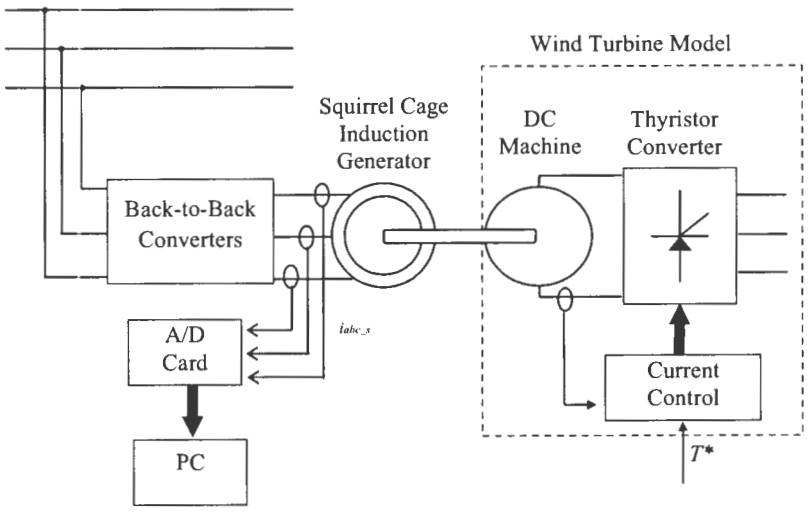

Figure 4.21: Schematic of the overall experimental Cage Rotor Induction Generator setup

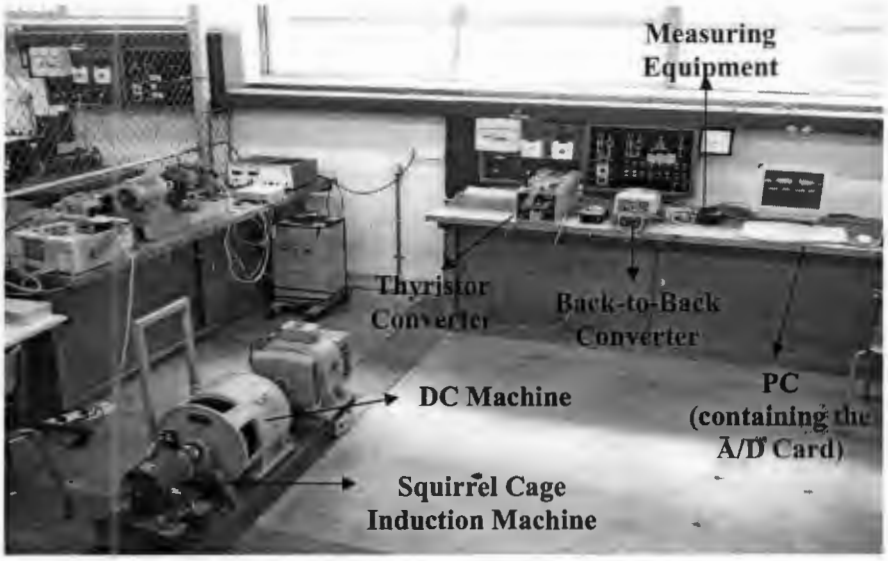

Figure 4.22: Experimental setup in the Machines Laboratory

4.6 Conclusions

The laboratory setup used for the modeling of the two wind generator systems has been fully described. The implementation of the cage rotor induction generator system was simpler since the drive was readily available, whereas the doubly-fed induction generator drive was implemented from fundamental principles. The ACE Kit, which was used for the experimental implementation of the doubly-fed induction generator drive, proves to be an invaluable tool for rapid testing of control prototypes. The two wind generator systems now serve as a test bed for the implementation of the more common faults on the two machines, so as to allow for further fault detection research on these wind generators.

Chapter 5

5. SIMULATED AND EXPERIMENTAL RESULTS

5.1 Introduction

This chapter discusses the results attained from the tests carried out on the two wind generator systems. Simulations are only performed on the doubly-fed system since the control strategies employed were derived from fundamental principles which needed to be validated before being implemented experimentally. The simulations were performed in Matlab-Simulink as discussed in Chapter 4, whereby all simulation parameters are based on the machine and experimental parameters used in the laboratory setup. The experimental results attained are that of the experimental setups described in Chapter 4. For the simulated and experimental tests, both steady state and transient responses are captured.

5.2 Doubly-Fed Induction Generator System

5.2.1 Supply-Side Converter

The tests carried out were used to validate the ability of the supply-side converter to allow for bi-directional power flow. During the initial tests, the DC-link voltage is maintained at 300V and i_{qc}^* is set to zero (i.e. no reactive power flow).

Figs 5.1 and 5.2 indicate the simulated and experimental 3 phase supply voltages and currents during the sub-synchronous operation of the DFIG system, whereby the supply-side converter operates in rectifying mode. This is validated by the 0° phase displacement between the phase voltages and phase currents, corresponding to a unity displacement factor. Figs 5.3 and 5.4 illustrate the simulated and experimental DC-link voltage during this operation. As mentioned above the DC-link voltage was kept at 300V, and from the diagrams it is evident that the supply-side control loop ensured minimal deviation from this value during steady state conditions.

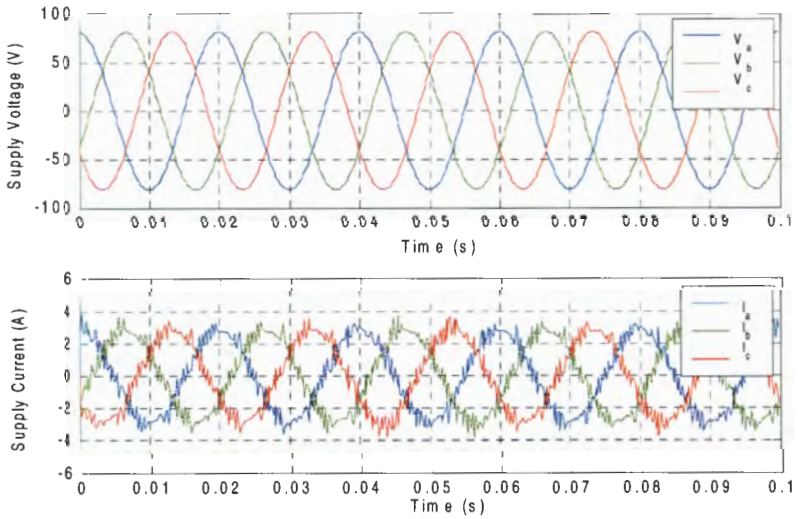

Figure 5.1: Simulated supply voltages and currents for the supply-side converter during rectifying mode

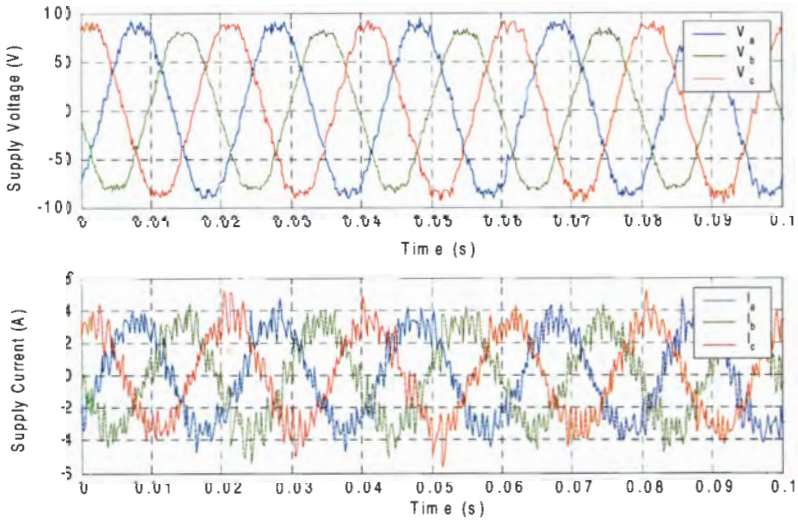

Figure 5.2: Experimental supply voltages and currents for the supply-side converter during rectifying mode

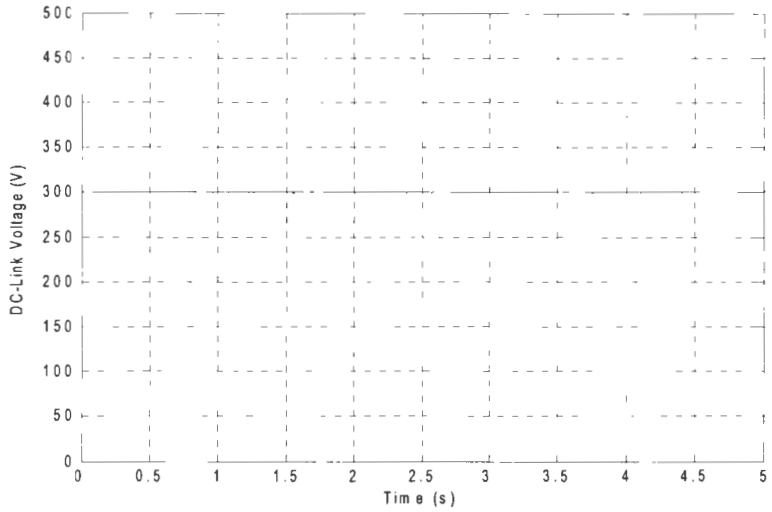

Figure 5.3: Simulated DC-Link Voltage during rectifying mode

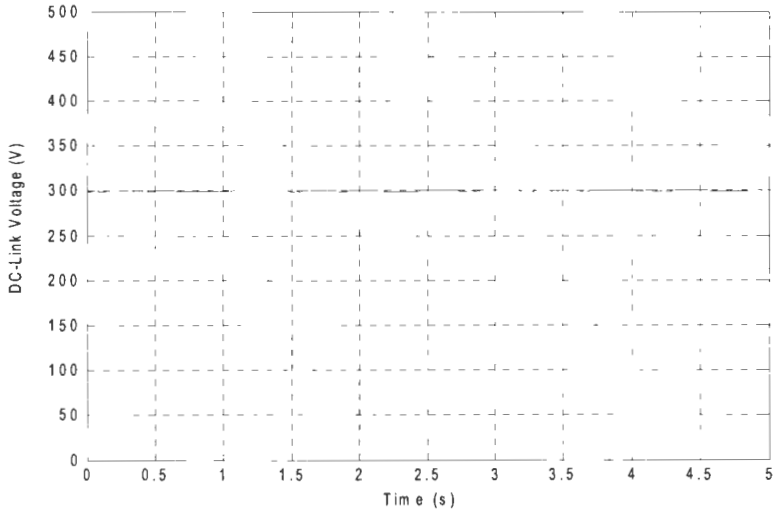

Figure 5.4: Experimental DC-Link Voltage during rectifying mode

Figs 5.5 and 5.6 shows the simulated and experimental 3 phase supply voltages and currents of the converter operating in inverting mode, corresponding to super-synchronous operation. This is illustrated by the 180° phase displacement between the phase voltages and phase currents. Figs 5.7

and 5.8 show the simulated and experimental DC-link voltage being maintained at 300V during inverting mode.

This validates the ability of the supply-side converter to achieve bi-directional power flow.

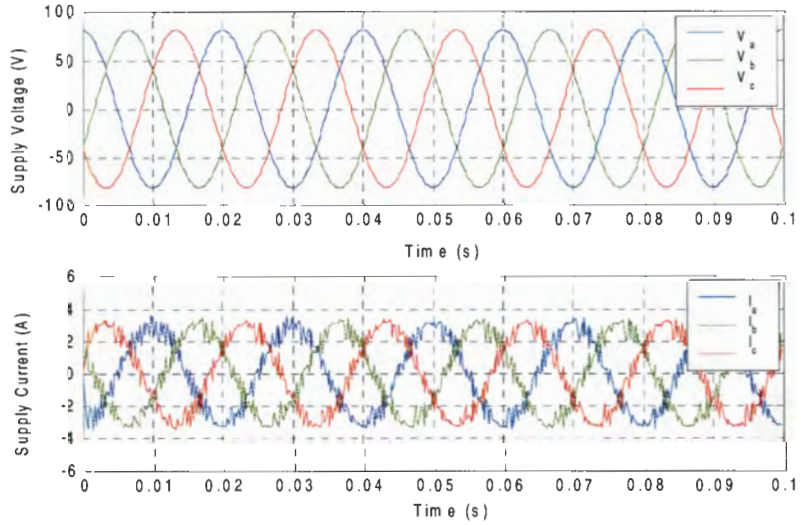

Figure 5.5: Simulated supply voltages and currents for the supply-side converter during inverting mode

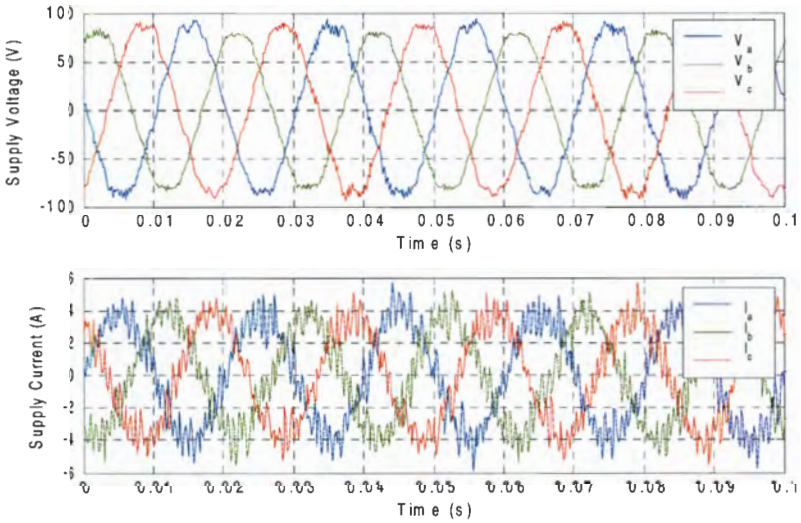

Figure 5.6: Experimental supply voltages and currents for the supply-side converter during inverting mode

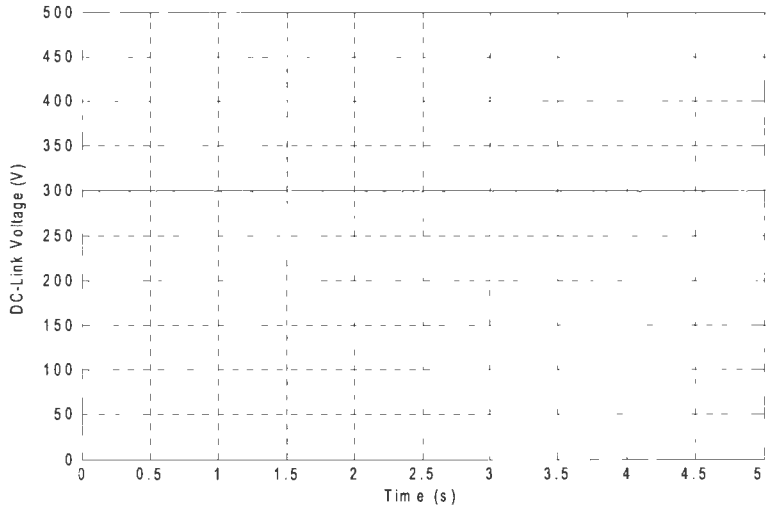

Figure 5.7: Simulated DC-Link Voltage during inverting mode

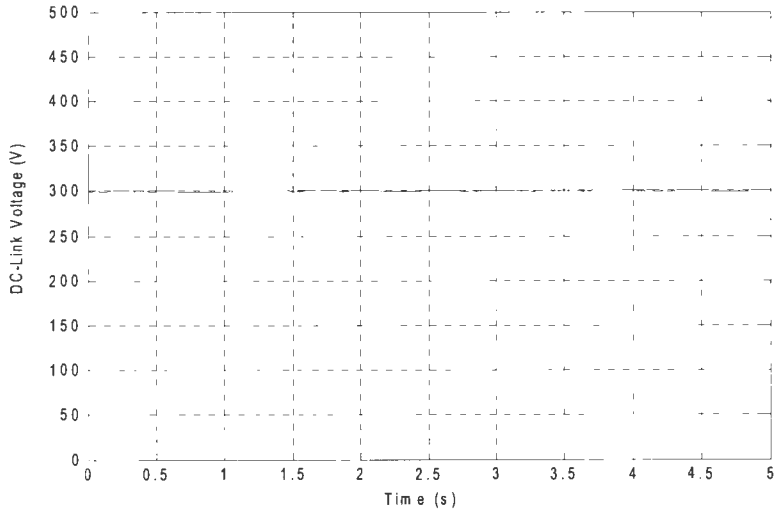

Figure 5.8: Experimental DC-Link Voltage during inverting mode

The following diagrams illustrate the ability of the supply-side converter to achieve a leading and lagging power factor while in rectifying mode. During the simulated and experimental tests, the DC-link voltage is held at 300V while i_{Qe}^{*} is varied from 3A to -3A at t=0.05s (simulation) and t=0.0475s (experimentally). As i_{Qe}^{*} is maintained at 3A, the phase currents lag the phase

voltages by 45°. When i_{q^*} is changed to -3A, the phase currents then lead the phase voltage by 45°. This illustrates the ability of the system to achieve a leading and lagging power factor while in rectifying mode.

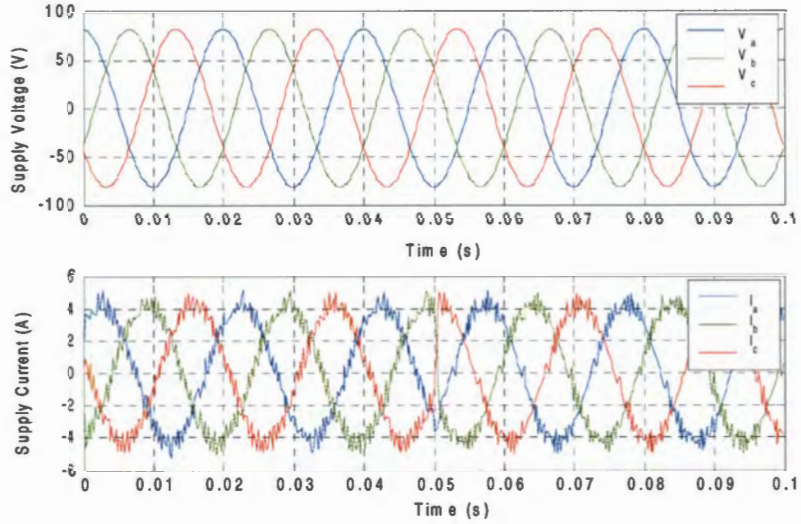

Figure 5.9: Simulated supply voltages and currents for the supply-side converter during rectifying mode

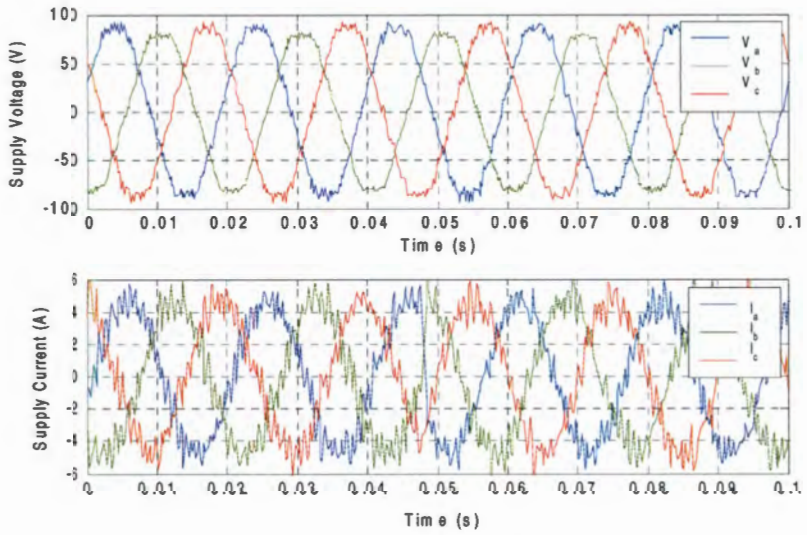

Figure 5.10: Experimental supply voltages and currents for the supply-side converter during rectifying mode

Figs 5.11 and 5.12 show the converter operating in inverting mode, whereby the DC-link voltage is maintained at 300V while i_q^{e*} is varied from 3A to -3A at t=0.05s, for both simulated and experimental tests. It is evident that a lagging and leading power factor is once again achieved, by the shift in phase of the supply currents.

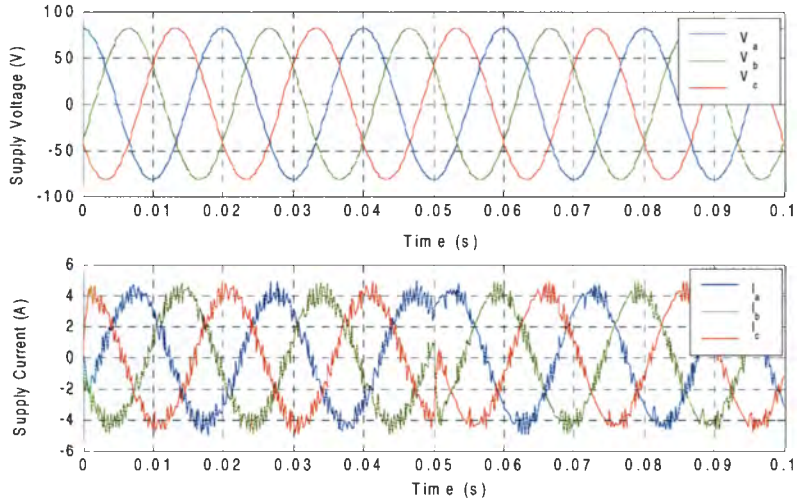

Figure 5.11: Simulated supply voltages and currents for the supply-side converter during inverting mode

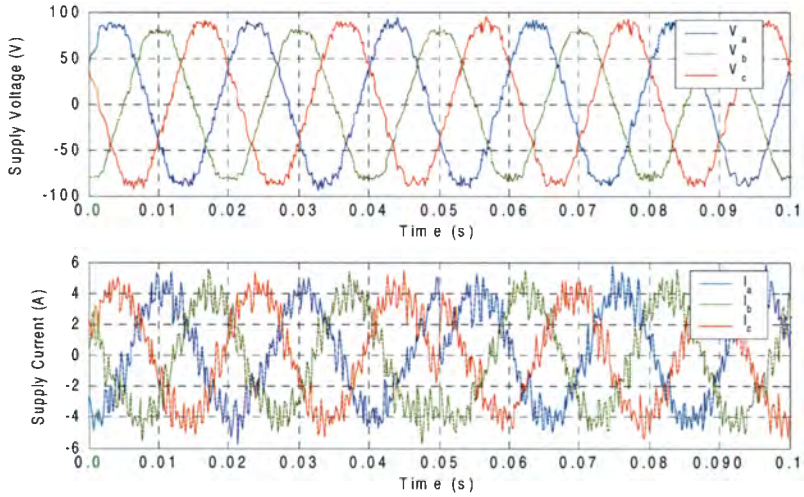

Figure 5.12: Experimental supply voltages and currents for the supply-side converter during inverting mode

This illustrates the ability of the supply-side converter to deliver or receive reactive power from the grid, for both sub-synchronous and super-synchronous operation.

The experimental results prove to be very similar to the simulated results thus validating the capability of the system to maintain the DC-link voltage at a particular value and to regulate the reactive power.

5.2.2 Rotor-Side Converter

Simulations were performed for both *method 1* and *method 2* (as discussed in section 3.4), however the simulated results attained for both methods are identical and therefore only *method 1*'s results are shown. *Method 1* is also used experimentally as it reduced the cycle time of the processor, allowing for a faster sampling and switching time.

The simulated and experimental results indicated in the diagrams below, shows the system operating at 1120rpm (25% below synchronous speed) and 1880rpm (25% above synchronous speed), at a constant torque of 7Nm. This illustrates the ability of the system to operate within the sub-synchronous and super-synchronous regions.

The first set of results shows the system in sub-synchronous operation, whereby power is absorbed by the rotor. Figs 5.13 and 5.14 indicates the rotor speed being maintained at 1120rpm by the rotor-side control loop for the simulated and experimental case. The simulated and experimental rotor currents are then illustrated in Figs 5.15 and 5.16 for the above condition. The hysterisis band is evident in the diagrams as a result of the hysterisis current controller. Figs 5.17 and 5.18 shows the stator phase voltages and currents which are used to calculate the stator flux vector.

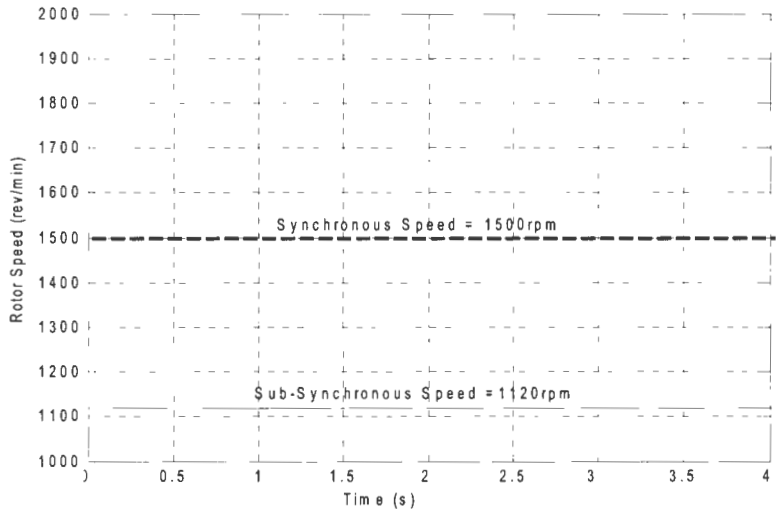

Figure 5.13: Simulated rotor speed response for operation at 1120rpm

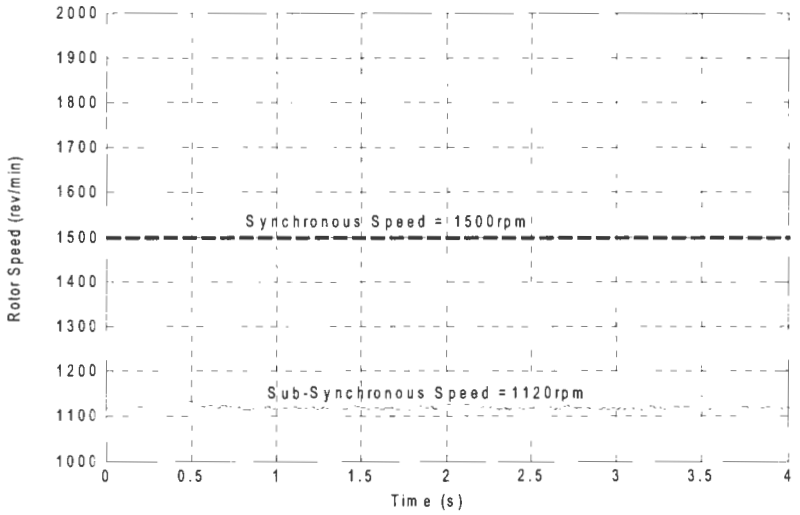

Figure 5.14: Experimental rotor speed response for operation at 1120rpm

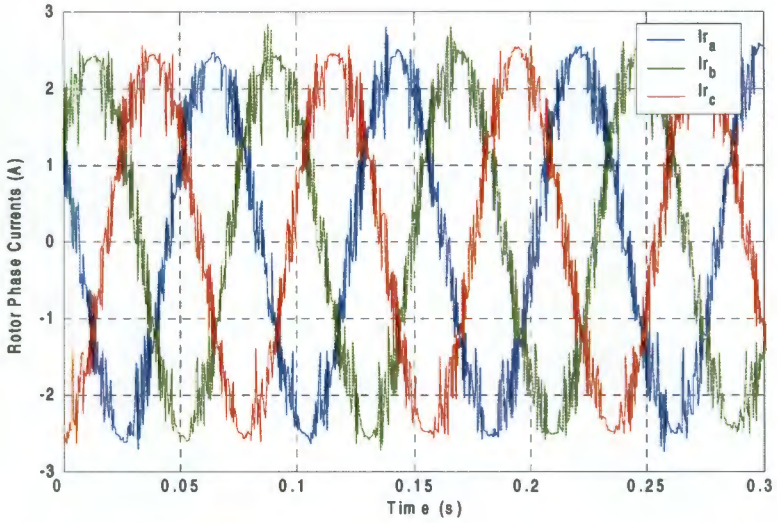

Figure 5.15: Simulated rotor phase currents during sub-synchronous operation

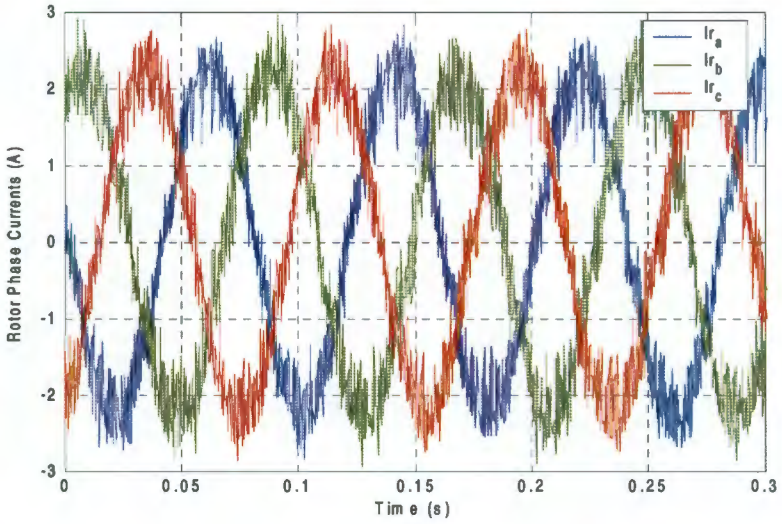

Figure 5.16: Experimental rotor phase currents during sub-synchronous operation

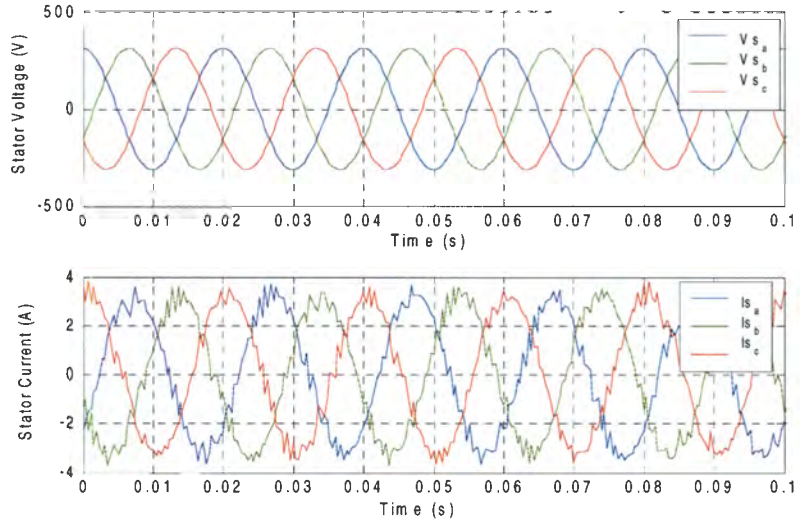

Figure 5.17: Simulated stator phase currents and voltages during sub-synchronous operation

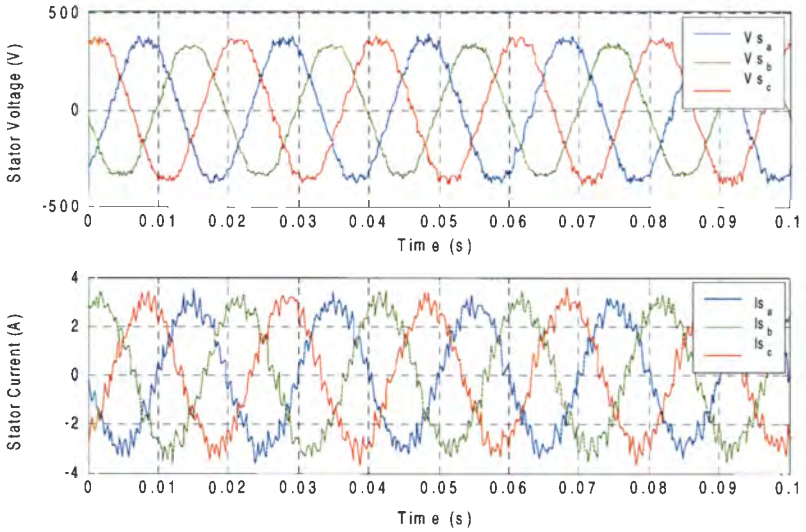

Figure 5.18: Experimental stator phase currents and voltages during sub-synchronous operation

When the machine operates at 1120rpm (sub-synchronous region), the slip is calculated to be 0.253. As shown in Chapter 3, the theoretical mechanical, rotor and stator powers for sub-synchronous operation (neglecting losses), are calculated to be:

the total input power is 821.03W *(P_m=7x117.29)*, from equation 4.3

the stator power is 1099.56W *(P_s=7x157.08),* from equation 4.1

the rotor power is -278.19W *(P_r=1099.56x-0.253)*, from equation 4.2.

Figs 5.19 and 5.20 show the simulated and experimental stator power, which is delivered to the grid. The mean value for the simulated power is 998.1W and experimentally it's calculated to be 942W, thus the losses amount to 101.46W and 157.56W of power, respectively. Figs 5.21 and 5.22 indicates the power being delivered by the rotor for the two cases, and the mean value is calculated to be -330.5W (simulation) and -442.1W (experimentally). The losses contributed by the rotor and the converter amounts to 52.31W(simulation) and 163.91W (experimentally) of power. It is evident that losses of the simulation are less than the experimental case, however this is to be expected due to non-ideal conditions and equipment which the simulations fail to take into account. Since the theoretical predictions neglect losses, it is appropriate to use this to validate the attained results.

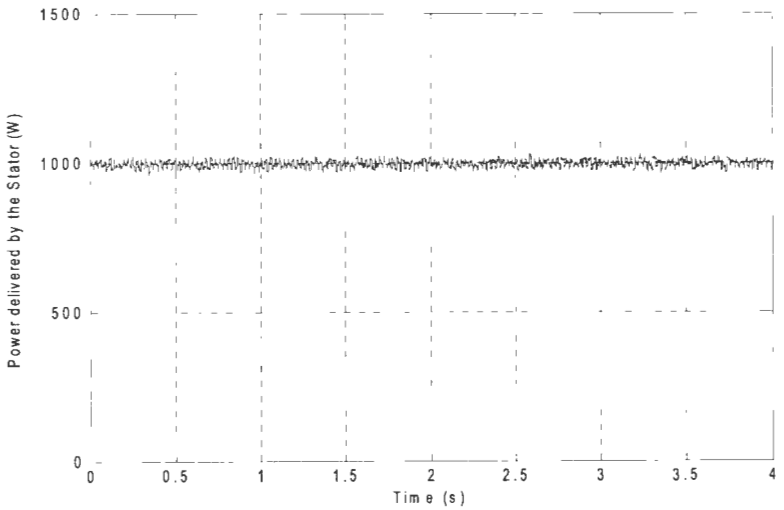

Figure 5.19: Simulated power delivered by the stator during sub-synchronous operation

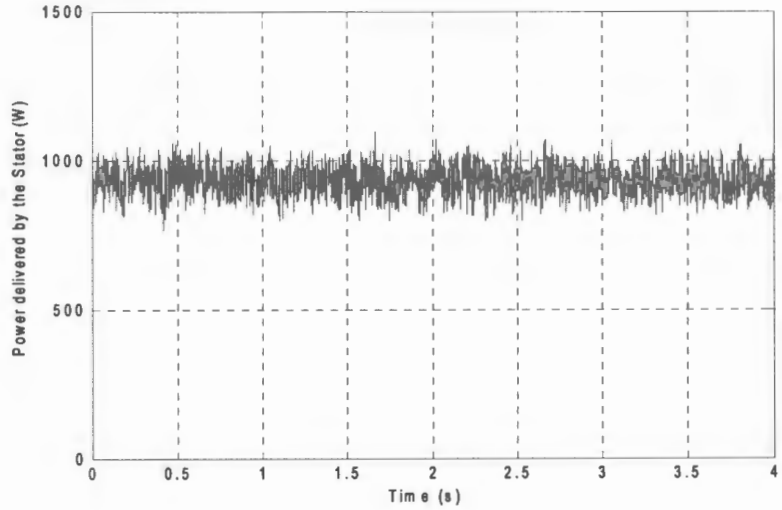

Figure 5.20: Experimental power delivered by the stator during sub-synchronous operation

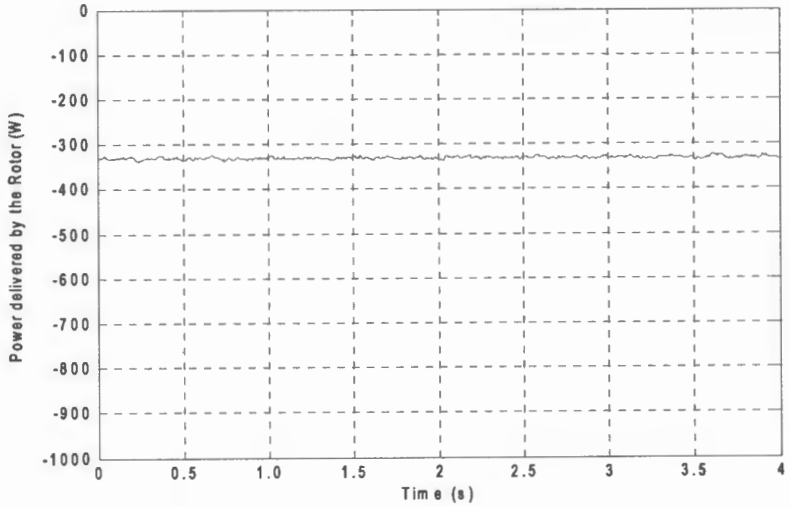

Figure 5.21: Simulated power delivered by the rotor during sub-synchronous operation

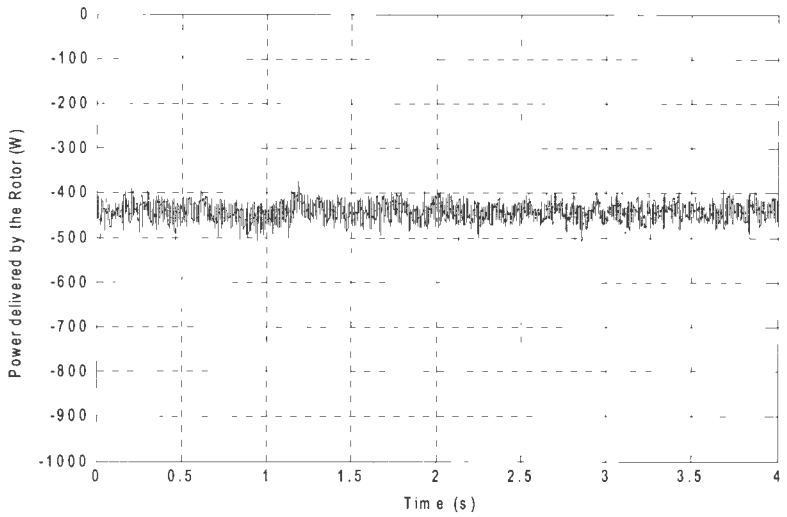

Figure 5.22: Experimental power delivered by the rotor during sub-synchronous operation

The next set of results show the system operating in the super-synchronous region (1880rpm), whereby both the rotor and stator deliver power to the grid. Figs 5.23 and 5.24 illustrates the rotor speed being maintained at 1880rpm, by the supply-side control loop, and Figs 5.25 and 5.26 shows the rotor currents during this operation for the simulated and experimental case. The following two diagrams then show the stator phase voltages and currents, whereby the phase displacement between the voltages and currents are the same as during the sub-synchronous operation.

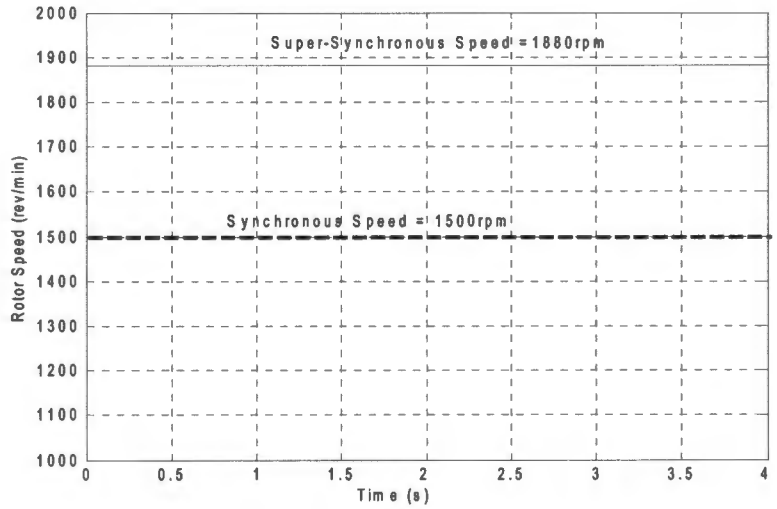

Figure 5.23: Simulated rotor speed response for operation at 1880rpm

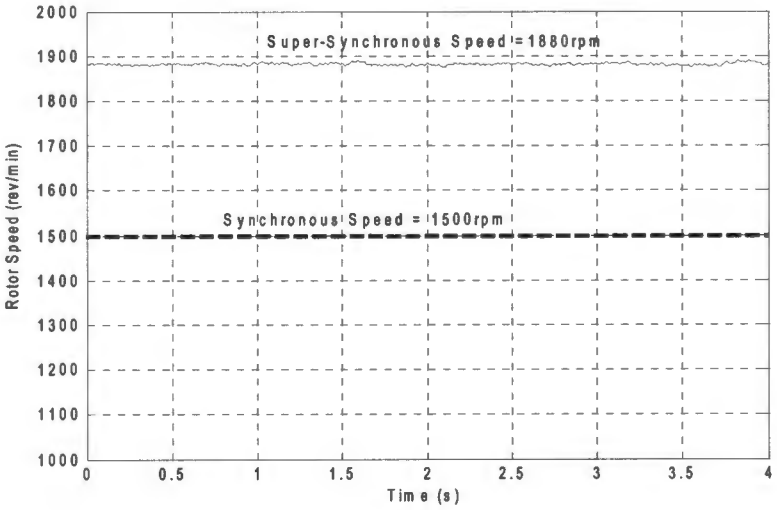

Figure 5.24: Experimental rotor speed response for operation at 1880rpm

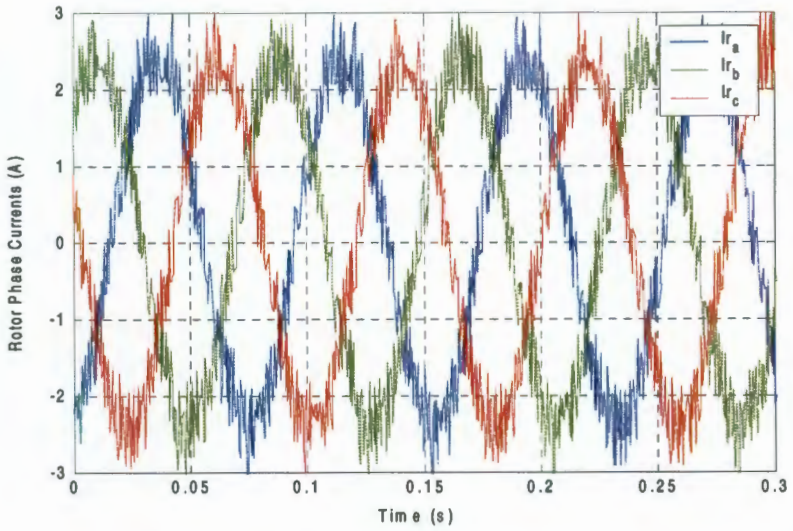

Figure 5.25: Simulated rotor phase currents during super-synchronous operation

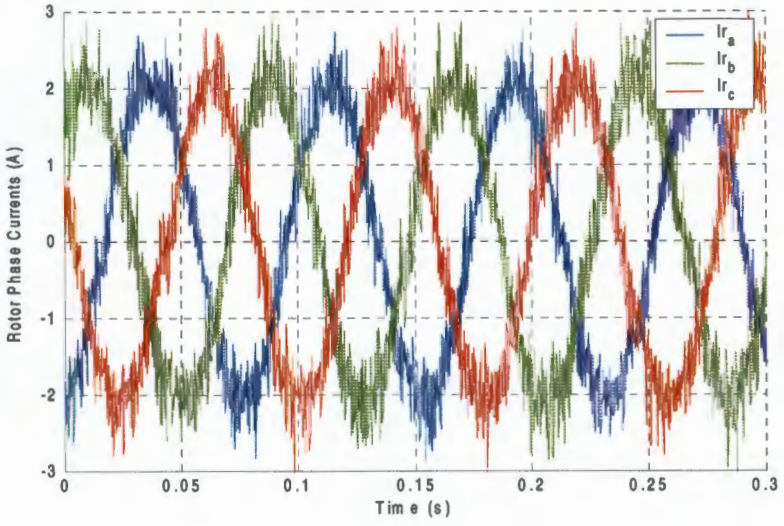

Figure 5.26: Experimental rotor phase currents during super-synchronous operation

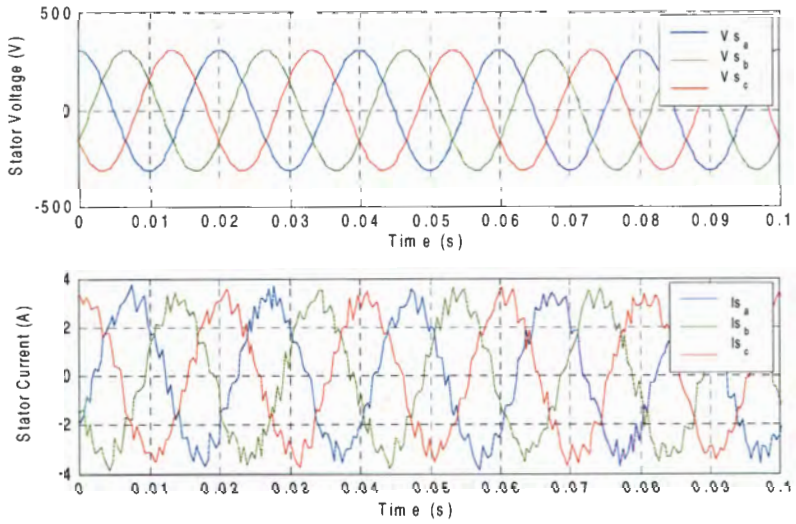

Figure 5.27: Simulated stator phase currents and voltages during super-synchronous operation

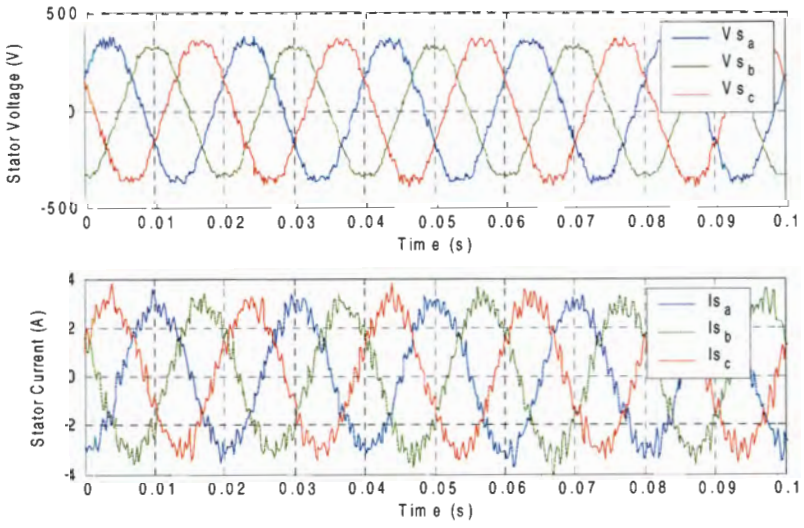

Figure 5.28: Experimental stator phase currents and voltages during super-synchronous operation

The theoretical mechanical, rotor and stator powers for super-synchronous operation (neglecting losses), are calculated to be:

the total input power is 1378.09W *(P_m=7x196.87)*, from equation 4.3

the stator power is 1099.56W *(P_s=7x157.08)*, from equation 4.1

the rotor power is 278.19W *(P_r=1099.56x0.253)*, from equation 4.2

The simulated and experimental stator power being delivered to the grid is shown in Figs 5.29 and 5.30. The mean value of the simulated power is 999.6W and experimentally it's calculated to be 906.4W, thus 99.96W (simulated) and 193.16W (experimental) of power is dissipated respectively. Figs 5.31 and 5.32 indicate the power being delivered by the rotor, and the mean value for the simulated and experimental case is 228.5W and 136W respectively. 49.69W (simulation) and 142.19W (experimental) of power is dissipated due to the converter and the rotor losses.

Once again the losses of the simulation are less than that of the experimental case, as predicted earlier and the theoretical values validate the results attained.

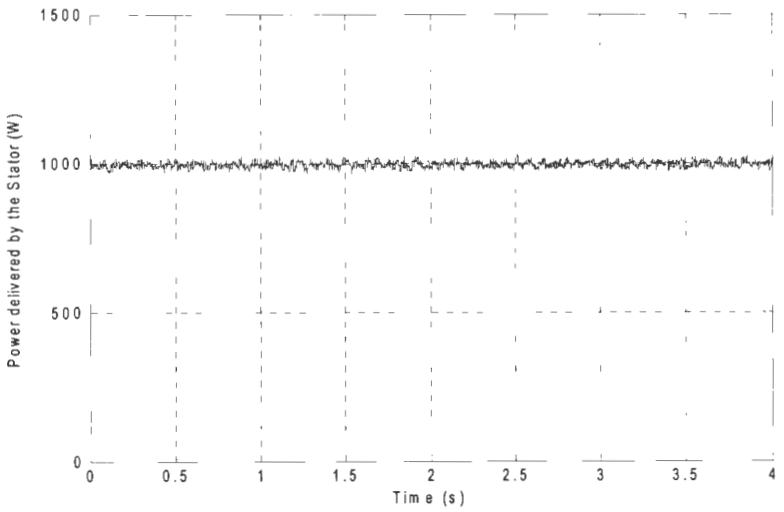

Figure 5.29: Simulated power delivered by the stator during super-synchronous operation

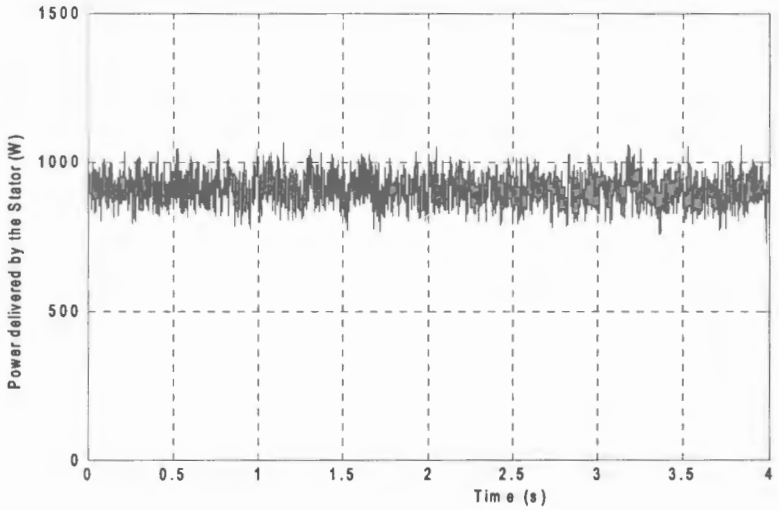

Figure 5.30: Experimental power delivered by the stator during super-synchronous operation

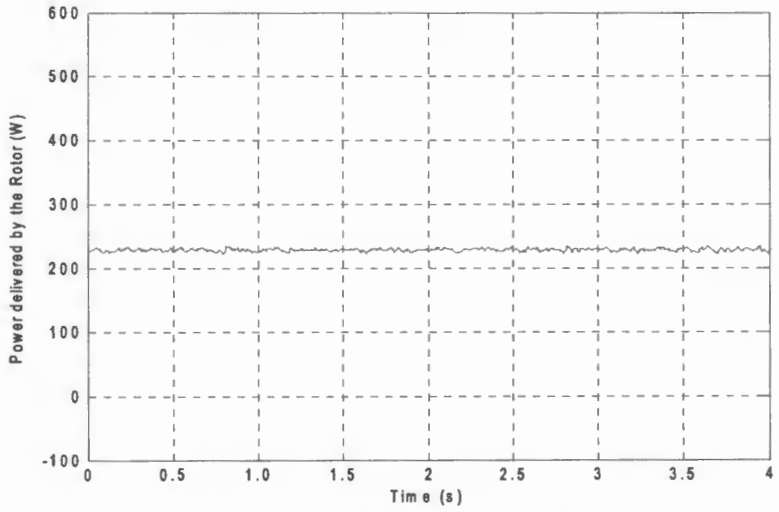

Figure 5.31: Simulated power delivered by the rotor during super-synchronous operation

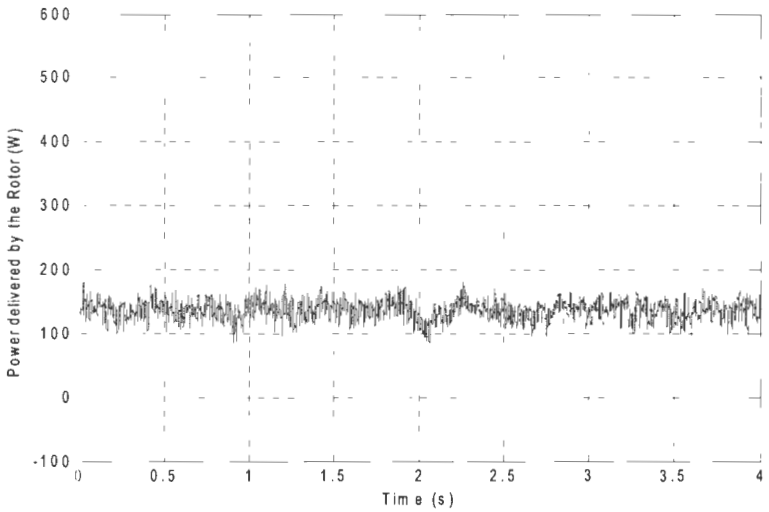

Figure 5.32: Experimental power delivered by the rotor during super-synchronous operation

The next set of results shows the transient response of the system as the speed is ramped up from 1120rpm to 1880rpm, over 5 seconds. During the tests, the Torque is still maintained at 7Nm. The simulated and experimental results will again be discussed and shown in pairs. Figs 5.33 and 5.34 show the speed response of the system for a change in speed. The experimental result shows that it requires approximately 5 seconds for the system to stabilise at 1880rpm. Figs 5.35 and 5.36 then shows the rotor phase currents response as the generator moves through synchronous speed. Figs 5.37 and 5.38 shows the response of the DC-link voltage during the speed change. A fairly slow PI controller is used for the supply-side converter since the response speed of the DC-link voltage is not critical. The overshoot for both cases does not surpass 305V.

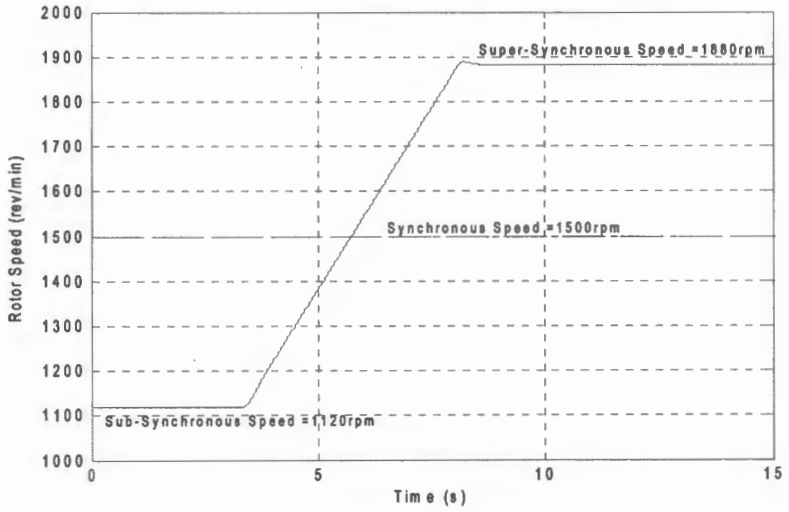

Figure 5.33: Simulated rotor speed response for operation through synchronous speed

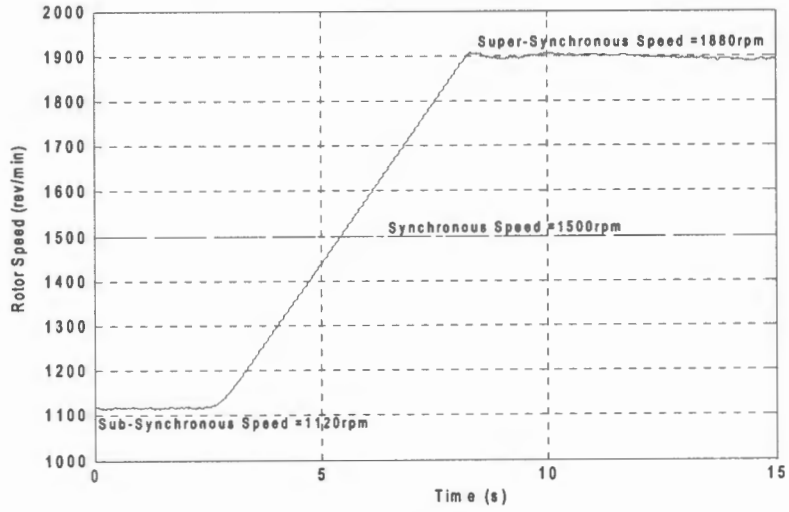

Figure 5.34: Experimental rotor speed response for operation through synchronous speed

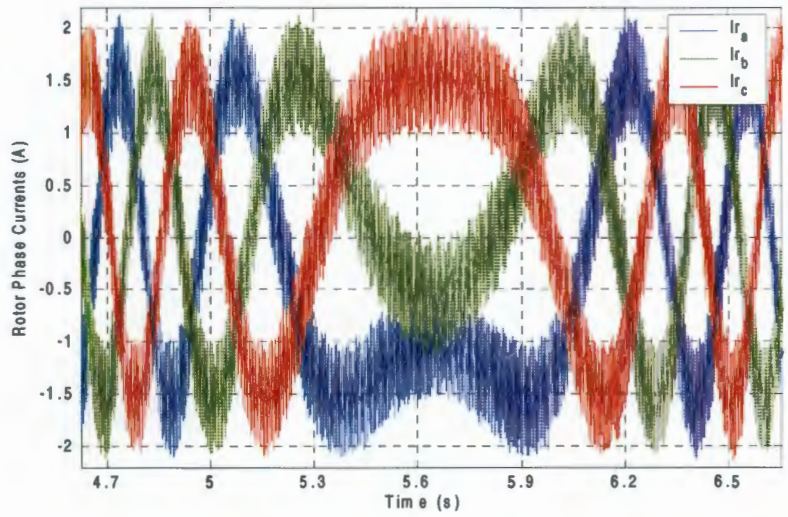

Figure 5.35: Simulated rotor phase currents response for operation through synchronous speed

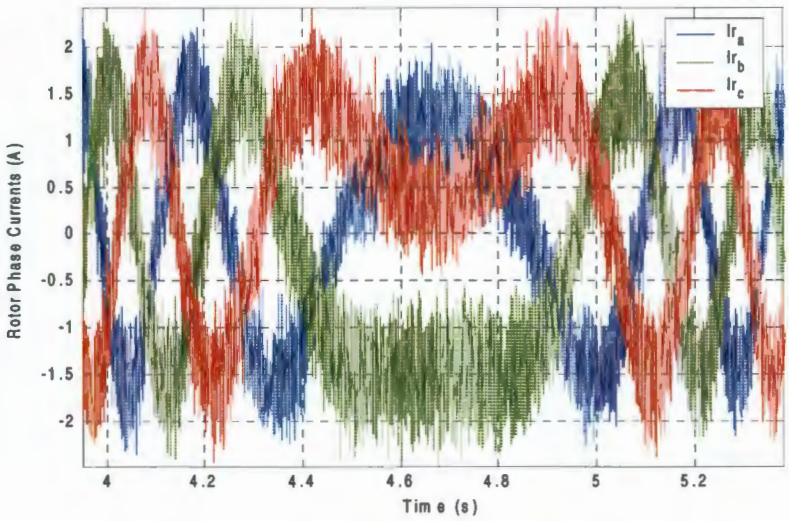

Figure 5.36: Experimental rotor phase currents response for operation through synchronous speed

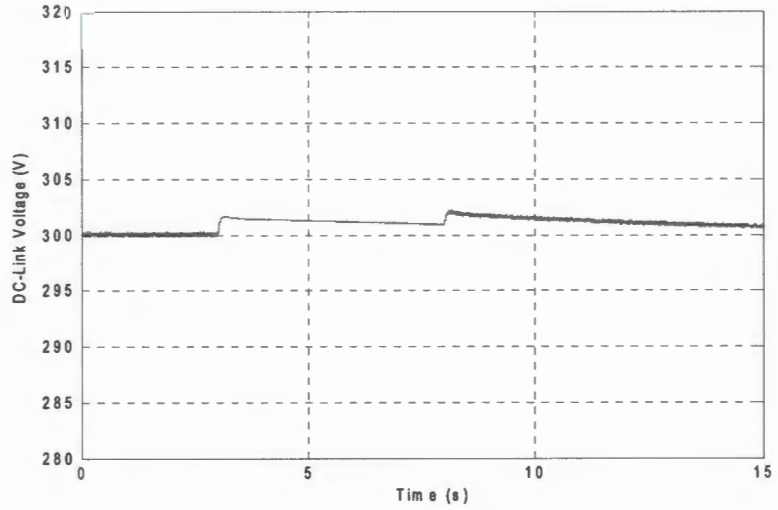

Figure 5.37: Simulated DC-Link voltage for operation through synchronous speed

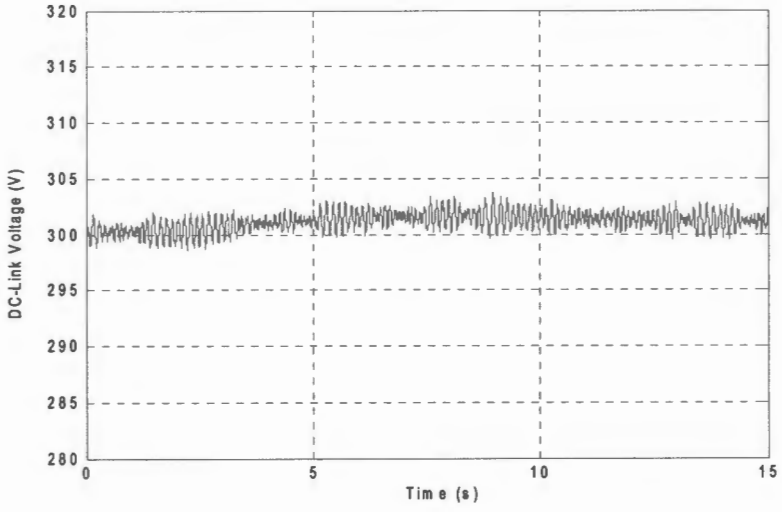

Figure 5.38: Experimental DC-Link voltage for operation through synchronous speed

5.3 Cage Rotor Induction Generator System

The following results show the stator currents of the generator for the experimental setup discussed in the previous chapter. The system was not simulated since the AC drive used is a commercial unit, unlike the doubly-fed system whereby the control of the back-to-back converters needed to be validated via simulations before it could be implemented experimentally.

Fig. 5.39 and 5.40 shows the stator currents of the generator for synchronous operation at 750rpm and 1500 rpm respectively. This is evident from the frequency of the stator currents. The rotor speeds would be higher than the two respective synchronous speeds, so as create slip and thus generate. Fig. 5.41 shows the transient response of the stator current for a single phase as the synchronous speeds are ramped up from 750rpm to 1500rpm, representing an increase in wind speed.

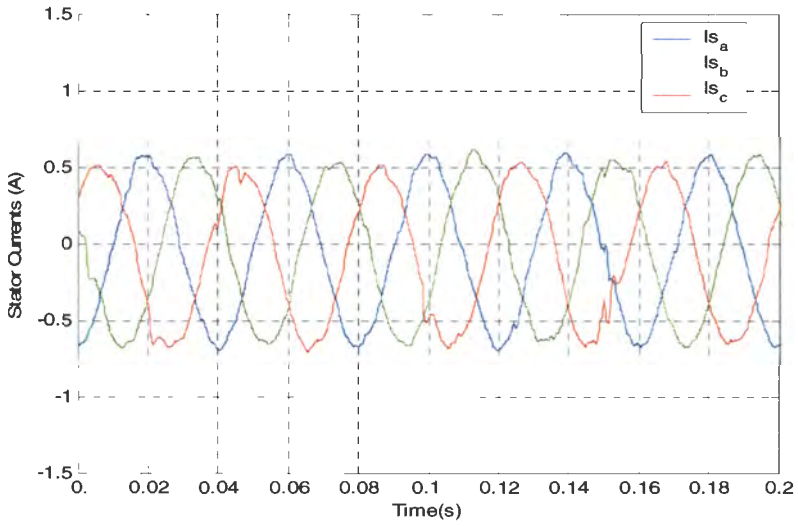

Figure 5.39: Stator currents for synchronous operation at 750rpm

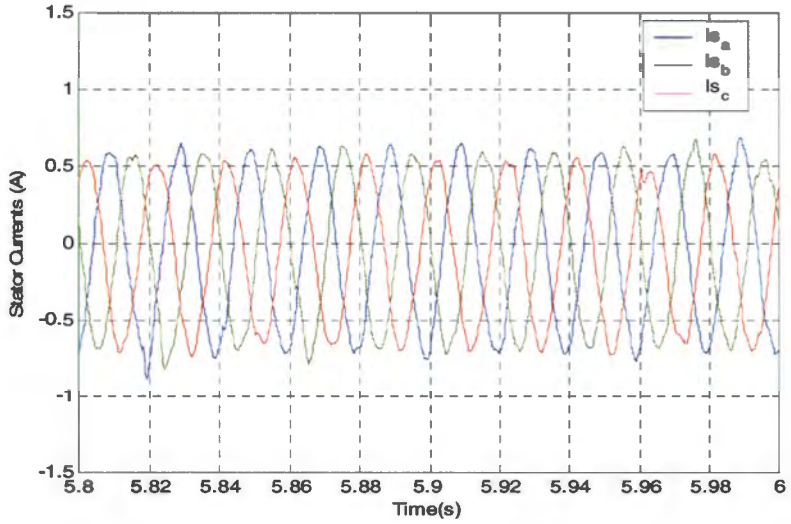

Figure 5.40: Stator currents for synchronous operation at 1500rpm

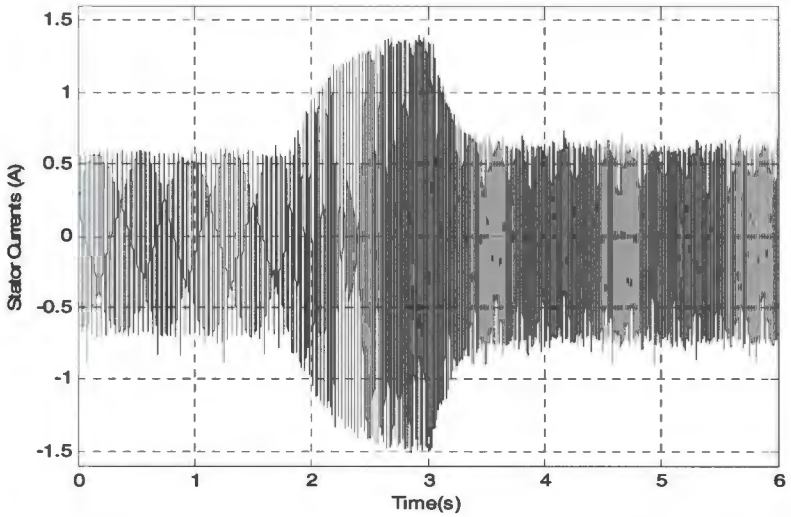

Figure 5.41: Stator currents for a ramp in speed

5.4 Conclusions

The results attained for the two systems have been shown and discussed. They show the systems operating under steady state and transient conditions. The DFIG system was simulated so as to validate the operation of the experimental system. The supply-side converter was shown to control the DC-link voltage and the reactive power flow while the rotor-side converter was shown to control the speed of the generator, with the use of a PI controller. The bi-directional power flow capabilities of the drive was also shown as the generator operated within the sub-synchronous and super-synchronous regions. The cage rotor induction generator results show the stator currents for steady state and transient operation. The transient represents a rise in wind speed, thus producing a ramp in the generator speed as the system tracks the wind speed for maximum power point tracking. This is evident by the increase in the stator current frequency.

Chapter 6

6. EXPERIMENTAL PROCEDURE FOR PLACING FAULTS ON WIND GENERATOR SYSTEMS

6.1 Introduction

There is a constant need for the reduction of operational and maintenance costs of wind generators. The most efficient way of reducing these costs would be by the early detection of the degeneration of the generator's health, facilitating a proactive response, minimising downtime, and maximising productivity [26].

In general the more common induction machine failures include broken rotor bars, stator insulation breakdown and bearing failures. Some of the other assymetrical faults, which may occur while still in operation, include [24]:

- Inter-turn fault of a stator phase winding
- Inter-turn fault of a rotor phase winding
- Abnormal connection of the rotor and/or stator windings
- Static and /or dynamic air-gap irregularities

There are many techniques and tools available, which are used to monitor the condition of these machines, thus prolonging their life span. Some of the technology used for monitoring includes sensors, which may measure speed, output torque, vibrations, temperature, flux densities, etc. These sensors are together coupled with algorithms and architectures, which allows for efficient monitoring of the machine's condition [23].

The most popular methods of induction machine condition monitoring utilize the steady-state spectral components of the stator quantities. These spectral components can include voltage, current and power and can be used to detect broken rotor bars, bearing failures, air gap eccentricities. Presently, many techniques that are based on steady-state analysis are being applied to wind generators. However, the operation of wind generators is predominantly

transient, therefore prompting the development of non-stationary techniques for fault detection.

This chapter describes methods for implementation of the more common faults on the two generator systems. The system served as a test bed for further research into the evaluation and development of a non stationary fault detection technique. An inter-turn stator fault is placed on the DFIG and a broken rotor bar fault is placed in the squirrel cage induction machine. Attempts are also made to identify the faults from measurements and by using a steady state fault analysis technique, i.e. Motor Current Signature Analysis (MCSA).

6.2 Experimental Fault Arrangements

6.2.1 Practical Technique to Simulate an Inter-Turn Stator Fault in the DFIG

An inter-turn fault of a stator phase winding is a result of the deterioration of insulation between the individual coils. This is in essence a short circuitry of the stator phase winding, which changes the symmetrical stator currents to one which is assymetrical. For predicting the electrical behaviour from the stator supply due to an inter-turn fault, it would appear that the impedance of the short-circuited stator winding has decreased. The degree to which it's impedance has decreased depends on the severity of the fault. To simulate the inter-turn fault on the DFIG, the impedance of the stator phase winding is decreased by placing a resistor in parallel with the winding, as shown in Fig. 6.1 [24]. Two resistor values are chosen (i.e. 180Ω and 280Ω), to illustrate a change in the severity of the fault. The stator phase winding is connected in star.

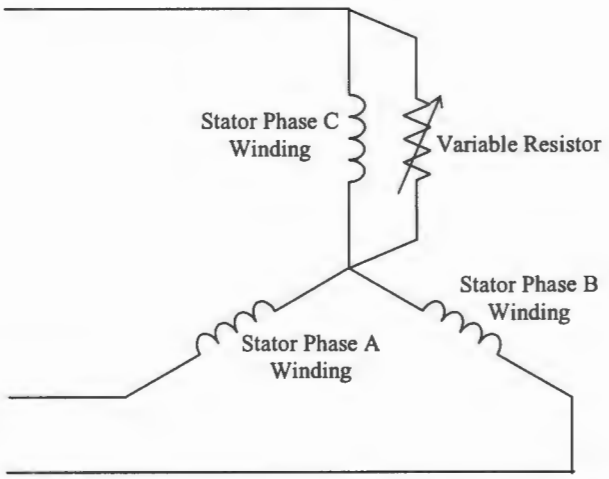

Figure 6.1: Simulated stator turn-to-turn fault

6.2.2 Broken Rotor Bar fault in the Squirrel Cage Induction Generator

Two squirrel cage induction machines, described in the experimental setup, are used in the experimental tests. Only one of the machines is damaged, so as to provide a comparative study into the effect of the electrical behaviour caused by the broken rotor bar. Breaking one of the rotor bars is achieved by simply drilling a hole into a rotor bar as shown in Fig. 6.2

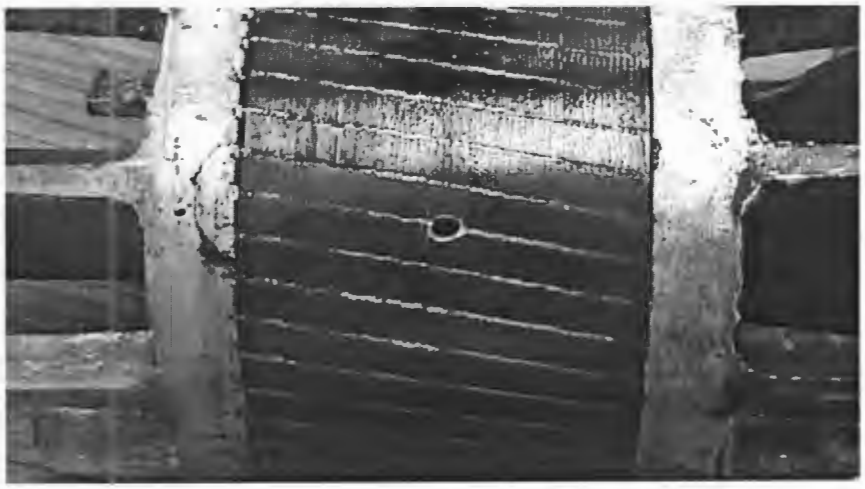

Figure 6.2: Broken rotor bar in the squirrel cage induction machine

6.3 Experimental Results

6.3.1 Doubly-Fed Induction Generator WECS

The experimental results show the DFIG operating in steady-state and transient conditions. The steady-state results show the DFIG operating at 1120rpm and 1880 rpm respectively. The transient captured shows the speed change of the DFIG as it is ramped up from 1120rpm to 1880rpm over 5 seconds. This illustrates the ability of the system to operate within sub-synchronous and super-synchronous regions, since the synchronous speed is 1500rpm. For each of the speed conditions, the machine is operated under three different conditions. The first condition illustrates the machine operating without any faults placed on the machine. The next two conditions illustrate the simulated inter-turn fault placed on one stator phase winding, as mentioned in the previous section. Only the phase affected by the fault changes are shown in the experimental results.

Fig. 6.3 shows the stator currents of the DFIG, operating at 1120rpm, for the three conditions mentioned above. The effect of placing faults on the machine is clearly evident in the distortion of the currents in comparison to the healthy state. These differences are also evident in Fig. 6.4, which shows the stator current response of the machine while operating at 1880rpm. Fig. 6.5 shows the transient response of the stator currents as it ramps up in speed from 1120rpm to 1880rpm. The noticeable difference between the healthy and faulty states is the slight rise in faulty stator currents before 1880rpm is reached, whilst during the healthy state, their appears to be a decline in current before the 1880rpm is reached. Comparisons between the 2 fault conditions for each figure shows a difference in the magnitude of the stator currents, indicating the greater severity in the simulated fault by using the 180Ω resistor.

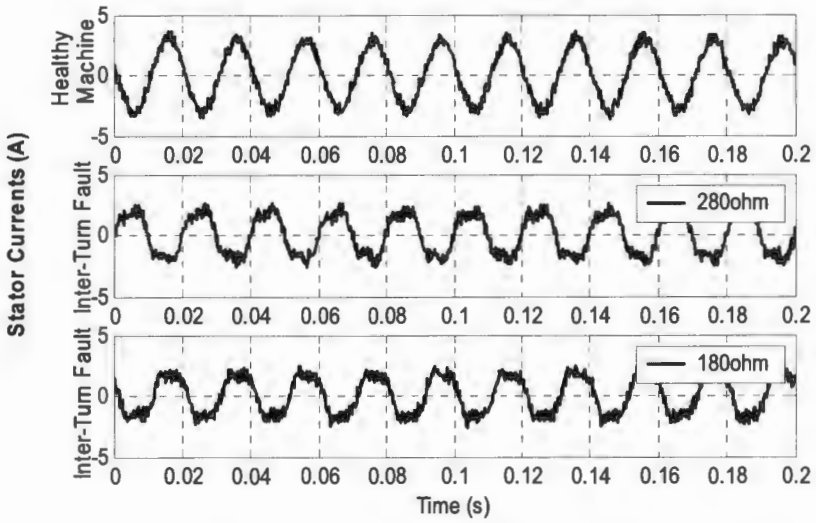

Figure 6.3: Stator currents for sub-synchronous operation (1120rpm)

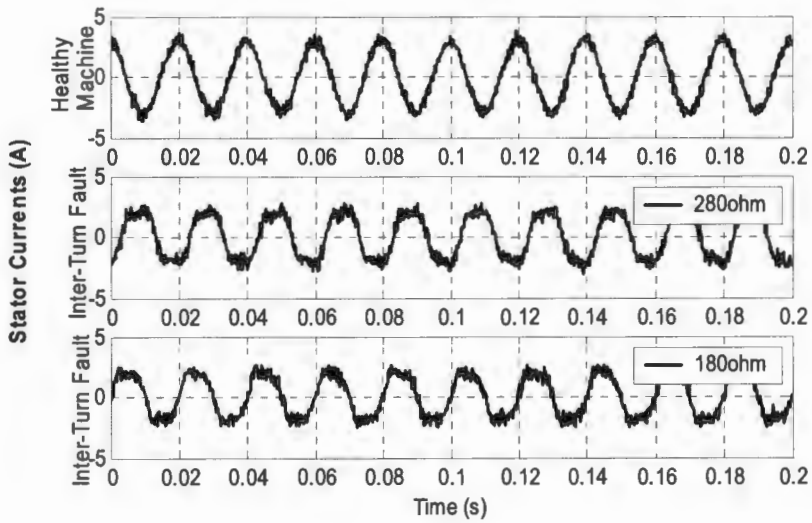

Figure 6.4: Stator currents for super-synchronous operation (1880rpm)

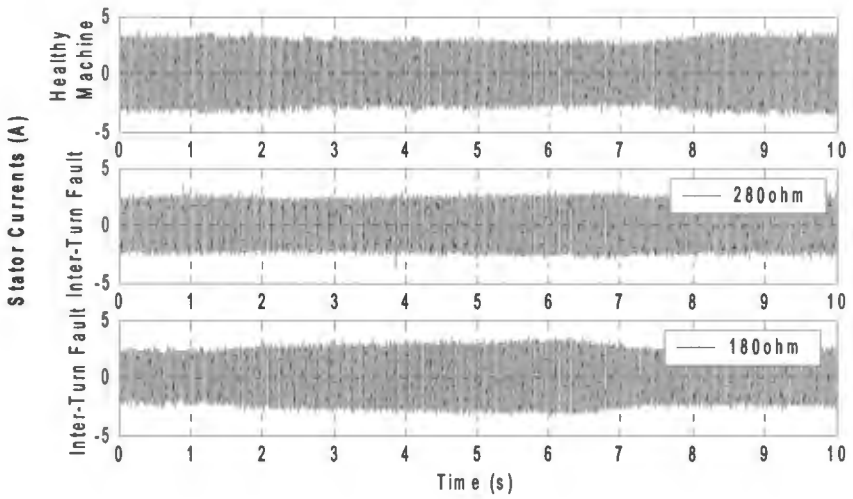

Figure 6.5: Stator currents for operation through synchronous speed

6.3.2 Squirrel Cage Induction Generator WECS

The tests carried out show the machines operating in steady state and transient conditions. The healthy state of the machine, as indicated in the figures below, refers to the machine operating in the absence of faults and the damaged machine refers to the machine operating with the broken rotor bar. Fig. 6.6 and Fig. 6.7 show the stator currents, for the two health conditions, as the machine is operated at 825rpm and 1650rpm respectively. The increase in speed of the machine, from 825rpm to 1650rpm, is evident by the doubling of the current frequency. Fig. 6.8 shows the transient response as the speed is increased from 825rpm to 1650rpm, representing a sudden increase in wind speed thus accelerating the wind turbine. From the results, there are no conclusive differences between the healthy state and the damaged machine for steady state and transient states.

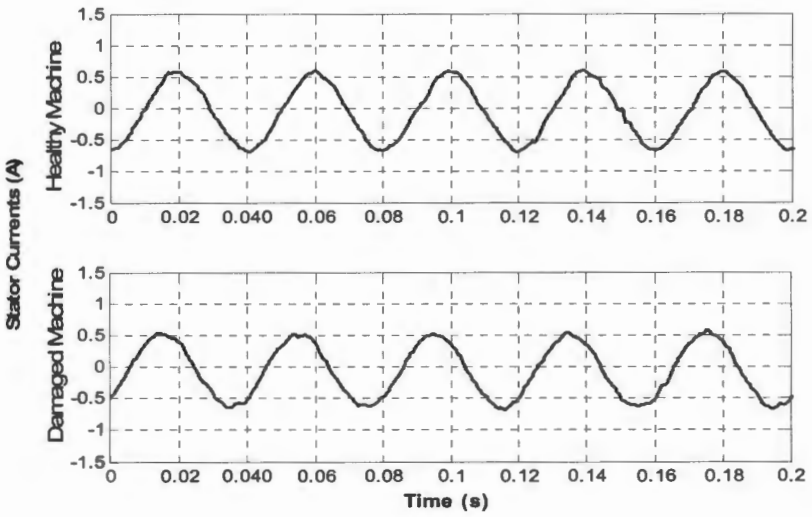

Figure 6.6: Stator currents for operation at 825rpm

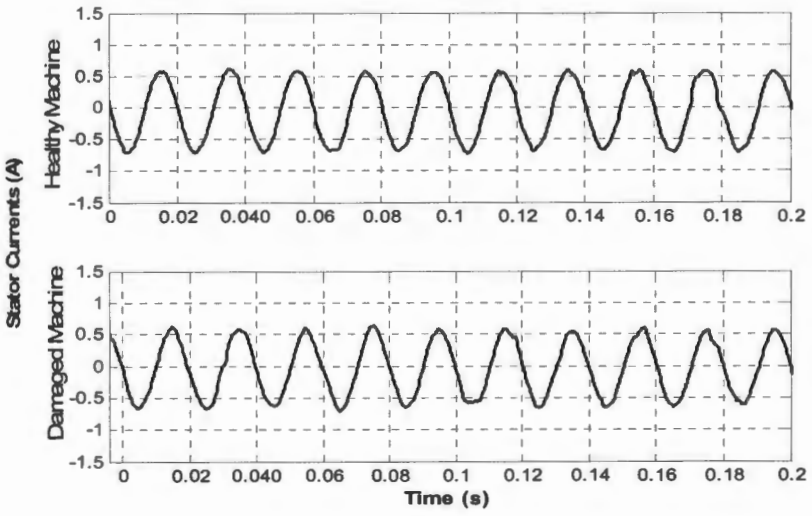

Figure 6.7: Stator currents for synchronous operation at 1650rpm

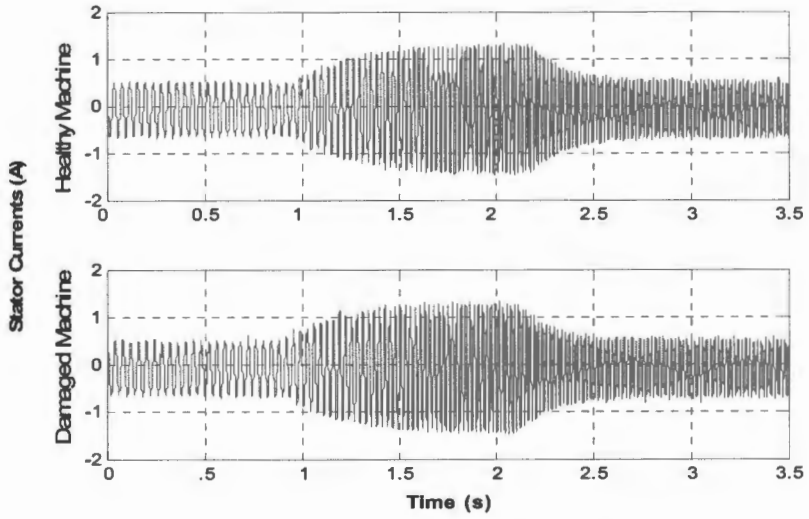

Figure 6.8: Stator currents for ramp in speed

6.4 Motor Current Signature Analysis (MCSA)

A popular method of induction machine fault detection utilizes the steady-state spectral components of the stator quantities. Although there are many diagnostic variables which may be used, i.e. voltage, power, vibration, etc., the most popular utilizes the current and is known as Motor Current Signature Analysis (MCSA). The accuracy of this technique depends on the loading of the machine, the signal to noise ratio of the spectral components being examined and the ability to maintain a constant speed to facilitate the operation of the algorithm [23]. MCSA will be used to attempt to identify the faults placed on the machines.

6.4.1 Theoretical Principles

The objective of MCSA is to attain a frequency spectrum of the stator currents and to identify the current components which are characteristic of faults. The equation below gives the frequency components which are characteristic of a shorted stator turn [24].

$$f_{st} = f_1\left[\frac{n}{p}(1-s)\pm k\right] \qquad (6.1)$$

f_{st} stator frequency components that are a function of shorted turns,

f_i supply frequency, n = 1,2,3,..., k = 1,3,5,..., p is the pole-pairs, s is the per unit slip

Classically, broken rotor bars can be detected by monitoring the stator current spectral components [23], as identified by equation 6.2.

$$f_{sb} = f_s(1 \pm 2s) \qquad (6.2)$$

f_{sb} are the frequencies of sidebands due to broken rotor bars, f_s is the stator fundamental frequency, s is the per unit slip.

This method of broken rotor bar detection is based on the following assumptions:

- The speed of the machine is constant and known.
- The slip is accurately measured.
- The stator fundamental frequency is constant.
- The load is constant.
- The machine is sufficiently loaded in order to separate the sidebands from the fundamental.
- The signal to noise ratio of the spectral components

As shown by equations 6.1 and 6.2, the inter-turn fault frequency components and the broken rotor bar fault components are dependent upon slip. Therefore during transient conditions, where there are changes in speed, these components are continuously changing and identifying these frequencies becomes difficult.

Using the Fast Fourier Transform (FFT) in Matlab (as shown in Appendix K), a frequency spectrum of the stator currents is shown and examined, for the conditions mentioned in the previous section.

6.4.2 *Analysis and Discussion of Results for the DFIG*

Fig. 6.9 shows the stator current spectrum for the machine operating at 1120rpm. During the inter-turn fault conditions, there appears to be a new current component existing around 124.7Hz, which corresponds to the theoretical predictions as given by equation 6.1, with n=4 and k=1. Fig. 6.10 shows the stator current spectrum for the machine operating at 1880rpm. There also appears to be a new component at 175.3Hz for the fault conditions,

which also corresponds to the theory, with n=4 and k=1. Fig. 6.11 shows the current spectrum during the transient response. There appears to be no identifiable fault components for the faulty conditions. This is due to the change in slip as the speed is changed, thus continuously changing the position of the fault component.

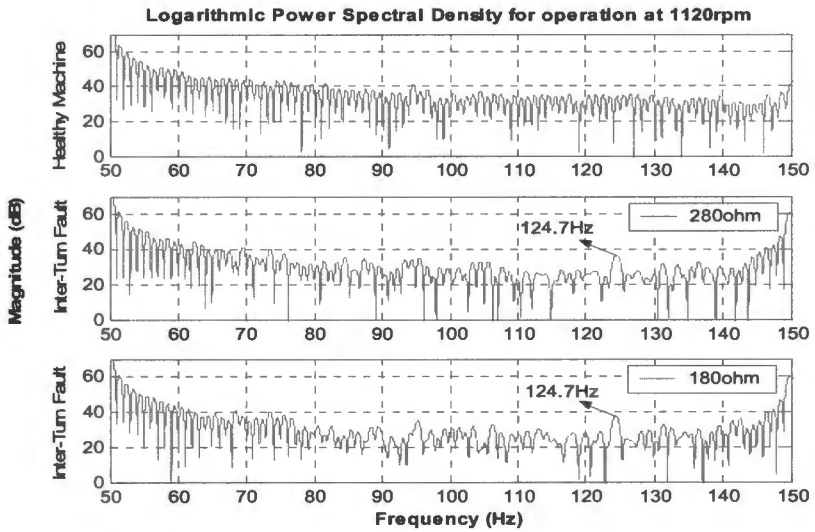

Figure 6.9: Spectrum of stator currents for sub-synchronous operation (1120rpm)

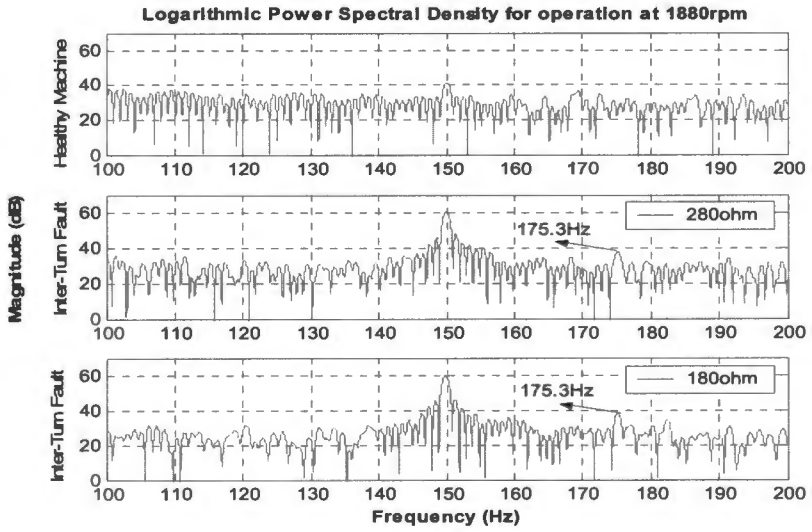

Figure 6.10: Spectrum of stator currents for super-synchronous operation (1880rpm)

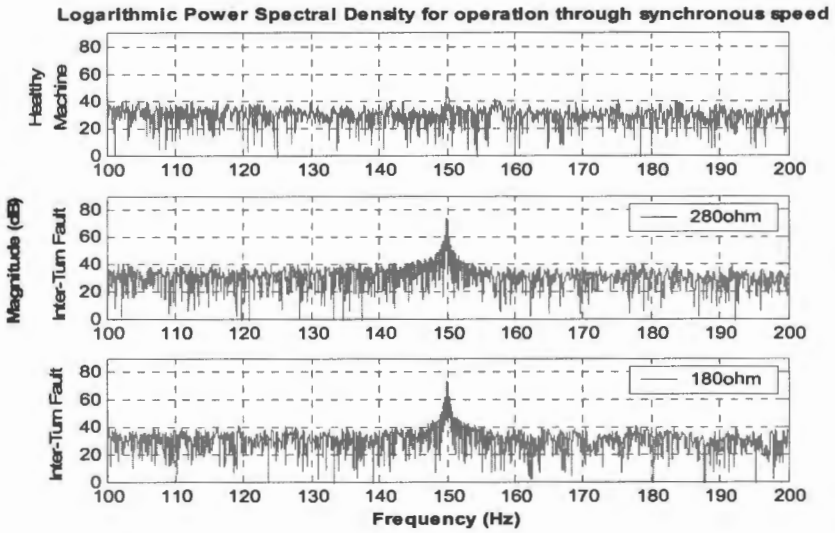

Figure 6.11: Spectrum of stator currents for operation through synchronous operation

As predicted, the fault components of the steady state conditions are identifiable, however for the transient response, no fault components could be identified.

6.4.3 Analysis and Discussion of Results for the Squirrel Cage Induction Generator

Fig. 6.12 shows the stator current spectrum for the healthy and damaged machine operating at 825rpm. From the spectrum it is evident that the synchronous frequency of the stator is 25Hz. Fig. 6.13 shows the stator current spectrum for operation at 1650rpm, whereby the synchronous frequency of the stator currents are located at 50Hz. Fig. 6.14 shows the spectrum for a ramp in speed from 825rpm to 1650rpm, while maintaining a slip of 0.1. This is evident by the change in the fundamental component from 25Hz to 50Hz.

There appears to be no difference between the healthy and damaged machine for the steady state speed conditions. Using equation 6.2, the fault component

for operation at 825rpm should be located at 30Hz and for operation at 1650rpm it should be located at 60Hz. However, there are numerous factors which affect the ability to identify these components, as mentioned earlier, and the slightest of changes to any one of these factors could vary the location or magnitude of the fault frequency's. From Fig. 6.14, it is clearly evident that these fault components would certainly be difficult to identify during transient conditions using the FFT, since not only will the fundamental be changing but also the fault frequency.

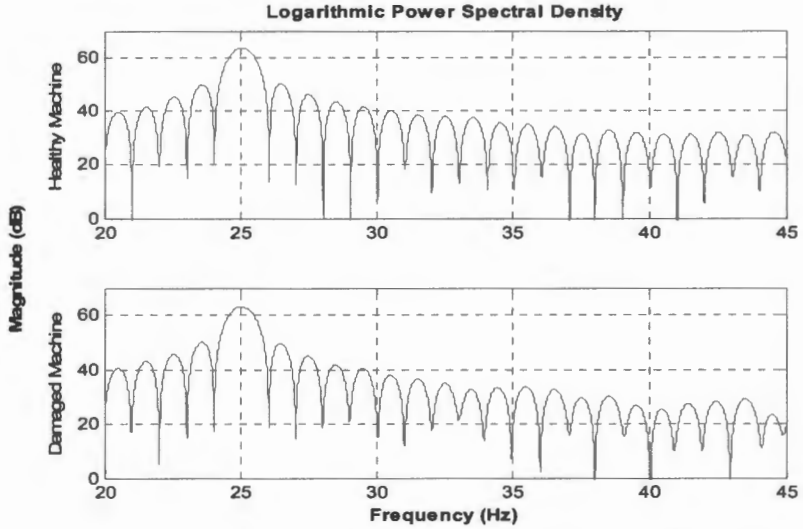

Figure 6.12: Stator current spectrum for operation at 825rpm

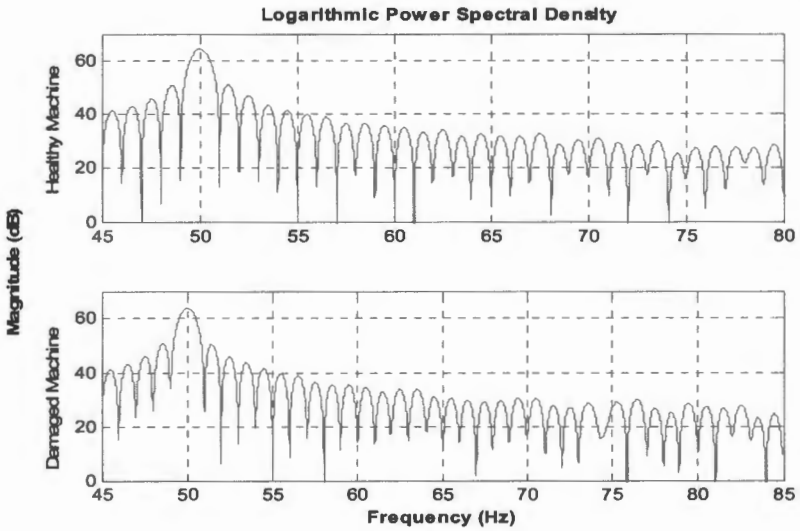

Figure 6.13: Stator current spectrum for operation at 1650rpm

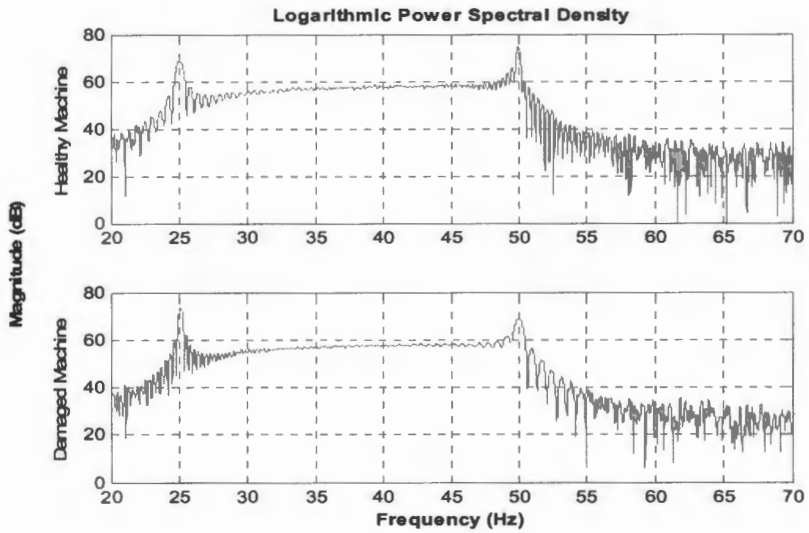

Figure 6.14: Stator current spectrum for a ramp in speed

The MCSA results attained for the two systems have indicated some of the challenges faced by using the Fast Fourier Transform especially during transients. To address this problem a PhD student, Mr. H. Douglas, under the supervision of Prof. P. Pillay, has developed a new algorithm for transient MCSA using wavelets. Using the measured results attained in this project and the newly developed algorithm, he was able to detect faults during transient and steady state conditions. The findings of the broken rotor bar case have been published in the IEEE Transactions on Industry Applications [27] and the findings of the inter-turn fault has been submitted to the IEEE IAS annual meeting in 2005. This non-stationary fault detection technique proves to be well suited for wind generators since they operate predominately in the transient.

6.5 Conclusions

The details for implementation of two of the more common faults in induction machines have been described.

Time-domain analysis for the identification of a rotor bar fault on a squirrel cage induction WECS proves to be difficult since there are no significant differences between the healthy and damaged machine results for steady state and transient responses. Although there does appear to be a difference in the time-domain analysis between the healthy machine and the stator inter-turn faults, this proves to be ineffective since the differences cannot be identified unambiguously and would clearly be dependent on the severity of the fault. According to the mathematics, the broken bar fault frequency components should be identifiable at specific values for steady state operation, however these fault components depend on many factors and any changes would cause a change in the fault component, making it very difficult to try and identify these fault components. MCSA fails when the analysis is performed under transient conditions.

The results attained in this chapter, were used for the testing of a newly developed algorithm for transient MCSA using wavelets. The algorithm proved to be extremely successful as it was able to unambiguously identify the faults for the different fault cases. It is recommended that this non-stationary fault detection technique be implemented on wind generators since their operation is predominately in the transient.

Chapter 7

7. CONCLUSIONS

Based on the findings of this research, the following conclusions have been drawn:

1. **Transient Model and Field Orientated Control of an Induction Machine**

The transient modeling of an induction machine formed a critical part in understanding the operation of the machine. It was also essential in the development of the fundamental equations used for the rotor field orientated control. These steps were necessary for the development of the doubly-fed induction generator drive so as to achieve speed control from the rotor-side of the machine.

2. **Control of a Doubly-Fed Induction Generator (DFIG) using Back-to-Back Converters**

The implementation of the DFIG drive was achieved by the use of back-to-back converters in the rotor circuit. The rotor-side converter used the mathematical equations derived for the rotor field orientated control so as to attain speed control with the use of a PI controller. The supply-side converter used a vector control approach for control of the reactive power flow and DC-link voltage. Since the DFIG is designed to operate below and above synchronous speed, the drive should be capable of bi-directional power flow since the rotor power is slip dependent. The use of current controllers also simplified the implementation of the control strategyies for the machine, since torque is proportional to the current.

3. Experimental Setup of the Two Variable Speed-Wind Induction Generator Systems

The modeling of the two wind generator systems were achieved experimentally. The cage rotor induction generator system was implemented with the use of a commercially available drive, whereas the DFIG drive had been implemented from fundamental principles with the use of the ACE Kit, which proved to be an invaluable tool for rapid testing of control prototypes. The controller card (part of the ACE Kit) was only switched at a maximum frequency of 5kHz due to its computational ability. However, the switching frequency employed in the prototype confirms that the control techniques can be extended to higher power levels. The greatest difficulty faced by the employment of the controller card was the limited number of analogue inputs, however this was solved by making calculated assumptions.

A DC machine and a thyristor converter were successfully used to simulate the wind turbine.

4. The Simulated and Experimental Results of the Wind Generator Systems

The tests carried out on the two wind generator systems show the systems operating under transient and steady state conditions. The simulation results for the DFIG system validated the experimental operation of the system. The supply-side converter was shown to control the reactive power flow and the DC-Link voltage while the rotor-side converter was shown to control the speed of the generator.

The transient responses of the two wind generator systems illustrates their ability to track changes in wind speed by accordingly changing the generator speed thus extracting maximum energy from the wind turbine (Maximum Power Point Tracking). The results of the tests carried on the two wind generator systems, validated a successful implementation of the systems.

5. Experimental Procedure for Placing Faults on Wind Generator Systems

Two of the more common induction machine faults (i.e. broken rotor bar and inter-turn stator fault) had been implemented on the wind generators. Time domain analysis and Motor Current Signature Analysis was then used in an attempt to identify the faults. Time domain analysis proved to be ineffective for the broken rotor bar case although there were noticeable differences for the inter-turn stator fault, these differences cannot be identified unambiguously and are clearly dependent on the severity of the fault. The Motor Current Signature Analysis implemented here was not able to identify the broken rotor bar fault components for both steady state conditions, simply because there are just too many constraints and assumptions made on the machines operating conditions before the broken rotor bar fault components may be identified. However, it was able to identify the inter-turn stator fault components for steady state operation. MCSA failed under transient conditions since the fault components are slip dependant and trying to identify these components during speed changes is difficult.

The results attained from the systems served as a platform for further research into the evaluation and development of a algorithm for transient MCSA using wavelets. The algorithm proved to be extremely successful as it was able to unambiguously identify the faults for the different fault cases. It is recommended that this non-stationary fault detection technique be implemented on wind generators since their operation is predominately in the transient.

LIST OF REFERENCES

[1] C.V. Nayar, J.H. Bundell, "Modelling and Simulation of a Wind-Driven Wound Rotor Induction Generator with Tip-Speed Ratio Control", Electric Energy Conference 1987, Adelaide, 6-9 October 1987

[2] B. Connor, W. E. Leithead, "Performance Assessment of Variable-Speed Wind Turbines", Opportunities and Advances in Internnational Power Generation, 18-20th March 1996, Conference Publication No.419, IEE, 1996

[3]S.R. Chellapilla and B. H. Chowdhury, "A Dynamic Model if Induction Generators for Wind Power Studies", IEEE,2003

[4] J.F. Manwell, J.G. McGowan, A.L. Rogers, "Wind Energy Explained", John Wiley&Sons,2002

[5] R.V. Singo, "Maximum Power Point Tracking of a Permanent Magnet Synchronous Wind Generator". Thesis. Department of Electrical Engineering. University of Cape Town. October 2002

[6] Rajib Datta, V.T. Ranganathon, "Variable Speed Wind Power Generation Using Doubly Fed Wound Rotor Induction Machine-a comparison with alternative schemes," IEEE Transactions On Energy Conversion, Vol.17, No. 3, pp 414-421, September 2002

[7] Chris S. Brune, "Experimental Evaluation of Variable Speed, Doubly-Fed Wind-Power Generation System," IEEE Transactions on Industry Applications, Vol.30, No. 3, May/June 1994

[8] B.S. Borowy, Z.M. Salameh, "Dynamic Response of a Stand Alone Wind Energy Conversion System with Battery Energy Storage to a Wind Gust," IEEE Transactions on Energy Conversion, Vol.12, No.1, March 1997

[9] Tomas Petru and Torbjorn Thiringer, "Modelling of Wind Turbines for Power System Studies," IEEE Transactions on Power Systems, Vol.17, No. 4, Nov 2002

[10] S.A. Papathanassiou, M.P. Papadopoulas, "Dynamic Behaviour of Variable Speed Wind Turbines Under Stochastic Wind," IEEE Transactions on Energy Conversion, Vol. 14, No. 4, Dec 1999

[11] Andrew Miller, Edward Muljadi, Donald S. Zinger, "A Variable Speed Wind Turbine Power Control," IEEE Transactions On Energy Conversion, Vol.12, No. 2, pp 414-421, June 1997

[12]R. Pena, J.C. Clare and G.M. Asher, "Doubly Fed Induction Generator using Back-to-Back PWM Converters and its Application to Variable Speed Wind Energy Generation," IEE Proc.-Electr. Power Appl., Vol. 143, No. 3, pp231-241, May 1996

[13]Andrzej M. Trzynadlowski, "The Field Orientation Principle in Control of Induction Motors," Kluwer Academic Publishers

[14]K Hamann, "Field Orientated Control of an Induction Motor," BSc Thesis, University of Cape Town, October 1999

[15]Peter Vas, "Sensorless Vector and Direct Torque Control," Oxford University Press, 1998

[16]EEE480C Lecture Notes, "Reference Frame Transformations". Department of Electrical Engineering. University of Cape Town, July 2001

[17]Andreas Petersson, "Analysis, Modeling and Control of Doubly-Fed Induction Generators for Wind Turbines", Department of Electric Power Engineering. Chalmers University of Technology. Göteborg, Sweden. 2003

[18]P. Pillay, "Modeling, Performance and Design of Sinusoidal- and Rectangular-Fed Permanent Magnet Motor Drives", Michigan, 1991

[19]Ned Mohan, Tore M. Undeland, William P. Robbins, "Power Electronics-Converters, Applications and Design", 2nd Edition. John Wiley and Sons, Inc. 1995

[20]S. Muller, M. Deike, R.W. de Donker, "Doubly Fed Induction Generator Systems for Wind Turbines", IEEE Industry Applications magazine, May/June 2002, pp26-33

[21]T. Wildi, "Electric Machines, Drives, and Power Systems", 4th Edition, Prentice-Hall, Inc., 2000

[22]P.C. Sen, "Principles of Electric Machines and Power Electronics", 2nd Edition, John Wiley & Sons, 1997

[23] P.Barendse, H. Douglas and P.Pillay, "Condition Monitoring of Wind Generators for Wind Energy Conversion Systems", WWEC 2003, 2nd World Wind Energy Conference, Cape Town, South Africa, 23-26 Nov 2003

[24] L.M. Popa, B Bak-Jensen, Ewen Ritchie and Ion Boldea, "Condition Monitoring of Wind Generators", IEEE Industry Applications Society 38th Annual Meeting, IAS03, Salt Lake City, Utah USA, October 2003

[25] S. M. A. Cruz and A. J. Marques Cardoso, "Stator Winding Fault Diagnosis in Three-Phase Synchronous and Asynchronous Motors, by the Extended Park's Vector Approach", IEEE Transactions on Industry Applications, Vol. 37, No. 5, Sept/Oct 2001

[26]P.Barendse, "Motor Signature Analysis as a Tool for Motor Fault Detection", Thesis, Department of Electrical Engineering, University of Cape Town, Oct 2001

[27] H. Douglas, P. Pillay, A. K. Ziarani, "A new algorithm for transient motor current signature analysis using wavelets", IEEE Transactions on Industry Applications, Vol. 40, No. 5, Sept/Oct 2004

APPENDIX A

DYNAMIC EQUIVALENT SIMULATION MODELS OF THE INDUCTION MACHINE IN THE STATIONARY AND SYNCHRONOUS REFERENCE FRAMES (PSPICE)

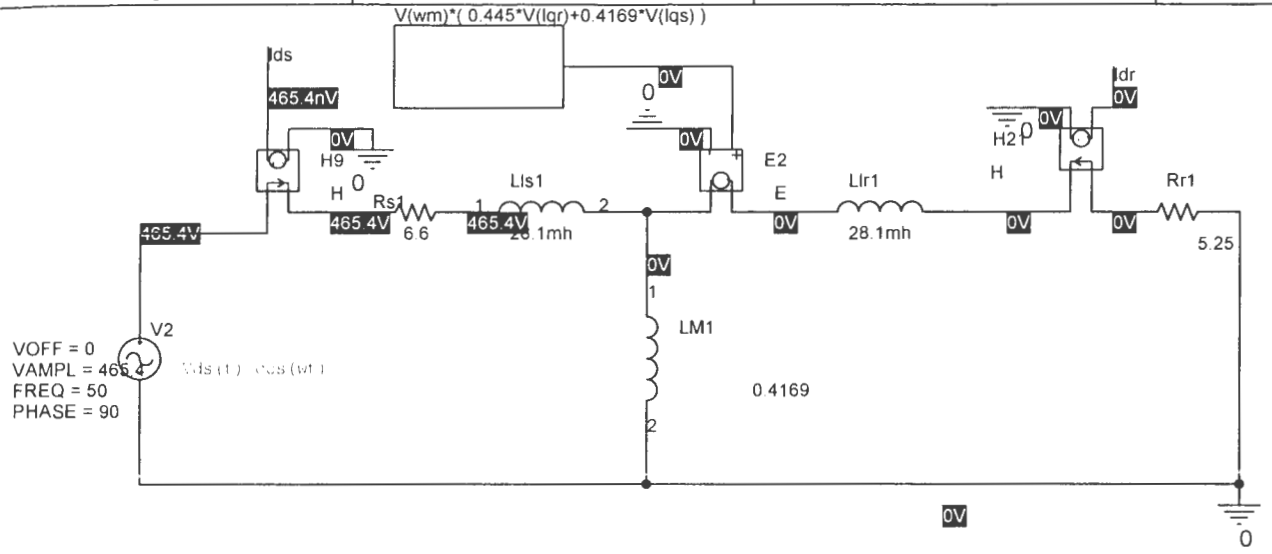

D-Axis

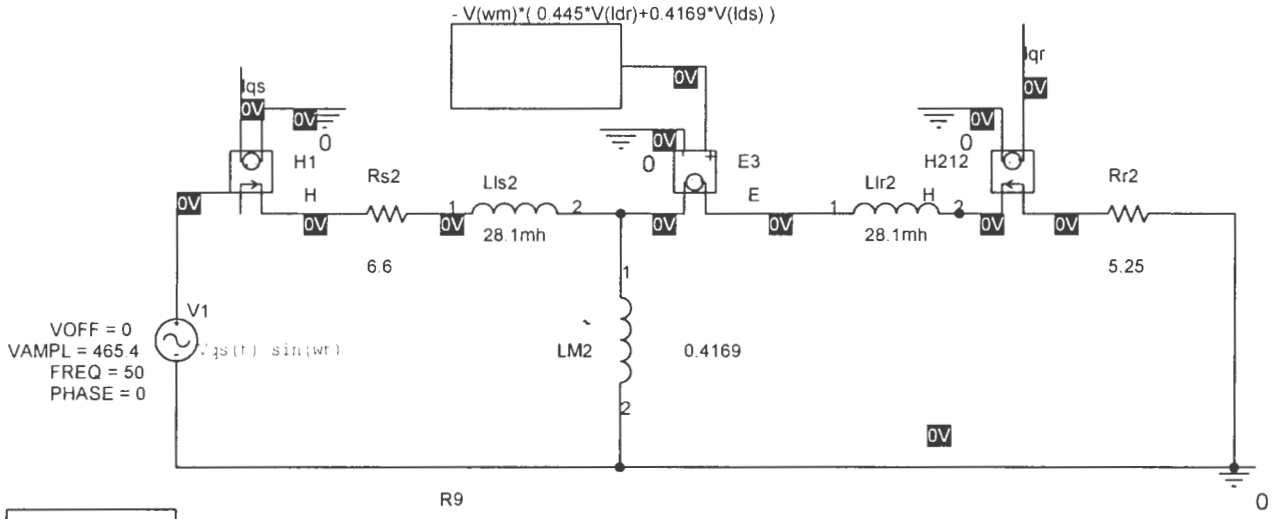

Q-Axis

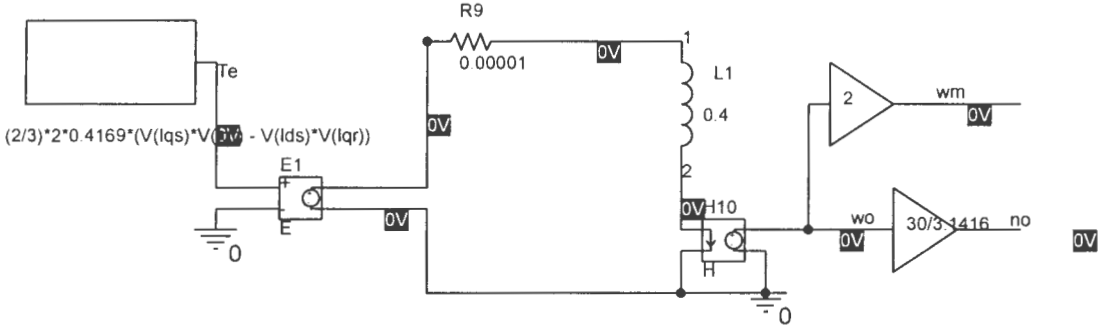

Title: INDUCTION MACHINE - STATIONARY REFERENCE FRAME		
Size: A	Document Number: By: Paul Barendse	Rev: <RevCode>
Date: Friday, August 20, 2004	Sheet 1 of 1	

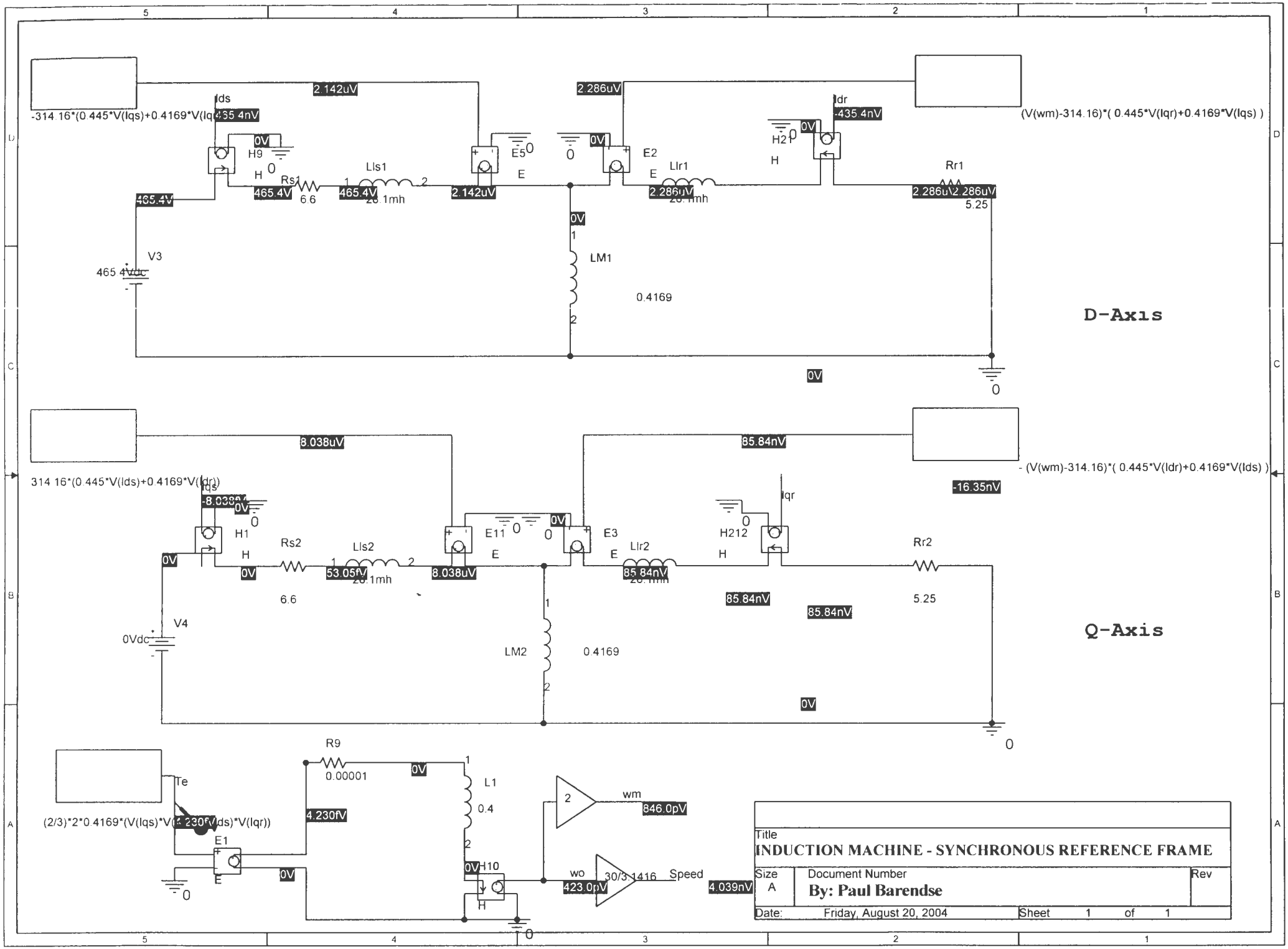
-314.16*(0.445*V(Iqs)+0.4169*V(Ids)
Ids
2.142uV
2.286uV
Idr
(V(wm)-314.16)*(0.445*V(Iqr)+0.4169*V(Iqs))
H9
Rs1
6.6
Lls1
26.1mh
E5
E2
Llr1
H2
Rr1
5.25
V3
LM1
0.4169
D-Axis
314.16*(0.445*V(Ids)+0.4169*V(Idr))
8.038uV
85.84nV
- (V(wm)-314.16)*(0.445*V(Idr)+0.4169*V(Ids))
-16.35nV
Iqr
H1
Rs2
Lls2
53.05fV
E11
E3
Llr2
H212
Rr2
V4
0Vdc
LM2
Q-Axis
R9
0.00001
L1
0.4
Te
(2/3)*2*0.4169*(V(Iqs)*V(Ids)*V(Iqr))
4.230fV
E1
H10
wm
846.0pV
wo
423.0pV
30/3.1416
Speed
4.039nV
Title
INDUCTION MACHINE - SYNCHRONOUS REFERENCE FRAME
Size
A
Document Number
By: Paul Barendse
Rev
Date:
Friday, August 20, 2004
Sheet
1
of
1

APPENDIX B

IGBT MODULES:

- **SKM 100GB 123D**
- **SKM 200GB 123D**

SEMIKRON

Absolute Maximum Ratings Symbol	Conditions [1]	Values		Units
V_{CES}		1200		V
V_{CGR}	R_{GE} = 20 kΩ	1200		V
I_C	T_{case} = 25/80 °C	100 / 90		A
I_{CM}	T_{case} = 25/80 °C; t_p = 1 ms	200 / 180		A
V_{GES}		± 20		V
P_{tot}	per IGBT, T_{case} = 25 °C	690		W
T_j, (T_{stg})		– 40 . . . +150 (125)		°C
V_{isol}	AC, 1 min.	2 500 [7]		V
humidity	DIN 40 040	Class F		
climate	DIN IEC 68 T.1	40/125/56		
Inverse Diode			FWD [6]	
I_F = – I_C	T_{case} = 25/80 °C	95 / 65	130 / 90	A
I_{FM} = – I_{CM}	T_{case} = 25/80 °C; t_p = 1 ms	200 / 180	200 / 180	A
I_{FSM}	t_p = 10 ms; sin.; T_j = 150 °C	720	1100	A
I^2t	t_p = 10 ms; T_j = 150 °C	2600	6000	A^2s

Characteristics Symbol	Conditions [1]	min.	typ.	max.	Units
$V_{(BR)CES}$	V_{GE} = 0, I_C = 4 mA	≥ V_{CES}	–	–	V
$V_{GE(th)}$	V_{GE} = V_{CE}, I_C = 2 mA	4,5	5,5	6,5	V
I_{CES}	V_{GE} = 0, T_j = 25 °C	–	0,1	1,5	mA
	V_{CE} = V_{CES}, T_j = 125 °C	–	6	–	mA
I_{GES}	V_{GE} = 20 V, V_{CE} = 0	–	–	300	nA
V_{CEsat}	I_C = 75 A, V_{GE} = 15 V;	–	2,5(3,1)	3(3,7)	V
V_{CEsat}	I_C = 100 A, T_j = 25 (125) °C	–	2,8(3,6)	–	V
g_{fs}	V_{CE} = 20 V, I_C = 75 A	31	–	–	S
C_{CHC}	per IGBT	–	–	350	pF
C_{ies}	V_{GE} = 0	–	5	6,6	nF
C_{oes}	V_{CE} = 25 V	–	720	900	pF
C_{res}	f = 1 MHz	–	380	500	pF
L_{CE}		–	–	30	nH
$t_{d(on)}$	V_{CC} = 600 V	–	30	60	ns
t_r	V_{GE} = +15 V, - 15 V [3]	–	70	140	ns
$t_{d(off)}$	I_C = 75 A, ind. load	–	450	600	ns
t_f	R_{Gon} = R_{Goff} = 15 Ω	–	70	90	ns
E_{on} [5]	T_j = 125 °C	–	10	–	mWs
E_{off} [5]		–	8	–	mWs
Inverse Diode [8]					
V_F = V_{EC}	I_F = 75 A, V_{GE} = 0 V;	–	2,0(1,8)	2,5	V
V_F = V_{EC}	I_F = 100 A, T_j = 25 (125) °C	–	2,25(2,05)	–	V
V_{TO}	T_j = 125 °C	–	–	1,2	V
r_T	T_j = 125 °C	–	12	15	mΩ
I_{RRM}	I_F = 75 A; T_j = 25 (125) °C [2]	–	27(40)	–	A
Q_{rr}	I_F = 75 A; T_j = 25 (125) °C [2]	–	3(10)	–	µC
FWD of types "GAL", "GAR" [8]					
V_F = V_{EC}	I_F = 75 A, V_{GE} = 0 V;	–	1,85(1,6)	2,2	V
V_F = V_{EC}	I_F = 100 A, T_j = 25 (125) °C	–	2,0(1,8)	–	V
V_{TO}	T_j = 125 °C	–	–	1,2	V
r_T	T_j = 125 °C	–	9	11	mΩ
I_{RRM}	I_F = 75 A; T_j = 25 (125) °C [2]	–	30(45)	–	A
Q_{rr}	I_F = 75 A; T_j = 25 (125) °C [2]	–	3,5(11)	–	µC
Thermal Characteristics					
R_{thjc}	per IGBT	–	–	0,18	°C/W
R_{thjc}	per diode / FWD "GAL; GAR"	–	–	0,50/0,36	°C/W
R_{thch}	per module	–	–	0,05	°C/W

SEMITRANS® M IGBT Modules

SKM 100 GB 123 D
SKM 100 GAL 123 D [6]
SKM 100 GAR 123 D [6]

SEMITRANS 2

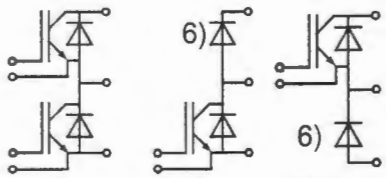

Features

- MOS input (voltage controlled)
- N channel, Homogeneous Si
- Low inductance case
- Very low tail current with low temperature dependence
- High short circuit capability, self limiting to 6 * I_{cnom}
- Latch-up free
- Fast & soft inverse CAL diodes [8]
- Isolated copper baseplate using DCB Direct Copper Bonding Technology
- Large clearance (10 mm) and creepage distances (20 mm).

Typical Applications: → B 6 -115

- Switching (not for linear use)

1) T_{case} = 25 °C, unless otherwise specified
2) I_F = – I_C, V_R = 600 V, – di_F/dt = 800 A/µs, V_{GE} = 0 V
3) Use V_{GEoff} = -5 ... -15 V
5) See fig. 2 + 3; R_{Goff} = 15 Ω
6) The free-wheeling diodes of the GAL and GAR types have the data of the inverse diodes of SKM 150 GB 123 D
7) V_{isol} = 4000 V_{rms} on request
8) CAL = Controlled Axial Lifetime Technology.

Cases and mech. data → B6-116

SEMIKRON

Absolute Maximum Ratings		Values		
Symbol	Conditions [1]	... 123 D	... 123 D1	Units
V_{CES}		1200		V
V_{CGR}	R_{GE} = 20 kΩ	1200		V
I_C	T_{case} = 25/80 °C	200 / 180		A
I_{CM}	T_{case} = 25/80 °C; t_p = 1 ms	400 / 360		A
V_{GES}		± 20		V
P_{tot}	per IGBT, T_{case} = 25 °C	1380		W
T_j, (T_{stg})		– 40 . . .+150 (125)		°C
V_{isol}	AC, 1 min.	2 500 [7]		V
humidity	DIN 40 040	Class F		
climate	DIN IEC 68 T.1	40/125/56		
Inverse Diode			FWD [6]	
$I_F = -I_C$	T_{case} = 25/80 °C	200 / 130	260 / 180	A
$I_{FM} = -I_{CM}$	T_{case} = 25/80 °C; t_p = 1 ms	400 / 360	400 / 360	A
I_{FSM}	t_p = 10 ms; sin.; T_j = 150 °C	1450	1800	A
I^2t	t_p = 10 ms; T_j = 150 °C	10 500	24 200	A^2s

Characteristics					
Symbol	Conditions [1]	min.	typ.	max.	Units
$V_{(BR)CES}$	V_{GE} = 0, I_C = 4 mA	≥ V_{CES}	–	–	V
$V_{GE(th)}$	V_{GE} = V_{CE}, I_C = 6 mA	4,5	5,5	6,5	V
I_{CES}	V_{GE} = 0, T_j = 25 °C	–	0,2	3	mA
	V_{CE} = V_{CES}, T_j = 125 °C	–	12	–	mA
I_{GES}	V_{GE} = 20 V, V_{CE} = 0	–	–	1	µA
V_{CEsat}	I_C = 150 A, V_{GE} = 15 V; T_j = 25 (125) °C	–	2,5(3,1)	3(3,7)	V
V_{CEsat}	I_C = 200 A, V_{GE} = 15 V; T_j = 25 (125) °C	–	2,8(3,6)	–	V
g_{fs}	V_{CE} = 20 V, I_C = 150 A	95	–	–	S
C_{CHC}	per IGBT	–	–	700	pF
C_{ies}	V_{GE} = 0	–	10	13	nF
C_{oes}	V_{CE} = 25 V	–	1,5	2	nF
C_{res}	f = 1 MHz	–	0,8	1,2	nF
L_{CE}		–	–	20	nH
$t_{d(on)}$	V_{CC} = 600 V	–	220	400	ns
t_r	V_{GE} = -15 V / +15 V [3]	–	100	200	ns
$t_{d(off)}$	I_C = 150 A, ind. load	–	600	800	ns
t_f	R_{Gon} = R_{Goff} = 5,6 Ω	–	70	100	ns
E_{on} [5]	T_j = 125 °C	–	24	–	mWs
E_{off} [5]		–	17	–	mWs
Inverse Diode [8]					
$V_F = V_{EC}$	I_F = 150 A, V_{GE} = 0 V; T_j = 25 (125) °C	–	2,0(1,8)	2,5	V
$V_F = V_{EC}$	I_F = 200 A, V_{GE} = 0 V; T_j = 25 (125) °C	–	2,25(2,05)	–	V
V_{TO}	T_j = 125 °C	–	–	1,2	V
r_T	T_j = 125 °C	–	5	7	mΩ
I_{RRM}	I_F = 150 A; T_j = 25 (125) °C [2]	–	55(80)	–	A
Q_{rr}	I_F = 150 A; T_j = 25 (125) °C [2]	–	8(20)	–	µC
FWD of types "GAL", "GAR" "123D1" [8] [6]					
$V_F = V_{EC}$	I_F = 150 A, V_{GE} = 0 V; T_j = 25 (125) °C	–	1,85(1,6)	2,2	V
$V_F = V_{EC}$	I_F = 200 A, V_{GE} = 0 V; T_j = 25 (125) °C	–	2,0(1,8)	–	V
V_{TO}	T_j = 125 °C	–	–	1,2	V
r_T	T_j = 125 °C	–	3	5,5	mΩ
I_{RRM}	I_F = 150 A; T_j = 25 (125) °C [2]	–	60(90)	–	A
Q_{rr}	I_F = 150 A; T_j = 25 (125) °C [2]	–	8(23)	–	µC
Thermal Characteristics					
R_{thjc}	per IGBT	–	–	0,09	°C/W
R_{thjc}	per diode / FWD "GAL; GAR"	–	–	0,25/0,18	°C/W
R_{thch}	per module	–	–	0,038	°C/W

SEMITRANS® M IGBT Modules

SKM 200 GA 123 D *)
SKM 200 GB 123 D
SKM 200 GB 123 D1 [6]
SKM 200 GAL 123 D [6]
SKM 200 GAR 123 D [6]

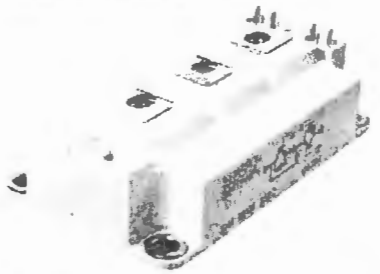

SEMITRANS 3

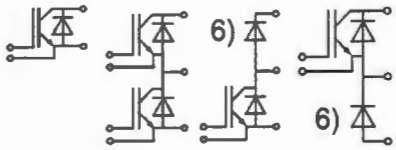

GA GB GAL GAR

Features

- MOS input (voltage controlled)
- N channel, Homogeneous Si
- Low inductance case
- Very low tail current with low temperature dependence
- High short circuit capability, self limiting to 6 * I_{cnom}
- Latch-up free
- Fast & soft inverse CAL diodes [8]
- Isolated copper baseplate using DCB Direct Copper Bonding Technology
- Large clearance (13 mm) and creepage distances (20 mm).

Typical Applications: → B6 - 153

- Switching (not for linear use)

1) T_{case} = 25 °C, unless otherwise specified
2) $I_F = -I_C$, V_R = 600 V, $-di_F/dt$ = 1500 A/µs, V_{GE} = 0 V
3) Use V_{GEoff} = -5 ... -15 V
5) See fig. 2 + 3; R_{Goff} = 5,6 Ω
6) The free-wheeling diodes of the GAL and GAR types have the data of the inverse diodes of SKM 300 GA 123 D
7) V_{isol} = 4000 V_{rms} on request
8) CAL = Controlled Axial Lifetime Technology.

Cases and mech. data → B6-154
*) **SEMITRANS 4 → B6-168**

APPENDIX C

SEMIKRON SKHI61 DRIVER BOARD

SEMIKRON

Absolute Maximum Ratings

Symbol	Term	Values	Units
V_S	Supply voltage primary	15,6	V
V_{iH}	Input signal voltage	V_S + 0,3	V
$Iout_{PEAK}$	Output peak current	2	A
$Iout_{AVmax}$	Output average current (T_A = 85° C)	20	mA
f_{max}	Max. switching frequency (C_{GE} < 9nF)	50	kHz
V_{CE}	Collector emitter voltage sense across the IGBT (for 1200V-IGBTs)	900	V
dv/dt	Rate of rise and fall of voltage (secondary to primary side)	15	kV/µs
V_{isolIO}	Isolation test voltage input - output (2 sec. AC)	2500	V
V_{isol12}	Isolation test voltage ouput 1 - output 2 (2 sec. AC)	1500	V
R_{Gonmin}	Minimum rating for R_{Gon}	10	Ω
$R_{Goffmin}$	Minimum rating for R_{Goff}	10	Ω
$Q_{out/pulse}$	Max. rating for gate charge per pulse T_A = 85° C	0,7	µC
	T_A = 55° C	1	µC
T_{op}	Operating temperature	- 40... + 85	°C
T_{stg}	Storage temperature	- 40... + 85	°C

Electrical Characteristics (T_a = 25 °C)

Symbol	Term		Values min.	typ.	max.	Units
V_S	Supply voltage primary side		14,4	15	15,6	V
I_{SO} [1]	Supply current	no load	160	–	200	mA
(SKHI61)	primary side	normal op.	–	–	450	mA
I_{SO} [1]	Supply current	no load	230	–	290	mA
(SKHI71)	primary side	normal op.	–	–	550	mA
V_{iT+}	Input threshold voltage (High)		4,0	–	–	V
V_{iT-}	Input threshold voltage (Low)		–	–	1,5	V
R_{in}	Input resistance		–	60	–	kΩ
$V_{G(on)}$	Turn on gate voltage output		–	14,9	–	V
$V_{G(off)}$	Turn off gate voltage output		–	-6,5	–	V
R_{GE}	Internal gate-emitter resistance		–	20	–	kΩ
f_{ASIC}	Asic system switching frequency		–	8	–	MHz
$t_{d(on)IO}$	Input-output turn-on propagation time		0,3	0,45	0,6	µs
$t_{d(off)IO}$	Input-output turn-off propagation time		0,3	0,45	0,6	µs
$t_{d(err)}$	Error input-output propagation time		1,15	1,3	1,5	µs
$t_{pERRRESET}$	Error memory reset time		7	15	27	µs
t_{TD}	Interlock dead time adjustable		0	–	4,1	µs
V_{CEstat}	Reference voltage for V_{CE}-monitoring		–	5,8	–	V
t_{blank}	Blanking time		–	3,5	–	µs
C_{ps}	Coupling capacitance primary-secondary		–	40	–	pF
MTBF	Mean Time Between Failure T_a = 40° C		–	1	–	$^{*}10^6$ h
m	weight	SKHI 61	–	95	–	g
		SKHI 71	–	99	–	g
HxBxT	Dimensions		14 x 57 x 114			mm

[1] At T_a < -25° C the current consumption can be 1,6 times the rated maximum current for the first three operating minutes.

SEMIDRIVER®
6-Pack Driver
SKHI 61

- SIXPACK IGBT and MOSFET Driver

7-Pack Driver
SKHI 71

- SEVENPACK IGBT and MOSFET Driver

Features

- CMOS-compatible input buffers at V_{DD}=5V
- Short-circuit protection by V_{CE}-monitoring and Soft-Turn-Off
- Monitoring and turn-off
- Drive interlock top/bottom (optional)
- Signal transmission by opto-couplers
- Supply undervoltage protection (13V)
- Error latch/ output
- Suitable adapter PCB SKPC6006 as EVA-BOARD available

Typical Applications

- Driver for IGBT and MOSFET modules in three-phase-bridge circuits, inverter drives, UPS-facilities etc.

PIN array

Primary side PIN array

Pin	Symbol	Function	Pin	Symbol	Function
01	BS	Auxiliary earth connection	11	+15V	Supply voltage
02	BOT3	Driver signal BOT HB3	12	+15V	Supply voltage
03	TOP3	Driver signal TOP HB3	13	TDT1	Deadtime bit #1
04	BOT2	Driver signal BOT HB2	14	TDT2	Deadtime bit #2
05	TOP2	Driver signal TOP HB2	15	SEL	Deadtime on/off
06	BOT1	Driver signal BOT HB1	16	BSTD	Aux. earth for deadtime adjustment
07	TOP1	Driver signal TOP HB1	17	_ERRIN	_External error signal input
08	_ERR	_Error output Sixpack-driver	18	NC	reserved
09	BSS	System earth connection	19	BRK	Driver signal additional switch
10	BSS	System earth connection	20	_BERR	_Error output additional switch

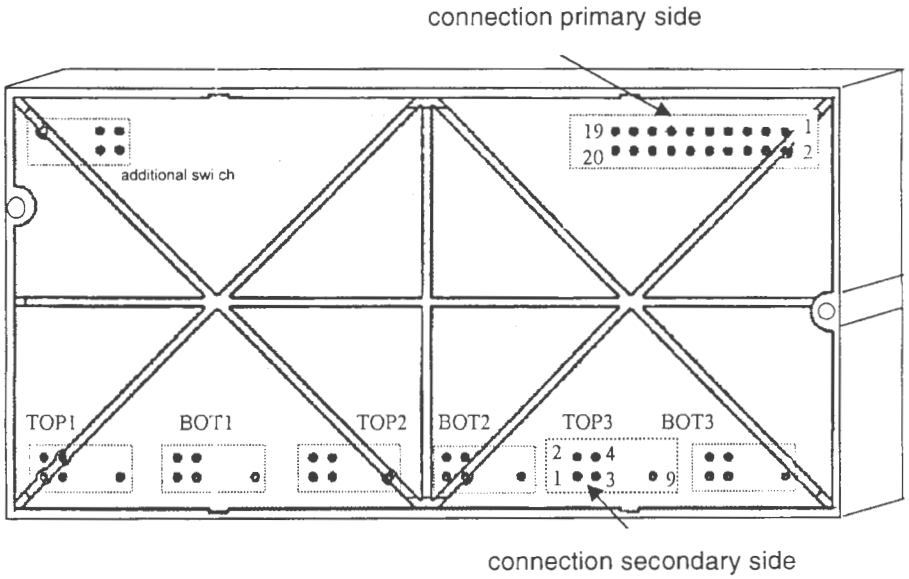

Fig. 1 Bottom view of the SKHiD 61 / SKHiD 71

Secondary side PIN array

Pin	Symbol	Function	Pin	Symbol	Function
01	R_{Gate}	Gate resistor input	04	$V_{CET}2$	VCE-threshold #2
02	$V_{CET}1$	VCE-threshold #1			
03	E	Emitter input	09	V_{CE}	Collector input

SEMIDRIVER®

SKHI 61 and SKHI 71

General properties and functions

The SKHI 61 and SKHI 71 are 6- and 7-channel drivers for IGBT- and MOSFET-modules and can be soldered directly onto the PCB. The drivers are physically separated.

Since all subassemblies necessary for operation have been integrated, there is no need for external components except for the gate resistors and the V_{CE}-circuitry. V_{CE}-thresholds and the blanking time are adjustable by integrating additional resistors and capacitors according to the customer's specifications.

Interlocking time can be adjusted by simple bridging of connector pins. The driver is equipped with a separate error input for immediate turn-off when receiving error signals from external components (e.g. over-temperature).

The independent seventh driver channel of the SKHI 71 guarantees for simple realisation of brake chopper, boost converter or PFC-circuit applications. By bridging of connector pins the driver error signal is transmitted directly to the SIXPACK-driver for turn-off.

Technical information

I. Primary side

The driver input signals may be transmitted directly to the driver inputs by the controller. The input signal circuit was designed to accept a wide voltage range (see table 1). The typical voltage level is at HCMOS level of V_{DD}=5V (0V=Off, +5V=On).

However, also 15V-signals may be applied with the same turn-on/turn-off thresholds without additional requirements. In this case the input resistance will be different (see table 1).

Status	Level / V			Input Impedance	
	min	typ	max	Ch. 1-6	Ch7
ON 5V	4,0	5,0	5,5	60 kΩ	2,4 kΩ
ON 15V	4,0	15,0	15,6	7 kΩ	1,6 kΩ
OFF 0V	-0,7	0	1,5	60 kΩ	2,4kΩ

Table 1: Input voltage level and input impedances

Error input signal

The error input signal can gather error signals of other hardware components, such as temperature sensors, in a "wired-or"-connection for direct turn-off of the driver. In this case an external pull-up resistor must not be connected.

Note: It is not possible to connect the error output of the SKHI 61/71 to an error input of the SKHI 61/71. But the error output of the chopper driver (SKHI 71) can be connected directly to the error input.

Error output signals

i) 6pack - driver

The error signal of the 6-PACK driver is equipped with an active push-pull output buffer which switches towards zero Volt in case of an error and actively towards + 5 V under operating conditions. The error memory may only be reset, if no error is pending and all cycle signal inputs are set to LOW for t > 9 µs at the same time. If any other external signals are intended to be connected to the error signal _ERR, the _ERR-signal must be uncoupled (see Figure 2) .

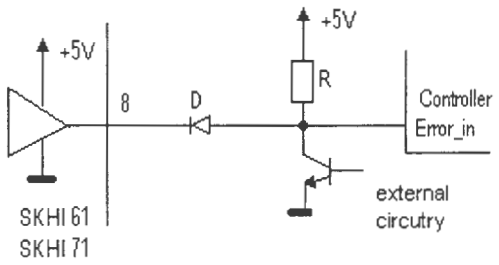

Fig. 2 _ERR-Signal in an „open-collector"-circuit

State _ERROR	Level / V		I / mA	Typical error memory set back time	
	min	max	max	6-PACK	seventh driver
Error	0	0.8	5	16µs	7µs
No error	4	5	5		

Table 2: Error output signal ratings

ii) chopper driver (only SKHI 71)

The error output signal of the additional driver has been designed as an open collector output. A pull-up resistor against the controller's +V_{CC} has to be connected to the controller input for error indication. In case of error, the signal is turned towards earth (zero Volt/ active LOW), otherwise the output will be highly resistive. The error signal of the additional switch will only be active as long as the input signal is on High-level. It is not logically connected to the other six input signals. The error signal of the additional switch may also be directly connected to the error input of the SIXPACK-driver, without requiring an external pull-up resistor. This may be advantageous, if the SIXPACK-driver has to be turned off in case of e.g. a brake chopper error or if only one error signal is evaluated by the controller.

Configuration pins

The configuration pins serve to adjust the TOP/BOTTOM interlocking time of all halfbridges. Due to the special pin design the interlocking time can be adjusted by a simple connection to the BSTD terminal (BSS potential) on the PCB without requiring external components.

Pin	4µs (factory set)	3 µs	2 µs	1 µs	no interlock)+
TDT1	open	open	GND	GND	X
TDT2	open	GND	open	GND	X
SEL	open	open	open	open	GND

Table 3: Values for interlocking time adjustment „X" = no effect

)+ TOP and BOTcan be switched simultaneously!

II. Secondary side

We have provided for five terminals per input. Two of them are required for driving the IGBT, one is for short-circuit protection. The remaining two have been designed for optional adjustment of the V_{CE}-threshold.

IGBT-driver signals

We have provided for one gate- and one emitter input pin per power switch, i.e. there is one gate resistor for turn-on and turn-off each. The earth connection of the driver is directly connected to the IGBT's emitter via the emitter input, whereas a resistor of at least 10 Ω has to be connected to the gate circuit. This resistance is the minimum limit value controlled by the driver output buffer in order to limit the pulse currents to their peak value.

A 20 kΩ-resistor has been interconnected between gate and emitter (for the case that the supply voltage breaks down).

Gate-Emitter-voltage	min	Typ	max	Unit
OFF (neg.)	-10	-6.5	-5	V
ON	14,4	14,9	15,4	V
Temperature drift	12	14	16	mV/K

Table 4: Gate-emitter-voltage at T_A = 25 °C

V_{CE} -threshold and V_{CE} -monitoring

V_{CE}-monitoring is done by connection of the driver collector pin to the collector of the power semiconductor.

If the turn-off threshold for short-circuit protection is to be reduced (standard 5,8 V), a resistor has to be connected between the V_{CET1}-threshold#1 pin 2 and V_{CET2}-threshold#2 pin 4 (see fig. 4; Value to be calculated by equation 1). Please do not forget to adapt the blanking time[1] accordingly.

This can be done by attaching a capacitor (value to be calculated by equation 2) between V_{CE}-threshold (pin 2) and earth (pin 3). The V_{CE}-threshold may be adjusted to a minimum value of about 3 V (R_{VCE} = 0 Ω).

Equation 1

$$R_{VCE}[k\Omega] = \frac{11,86}{5,4 - 0,93\ V_{CE}} - 4,75$$

1. Blanking time: time between turn-on of the power semiconductor and V_{CE}-registration

Equation 2

$$C_{VCE}[nF] = \frac{t_{blank}[\mu s] \cdot (72,75 + R_{VCE}[k\Omega])}{(R_{VCE}[k\Omega] + 4,75) \cdot 36,08} - 0,1$$

The V_{CE}-threshold cannot be increased, so that the preset value of 5,8 V is the maximum value.

V_{CE}-monitoring can also be suppressed by connecting the collector pin V_{CE} of one driver to the belonging emitter pin E and not to the collector of the power semiconductor.

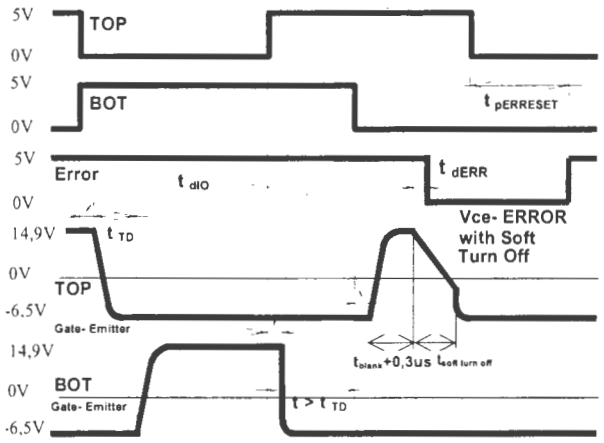

Fig. 3 Course diagram: TOP and BOT-inputs and signal Error compared to TOP and BOT-Gate-Emitter-signal (valid for all halfbridges).

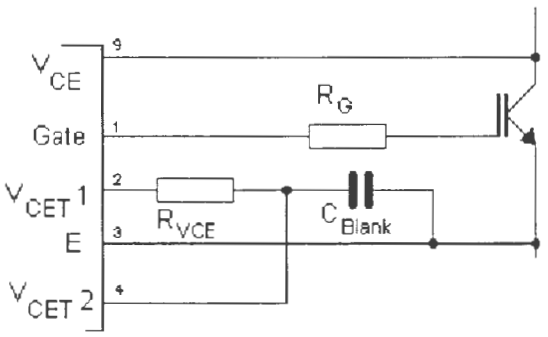

Fig. 4 Connection principle of a power switch with a specifically adjusted V_{CE}-threshold

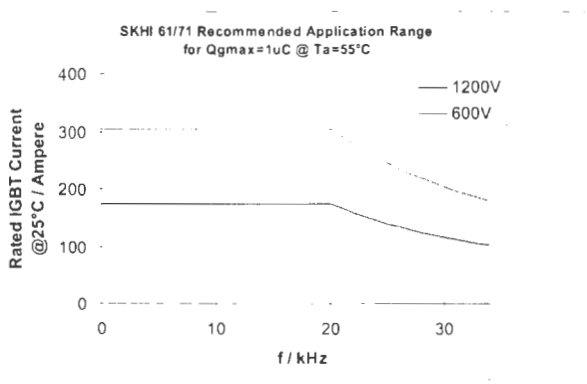

Fig. 5 Recommended application range

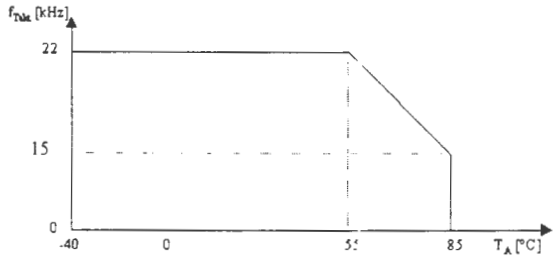

Fig. 6 Maximum cycling frequency at Q_{GE} = 1000 nC vs temperature

The application range can be calculated by the average output current of 20 mA and the repetetive acceptable peak current of 2 A. It has to be considered that the curves are valid for Q_{gmax} = 1 µC only.

operating the SKHI 61: besides the operating voltage only the six driver signals TOP1...BOT3 and the driver error output signal are connected to the controller on the primary side. The secondary side is working with the preset V_{CE}-threshold of 5,8 V.

Fig. 7 and 8 show examples for connection of a SKHI 71 for the application with MiniSKiiP (SKiiP 32 NAB 12) and the following adjustments:

- Temperature monitoring of the power semiconductor
- V_{CE}-threshold : 4,8 V
- Interlocking time : 2 µs
- Error blanking time for V_{CE}-threshold : 4 µs

Application Hints

To adjust different V_{CE} thresholds there is needed an additional resistor R_{VCE} and a capacitor C_{VCE} for each switch.

Gate resistor : $R_G = 33\ \Omega$

V_{CE}-threshold resistor: intended U_{VCE} = 4,8 V

Applying equation 1 R_{VCE} will result in

$$R_{VCE}[k\Omega] = \frac{11,86}{5,4 - 0,93 \cdot 4,8} - 4,75[k\Omega] = 7,9k\Omega$$

Next value taken from the E24-range: 8,25 k. The threshold voltage is recalculated with 8,25 kΩ.

V_{CE}-threshold at 4,82 V.

For the capacitor the blanking time may be calculated as: $t_{blanking}$ = 4 µs

$$C_{VCE}[nF] = \frac{4 \cdot (72,75 + 8,25)}{(8,25 + 4,75) \cdot 36,08} - 0,1 = 590pF$$

Thus there can be chosen a capacitor of 680 pF.

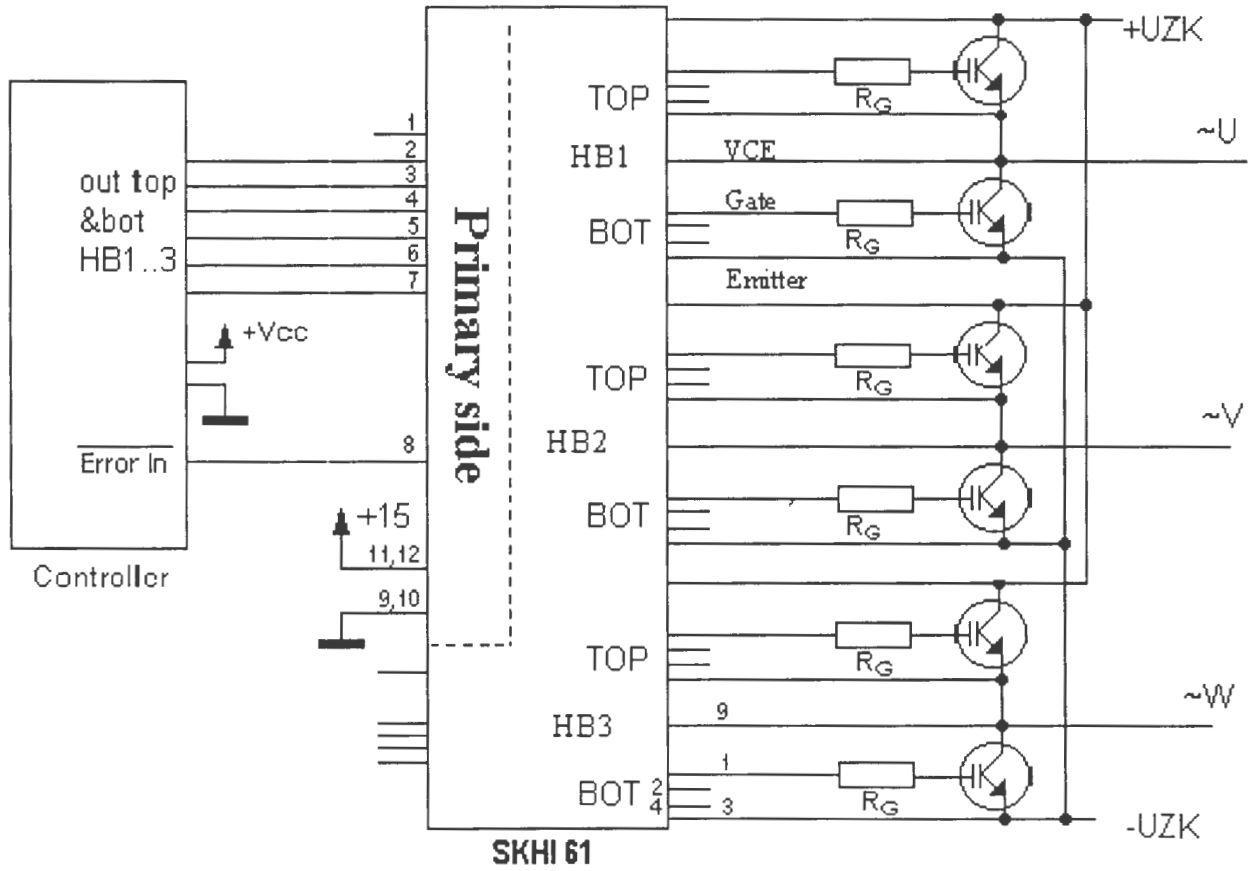

Fig. 7 SKHI 61 block diagram

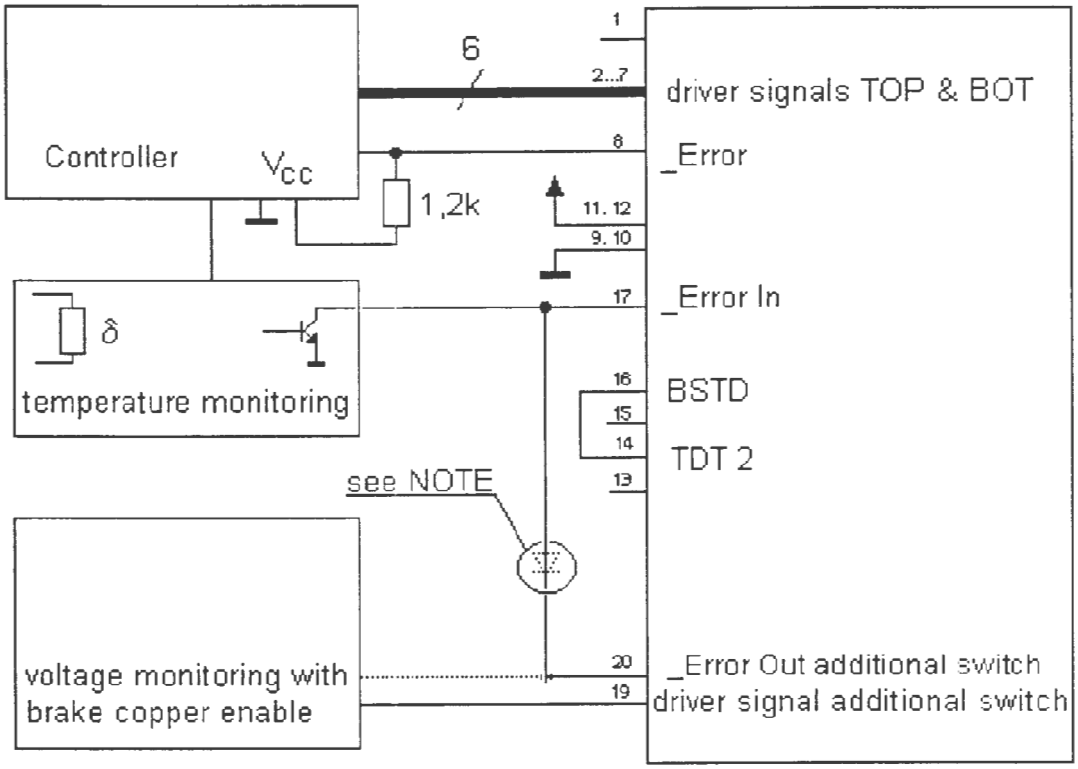

Fig. 8 Examply circuit for a SKHI 71 connected to the primary side

NOTE: If the _ErrorOut-signal of the additional switch (here brake chopper) is also needed for other evaluations, a Schottky diode has to be connected as shown in the figure above to uncouple the signal. Furthermore there has to be connected a pull-up resistor to the additional error output. It is useful to use a capacitor (typ. 100 pF, absolute maximum 2,2 nF) at the _ErrorIn to avoid undesired couplings.

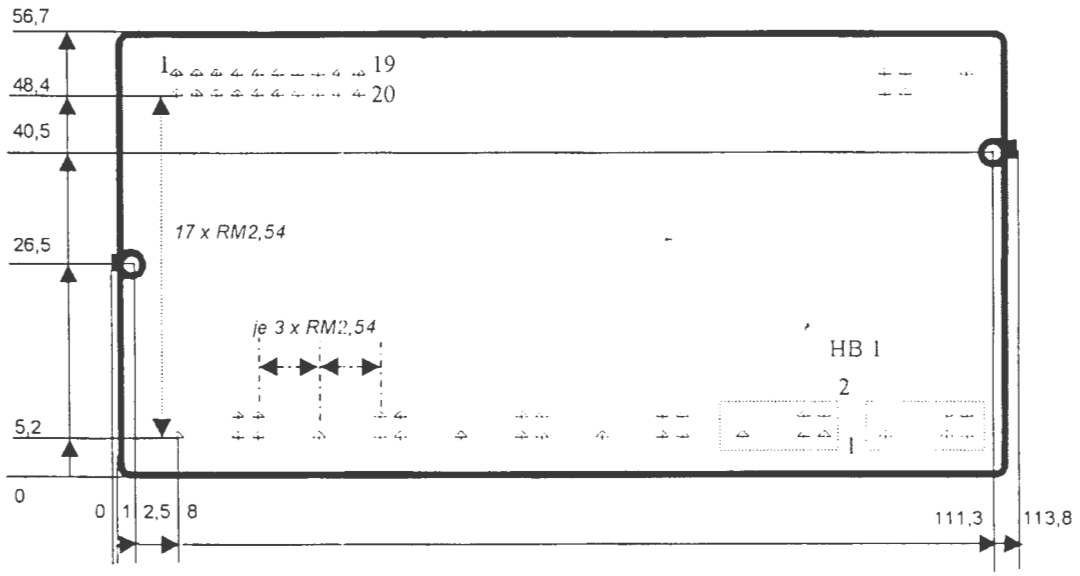

Fig. 9 Dimensional drawing, layout

View: tooling side (top view, driver put on top of the PCB)
Measurements taken in [mm]
Grid of connector pins; gaps between pins: RM2,54
Pin dimensions : 0,64 mm x 0,64 mm ; length 3,2 mm

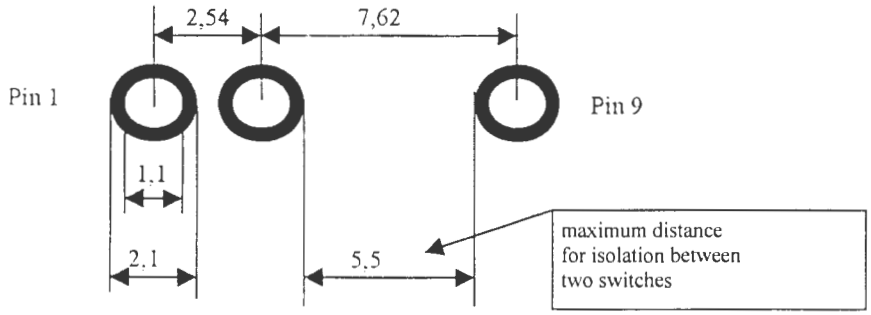

Fig. 10 Measurements in [mm] for solder pads (as a proposal for the design) and solder pad gaps (partial drawing)

APPENDIX D

LEM MODULES:

- **LV 25-P**
- **LA 25-NP**

Voltage Transducer LV 25-P

I_{PN} = 10 mA

V_{PN} = 10 .. 500 V

For the electronic measurement of voltages : DC, AC, pulsed..., with a galvanic isolation between the primary circuit (high voltage) and the secondary circuit (electronic circuit).

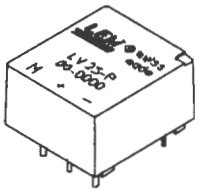

Electrical data

I_{PN}	Primary nominal r.m.s. current		10		mA
I_P	Primary current, measuring range		0 .. ± 14		mA
R_M	Measuring resistance		$R_{M\,min}$	$R_{M\,max}$	
	with ± 12 V	@ ± 10 mA_{max}	30	190	Ω
		@ ± 14 mA_{max}	30	100	Ω
	with ± 15 V	@ ± 10 mA_{max}	100	350	Ω
		@ ± 14 mA_{max}	100	190	Ω
I_{SN}	Secondary nominal r.m.s. current		25		mA
K_N	Conversion ratio		2500 : 1000		
V_C	Supply voltage (± 5 %)		± 12 .. 15		V
I_C	Current consumption		10 (@±15 V) + I_S		mA
V_d	R.m.s. voltage for AC isolation test[1], 50 Hz, 1 mn		2.5		kV

Accuracy - Dynamic performance data

X_G	Overall Accuracy @ I_{PN}, T_A = 25°C	@ ± 12 .. 15 V	±0.9		%
		@ ± 15 V (± 5 %)	±0.8		%
ε_L	Linearity		< 0.2		%
			Typ	Max	
I_O	Offset current @ I_P = 0, T_A = 25°C			±0.15	mA
I_{OT}	Thermal drift of I_O	0°C .. + 25°C	±0.06	±0.25	mA
		+ 25°C .. + 70°C	±0.10	±0.35	mA
t_r	Response time[2] @ 90 % of V_{PN}		40		µs

General data

T_A	Ambient operating temperature		0 .. + 70	°C
T_S	Ambient storage temperature		- 25 .. + 85	°C
R_P	Primary coil resistance @ T_A = 70°C		250	Ω
R_S	Secondary coil resistance @ T_A = 70°C		110	Ω
m	Mass		22	g
	Standards		EN 50178(97.10.01)	

Features

- Closed loop (compensated) voltage transducer using the Hall effect
- Insulated plastic case recognized according to UL 94-V0.

Principle of use

- For voltage measurements, a current proportional to the measured voltage must be passed through an external resistor R_1 which is selected by the user and installed in series with the primary circuit of the transducer.

Advantages

- Excellent accuracy
- Very good linearity
- Low thermal drift
- Low response time
- High bandwidth
- High immunity to external interference
- Low disturbance in common mode.

Applications

- AC variable speed drives and servo motor drives
- Static converters for DC motor drives
- Battery supplied applications
- Uninterruptible Power Supplies (UPS)
- Power supplies for welding applications.

Notes : [1] Between primary and secondary

[2] R_1 = 25 kΩ (L/R constant, produced by the resistance and inductance of the primary circuit).

981009/14

Dimensions LV 25-P (in mm. 1 mm = 0.0394 inch)

Bottom view

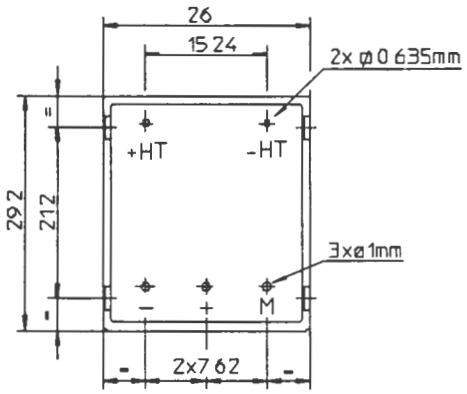

Right view

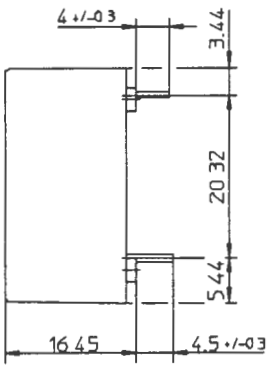

Top view

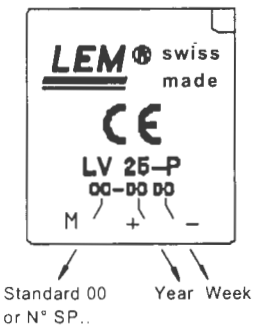

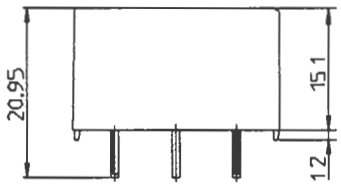

Secondary terminals

Terminal + : supply voltage + 12 .. 15 V
Terminal M : measure
Terminal - : supply voltage - 12 .. 15 V

Connection

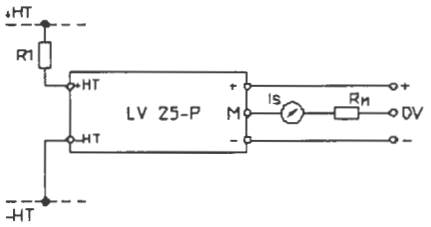

Back view

Mechanical characteristics

• General tolerance	± 0.2 mm
• Fastening & connection of primary	2 pins 0.635 x 0.635 mm
• Fastening & connection of secondary	3 pins ∅ 1 mm
• Recommended PCB hole	1.2 mm

Remarks

- I_S is positive when V_P is applied on terminal +HT.
- This is a standard model. For different versions (supply voltages, turns ratios, unidirectional measurements...), please contact us.

Instructions for use of the voltage transducer model LV 25-P

Primary resistor R_1 : the transducer's optimum accuracy is obtained at the nominal primary current. As far as possible, R_1 should be calculated so that the nominal voltage to be measured corresponds to a primary current of 10 mA.

Example: Voltage to be measured V_{PN} = 250 V

a) R_1 = 25 kΩ / 2.5 W, I_P = 10 mA Accuracy = ± 0.8 % of V_{PN} (@ T_A = +25°C)
b) R_1 = 50 kΩ / 1.25 W, I_P = 5 mA Accuracy = ± 1.6 % of V_{PN} (@ T_A = +25°C)

Operating range (recommended) : taking into account the resistance of the primary windings (which must remain low compared to R_1 in order to keep thermal deviation as low as possible) and the isolation, this transducer is suitable for measuring nominal voltages from 10 to 500 V.

Current Transducer LA 25-NP

I_{PN} = 5-6-8-12-25 A

For the electronic measurement of currents : DC, AC, pulsed, mixed, with a galvanic isolation between the primary circuit (high power) and the secondary circuit (electronic circuit).

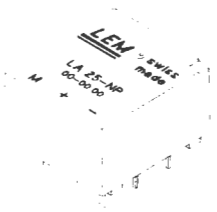

Electrical data

I_{PN}	Primary nominal r.m.s. current		25		At
I_P	Primary current, measuring range		0 .. ± 36		At
R_M	Measuring resistance		$R_{M\,min}$	$R_{M\,max}$	
	with ± 15 V	@ ± 25 At_{max}	100	320	Ω
		@ ± 36 At_{max}	100	190	Ω
I_{SN}	Secondary nominal r.m.s. current		25		mA
K_N	Conversion ratio		1-2-3-4-5 : 1000		
V_C	Supply voltage (± 5 %)		± 15		V
I_C	Current consumption		10 + I_S		mA
V_d	R.m.s. voltage for AC isolation test, 50 Hz, 1 mn		2.5		kV
V_b	R.m.s. rated voltage [1],	safe separation	600		V
		basic isolation	1700		V

Accuracy - Dynamic performance data

X	Accuracy @ I_{PN}, T_A = 25°C		± 0.5		%
ε_L	Linearity		< 0.2		%
			Typ	Max	
I_O	Offset current [2] @ I_P = 0, T_A = 25°C		± 0.05	± 0.15	mA
I_{OM}	Residual current [3] @ I_P = 0, after an overload of 3 x I_{PN}		± 0.05	± 0.15	mA
I_{OT}	Thermal drift of I_O	0°C .. + 25°C	± 0.06	± 0.25	mA
		+ 25°C .. + 70°C	± 0.10	± 0.35	mA
t_r	Response time [4] @ 90 % of $I_{P\,max}$		< 1		µs
di/dt	di/dt accurately followed		> 50		A/µs
f	Frequency bandwidth (- 1 dB)		DC .. 150		kHz

General data

T_A	Ambient operating temperature		0 .. + 70	°C
T_S	Ambient storage temperature		- 25 .. + 85	°C
R_P	Primary resistance per turn @ T_A = 25°C		< 1.25	mΩ
R_S	Secondary coil resistance @ T_A = 70°C		110	Ω
R_{IS}	Isolation resistance @ 500 V, T_A = 25°C		> 1500	MΩ
m	Mass		22	g
	Standards [5]		EN 50178	

Notes : [1] Pollution class 2
[2] Measurement carried out after 15 mn functionning
[3] The result of the coercive field of the magnetic circuit
[4] With a di/dt of 100 A/µs
[5] A list of corresponding tests is available

Features

- Closed loop (compensated) multi-range current transducer using the Hall effect
- Insulated plastic case recognized according to UL 94-V0.

Advantages

- Excellent accuracy
- Very good linearity
- Low temperature drift
- Optimized response time
- Wide frequency bandwidth
- No insertion losses
- High immunity to external interference
- Current overload capability.

Applications

- AC variable speed drives and servo motor drives
- Static converters for DC motor drives
- Battery supplied applications
- Uninterruptible Power Supplies (UPS)
- Switched Mode Power Supplies (SMPS)
- Power supplies for welding applications.

980909/8

Dimensions LA 25-NP (in mm. 1 mm = 0.0394 inch)

Bottom view

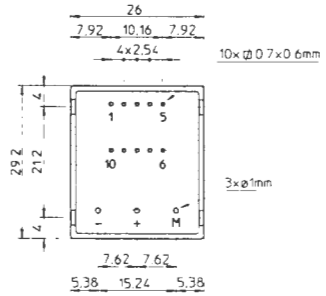

Right view

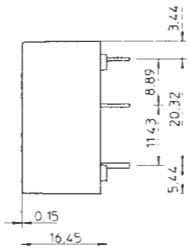

Top view

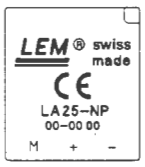

Standard 00 Year Week
or N° SP..

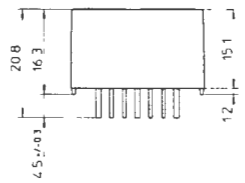

Secondary terminals

Terminal + : supply voltage + 15 V
Terminal M: measure
Terminal - : supply voltage - 15 V

Connection

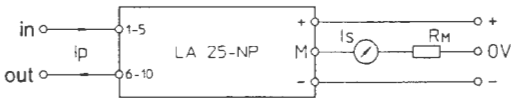

Number of primary turns	Primary current nominal I_{PN} [A]	Primary current maximum I_P [A]	Nominal output current I_{SN} [mA]	Turns ratio K_N	Primary resistance R_P [mΩ]	Primary insertion inductance L_P [µH]	Recommended connections
1	25	36	25	1/1000	0.3	0.023	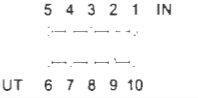
2	12	18	24	2/1000	1.1	0.09	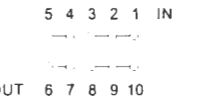
3	8	12	24	3/1000	2.5	0.21	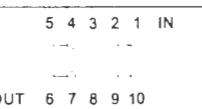
4	6	9	24	4/1000	4.4	0.37	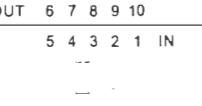
5	5	7	25	5/1000	6.3	0.58	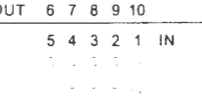

Mechanical characteristics

• General tolerance	± 0.2 mm
• Fastening & connection of primary	10 pins 0.7 x 0.6 mm
• Fastening & connection of secondary	3 pins ∅ 1 mm
• Recommended PCB hole	1.2 mm

Remarks

- I_S is positive when I_P flows from terminals 1, 2, 3, 4, 5 to terminals 10, 9, 8, 7, 6
- This is a standard model. For different versions (supply voltages, turns ratios, unidirectional measurements...), please contact us.

APPENDIX E

INCREMENTAL SHAFT ENCODER – RS 58-0/1000

Installation instructions

Incremental Shaft Encoder Type RI 58 / RI 59

HENGSTLER
Hengstler GmbH
Postfach 11 51 Tel. 07424 - 890
D-78550 Aldingen Fax 07424 - 89370

Item No. **2 522 480**, Edition: 3290699hu

Introduction

These installation instructions are provided for the connection and starting procedure of your shaft encoder.
For further informations see our Shaft Encoders Catalogue.

Safety and Operating Instructions

- The incremental shaft encoders of the type RI 58 / RI 59 model series are quality products manufactured in accordance with established electrical engineering standards.
  The units have been delivered from the factory in perfect conformance to safety regulations.
  To maintain this condition and to ensure trouble-free operation, please observe the technical specifications of this document.
- **Installation and mounting may only be performed by an electrotechnical expert!**
- The units may only be operated within the limits specified by the technical data.
- **Maximum operating voltages must not be exceeded!**
  The units are designed complying with VDE 0160, protection class III.
  To prevent dangerous structure-borne currents, the equipment has to be run on safety extra-low voltage (SELV) and must be in an area of equipotential bonding.
- Application: Industrial processes and control systems.
  Overvoltage at the connecting terminals must be limited to the values within overvoltage category II.
- Please avoid shocks to the housing – especially to the encoder shaft – and axial or radial overload to the encoder shaft
- Maximum accuracy and durability of our shaft encoders is only granted when using suitable couplings.
- The high-quality EMC-specifications are only valid together with standard-type cables and plugs. When using screened cables, the screen must broadly be connected with ground on both ends. Likewise, the voltage-supply cables should entirely be screened. If this is not possible you will have to take appropriate filtering measures.
- Installation environment and wiring are influential on the encoder's EMC: Thus the installer must secure EMC of the whole facility (device).
- Transient peaks on the power supply leads are to be limited by the pre-connected power unit to a maximum of 1000 V.
- In electrostaticly threatened areas please take care for neat ESD-protection of plug and connecting cable during installation work.

Mechanical data

Shaft diameter	6 / 6.35 / 7 / 9.52 / 10 / 12 mm	
Absolute max. shaft load	Ø 12 mm	radial 180 N (39 lbs)
		axial 140 N (30 lbs)
	Ø 7 ... 10 mm	radial 160 N (35 lbs)
		axial 107 N (24 lbs)
	Ø 6 mm / 6.35 mm	radial 110 N (24 lbs)
		axial 60 N (13 lbs)
Maximum speed	10,000 RPM	
Torque	≤ 0.5 Ncm (IP 64)	
Moment of inertia	synchro flange 14 gcm² approx.	
	clamping flange 20 gcm² approx.	
Protection class housing/ball bearing	IP 50/40, IP 65/64[1], IP 67/67	
Operating temperature	RI 58-O: -10 ... +70 °C / RI 58-T: -25 ... +100 °C	
Storing temperature	RI 58-O: -25 ... +85 °C / RI 58-T: -25 ... +100 °C	
Vibration performance (IEC 68-2-6)	100 m/s² (10 ... 2,000 Hz)	
Shock resistance (IEC 68-2-27)	1,000 m/s² (6 ms)	
Connection	1.5 m cable or flange box	
Housing	RI 58: aluminium, RI 59: high-grade steel	
Flange[2]	S = synchro flange, K, L = clamping flange,	
	G, Q = square flange, M = synchro clamping flange	
Weight	360 g approx.	
Bearing life	1 x 10^{10} revolutions (typ.) at 35% of full rated shaft load	
	1 x 10^{9} revolutions (typ.) at 75% of full rated shaft load	
	1 x 10^{8} revolutions (typ.) at 100% of full rated shaft load	

[1] no standing water allowed at the shaft entrance or at the ball bearing

[2] S, L: use threads M4 for fastening
K: use threads M3 for fastening
M: use threads 10-32 UNF for fastening

Electrical data

General design		as per DIN VDE 0160, protection class III, contamination level 2, overvoltage class II					
Screening		connected to housing					
Noise emission		as per EN 50081-2 (edition 1993)					
Noise immunity		as per EN 50082-2 (edition 1995)					
Power consumption		40 mA (5 V DC), 30 mA (24 V DC), 60 mA (10 V DC)					
Supply voltage U_B		5 V DC (SELV) ±10%			10 ... 30 V DC (SELV)		
Output circuit[1]		PP	PP	RS422	PP	PP compl.	RS422
Code letter		K	D	R, T	K	I	R
Output load [mA]		±10	±30	±30	±30	±30	±30
Output level [V]	High	≥2.5	≥2.5	≥2.5	U_B-3	U_B-3	≥2.5
	Low	≤0.5	≤0.5	≤0.5	≤2	≤2	≤0.5
Pulse rise time [ns]		250	100	100	2000	2000	100
Max. pulse frequency [kHz]		300	300	300	200	200	300
Pole protection of U_B		yes	no	no	yes	yes	yes
Short circuit proof		yes	1 chn.	1 channel	yes	yes	yes
Pulse duty factor		1 : 1					
Pulse width error		± 25° electrical					
Phase shift		90° (distance from Channel A to B is at least 0.45 µs, at 300 kHz)					
Pulse shape		rectangular					
Alarm output		Open Collector, NPN (5 mA, 24 V max. with U_B=5 VDC; 5 mA, 32 V max. with U_B=10...30 VDC)					

[1] PP=Push-pull; PP compl.=Push-pull complementary; RS422=Line driver

Incremental Shaft Encoder Type RI 58 / RI 59

Connection diagram

Colour (TPE)	Colour (PVC)	Output RS 422 + Sense (T)	RS 422 + Alarm (R)	Push-pull (K, D)	Push-pull complementary (I)
brown	white	Channel A	Channel A	Channel A	Channel A
green	white/brown	Channel $\bar{A}$	Channel $\bar{A}$		Channel $\bar{A}$
grey	green	Channel B	Channel B	Channel B	Channel B
pink	green/brown	Channel $\bar{B}$	Channel $\bar{B}$		Channel $\bar{B}$
red	yellow	Channel N	Channel N	Channel N	Channel N
black	yellow/brown	Channel $\bar{N}$	Channel $\bar{N}$		Channel $\bar{N}$
violet (white)[2]	yellow/black	Sense GND	$\overline{Alarm}$	$\overline{Alarm}$	$\overline{Alarm}$
blue	yellow/red	Sense V_{cc}	Sense V_{cc}		Sense V_{cc}
brown/green	red	5 V DC	5/10...30 V DC	5/10...30 V DC	10...30 V DC
white/green	black	GND	GND	GND	GND
Screen[1]	Screen[1]	Screen[1]	Screen[1]	Screen[1]	Screen[1]

[1] connected to encoder housing
[2] white for Sense (T)

Pinout of connector

CONIN 12 poles

Pin	RS 422 + Sense (T)	RS 422 + Alarm (R)	Push-pull (K, D)	Push-pull complementary (I)
1	Channel $\bar{B}$	Channel $\bar{B}$	N.C.	Channel $\bar{B}$
2	Sense V_{cc}	Sense V_{cc}	N.C.	Sense V_{cc}
3	Channel N	Channel N	Channel N	Channel N
4	Channel $\bar{N}$	Channel $\bar{N}$	N.C.	Channel $\bar{N}$
5	Channel A	Channel A	Channel A	Channel A
6	Channel $\bar{A}$	Channel $\bar{A}$	N.C	Channel $\bar{A}$
7	N.C.	$\overline{Alarm}$	$\overline{Alarm}$	$\overline{Alarm}$
8	Channel B	Channel B	Channel B	Channel B
9	N.C.*	N.C.*	N.C.*	N.C.*
10	GND	GND	GND	GND
11	Sense GND	N.C.	N.C	N.C.
12	5 V DC	5/10...30 V DC	5/10...30 V DC	10...30 V DC

* Screen for cable with CONIN-plug

BINDER 6 poles

Pin	Push-pull (K, D)
1	5/10...30 V DC
2	Channel A
3	Channel N
4	Channel B
5	$\overline{Alarm}$
6	GND

KPT 12-8 P

Pin	RS 422 (R), Push-pull complementary (I)
1/A	Channel B
2/B	Channel $\bar{B}$
3/C	Channel $\bar{A}$
4/D	Channel A
5/E	5/10...30 V DC
6/F	GND
7/G	Channel N
8/H	Channel $\bar{N}$

N.C. = Not Connected

(Pinout of connector)

MIL 6 poles

Pin	Push-pull (K, D)
1/A	5/10...30 V DC
2/B	Channel A
3/C	Channel B
4/D	Channel N
5/E	GND
6/F	Screen

MIL 7 poles

Pin	Push-pull (K, D)
1/A	Channel A
2/B	Channel B
3/C	Channel N
4/D	5/10...30 V DC
5/E	$\overline{Alarm}$
6/F	GND
7/G	Screen

MIL 10 poles

Pin	RS 422 (R), Push-pull compl. (I)	RS 422 (R) – US-pinout	Push-pull (K. D)
1/A	Channel A	Channel A	Channel A
2/B	Channel B	Channel B	Channel B
3/C	Channel N	Channel N	Channel N
4/D	5/10...30 V DC	5/10...30 V DC	5/10...30 V DC
5/E	$\overline{Alarm}$	$\overline{Alarm}$	$\overline{Alarm}$
6/F	GND	GND	GND
7/G	Channel $\bar{A}$	Screen	Screen
8/H	Channel $\bar{B}$	Channel $\bar{A}$	N.C.
9/I	Channel $\bar{N}$	Channel $\bar{B}$	N.C.
10/J	Screen	Channel $\bar{N}$	Screen

Ordering code (see identification plate)

Supply voltage
A 5 V DC
E 10 ... 30 V DC

Type of flange
A Synchro flange adapter
C Square flange adapter;58 x 58
G Square flange adapter; 80 x 80
K Clamping flange (M3 fastening thread)
L Clamping flange (M4 fastening thread)
M Synchro clamping flange; Ø 63,5
Q Square flange; 63,5 x 63,5
S Synchro flange

Shaft diameter
1 6 mm (S)
2 10 mm (K, Q)
3 7 mm (K, G)
5 6,35 mm (S)
6 9,52 mm (K, Q, M)
7 12 mm (K)

RI 58 / RI 59 – [ ] / [ ] [ ] [ ] · [ ] [ ] [ ] [ ] [3]

Number of pulses
1 ... 10,000

Protection class
1 IP 50
4 IP 64
7 IP 67

Output
T RS 422 (TTL) + Sense
K Push-pull short circuit proof
I Push-pull complementary
R RS 422 + Alarm
D Push-pull 5 V, 30 mA

Type designation
58 Standard
59 High-grade Steel

Type of connection
A Cable PVC, axial
B Cable PVC, radial
C CONIN connector, axial clockwise
D CONIN connector, radial clockwise
E Cable TPE, axial
F Cable TPE, radial
G CONIN connector, axial counterclockwise
H CONIN connector, radial counterclockwise
J BINDER, 6 poles, radial
N BINDER, 6 poles, axial
O MIL MS, 10 poles, axial[1]
K MIL MS, 10 poles, radial[1]
P MIL MS, 7 poles, axial
L MIL MS, 7 poles, radial
M MIL MS, 6 poles, axial
Q MIL MS, 6 poles, radial
R MIL MS, 10 poles, axial[2]
T MIL MS, 10 poles, radial[2]
1 KPT 12-8P, axial
2 KPT 12-8P, radial

[1] Euro pinout
[2] US pinout
[3] Special types are additionally marked by an ordering code -S.
In this case customer specifications are to be applied.
If you don't know these please call us for the specifications, indicating the encoder ordering code.

Item No. 2 522 480, 3290699hu

APPENDIX F

QUAD DIFFERENTIAL LINE DRIVER– DS 26LS31C

National Semiconductor

June 1998

DS26LS31C/DS26LS31M
Quad High Speed Differential Line Driver

General Description

The DS26LS31 is a quad differential line driver designed for digital data transmission over balanced lines. The DS26LS31 meets all the requirements of EIA Standard RS-422 and Federal Standard 1020. It is designed to provide unipolar differential drive to twisted-pair or parallel-wire transmission lines.

The circuit provides an enable and disable function common to all four drivers. The DS26LS31 features TRI-STATE® outputs and logically ANDed complementary outputs. The inputs are all LS compatible and are all one unit load.

Features

- Output skew—2.0 ns typical
- Input to output delay—10 ns typical
- Operation from single 5V supply
- Outputs won't load line when V_{CC} = 0V
- Four line drivers in one package for maximum package density
- Output short-circuit protection
- Complementary outputs
- Meets the requirements of EIA Standard RS-422
- Pin compatible with AM26LS31
- Available in military and commercial temperature range

Logic and Connection Diagrams

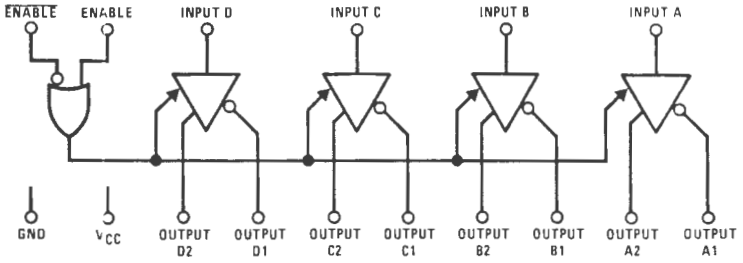

Dual-In-Line Package

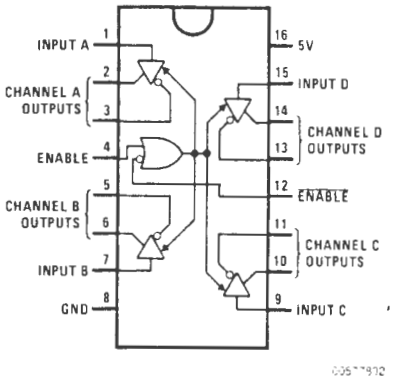

Top View

Order Number DS26LS31CM, or DS26LS31CN
See NS Package M16A or N16E
For Complete Military Product Specifications, refer to the appropriate SMD or MDS.
Order Number DS26LS31MJ/883, DS26LS31ME/883 or DS26LS31MW/883
See NS Package E20A, J16A or W16A

TRI-STATE® is a registered trademark of National Semiconductor Corporation

Absolute Maximum Ratings (Note 2)

If Military/Aerospace specified devices are required, please contact the National Semiconductor Sales Office/ Distributors for availability and specifications.

Supply Voltage	7V
Input Voltage	7V
Output Voltage	5.5V
Output Voltage (Power OFF)	−0.25 to 6V
Maximum Power Dissipation (Note 1) at 25°C	
Cavity Package	1509 mW
Molded DIP Package	1476 mW
SO Package	1051 mW

Operating Conditions

	Min	Max	Units
Supply Voltage, V_{CC}			
DS26LS31M	4.5	5.5	V
DS26LS31	4.75	5.25	V
Temperature, T_A			
DS26LS31M	−55	+125	°C
DS26LS31	0	+70	°C

Note 1: Derate cavity package 10.1 mW/°C above 25°C; derate molded DIP package 11.9 mW/°C above 25°C; derate SO package 8.41 mW/°C above 25°C.

Electrical Characteristics (Notes 3, 4, 5)

Symbol	Parameter	Conditions	Min	Typ	Max	Units
V_{OH}	Output High Voltage	I_{OH} = −20 mA	2.5			V
V_{OL}	Output Low Voltage	I_{OL} = 20 mA			0.5	V
V_{IH}	Input High Voltage		2.0			V
V_{IL}	Input Low Voltage				0.8	V
I_{IL}	Input Low Current	V_{IN} = 0.4V		−40	−200	μA
I_{IH}	Input High Current	V_{IN} = 2.7V			20	μA
I_I	Input Reverse Current	V_{IN} = 7V			0.1	mA
I_O	TRI-STATE Output Current	V_O = 2.5V			20	μA
		V_O = 0.5V			−20	μA
V_{CL}	Input Clamp Voltage	I_{IN} = −18 mA			−1.5	V
I_{SC}	Output Short-Circuit Current		−30		−150	mA
I_{CC}	Power Supply Current	All Outputs Disabled or Active		35	60	mA

Switching Characteristics

V_{CC} = 5V, T_A = 25°C

Symbol	Parameter	Conditions	Min	Typ	Max	Units
t_{PLH}	Input to Output	C_L = 30 pF		10	15	ns
t_{PHL}	Input to Output	C_L = 30 pF		10	15	ns
Skew	Output to Output	C_L = 30 pF		2.0	6.0	ns
t_{LZ}	Enable to Output	C_L = 10 pF, S2 Open		15	35	ns
t_{HZ}	Enable to Output	C_L = 10 pF, S1 Open		15	25	ns
t_{ZL}	Enable to Output	C_L = 30 pF, S2 Open		20	30	ns
t_{ZH}	Enable to Output	C_L = 30 pF, S1 Open		20	30	ns

Note 2: "Absolute Maximum Ratings" are those values beyond which the safety of the device cannot be guaranteed. They are not meant to imply that the devices should be operated at these limits. The tables of "Electrical Characteristics" provide conditions for actual device operation.

Note 3: Unless otherwise specified min/max limits apply across the −55°C to +125°C temperature range for the DS726LS31M and across the 0°C to +70°C range for the DS26LS31. All typicals are given for V_{CC} = 5V and T_A = 25°C.

Note 4: All currents into device pins are positive; all currents out of device pins are negative. All voltages are referenced to ground unless otherwise specified.

Note 5: Only one output at a time should be shorted.

APPENDIX G

OPAMP – LM324

National Semiconductor

August 2000

LM124/LM224/LM324/LM2902
Low Power Quad Operational Amplifiers

General Description

The LM124 series consists of four independent, high gain, internally frequency compensated operational amplifiers which were designed specifically to operate from a single power supply over a wide range of voltages. Operation from split power supplies is also possible and the low power supply current drain is independent of the magnitude of the power supply voltage.

Application areas include transducer amplifiers, DC gain blocks and all the conventional op amp circuits which now can be more easily implemented in single power supply systems. For example, the LM124 series can be directly operated off of the standard +5V power supply voltage which is used in digital systems and will easily provide the required interface electronics without requiring the additional ±15V power supplies.

Unique Characteristics

- In the linear mode the input common-mode voltage range includes ground and the output voltage can also swing to ground, even though operated from only a single power supply voltage
- The unity gain cross frequency is temperature compensated
- The input bias current is also temperature compensated

Advantages

- Eliminates need for dual supplies
- Four internally compensated op amps in a single package
- Allows directly sensing near GND and V_{OUT} also goes to GND
- Compatible with all forms of logic
- Power drain suitable for battery operation

Features

- Internally frequency compensated for unity gain
- Large DC voltage gain 100 dB
- Wide bandwidth (unity gain) 1 MHz (temperature compensated)
- Wide power supply range:
  Single supply 3V to 32V
  or dual supplies ±1.5V to ±16V
- Very low supply current drain (700 µA)—essentially independent of supply voltage
- Low input biasing current 45 nA (temperature compensated)
- Low input offset voltage 2 mV and offset current: 5 nA
- Input common-mode voltage range includes ground
- Differential input voltage range equal to the power supply voltage
- Large output voltage swing 0V to V^+ − 1.5V

Connection Diagram

Dual-In-Line Package

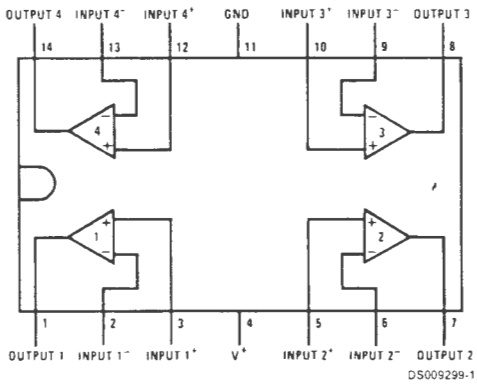

Top View

Order Number LM124J, LM124AJ, LM124J/883 (Note 2), **LM124AJ/883** (Note 1), **LM224J, LM224AJ, LM324J, LM324M, LM324MX, LM324AM, LM324AMX, LM2902M, LM2902MX, LM324N, LM324AN, LM324MT, LM324MTX or LM2902N LM124AJRQML and LM124AJRQMLV**(Note 3)
See NS Package Number J14A, M14A or N14A

Note 1: LM124A available per JM38510/ 1006

Note 2: LM124 available per JM38510/11005

Connection Diagram (Continued)

Note 3: See STD Mil DWG 5962R39504 for Radiation Tolerant Device

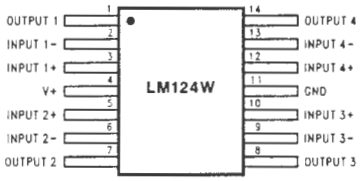

DS009299-33

Order Number LM124AW/883, LM124AWG/883, LM124W/883 or LM124WG/883
LM124AWRQML and LM124AWRQMLV(Note 3)
See NS Package Number W14B
LM124AWGRQML and LM124AWGRQMLV(Note 3)
See NS Package Number WG14A

Schematic Diagram (Each Amplifier)

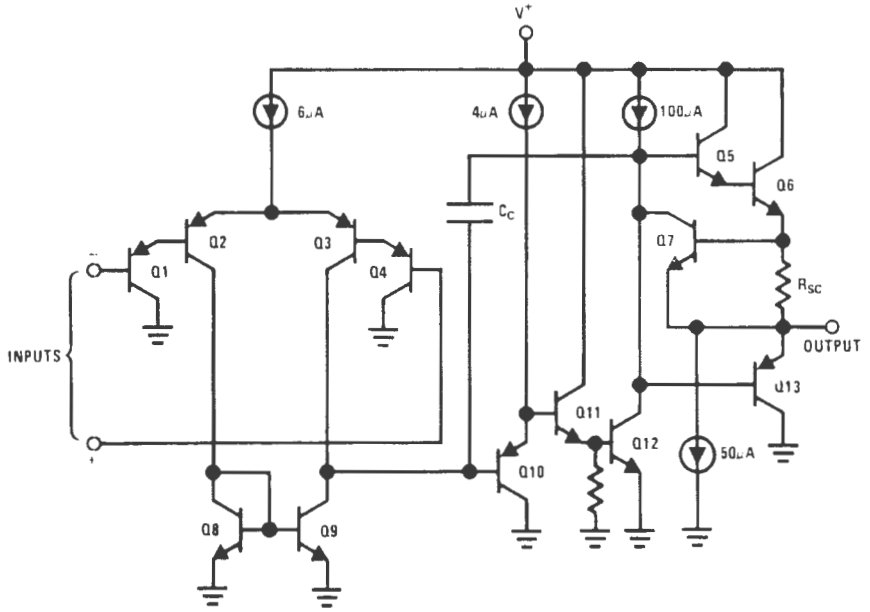

DS009299-2

Electrical Characteristics (Continued)

V^+ = +5.0V, (Note 7), unless otherwise stated

Parameter		Conditions		LM124A			LM224A			LM324A			Units
				Min	Typ	Max	Min	Typ	Max	Min	Typ	Max	
Power Supply Rejection Ratio		V^+ = 5V to 30V (LM2902, V^+ = 5V to 26V), T_A = 25°C		65	100		65	100		65	100		dB
Amplifier-to-Amplifier Coupling (Note 11)		f = 1 kHz to 20 kHz, T_A = 25°C (Input Referred)			−120			−120			−120		dB
Output Current	Source	V_{IN}^+ = 1V, V_{IN}^- = 0V, V^+ = 15V, V_O = 2V, T_A = 25°C		20	40		20	40		20	40		mA
	Sink	V_{IN}^- = 1V, V_{IN}^+ = 0V, V^+ = 15V, V_O = 2V, T_A = 25°C		10	20		10	20		10	20		
		V_{IN}^- = 1V, V_{IN}^+ = 0V, V^+ = 15V, V_O = 200 mV, T_A = 25°C		12	50		12	50		12	50		µA
Short Circuit to Ground		(Note 5) V^+ = 15V, T_A = 25°C			40	60		40	60		40	60	mA
Input Offset Voltage		(Note 8)				4			4			5	mV
V_{OS} Drift		R_S = 0Ω			7	20		7	20		7	30	µV/°C
Input Offset Current		$I_{IN(+)} - I_{IN(-)}$, V_{CM} = 0V				30			30			75	nA
I_{OS} Drift		R_S = 0Ω			10	200		10	200		10	300	pA/°C
Input Bias Current		$I_{IN(+)}$ or $I_{IN(-)}$			40	100		40	100		40	200	nA
Input Common-Mode Voltage Range (Note 10)		V^+ = +30V (LM2902, V^+ = 26V)		0		V^+−2	0		V^+−2	0		V^+−2	V
Large Signal Voltage Gain		V^+ = +15V (V_O Swing = 1V to 11V) $R_L \geq 2$ kΩ		25			25			15			V/mV
Output Voltage Swing	V_{OH}	V^+ = 30V (LM2902, V^+ = 26V)	R_L = 2 kΩ	26			26			26			V
			R_L = 10 kΩ	27	28		27	28		27	28		
	V_{OL}	V^+ = 5V, R_L = 10 kΩ			5	20		5	20		5	20	mV
Output Current	Source	V_O = 2V	V_{IN}^+ = +1V, V_{IN}^- = 0V, V^+ = 15V	10	20		10	20		10	20		mA
	Sink		V_{IN}^- = +1V, V_{IN}^+ = 0V, V^+ = 15V	10	15		5	8		5	8		

Electrical Characteristics

V^+ = +5.0V, (Note 7), unless otherwise stated

Parameter	Conditions	LM124/LM224			LM324			LM2902			Units
		Min	Typ	Max	Min	Typ	Max	Min	Typ	Max	
Input Offset Voltage	(Note 8) T_A = 25°C		2	5		2	7		2	7	mV
Input Bias Current (Note 9)	$I_{IN(+)}$ or $I_{IN(-)}$, V_{CM} = 0V, T_A = 25°C		45	150		45	250		45	250	nA
Input Offset Current	$I_{IN(+)}$ or $I_{IN(-)}$, V_{CM} = 0V, T_A = 25°C		3	30		5	50		5	50	nA
Input Common-Mode Voltage Range (Note 10)	V^+ = 30V, (LM2902, V^+ = 26V), T_A = 25°C	0		V^+−1.5	0		V^+−1.5	0		V^+−1.5	V
Supply Current	Over Full Temperature Range $R_L = \infty$ On All Op Amps										mA
	V^+ = 30V (LM2902 V^+ = 26V)		1.5	3		1.5	3		1.5	3	
	V^+ = 5V		0.7	1.2		0.7	1.2		0.7	1.2	
Large Signal Voltage Gain	V^+ = 15V, $R_L \geq 2$kΩ, (V_O = 1V to 11V), T_A = 25°C	50	100		25	100		25	100		V/mV
Common-Mode Rejection Ratio	DC, V_{CM} = 0V to V^+ − 1.5V, T_A = 25°C	70	85		65	85		50	70		dB
Power Supply Rejection Ratio	V^+ = 5V to 30V (LM2902, V^+ = 5V to 26V),	65	100		65	100		50	100		dB

Electrical Characteristics (Continued)

V^+ = +5.0V, (Note 7), unless otherwise stated

Parameter		Conditions		LM124/LM224			LM324			LM2902			Units
				Min	Typ	Max	Min	Typ	Max	Min	Typ	Max	
		T_A = 25°C											
Amplifier-to-Amplifier Coupling (Note 11)		f = 1 kHz to 20 kHz, T_A = 25°C (Input Referred)			−120			−120			−120		dB
Output Current	Source	V_{IN}^+ = 1V, V_{IN}^- = 0V, V^+ = 15V, V_O = 2V, T_A = 25°C		20	40		20	40		20	40		mA
	Sink	V_{IN}^- = 1V, V_{IN}^+ = 0V, V^+ = 15V, V_O = 2V, T_A = 25°C		10	20		10	20		10	20		mA
		V_{IN}^- = 1V, V_{IN}^+ = 0V, V^+ = 15V, V_O = 200 mV, T_A = 25°C		12	50		12	50		12	50		µA
Short Circuit to Ground		(Note 5) V^+ = 15V, T_A = 25°C			40	60		40	60		40	60	mA
Input Offset Voltage		(Note 8)				7			9			10	mV
V_{OS} Drift		R_S = 0Ω			7			7			7		µV/°C
Input Offset Current		$I_{IN(+)} - I_{IN(-)}$, V_{CM} = 0V				100			150		45	200	nA
I_{OS} Drift		R_S = 0Ω			10			10			10		pA/°C
Input Bias Current		$I_{IN(+)}$ or $I_{IN(-)}$			40	300		40	500		40	500	nA
Input Common-Mode Voltage Range (Note 10)		V^+ = +30V (LM2902, V^+ = 26V)		0		V^+−2	0		V^+−2	0		V^+−2	V
Large Signal Voltage Gain		V^+ = +15V (V_O Swing = 1V to 11V), $R_L \geq 2$ kΩ		25			15			15			V/mV
Output Voltage Swing	V_{OH}	V^+ = 30V (LM2902, V^+ = 26V)	R_L = 2 kΩ	26			26			22			V
			R_L = 10 kΩ	27	28		27	28		23	24		
	V_{OL}	V^+ = 5V, R_L = 10 kΩ			5	20		5	20		5	100	mV
Output Current	Source	V_O = 2V	V_{IN}^+ = +1V, V_{IN}^- = 0V, V^+ = 15V	10	20		10	20		10	20		mA
	Sink		V_{IN}^- = +1V, V_{IN}^+ = 0V, V^+ = 15V	5	8		5	8		5	8		

Note 4: For operating at high temperatures, the LM324/LM324A/LM2902 must be derated based on a +125°C maximum junction temperature and a thermal resistance of 88°C/W which applies for the device soldered in a printed circuit board, operating in a still air ambient. The LM224/LM224A and LM124/LM124A can be derated based on a +150°C maximum junction temperature. The dissipation is the total of all four amplifiers — use external resistors, where possible, to allow the amplifier to saturate of to reduce the power which is dissipated in the integrated circuit.

Note 5: Short circuits from the output to V^+ can cause excessive heating and eventual destruction. When considering short circuits to ground, the maximum output current is approximately 40 mA independent of the magnitude of V^+. At values of supply voltage in excess of +15V, continuous short-circuits can exceed the power dissipation ratings and cause eventual destruction. Destructive dissipation can result from simultaneous shorts on all amplifiers.

Note 6: This input current will only exist when the voltage at any of the input leads is driven negative. It is due to the collector-base junction of the input PNP transistors becoming forward biased and thereby acting as input diode clamps. In addition to this diode action, there is also lateral NPN parasitic transistor action on the IC chip. This transistor action can cause the output voltages of the op amps to go to the V^+ voltage level (or to ground for a large overdrive) for the time duration that an input is driven negative. This is not destructive and normal output states will re-establish when the input voltage, which was negative, again returns to a value greater than −0.3V (at 25°C).

Note 7: These specifications are limited to −55°C ≤ T_A ≤ +125°C for the LM124/LM124A. With the LM224/LM224A, all temperature specifications are limited to −25°C ≤ T_A ≤ +85°C. the LM324/LM324A temperature specifications are limited to 0°C ≤ T_A ≤ +70°C, and the LM2902 specifications are limited to −40°C ≤ T_A ≤ +85°C.

Note 8: V_O = 1.4V, R_S = 0Ω with V^+ from 5V to 30V; and over the full input common-mode range (0V to V^+ − 1.5V) for LM2902, V^+ from 5V to 26V.

Note 9: The direction of the input current is out of the IC due to the PNP input stage. This current is essentially constant, independent of the state of the output so no loading change exists on the input lines.

Note 10: The input common-mode voltage of either input signal voltage should not be allowed to go negative by more than 0.3V (at 25°C). The upper end of the common-mode voltage range is V^+ − 1.5V (at 25°C), but either or both inputs can go to +32V without damage (+26V for LM2902), independent of the magnitude of V^+.

Note 11: Due to proximity of external components, insure that coupling is not originating via stray capacitance between these external parts. This typically can be detected as this type of capacitance increases at higher frequencies.

Note 12: Refer to RETS124AX for LM124A military specifications and refer to RETS124X for LM124 military specifications.

Note 13: Human body model, 1.5 kΩ in series with 100 pF.

APPENDIX H

DS 1104 R&D CONTROLLER BOARD

DS1104 R&D Controller Board

A Powerful Prototyping System in Your PC

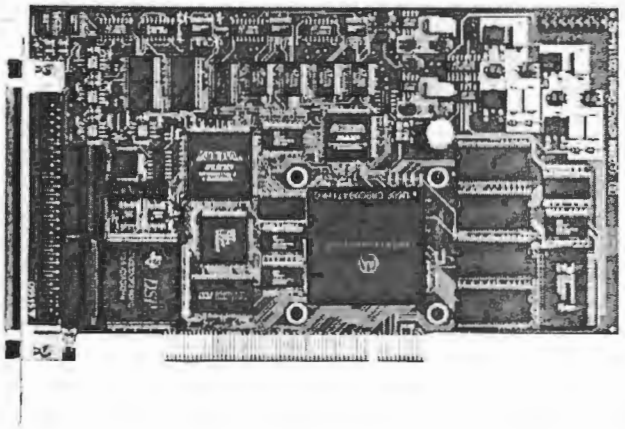

- **Cost-effective system for controller development**
- **Single-board PCI hardware for use in PCs**
- **Set of intelligent I/O on-board**
- **Fully programmable from the Simulink block diagram environment**

The DS1104 R&D Controller Board is a piece of hardware that upgrades your PC to a powerful development system for rapid control prototyping („R&D" stands for research & development).

The real-time hardware based on PowerPC technology and its set of I/O interfaces makes the board an ideal solution for developing controllers in various industrial fields. The DS1104 R&D Controller Board is impressive proof that power does not necessarily have to be expensive. The DS1104 is available at a reasonable price, making it the perfect development system for industry and equally for universities.

Yet it still gives you all the benefits of a dSPACE Prototyper system: full graphical configuration, programming in Simulink/Stateflow from The MathWorks and experiment control with state-of-the-art software tools. The board can be installed in virtually any PC with a free PCI slot. So why not make your PC a powerful development tool?

Software Support

- DS1104 [illegible] (included)
- Experimen[illegible] and Plattform Manage[illegible] or hardware management (included)
- Program[illegible]ng from Simu[illegible]nk w[illegible]th Real-Tin[illegible]nte[illegible]ace (RT[illegible], p. 70)
- Microte[illegible] (C-compiler [illegible] PowerP[illegible]p[illegible]oce[illegible]or (p. 67)
- Experin[illegible] Control[illegible] (p. 88) and MLIB/MTR[illegible] (E[illegible] 102.

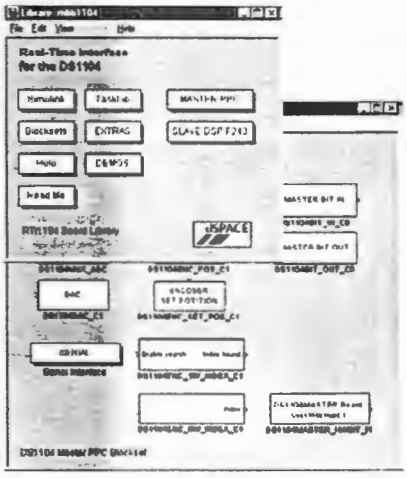

Real-Time i[illegible] Simulink b[illegible] configurati[illegible] lines, incre[illegible] and PWM[illegible]

[illegible] • dSPACE • Technologiepark 25 • [illegible]100 Paderborn • Germany • info@dspace[illegible] • www.dspace.de

Application Example: Induction Motor Control

In this example, an induction motor controller is developed with the DS1104. The slave DSP system was designed for applications in drive control, and the PowerPC's calculation power supports convenient simulation and a smooth development process. In combination with Simulink, the board makes it easy to verify and optimize control algorithms and parameters.

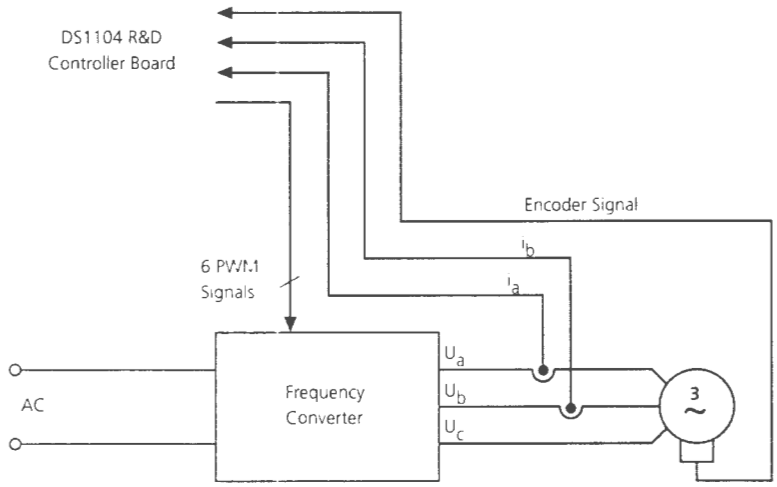

One of the board's incremental encoder interfaces picks up the encoder signal of the motor, while two A/D converters are required to analyze the motor currents. The DS1104 R&D Controller Board calculates the control algorithm on the basis of the measured values and determines the corresponding pulse width modulation (PWM) values. The three-phase PWM signals are generated on the board's DSP subsystem and determine the converter's output voltage and frequency.

Technical Details

Main Processor

- MPC8240, PowerPC 603e core, 250 MHz
- 32 KB internal cache

Timers

- 1 sample rate timer, 32-bit downcounter
- 4 general purpose timers, 32 bit
- 64-bit timebase for time measurement

Memory

- 32 MB synchronous DRAM (SDRAM)
- 8 MB boot flash for applications

Interrupt Control Unit

- Interrupts by timers, serial interface, slave DSP, incremental encoders, ADC, host PC and 4 external inputs
- PWM synchronous interrupt

Analog Input

- 4 ADC inputs with one ADC unit, 16 bit, multiplexed
- ± 10 V input voltage range
- 2 µs sampling time *)
- > 80 dB signal-to-noise ratio
- 4 ADC channels, 12 bit
- ± 10 V input voltage range
- 800 ns sampling time *)
- > 65 dB signal-to-noise ratio

Analog Output

- 8 channels, 16 bit, 10 µs max. settling time
- ± 10 V output voltage range

Real-Time Interface Execution Times for I/O blocks **)

	1 channel	all channels
Analog Input 16 bit	2.2 µs	10.1 µs
Analog Input 12 bit	1.5 µs	4.5 µs
Analog Output	1.2 µs	1.7 µs
Incremental Encoder Interface	1.2 µs	4.4 µs
Digital I/O (in/out)	(0.3 µs)	0.5/0.4 µs)

*) Speed and timing specifications describe the capabilities of the hardware components and circuits of our products. Depending on the software complexity, the attainable overall performance figures can deviate significantly from the hardware specifications.

**) Execution times are the times required by the real-time processor to execute the real-time code for the relevant I/O block generated by Real-Time Interface.

Incremental Encoder Interface

- Two digital inputs, TTL or RS422
- 24-bit digital incremental encoders
- Max. 1.65 MHz input frequency, i.e. fourfold pulse counts up to 6.6 MHz
- 5 V / 0.5 A sensor supply voltage

Digital I/O

- 20-bit digital I/O (bit-selectable direction)
- ± 5 mA output current

Serial Interface

- Serial UART (RS232, RS485 or RS422)

Slave DSP Subsystem

- Texas Instruments' DSP TMS320F240
- 4 kWord of dual-port RAM
- Three-phase PWM outputs plus 4 single PWM outputs
- Frequency measurement (F/D) and generation (D/F), 4 channels each
- 14 bits of digital I/O (TTL)

Physical Characteristics

- Power supply 5 V, 2.5 A / -12 V, 0.2 A / 12 V, 0.3 A
- Operating temperature 0 to 55 °C (32 to 131 °F)
- Requires one 33 MHz / 32-bit 5-V PCI slot

Order Number

DS1104 R&D Controller Board
- DS1104

Connector Panel
- CP1104

Combined Connector/LED Panel
- CLP1104

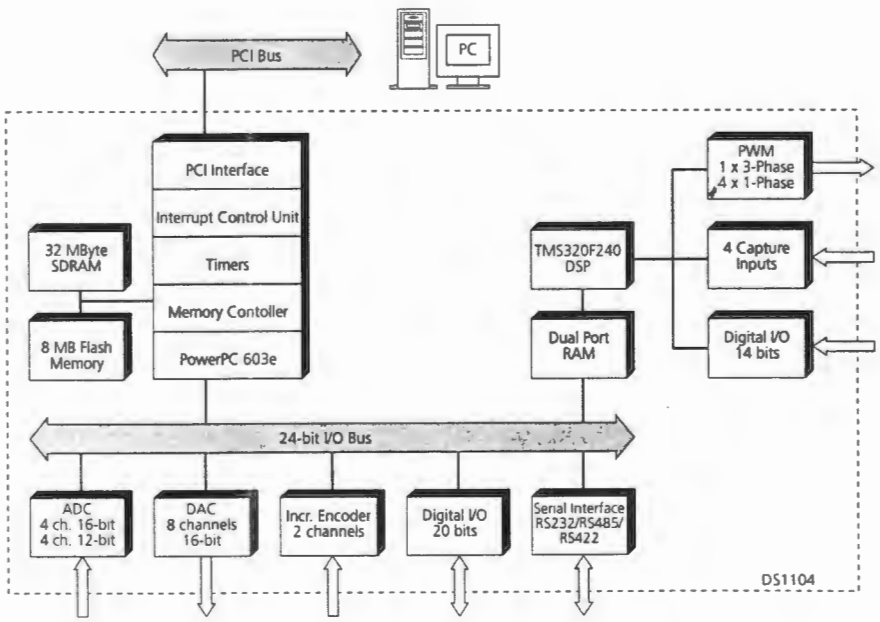

APPENDIX I

MATLAB SIMULINK MODELS OF THE DOUBLY-FED INDUCTION GENERATOR SYSTEM

CONTROL OF A DOUBLY-FED INDUCTION GENERATOR USING BACK-TO-BACK CONVERTERS

Rotor Side Control (Method2):

Field Orientation is with respect to the Stator Flux Vector

*Synchronous Speed = 2*pi*freq = 157.08 rad/s*
therefore
Subsynchronous Speed = 125.66 rad/s
Supersynchronous Speed = 157.08 rad/s

Control of Supply-Side Converter:

Orientation of the Reference Frame is with respect to the Supply Voltage Position

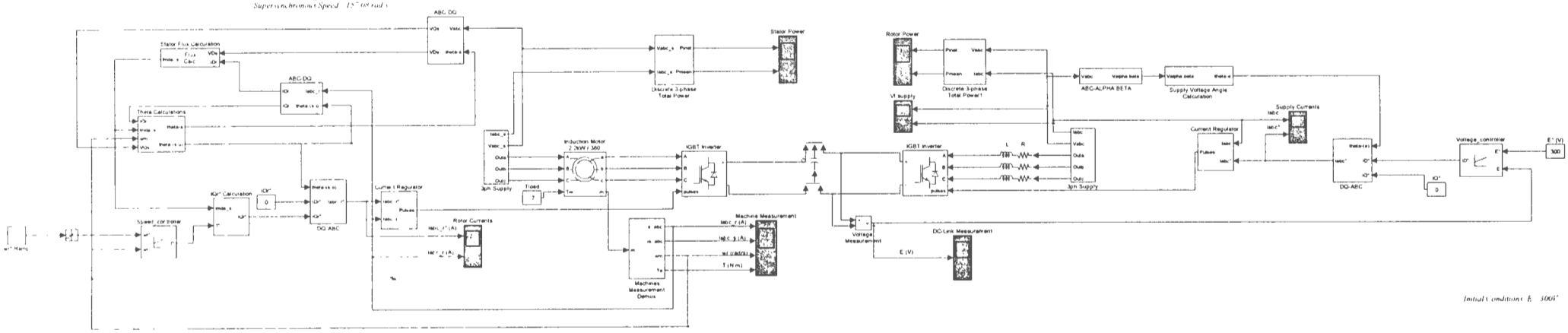

Initial Conditions: wm = 125 rad/s
Tload = 7 N.m

Initial Conditions: E = 300V

By: Paul Barendse

CONTROL OF A DOUBLY-FED INDUCTION GENERATOR USING BACK-TO-BACK CONVERTERS

Rotor Side Control (Method1):

Field Orientation is with respect to the Stator Flux Vector

*Synchronous Speed = 2*pi*f/p = 157.08rad/s*
therefore
Subsynchronous Speed = 157.08 rad/s
Supersynchronous Speed = 157.08 rad/s

Control of Supply-Side Converter:

Orientation of the Reference Frame is with respect to the Supply Voltage Position

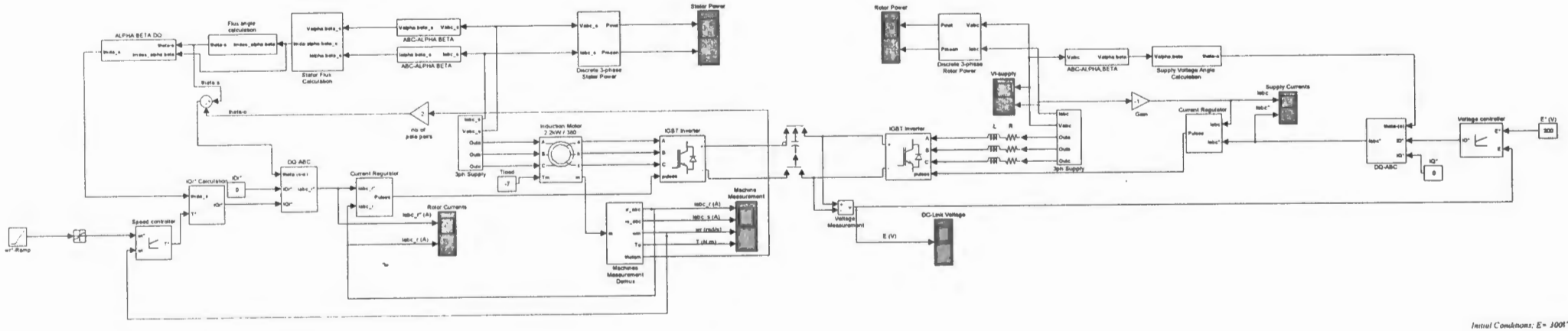

Initial Conditions: E= 300V

Initial Conditions: wm = 157rad/s
Tload = 7Nm

By: Paul Barendse

Rotor Side Control (Method1):

Field Orientation is with respect to the Stator Flux Vector

*Synchronous Speed = 2*pi*f/p =157.08rad/s*
therefore
Subsynchronous Speed < 157.08 rad/s
Supersynchronous Speed >157.08 rad/s

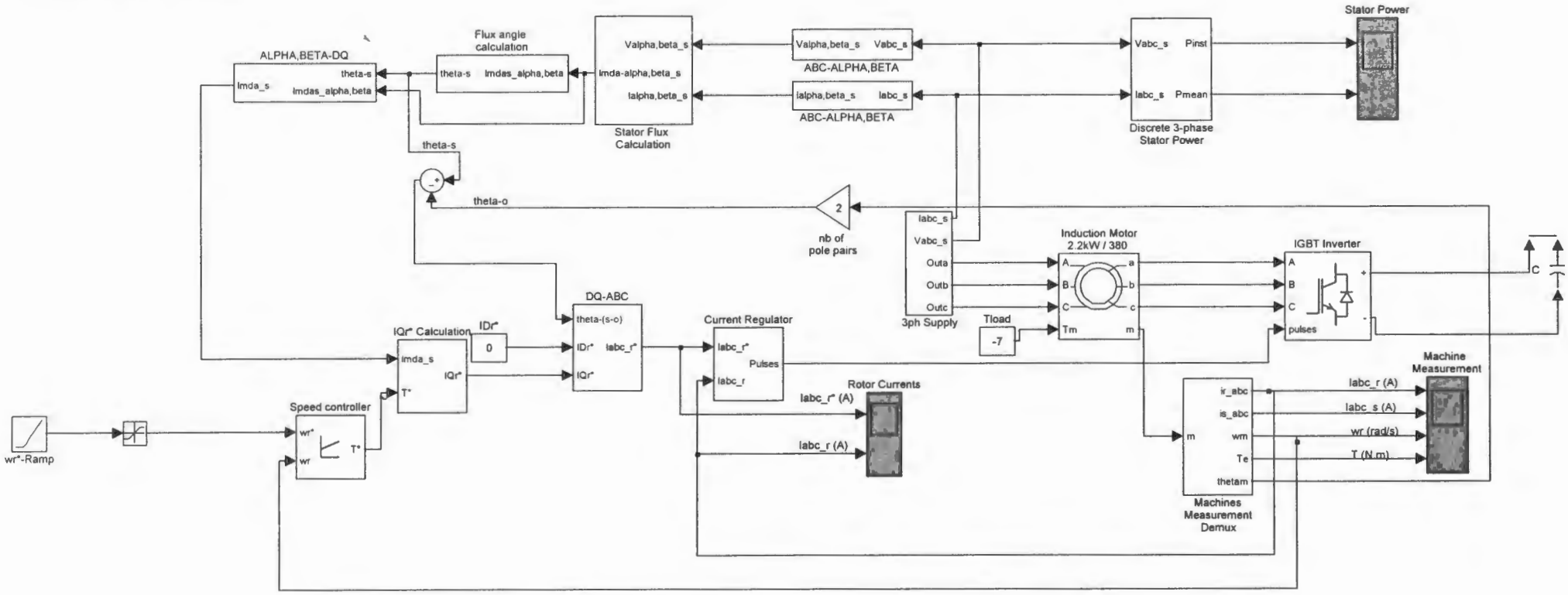

Initial Conditions: wm= 117rad/s
Tload=-7N.m

By: Paul Barendse

Rotor Side Control (Method2):

Field Orientation is with respect to the Stator Flux Vector

*Synchronous Speed 2*pi*f/p 157.08rad/s*
therefore
Subsynchronous Speed 157.08 rad/s
Supersynchronous Speed 157.08 rad/s

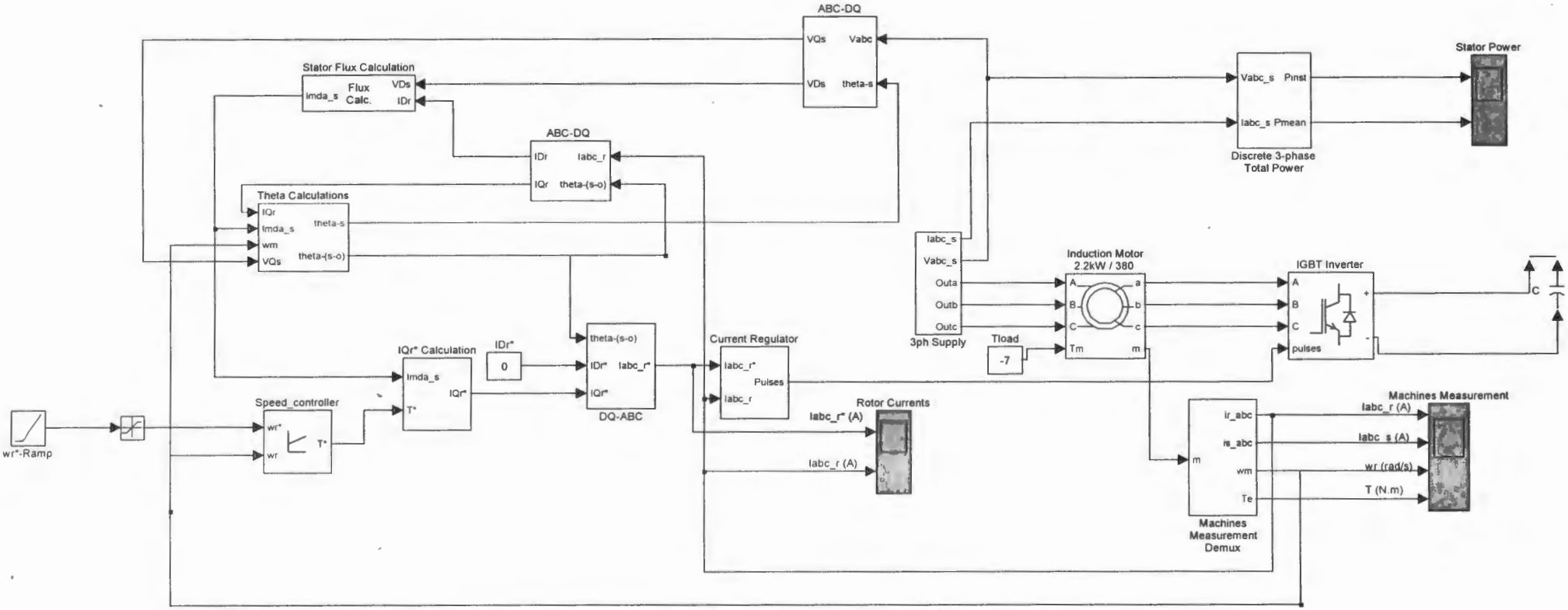

Initial Conditions: wm = 117rad/s
Tload = -7N.m

By: Paul Barendse

Control of Supply-Side Converter:

Orientation of the Reference Frame is with respect to the Supply Voltage Position

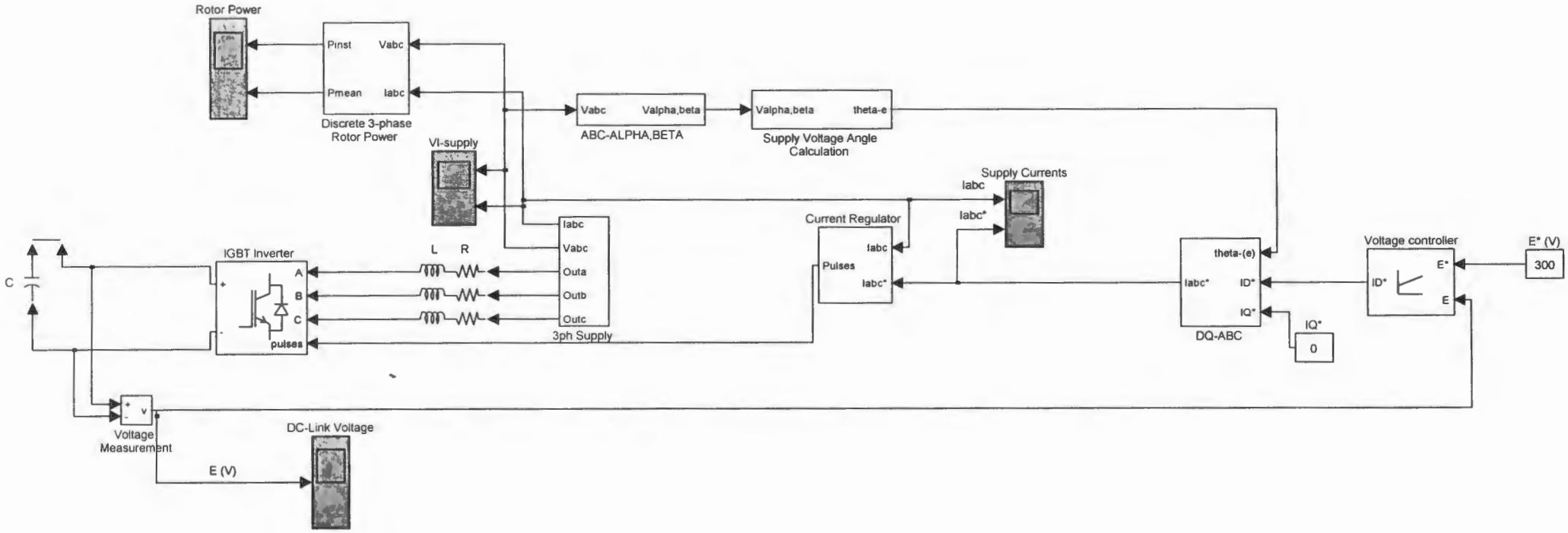

Initial Conditions: E= 300V

By: Paul Barendse

3-Phase Supply and Measurement

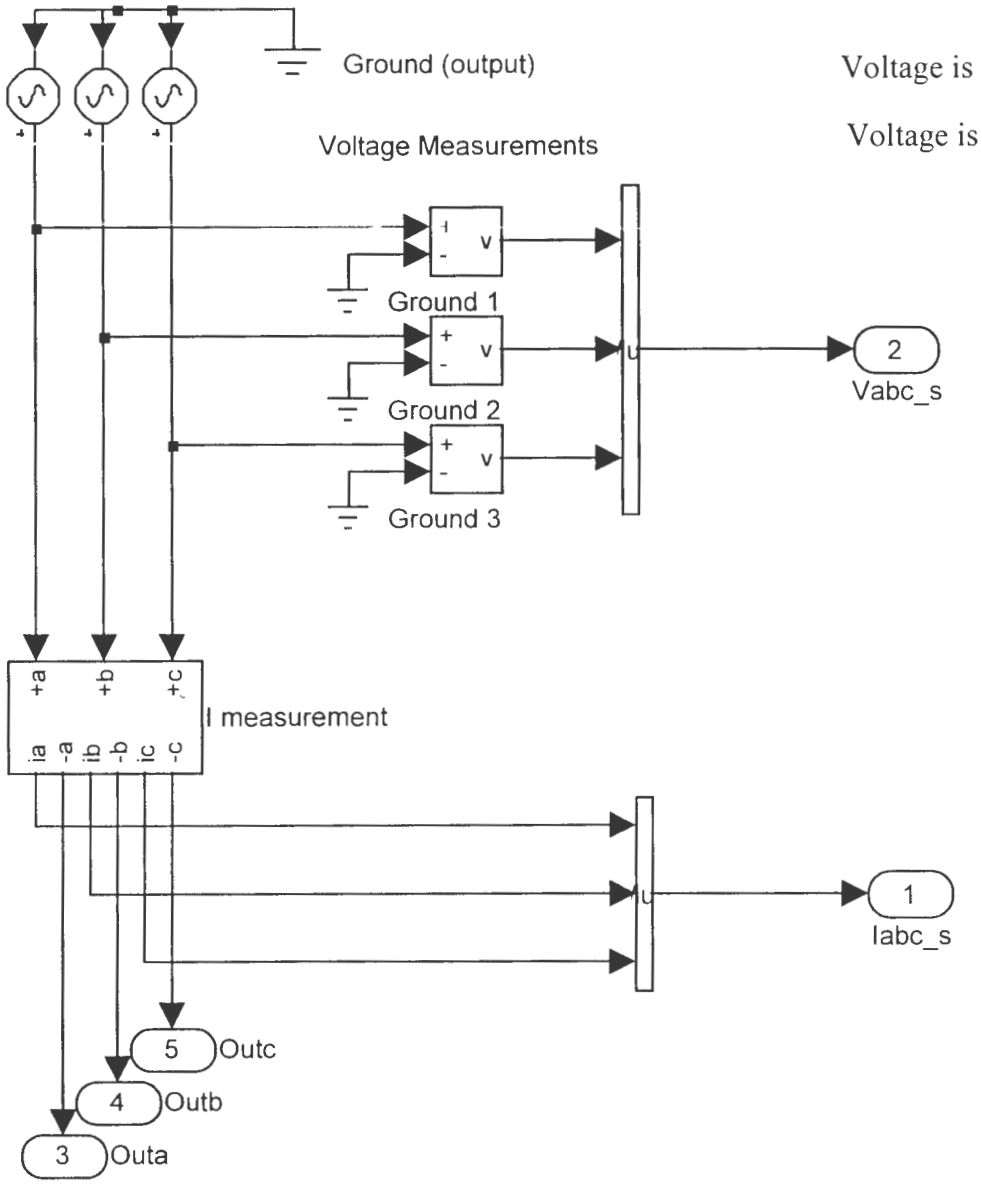

Voltage is set to 380V for the Rotor-Side Control

Voltage is set to 100V for the Supply-Side Control

A, B, C to ALPHA, BETA TRANSFORMATION

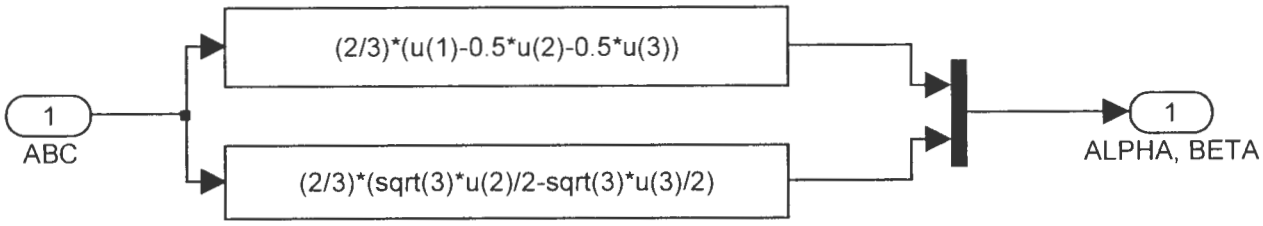

Clarke Transform: [2/3 -1/3 -1/3,
0 1/sqrt(3) -1/sqrt(3)]

STATOR FLUX CALCULATION

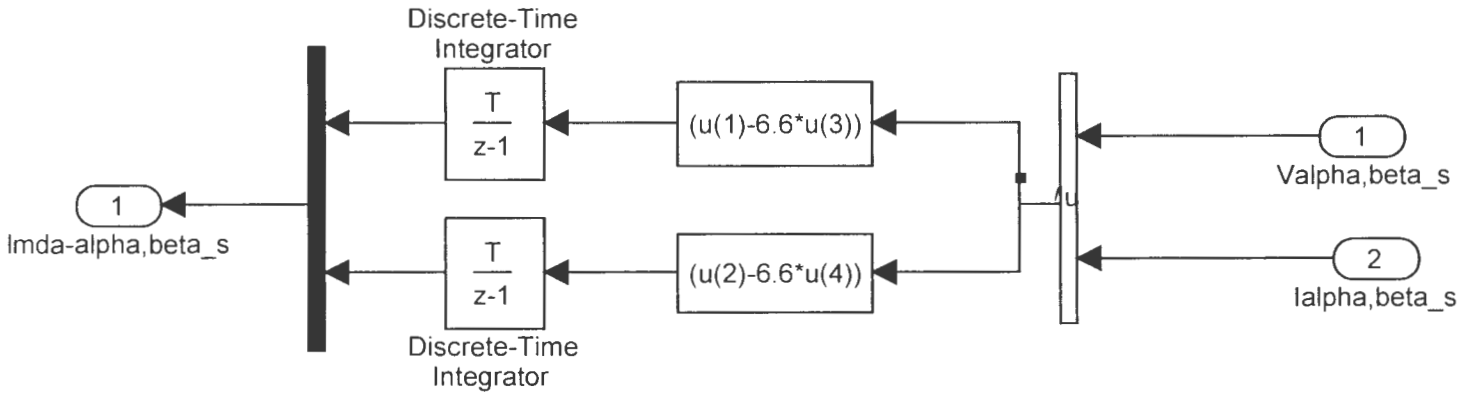

lmdas_alpha = integ(Vs_alpha - Rs .Is_alpha)

lmdas_beta = integ(Vs_beta - Rs .Is_beta)

Rs = 0.087 ohms

FLUX ANGLE CALCULATION

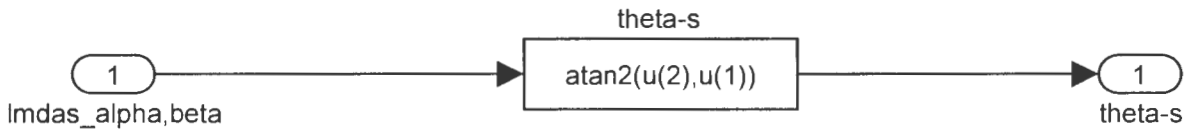

Theta-s=arctan(lmdas_beta/lmdas_alpha)

ALPHA, BETA to D, Q TRANSFORMATION-LMDA_S

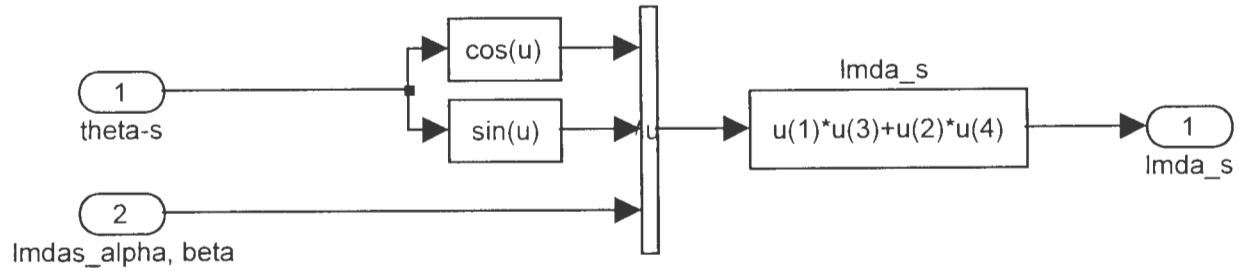

Parke Transform: [cos(wt) sin(wt),
-sin(wt) cos(wt)]

VOLTAGE CONTROLLER

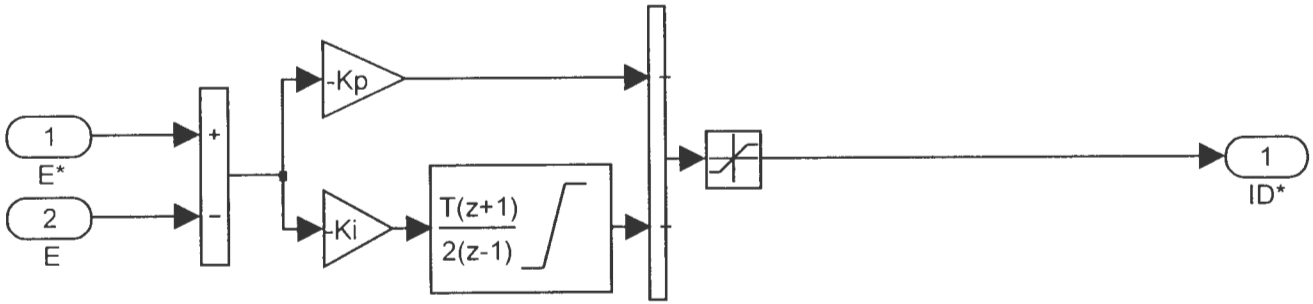

Kp=1.685

Ki=0.18

T=0.01s

SPEED CONTROLLER

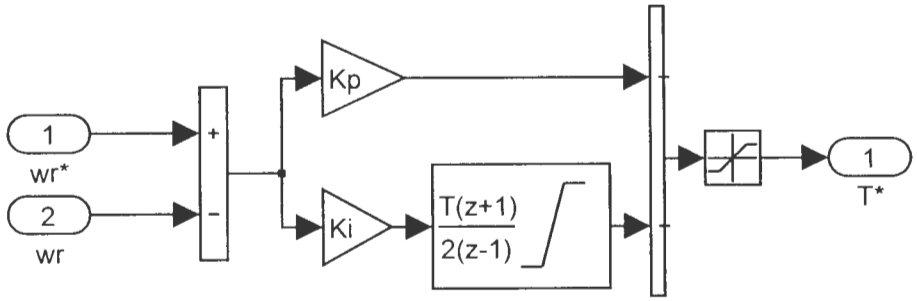

Kp=0.335

Ki=0.075

T=0.1s

IQr* CALCULATION

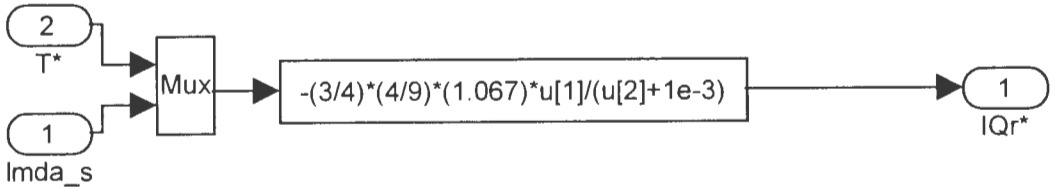

IQr*= -(3/P) * (4/9) * (Ls/Lm) * (T* / Lmda_s)

Lm = 416.98 mH

Ls = Ll's +Lm = 28.1 +416.98= 445.08mH

P= nb of poles = 4

ALPHA, BETA to D, Q TRANSFORMATION

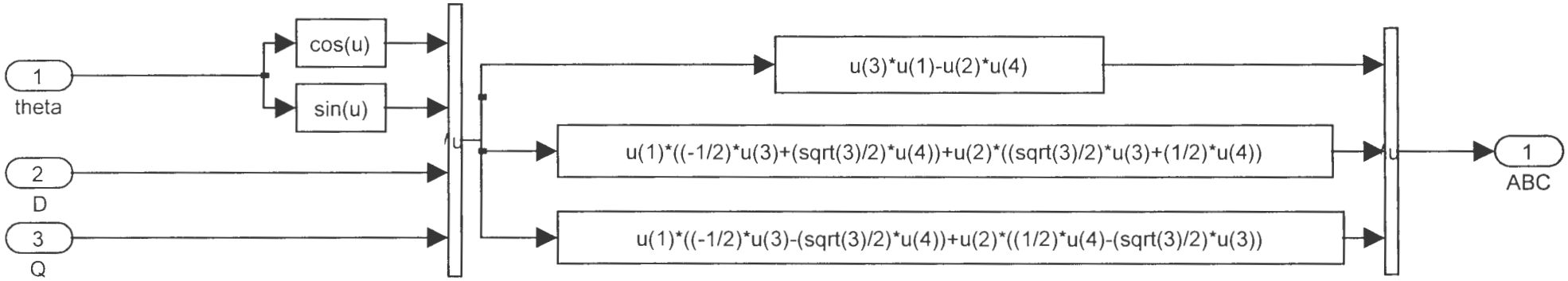

Inv Clarke/Parke Transform :[coswt -sinwt,
-(1/2)coswt + (sqrt(3)/2)sinwt (1/2)sinwt + (sqrt(3)/2)coswt,
-(1/2)coswt - (sqrt(3)/2)sinwt (1/2)sinwt - (sqrt(3)/2)coswt]

Discrete 3-phase Total Power

Pierre Giroux, Gilbert Sybille
Power System Simulation Laboratory
IREQ, Hydro-Quebec

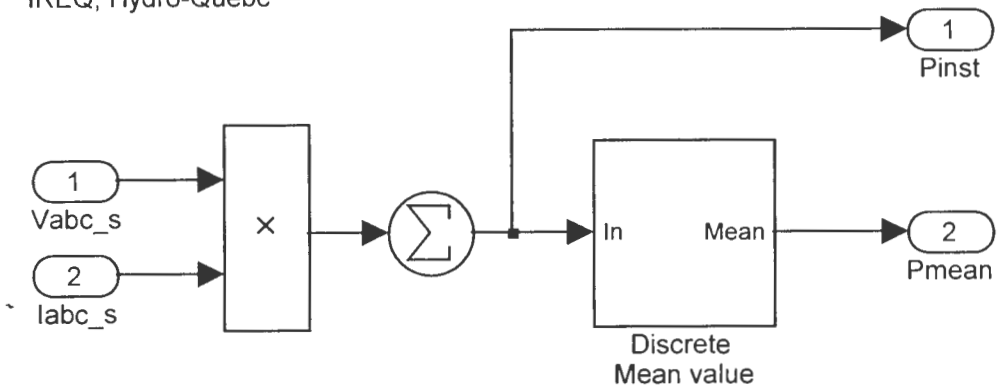

SUPPLY VOLTAGE ANGLE CALCULATION

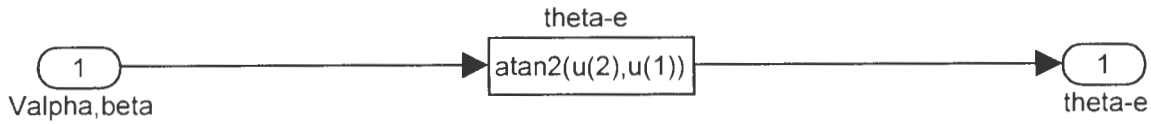

Theta-e=arctan(Vbeta/Valpha)

THETA CALCULATIONS

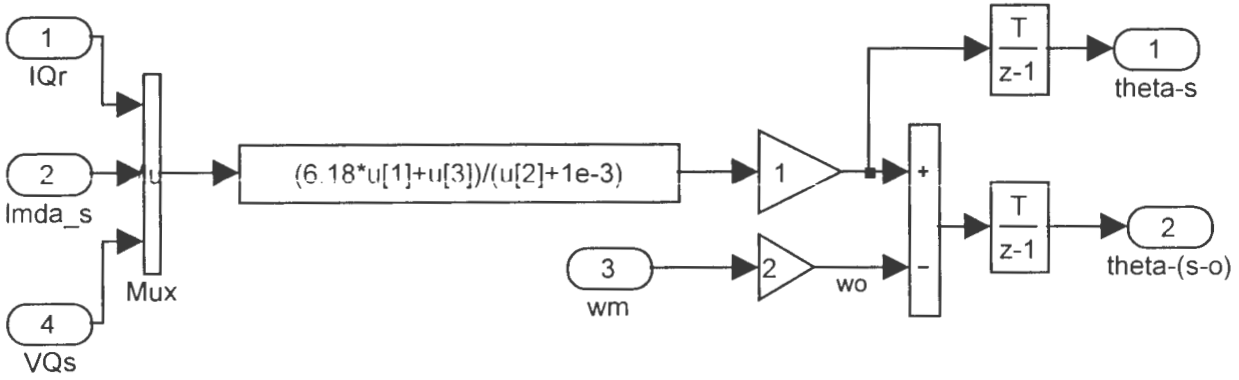

ws = Supply frequency (rad/s)-aligned with the stator flux vector = (1/Imda_s)*(VQs+(Lm/Ts)iQr)

wm= Rotor mechanical speed (rad/s)

wo= Rotor electrical speed (rad/s)

theta(s-o)= Electrical angle= integ (ws - wm)

theta(s)= Electrical angle= integ (ws)

Lm = 416.98mH

Ts = Ls / Rs = 0.067436s

Ls = Ll's +Lm =416.98 +28.1=445 mH

Rs = 6.6 ohms

STATOR FLUX CALCULATION

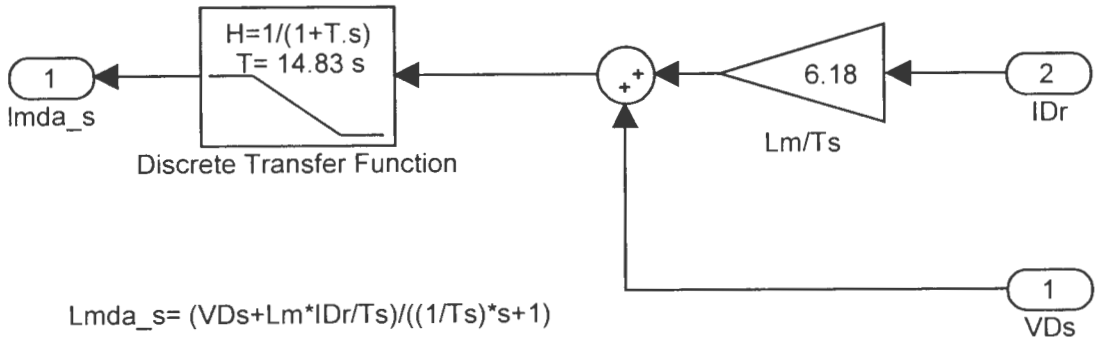

Lmda_s= (VDs+Lm*IDr/Ts)/((1/Ts)*s+1)

Lm = 416.98mH

Ts = Ls / Rs = 0.067436s

Ls = Ll's +Lm =416.98 +28.1=445 mH

Rs = 6.6 ohms

Current Regulator (Hysteresis Current Controller)

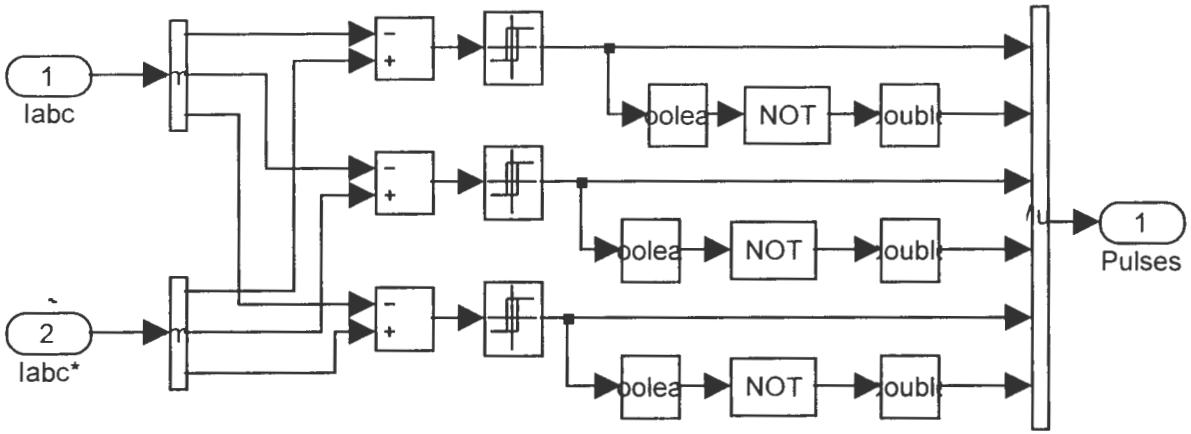

APPENDIX J

MATLAB SIMULINK MODELS WITH REAL-TIME INTERFACE (RTI) OF THE DOUBLY-FED INDUCTION GENERATOR SYSTEM

CONTROL OF A DOUBLY-FED INDUCTION GENERATOR USING BACK-TO-BACK CONVERTERS

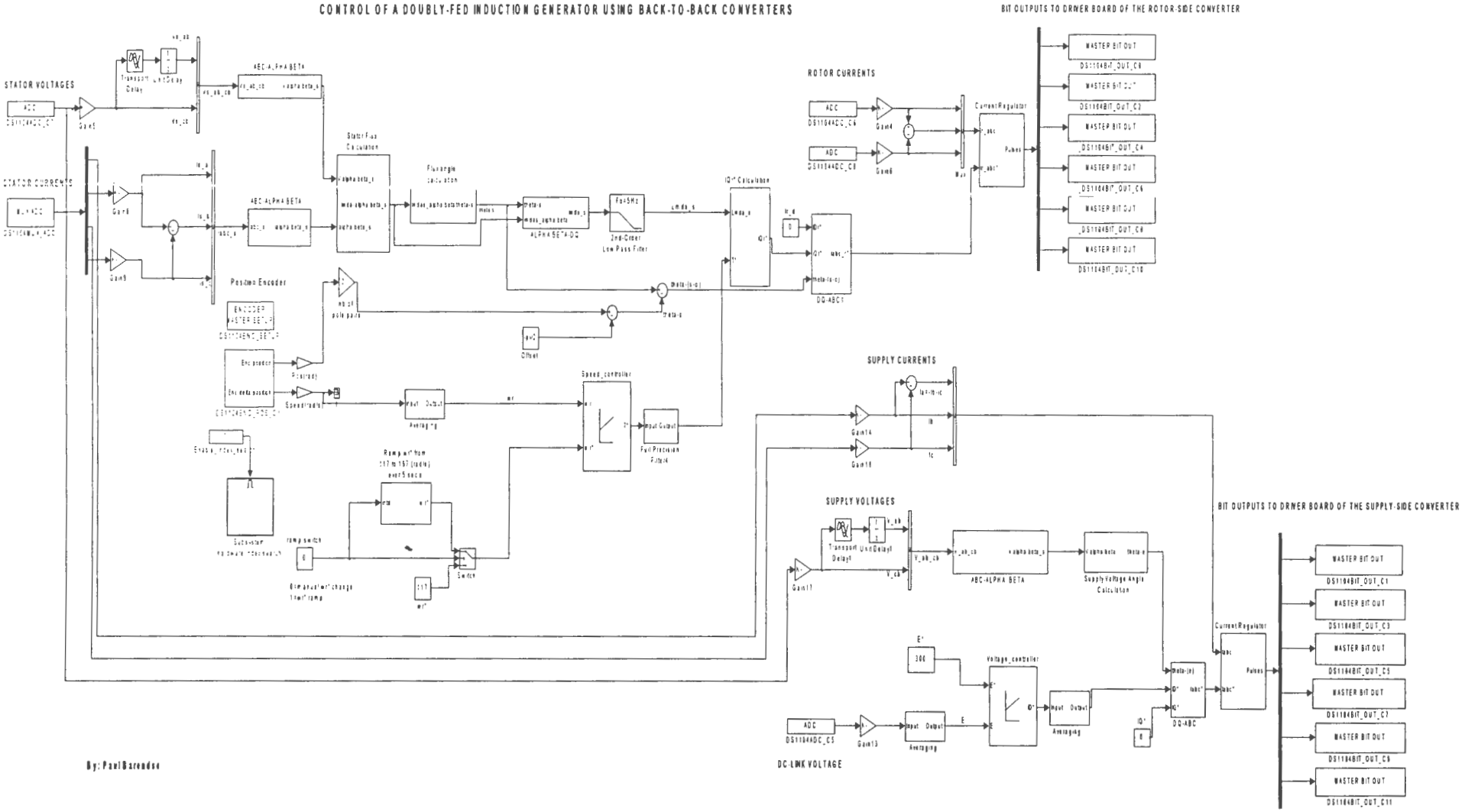

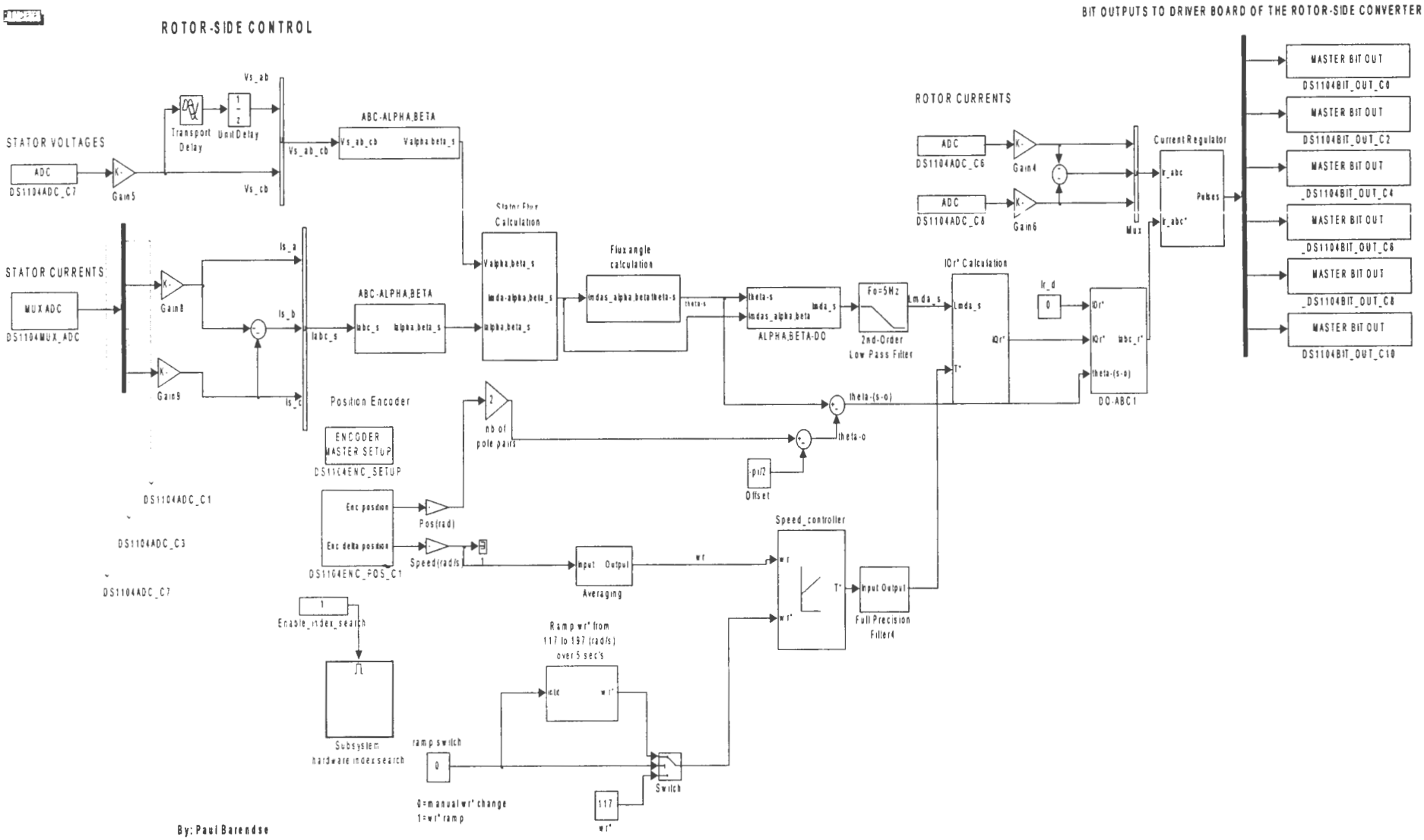
ROTOR-SIDE CONTROL
BIT OUTPUTS TO DRIVER BOARD OF THE ROTOR-SIDE CONVERTER
STATOR VOLTAGES
ADC
DS1104ADC_C7
Gain5
Transport Delay
Unit Delay
Vs_ab
Vs_cb
ABC-ALPHA,BETA
Vs_ab_cb
Valpha,beta_s
STATOR CURRENTS
MUX ADC
DS1104MUX_ADC
Gain8
Gain9
Is_a
Is_b
Is_c
Iabc_s
ABC-ALPHA,BETA
Ialpha,beta_s
Stator Flux Calculation
Valpha,beta_s
Imda-alpha,beta_s
Ialpha,beta_s
Flux angle calculation
Imdas_alpha,betatheta-s
theta-s
ALPHA,BETA-DQ
Imdas_alpha,beta
Imds_s
Fo=5Hz
2nd-Order Low Pass Filter
Lmds_s
ROTOR CURRENTS
ADC
DS1104ADC_C6
Gain4
ADC
DS1104ADC_C8
Gain6
Mux
IQr* Calculation
Lmds_s
IQr*
T*
Ir_d
0
IDr*
IQr*
Iabc_r*
theta-(s-o)
DQ-ABC1
Current Regulator
Ir_abc
Ir_abc*
Pulses
MASTER BIT OUT
DS1104BIT_OUT_C0
MASTER BIT OUT
DS1104BIT_OUT_C2
MASTER BIT OUT
DS1104BIT_OUT_C4
MASTER BIT OUT
DS1104BIT_OUT_C6
MASTER BIT OUT
DS1104BIT_OUT_C8
MASTER BIT OUT
DS1104BIT_OUT_C10
Position Encoder
ENCODER MASTER SETUP
DS1104ENC_SETUP
DS1104ADC_C1
DS1104ADC_C3
DS1104ADC_C7
Enc posdon
Enc delta posdon
DS1104ENC_POS_C1
Pos(rad)
Speed(rad/s
2
nb of pole pairs
theta-(s-o)
theta-o
-pi/2
Offset
Speed_controller
wr
wr*
T*
Input Output
Full Precision Filter4
Input Output
Averaging
wr
1
Enable_index_search
Subsystem
hardware index search
Ramp wr* from
117 to 197 (rad/s)
over 5 sec's
rate
wr*
ramp switch
0
0=manual wr* change
1=wr* ramp
Switch
117
wr*
By: Paul Barendse

CONTROL OF A DOUBLY-FED INDUCTION GENERATOR USING BACK-TO-BACK CONVERTERS

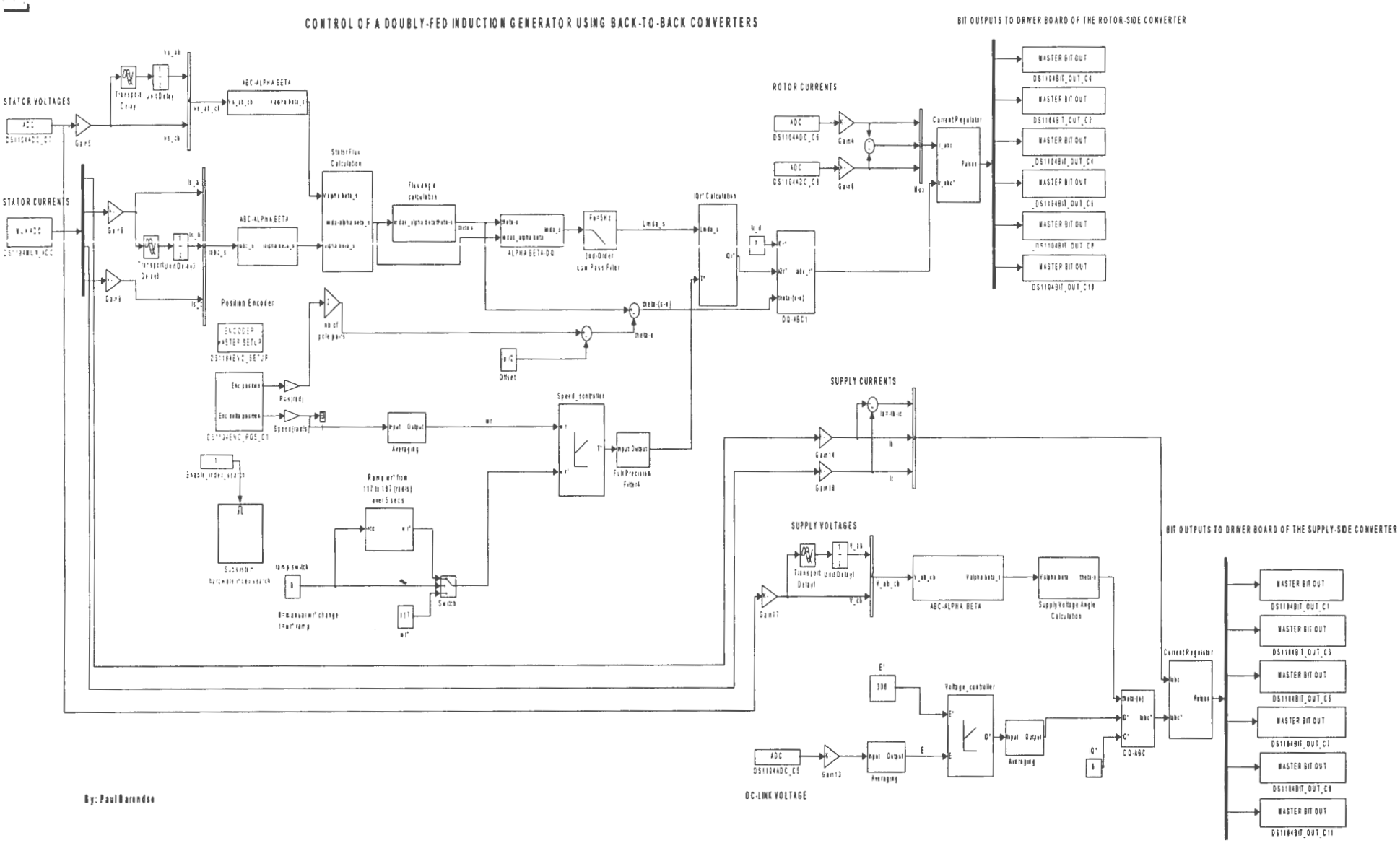

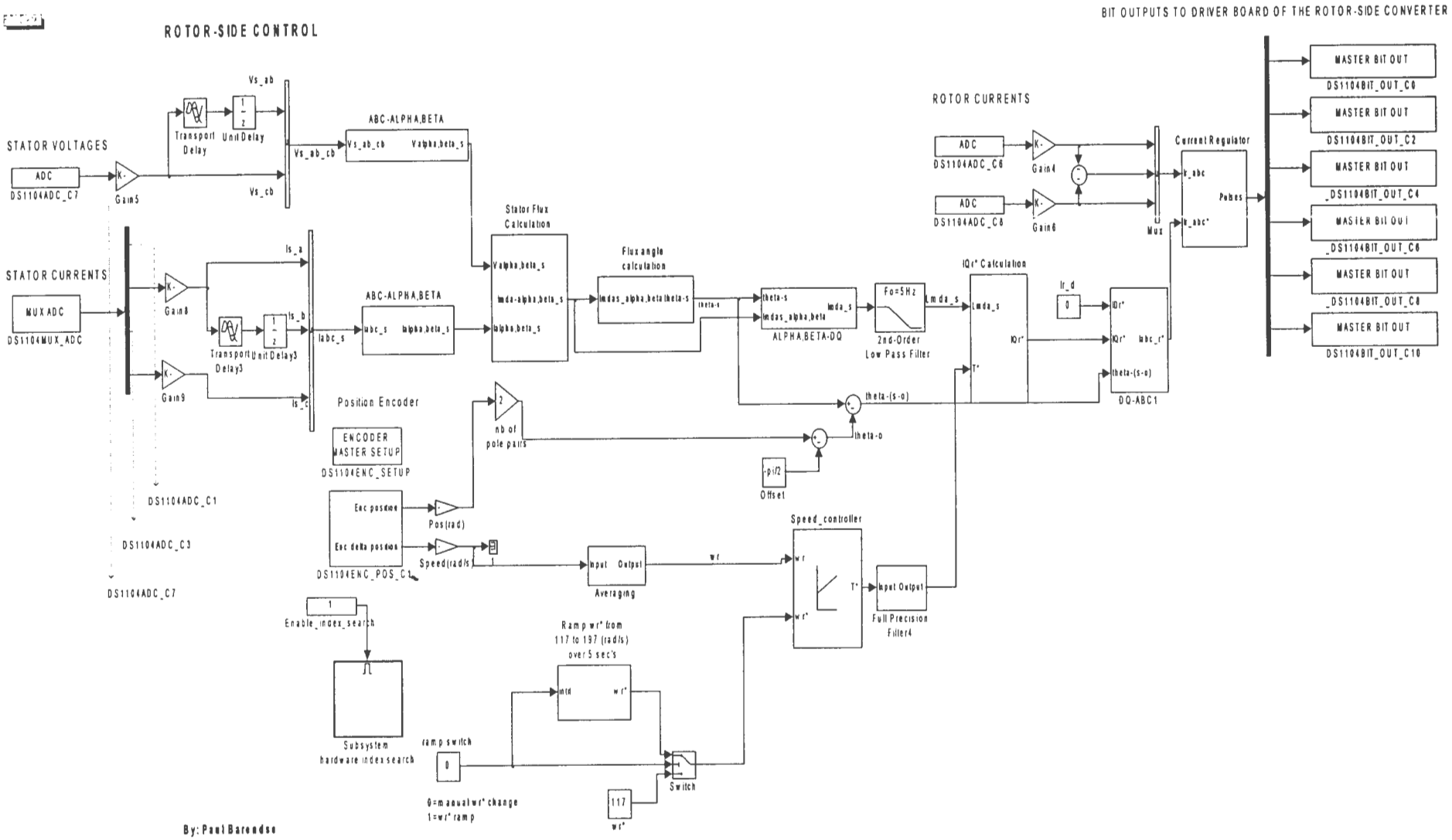
ROTOR-SIDE CONTROL
BIT OUTPUTS TO DRIVER BOARD OF THE ROTOR-SIDE CONVERTER
STATOR VOLTAGES
ADC
DS1104ADC_C7
Gain5
Transport Delay
Unit Delay
Vs_ab
Vs_cb
Vs_ab_cb
ABC-ALPHA,BETA
Vs_ab_cb
Valpha,beta_s
STATOR CURRENTS
MUX ADC
DS1104MUX_ADC
Gain8
Gain9
Transport Delay3
Unit Delay3
Is_a
Is_b
Is_c
Iabc_s
ABC-ALPHA,BETA
Iabc_s
Ialpha,beta_s
Stator Flux Calculation
Valpha,beta_s
lmda-alpha,beta_s
Ialpha,beta_s
Flux angle calculation
lmdas_alpha,beta
theta-s
theta-s
lmdas_alpha,beta
lmda_s
ALPHA,BETA-DQ
Fo=5Hz
2nd-Order Low Pass Filter
lmda_s
IQr* Calculation
lmda_s
IQr*
T*
Ir_d
0
IDr*
IQr*
Iabc_r*
theta-(s-o)
DQ-ABC1
ROTOR CURRENTS
ADC
DS1104ADC_C6
Gain4
ADC
DS1104ADC_C8
Gain6
Mux
Current Regulator
Ir_abc
Ir_abc*
Pulses
MASTER BIT OUT
DS1104BIT_OUT_C0
MASTER BIT OUT
DS1104BIT_OUT_C2
MASTER BIT OUT
DS1104BIT_OUT_C4
MASTER BIT OUT
DS1104BIT_OUT_C6
MASTER BIT OUT
DS1104BIT_OUT_C8
MASTER BIT OUT
DS1104BIT_OUT_C10
Position Encoder
ENCODER MASTER SETUP
DS1104ENC_SETUP
nb of pole pairs
theta-o
-pi/2
Offset
theta-(s-o)
DS1104ADC_C1
DS1104ADC_C3
DS1104ADC_C7
Enc posdeg
Enc delta posdeg
DS1104ENC_POS_C1
Pos(rad)
Speed(rad/s)
Averaging
wr
Speed_controller
wr
wr*
T*
Input Output
Full Precision Filter4
Enable_index_search
Subsystem
hardware index search
Ramp wr* from
117 to 197 (rad/s)
over 5 sec's
Integrator
wr*
ramp switch
0=manual wr* change
1=wr* ramp
Switch
117
wr*
By: Paul Barendse

RTICata

SUPPLY-SIDE CONTROL

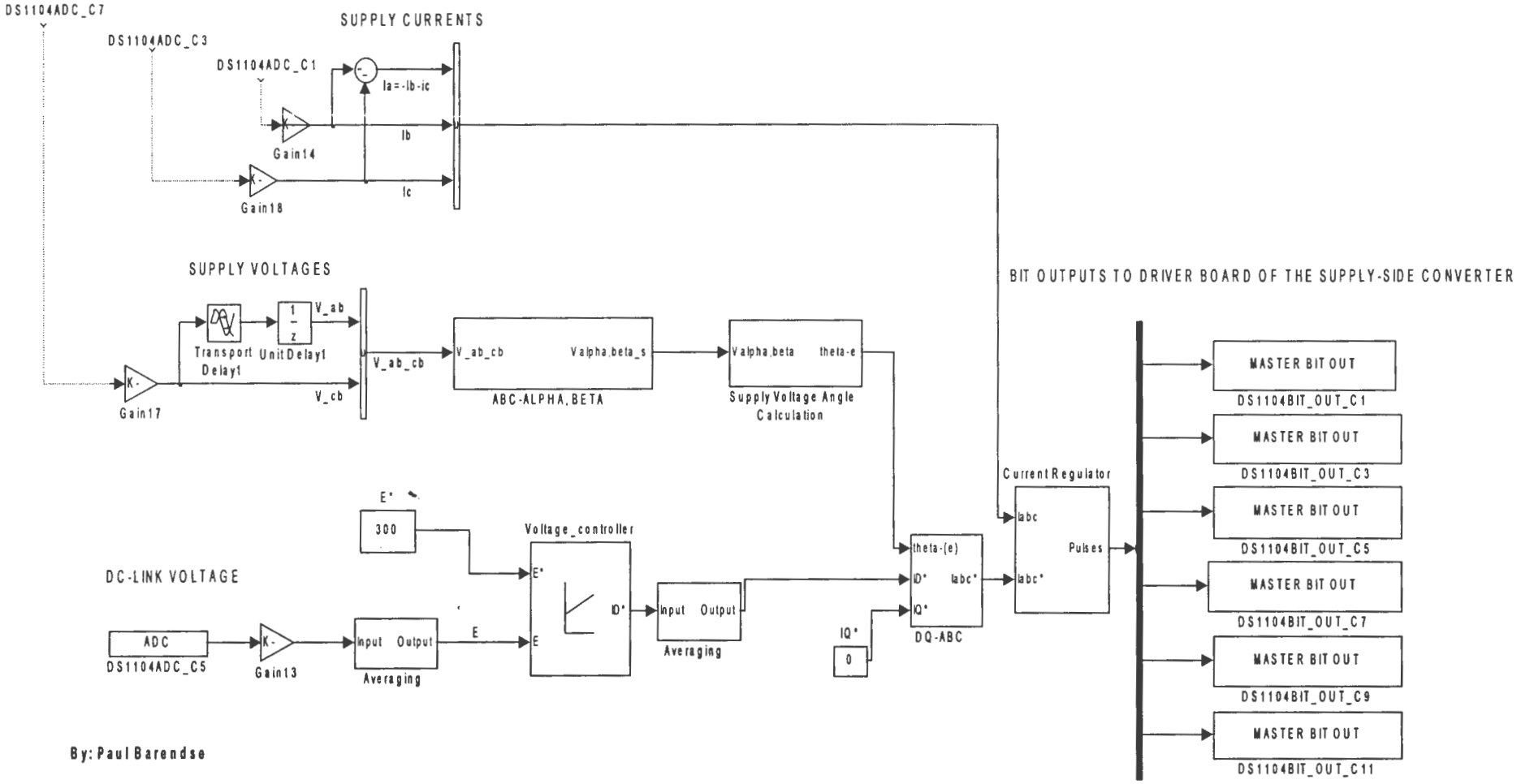

By: Paul Barendse

APPENDIX K

MATLAB CODE:

- **Stator current spectrum of the DFIG**
- **Stator current spectrum of the Squirrel Cage Induction Generator**

```
%//////////////////////FFT_Sub-Synchronous Speed//////////////////////

%By: Paul Barendse
%Date: 01/09/04


N=8192*32*2;
p=5001;
s=50;


figure(1)

%Healthy

i=healthy_ss_subsync.Y(6).Data;
i(p:N)=0;
I=fft(i,N);
n=length(I);
pI=abs(I(1:n/2)).^2;
subplot(3,1,1),plot(50/5240:50/5240:(50/5240)*n/2,10*log10(pI),'b');
axis([50 150 0 70]);
title('Logarithmic Power Spectral Density for operation at 1120rpm');
grid on


%280ohm Turn Fault

i=turnfault280ohm_ss_subsync.Y(7).Data;
i(p:N)=0;
I=fft(i,N);
n=length(I);
pI=abs(I(1:n/2)).^2;
subplot(3,1,2),plot(50/5252:50/5252:(50/5252)*n/2,10*log10(pI));
axis([50 150 0 70]);
ylabel('Magnitude (dB)');
grid on


%180ohm Turn Fault

i=turnfault180ohm_ss_subsync.Y(7).Data;
i(p:N)=0;
I=fft(i,N);
n=length(I);
pI=abs(I(1:n/2)).^2;
subplot(3,1,3),plot(50/5252:50/5252:(50/5252)*n/2,10*log10(pI));
axis([50 150 0 70]);
xlabel('Frequency (Hz)');
grid on
```

```
%//////////////////////FFT_Super-Synchronous Speed//////////////////////

%By: Paul Barendse
%Date: 01/09/04


N=8192*32*2;
p=5001;
s=50;

figure(2)


%Healthy

i=healthy_ss_supersync.Y(7).Data;
i(p:N)=0;
I=fft(i,N);
n=length(I);
pI=abs(I(1:n/2)).^2;
subplot(3,1,1),plot(50/5240:50/5240:(50/5240)*n/2,10*log10(pI),'b');
axis([100 200 0 70]);
grid on
title('Logarithmic Power Spectral Density for operation at 1880rpm');


%280ohm Turn Fault

i=turnfault280ohm_ss_supersync.Y(7).Data;
i(p:N)=0;
I=fft(i,N);
n=length(I);
pI=abs(I(1:n/2)).^2;
subplot(3,1,2),plot(50/5252:50/5252:(50/5252)*n/2,10*log10(pI));
axis([100 200 0 70]);
ylabel('Magnitude (dB)');
grid on


%180ohm Turn Fault

i=turnfault180ohm_ss_supersync.Y(7).Data;
i(p:N)=0;
I=fft(i,N);
n=length(I);
pI=abs(I(1:n/2)).^2;
subplot(3,1,3),plot(50/5252:50/5252:(50/5252)*n/2,10*log10(pI));
axis([100 200 0 70]);
xlabel('Frequency (Hz)');
grid on
```

```
%//////////////////////FFT_Transient Response//////////////////////

%By: Paul Barendse
%Date: 01/09/04



N=8192*32*2;
p=50001;
s=50;

figure(3)

%Healthy

i=healthy_transient.Y(6).Data;
i(p:N)=0;
I=fft(i,N);
n=length(I);
pI=abs(I(1:n/2)).^2;
subplot(3,1,1),plot(50/5241:50/5241:(50/5241)*n/2,10*log10(pI),'b');
axis([100 200 0 90]);
grid on


%280ohm Turn Fault

i=turnfault280ohm_transient.Y(7).Data;
i(p:N)=0;
I=fft(i,N);
n=length(I);
pI=abs(I(1:n/2)).^2;
subplot(3,1,2),plot(50/5227:50/5227:(50/5227)*n/2,10*log10(pI));
axis([100 200 0 90]);
ylabel('Magnitude (dB)');
grid on


%180ohm Turn Fault

i=turnfault180ohm_transient.Y(7).Data;
i(p:N)=0;
I=fft(i,N);
n=length(I);
pI=abs(I(1:n/2)).^2;
subplot(3,1,3),plot(50/5246:50/5246:(50/5246)*n/2,10*log10(pI));
axis([100 200 0 90]);
xlabel('Frequency (Hz)');
grid on
```

```
%//////////////////////FFT_Broken Rotor Bar Fault_825rpm ////////////////
///////

%By: Paul Barendse
%Date: 01/09/04


N=8192*32*2;
p=5001;
s=50;


figure(1)

%Healthy

i=I.signals(1).values;
i(p:N)=0;
L=fft(i,N);
n=length(L);
pI=abs(L(1:n/2)).^2;
subplot(2,1,1),plot(50/(4*5240):50/(4*5240):(50/(4*5240))*n/2,10*log10(pI
,'k');
axis([20 45 0 70]);
title('Logarithmic Power Spectral Density');
grid on
ylabel('Healthy Machine');


%Broken Rotor Bar

i=If.signals(1).values;
i(p:N)=0;
L=fft(i,N);
n=length(L);
pI=abs(L(1:n/2)).^2;
subplot(2,1,2),plot(50/(4*5240):50/(4*5240):(50/(4*5240))*n/2,10*log10(pI
,'k');
axis([0 70 0 70]);
ylabel('Damaged Machine');
xlabel('Frequency (Hz');
grid on
```

```
%//////////////////////FFT_Broken Rotor Bar Fault_1650rpm ////////////////
////////

%By: Paul Barendse
%Date: 01/09/04


N=8192*32*2;
p=5001;
s=50;


figure(1)

%Healthy

i=I.signals(1).values;
i(p:N)=0;
L=fft(i,N);
n=length(L);
pI=abs(L(1:n/2)).^2;
subplot(2,1,1),plot(50/5240:50/5240:(50/5240)*n/2,10*log10(pI),'k');
axis([0 150 0 70]);
title('Logarithmic Power Spectral Density for operation at 1650rpm');
grid on
ylabel('Healthy Machine');


%Broken Rotor Bar

i=If.signals(1).values;
i(p:N)=0;
L=fft(i,N);
n=length(L);
pI=abs(L(1:n/2)).^2;
subplot(2,1,2),plot(50/5240:50/5240:(50/5240)*n/2,10*log10(pI),'k');
axis([0 150 0 70]);
ylabel('Damaged Machine');
xlabel('Frequency (Hz');
grid on
```

```
%//////////////////////FFT_Transient Response_Broken Rotor Bar Fault////
//////////////////

%By: Paul Barendse
%Date: 01/09/04



N=8192*32*2;
p=30001;
s=50;

figure(3)

%Healthy

i=I.signals(1).values;
i(p:N)=0;
I=fft(i,N);
n=length(I);
pI=abs(I(1:n/2)).^2;
subplot(2,1,1),plot(50/5241:50/5241:(50/5241)*n/2,10*log10(pI),'b');
axis([20 80 0 80]);
grid on
ylabel('Healthy Machine');
title('Logarithmic Power Spectral Density');

%Broken Rotor Bar

i=If.signals(1).values;
i(p:N)=0;
I=fft(i,N);
n=length(I);
pI=abs(I(1:n/2)).^2;
subplot(2,1,2),plot(50/5227:50/5227:(50/5227)*n/2,10*log10(pI));
axis([20 80 0 80]);
ylabel('Damaged Machine');
grid on

xlabel('Frequency (Hz');
```